



HAL
open science

Beyond the gap of pressure: XPS studies of interfaces at near ambient pressures

Héloïse Tissot

► **To cite this version:**

Héloïse Tissot. Beyond the gap of pressure: XPS studies of interfaces at near ambient pressures. Analytical chemistry. Université Pierre et Marie Curie - Paris VI, 2014. English. NNT : 2014PA066615 . tel-01146994

HAL Id: tel-01146994

<https://theses.hal.science/tel-01146994>

Submitted on 29 Apr 2015

HAL is a multi-disciplinary open access archive for the deposit and dissemination of scientific research documents, whether they are published or not. The documents may come from teaching and research institutions in France or abroad, or from public or private research centers.

L'archive ouverte pluridisciplinaire **HAL**, est destinée au dépôt et à la diffusion de documents scientifiques de niveau recherche, publiés ou non, émanant des établissements d'enseignement et de recherche français ou étrangers, des laboratoires publics ou privés.

**THÈSE DE DOCTORAT DE
L'UNIVERSITÉ PIERRE ET MARIE CURIE**

Spécialité

Chimie physique et chimie analytique de Paris Centre

Présentée par

Héloïse Tissot

Pour obtenir le grade de

DOCTEUR de l'UNIVERSITÉ PIERRE ET MARIE CURIE

**Beyond the gap of pressure : XPS studies of
interfaces at near ambient pressures**

soutenue le 23 septembre 2014
devant le jury composé de :

M. Hendrik BLUHM	Rapporteur
Mme Petra RUDOLF	Rapporteur
Mme Fabienne TESTARD	Examineur
M. Rodolphe VUILLEUMIER	Examineur
M. Fausto SIROTTI	Examineur
M. Fabio FINOCCHI	Examineur
M. François ROCHET	Directeur de thèse

Contents

Introduction	8
1 X-ray Photoelectron Spectroscopy (XPS)	15
1.1 X-ray Photoelectron Spectroscopy (XPS)	15
1.1.1 Photoemission in solid	15
1.1.2 Sampling depth	18
1.1.3 Chemical shift and Binding energy	19
1.2 Near Ambient Pressure X-ray Photoelectron Spectroscopy (NAP-XPS) . .	22
1.2.1 The electron spectrometer: SPECS electron spectrometer PHOI- BOS 150 NAP	23
1.2.2 Beamline and differential pumping	27
1.2.3 The whole NAP-XPS experiment	27
2 The clean Si(001)-2×1 surface	29

2.1	Structure of bulk silicon	29
2.2	Surface reconstruction	30
2.3	Scanning Tunneling Microscopy investigation of the clean Si(001) surface	31
2.4	XPS studies of clean Si(001)-2×1	32
2.4.1	Cleaning procedure	32
2.4.2	XPS Characterization	33
3	Silicon monomers and self-organization following spontaneous dissociative adsorption of TEOS	37
3.1	XPS results	39
3.1.1	Si 2p core-level XPS analysis	39
3.1.2	C 1s core-level XPS analysis	42
3.1.3	O 1s core-level XPS analysis	43
3.2	STM measurements	44
3.3	DFT calculations	48
3.4	Summary	52
4	Silicon monomer diffusion on the clean and the TEOS covered Si(001)-2×1 surface	55
4.1	Overview: Silicon monomer diffusion on the clean Si(001)-2×1 surface . .	55
4.1.1	Ab initio methods	56
4.1.2	Empirical or semi-empirical interaction potentials	60
4.2	The energy landscape of a Si adatom on the Si(001) surface	62
4.2.1	The Si(001)-2×2 surface	62
4.2.2	The Si(001)-8×4 surface	65
4.2.3	Influence of the slab dimension	70

4.2.4	GGA vs LDA	71
4.3	The energy landscape of a Si adatom on the ethoxy-covered Si(001) surface	72
4.4	Summary	75
5	Dissociation of Ethoxysilane on Si(001)-2×1 and Si(111)-7×7 at Room Temperature	77
5.1	TMOS and TEOS reaction on Si(001)-2×1 at room temperature	80
5.1.1	Si 2p core-level XPS analysis	80
5.1.2	O 1s core-level XPS analysis	83
5.1.3	C 1s core-level XPS analysis	84
5.2	TMOS and TEOS reaction on Si(111)-7×7 at room temperature	90
5.2.1	Si 2p core-level XPS analysis	90
5.2.2	O 1s core-level XPS analysis	94
5.2.3	C 1s core-level XPS analysis	94
5.3	Reactions mechanisms of alkoxy-silanes on silicon surfaces	99
5.4	Summary	102
6	Atomic layer deposition on Si(001) surface using TEOS as a precursor and monitored by NAP-XPS	105
6.1	Atomic layer deposition (ALD)	105
6.2	ALD process monitored by NAP-XPS	107
6.2.1	First step: Exposure to TEOS	108
6.2.2	Second step: Exposure to water	113
6.3	Beam damage on the silicon surface	117
6.4	Summary	120
7	Ion segregation at liquid water/gas interface	123

7.1	The liquid water/ vapor interface	124
7.1.1	Liquid water surface structure	124
7.1.2	Ions behavior at liquid water/ vapor interface	125
7.2	NAP-XPS analysis of the water surface: the ions behavior	128
7.2.1	Analysis conditions	128
7.2.2	Carbon contamination	129
7.2.3	Cation behavior	130
7.2.4	Anion behavior	136
7.3	Work function measurements and electronic level diagrams	143
7.3.1	Measurement of the secondary electron cutoff and determination of the work function	143
7.3.2	Work function measurements and electronic level diagrams	148
7.3.3	Electronic level alignments	150
7.4	Summary	153
8	The swelling properties of clays monitored by NAP-XPS	155
8.1	Clay Minerals	157
8.1.1	Clay layers: atomic structure and charge	157
8.1.2	Clay swelling/hydration	161
8.2	Sample preparation	167
8.3	NAP-XPS measurements	167
8.4	Cs-hectorite	169
8.5	Na-hectorite	171
8.5.1	NAP-XPS measurements on Na-hectorite	171
8.5.2	Binding energy shift interpretation	173

Contents

8.5.3 Sodium chloride solution	176
8.6 Sr-hectorite	177
8.7 Solvation energies	180
8.8 Summary	183
Conclusion	185
Bibliography	189

AFM: Atomic Force Microscopy
ALD: Atomic Layer Deposition
BE: Binding Energy
CPD: Contact Potential Difference
CVD: Chemical Vapor Deposition
DFT: Density Functional Theory
fwhm: Full Width at Half Maximum
GGA: Generalized Gradient Approximation
GW: Gaussian width at half maximum
IMFP: Inelastic Mean Free Path
IP: Ionization Potentials
KE: Kinetic Energy
LDA: Local-Density Approximation
LW: Lorentzian width at half maximum
ML: Mono-Layer
NAP-XPS: Near Ambient Pressure X-ray Photoelectron Spectroscopy
RH: Relative Humidity
SCLS: Surface Core-Level Shifts
STM: Scanning Tunneling Microscopy
TEOS: TetraEthOxySilane
TMOS: TetraMethOxySilane
UHV: Ultra High Vacuum
VL: Vacuum Level
XPS: X-ray Photoelectron Spectroscopy

Introduction

In many processes or technological objects, such as coating deposition, advanced material processing for electronics, magnetic or optical devices, electrochemical processes at an electrode, sensors and catalysis, etc. the interface between a surface of a solid and a liquid or a gas phase, plays a prominent role. Analogously, environmental sciences and sciences of the Living integrate into their models chemical reactions taking place at solid/liquid or liquid/gas interfaces.[1], [2], [3]

X-ray Photoelectron Spectroscopy (XPS) is a powerful technique for interface analysis and has been widely use in the case of solid surface. The main advantage of XPS is its sensitivity to the material surface. Indeed, due to the low electron mean free path of electrons in a solid, only the photoelectrons at the extreme outer surface (1-10 nm) can escape the sample. However, XPS has traditionally been conducted under ultra-high vacuum (UHV) conditions. UHV conditions are utilized for two reasons. First, the analyzers are designed to work under UHV conditions. Second, the electrons must reach the detector and their mean free path is short at high pressures. For example, at a pressure of 1 mbar, 100 eV electrons will travel 1 mm while under UHV conditions, the mean free path increases to 10^5 m. UHV chambers ($\sim 10^{-10}$ mbar) help maximize the mean

free path so that a high number of electrons will reach the detector/analyzer and the signal/noise ratio will increase making it possible to analyze the spectrum produced. This constraint makes UHV the standard environment of XPS experiments.

In order to make possible the use of XPS on a larger pressure range, a few groups around the world have designed a photoemission equipment that can operate under near ambient pressure (up to 5 mbar). The Berkeley group (M. Salmeron LBNL-Materials Sciences Division, H. Bluhm LBNL-Chemical Sciences Division), who pioneered this field, has two such setups installed at the Advanced Light Source.[4] The Fritz Haber Institute has built a high pressure XPS based on the Berkeley prototype, installed at BESSY synchrotron (Berlin), since 2002.[5] Several Ambient Pressure XPS (AP-XPS) instrument are in construction or already operational all around the world.[6]

The building of AP-XPS analyzers of the Berkeley type, able to operate at pressures in the range of 1 mbar, about 7 orders of magnitude higher than the pressure limit of conventional UHV equipment, is both a technological and conceptual breakthrough. Differential pumping stages allow the sample to remain at environmental pressures, while maximizing the mean free path of emitted electrons, so they can reach the detector. Additionally, voltages are applied to electrostatic lenses in the unit to accelerate and focus the electrons onto the focal plane of the electron energy analyzer.

A similar system (Near Ambient Pressure XPS, NAP-XPS), described in details in chapter 1, was delivered in December 2012 and installed at TEMPO beamline in February 2013. The first beamtime occurred in May 2013. During my thesis that started in October 2011, two different projects were developed, both related to interface analysis using the NAP-XPS instrument.

The first project deals with the Chemical Vapor Deposition process (CVD) for electronic applications. This was, indeed, a topic proposed in the research project (SAPRES) funded by the Agence Nationale de la Recherche. Generally speaking, organosilane molecules are used to functionalize the surface of (oxidized) silicon wafers.[7], [8], [9] More specifically, tetraethoxysilane ($\text{Si}[\text{OC}_2\text{H}_5]_4$, TEOS), combined with an oxidizing agent (often water), is a popular precursor in the deposition of (multilayer) silica films by CVD or Atomic Layer Deposition (ALD).[10], [11], [12], [13], [14], [15], [16] On the

other hand, its use as a surface modifier at a molecular level was much less explored.

In particular, much less is known on the elementary microscopic processes occurring between the organosilicon molecule and the silicon surfaces, including dissociation, adsorption of the dissociation fragments and further surface reaction of these products. Understanding TEOS reactivity on silicon surfaces, using advanced surface science techniques (like synchrotron radiation XPS and Scanning Tunneling Microscopy (STM)), is necessary for a better control of dielectric film growth.

As far as the NAP-XPS machine was not yet installed when I started my thesis work, we first examined the deposition of TEOS on clean Si(001)- 2×1 at room temperature, up to pressures in the 10^{-8} mbar range, using UHV XPS setups. These experiments were conceived as control experiments for the anhydrous deposition of the molecule on a well characterized clean surface, guaranteed by the low base pressures in the analysis chambers (low 10^{-10} mbar). In fact, we were convinced that the NAP experiments involving mbars of TEOS and water would have led to more intricate situations (due to the relatively high background pressure of the reactive species expected in the 10^{-8} mbar range). However, the outcomes of the UHV XPS experiments combined with STM (the observation of a self-assembly of the ethoxy units every second dimer row) were interesting and encouraged us to perform theoretical calculations of the electronic structure.

Chapter 2 presents the clean Si(001)- 2×1 surface. Then, chapter 3 describes the adsorption of TEOS, at low coverage, on the Si(001)- 2×1 surface at 300 K, studied through a joint experimental and theoretical approach, combining STM and synchrotron radiation XPS with first-principles simulations within the Density Functional Theory (DFT). It shows that all Si – O bonds within the TEOS molecules are broken upon adsorption, releasing one Si atom per dissociated molecule, while the ethoxy ($-\text{OC}_2\text{H}_5$) groups form new Si – O bonds with surface Si dimers.

The release of the silicon monomer by TEOS dissociation on the surface is analyzed, in more details, in chapter 4 by DFT calculations, in order to understand how TEOS fragments influence the diffusion of the monomer on the silicon surface. This work was realized in close collaboration with Dr. F. Finocchi at the Institut des NanoSciences de

Paris (INSP, UPMC).

At higher coverage, the dissociation channel presented in chapter 3 is superseded by a second mechanism involving the breaking of C – O bonds. It leads to the attachment of alkyl moieties to the surface, probably, due to the presence of the silicon monomers produced during the initial regime. To understand these mechanisms, we compare, in chapter 5, the adsorption of tetraethoxysilane and tetramethoxysilane (TEOS, $\text{Si}[\text{OC}_2\text{H}_5]_4$ and TMOS, $\text{Si}[\text{OCH}_3]_4$) on the Si(001)- 2×1 and Si(111)- 7×7 surface at 300 K.

Chapter 6 explores, using the NAP-XPS instrument, the main application of TEOS: its use as a precursor in ALD process for the deposition of thin silicon oxide layers on silicon surfaces. The NAP experiment with TEOS illustrates the paradigmatic shift with respect to UHV experiments. By increasing the pressure of reactants to the mbar range (TEOS and water) and measuring while dosing, we were confronted to a series of unusual issues. The concept of clean surface had to be abandoned, to be replaced by that of starting surface (the Si (001) surface, water-dosed under 10^{-8} mbar). The decomposition of the gas phase, while measuring, leads us to find measurement conditions that eliminate (or at least mitigate) this effect. Finally, by increasing the water pressure and noticing (via the O 1s core-levels) the absence of liquid water layers on the surface, we finally obtained well controlled conditions to check whether the ethoxy units present at the surface can be hydrolyzed or not, a key point to discuss ALD processes.

The second project focuses on environmental molecular chemistry issues, more specifically water/minerals and vapor/liquid water interfaces. In the study of these systems, the NAP-XPS machine acquiring spectra under pressures in the 10 mbar range finds its "raison d'être", as liquid water needs to be condensed on cooled substrates (at around 8 °C).

It is well known that ionic species, present at the surface of water droplets, are involved, in key chemical reactions in the troposphere. Chlorine atoms can significantly affect the tropospheric ozone balance in marine atmosphere and react, in atmospheric sea salt particles, with nitrogen oxides. Their behavior into the liquid and the possible interactions with the gas phase at the liquid surface need to be understood.[17] In chap-

ter 7, we investigated the behavior of sodium halide salt at the liquid water surface and we tried to answer several questions. How are ions distributed at the surface? What is the influence of the anion polarizability on its behavior? And are anions and cations spatially separated?

Interactions between water and minerals were also studied in close collaboration with PHENIX laboratory (UPMC). Clay minerals have various industrial applications, beginning with their use in ceramic ware, paper-making, removal of impurities, decolorizing and more recently as molecular sieves, in catalysis. In relation with environmental issues, wind blown clay dusts are the place of key chemical reactions in atmospheric chemistry.[18] Clay repository are also used for CO₂ sequestration and geological storage of long half-time radioactive waste. [19], [20], [21], [22], [23] Therefore, the way water permeates the clay bands or soaks the dusts is of fundamental interest. In chapter 8, we present an example of the chemical characterization of clays by NAP-XPS, where we demonstrate that core-level XPS can monitor the hydration process of the interlayer counterion of swelling clays.

Chapter 1

X-ray Photoelectron Spectroscopy (XPS)

1.1 X-ray Photoelectron Spectroscopy (XPS)

Photoelectron Spectroscopy is one of the most suitable techniques used to investigate solid surfaces. It utilizes photo-ionization and analysis of the kinetic energy distribution of the emitted photoelectrons to study the composition, chemistry and electronic states of the surface region of a sample. It was developed by a Swedish scientist, Kai Siegbahn, who demonstrated the use of XPS as an analytical tool. His efforts in the domain were awarded with a Nobel Prize in 1981.

The concept of photoelectron spectroscopy is based on the photoelectric effect. When a sample surface is irradiated with monochromatic photons of energy $h\nu$ (generally 100 – 2000 eV), electrons are emitted from the sample surface.

Depending on the energy, two types of spectroscopies are distinguished: the photoemission in the ultra violet region (Ultra violet Photoelectron Spectroscopy, UPS) that allows to eject the electrons from the valence band and photoemission by X-Rays (X-Ray Photoelectron Spectroscopy, XPS) that allows to eject electrons from the core level.

1.1.1 Photoemission in solid

The theoretical model of the photoemission process was developed by Berglund and Spicer in 1964.[24] The photoemission process is described as a three-steps model. In this approach, optical excitation between two Bloch states, transport of the electron

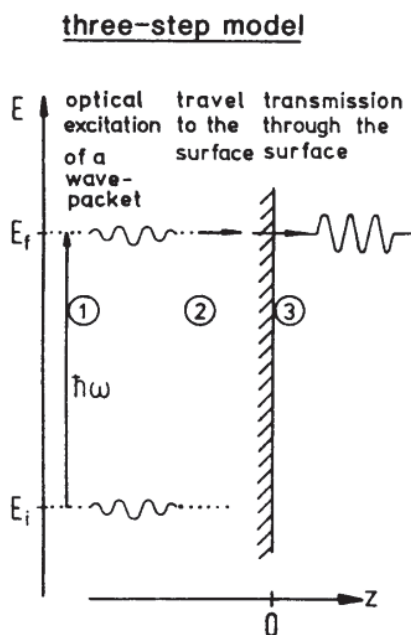


Figure 1.1: The steps of the three step model are (1) excitation of the electron to a Bloch final state inside the crystal, (2) transport of the electron to the surface, (3) escape of the electron to the vacuum

to the surface and escape of the electron through the surface into the vacuum are treated separately (Figure 1.1).

A simple explanation of the three steps model can be given as follows:

1. Photon ionization.

An atom can absorb a photon with sufficient energy then it could be ionized causing an electron to escape from a bound state to a free state. The transition probability is related to the cross-section of the interaction process that depends on the photon energy, the atom from which the electron comes from and the electronic shell from which the photoelectron is ejected.

2. Photoelectron transport to the surface.

The surface sensitivity of this technique arises from the strong interaction of electrons with matter. Before escaping from a solid the electron can interact with the matter in different ways, giving rise to different photoemission structures Fig-

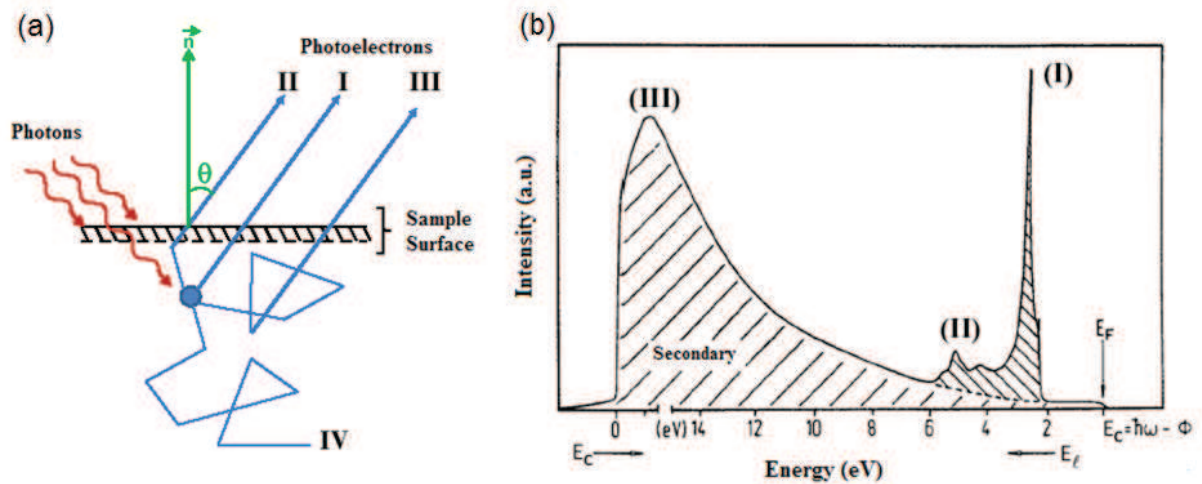


Figure 1.2: (a) Photoelectron-matter interaction near the surface after X-ray or UV irradiation; (b) Schematic representation of a photoemission spectrum

ure 1.2:

- Elastically scattered electrons which have escaped from the solid without suffering energy loss. These lead to the main photoemission peak (case I).
- Inelastically scattered electrons which have lost kinetic energy on their way out of the solid. Such kinetic energy losses may arise due to electron-phonon (broadening), electron-electron (intra or interband transitions; few eV) or electron plasmon (few eV up to about 30 eV) transitions. These types of electrons give rise to a peak broadening or to satellites peaks (case II).
- Electrons that have undergone many inelastic scattering processes and lost the energy information of their original levels. They are termed as secondary electrons (case III).
- Electrons that have lost too much energy due to inelastic scattering processes and cannot escape from the surface (case IV).

3. Crossing the surface.

At the surface, the electrons have to overcome a potential barrier called the work function of the sample, ϕ_s . The work function is the minimum energy required

to move an electron from the Fermi level into vacuum. The energy of the emitted photoelectron is given by equation (1.1) where E_K is the kinetic energy of the ejected electron, $h\nu$ the photon energy, E_B the binding energy of the core electron and ϕ_s the work function of the sample:

$$E_K = h\nu - E_B - \phi_s \quad (1.1)$$

The BE of the photoelectron is defined as the energy required to free electrons from their atomic orbits. In a metal it is conventionally measured with respect to the Fermi level. During a measurement the sample holder and the analyzer are placed in electrical contact and grounded to prevent the charging of the sample surface. In this configuration, the Fermi level of the sample and the analyzer are aligned (Figure 1.3). Then, the kinetic energy measured through the analyzer (E_{KM}) has to take into account only the work function of the analyzer, i.e., $\phi_{analyzer}$ (we do not need to know the work function of the sample ϕ_s):

$$E_{KM} = h\nu - E_B - \phi_{analyzer} \quad (1.2)$$

The kinetic energy of the emitted photoelectrons can be measured and the distribution of the emitted electrons are presented in an XPS spectrum as a function of kinetic energy (KE) or binding energy (BE).

1.1.2 Sampling depth

While probing surfaces with XPS, a useful signal is obtained from a depth of around 10 to 100 Å. The thickness of the layer that can be analyzed is called sampling depth which is related to the inelastic mean free path (IMFP) of the generated photoelectrons. As described previously, electrons can undergo inelastic collisions before they escape the surface. The IMFP λ is defined as follows: the probability of suffering an inelastic scattering over an infinitesimal distance dx is dx/λ . λ is also the average distance traveled by the electron before it suffers an inelastic loss. The probability of the electron

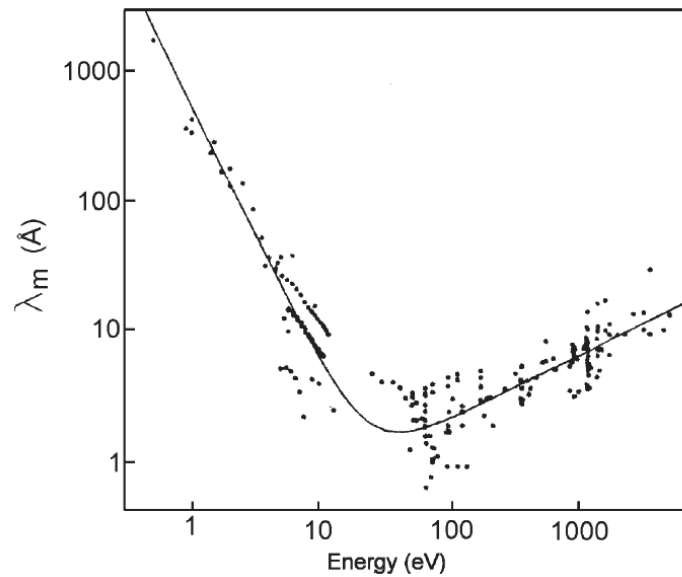


Figure 1.4: IMPF (λ_m) as a function of KE for various solid elements.[25]

trons (ion) and a free photoelectron).

$$BE = E_{final}(n-1) - E_{initial}(n) \quad (1.4)$$

In the approximation of frozen orbitals, i.e. in the absence of relaxation due to electronic rearrangement following the photoemission process, it corresponds (Koopmans theorem) to the orbital energy ($-\epsilon_i$). However, after the photoionization process, the surrounding orbitals relax around the core hole to screen it.

The BE of an electron depends on the chemical environment of the element. Indeed, the energies of the core electrons, which are measured with XPS, are influenced by the Coulomb interaction with the other electrons and the attractive potential of the nuclei. Changes in the chemical environment cause a spatial redistribution of the valence electrons, which influences the measured BE of the core electrons. For example withdrawal of valence electron charge causes an increase in BE while addition of valence electron charge causes a decrease in BE. The variation of BE results in the shift of the corresponding XPS peak. This change in BE of a core electron of an element due to a change in the chemical bonding of that element is called a chemical shift $\Delta\zeta$. If the

Fermi level of the sample is taken as a reference then:

$$\Delta\tilde{\zeta} = -\Delta\epsilon_i - \Delta E^R + \Delta E_F \quad (1.5)$$

where:

- $\Delta\epsilon_i$ is the initial state contribution, and it is the real chemical shift. This term expresses potential modification due to the chemical bond between atoms, acting on the electrons. This could be analyzed using a simple physical model. We consider a point charge e (which represent the core hole) surrounded by the valence charge at a distance r (approximately the distance from the nucleus). Thanks to the Gauss theorem we have:

$$\Delta\epsilon_i \propto \frac{C\delta q}{r} \quad (1.6)$$

where C (constant) > 0 and δq is the charge transferred to the ligand. If $\delta q > 0$ then the atom loses charge by bonding to a more electronegative ligand, the initial state energy decreases, if $\delta q < 0$ then the atom gives charge by bonding to a less electronegative ligand, the initial state energy increases.

- ΔE^R is the final state shift, it is due to the screening capacity of the core-hole by the environment (extra-atomic relaxation). In a solid, the extra-atomic relaxation energy is approximated by the electrostatic polarization energy around the hole. Indeed, the creation of a point charge (hole) in a dielectric will polarize the surrounding volume (inducing an oriented array of dipoles). A scheme of the situation is a screening cloud that surrounds the positive charge, the energy associated with this extra-atomic screening is:

$$\Delta E^R = \frac{1}{4\pi\epsilon_0} (1 - \epsilon_r^{-1}) \frac{e^2}{2r_0} \quad (1.7)$$

where ϵ_r is the static relative dielectric constant, e is the electronic charge and r_0 is the effective screening radius.[26]

- ΔE_F takes into account the modification of the Fermi level position. In the case of a semiconductor, the Fermi level position in the gap depends on the doping (n or p), on the number of dopants and on the temperature. Moreover, the change of symmetry at the surface induces a modification of the band structure creating for example new gap states which determine the position of the Fermi level at the surface and then the band bending. The adsorption of a molecule can also induce modification in the band bending and in the Fermi level position in the gap.

Chemical shifts are readily observable and interpretable in XPS spectra as core levels are discrete and generally of a well-defined energy. Atoms of a higher positive oxidation state exhibit a higher BE due to the extra coulombic interaction between the photoemitted electron and the ion core. This ability to discriminate between different oxidation states and chemical environments is one of the major strengths of the XPS technique.

1.2 Near Ambient Pressure X-ray Photoelectron Spectroscopy (NAP-XPS)

Decades of surface science in ultra high vacuum (UHV) has shown the power of electron spectroscopy in its various manifestations. However, due to the strong interaction of electrons and ions with the gas, this surface science technique has been used almost on solid surfaces, exclusively in high vacuum environment. Indeed, UHV chambers (10^{-9} mbar) help maximize the mean-free path, so that a high number of electrons will reach the detector/analyzer.

Experiments, designed for gaseous samples,[27] liquids,[28] and surfaces in a vapor atmosphere,[29] were developed, during the seventies, by the introduction of differentially pumped gas cells into the vacuum chamber in order to preserve the low pressure in the rest of the experiment.

Since then, and until the beginning of the new century, the field of Ambient-Pressure

X-ray Photoelectron Spectroscopy (AP-XPS) was developed continuously.[30] [31] [32] [33]

All these systems shared a same “passive” design in the sense that the emitted photoelectrons were simply admitted and spatially filtered through apertures separating the sample in high-pressure environment from the detection chamber at lower pressure. This was changed with the advent of a new design, developed by pioneering groups at the ALS and BESSY, where an electrostatic lens system was used to focus photoelectrons emitted through an aperture which significantly increases the transmission of the high-pressure-adapted analyzers.[34] [3] [35] This novel instrumentation made possible the investigation of fluid and solid samples at higher pressures than ever before.

Moreover, it is with the advent of third-generation synchrotron radiation sources that AP-XPS experienced its breakthrough. These sources deliver a much higher photon flux than conventional X-ray and second-generation synchrotron radiation sources. The high photon flux implies a very large flux of photoelectrons, and AP-XPS measurements become much more feasible in spite of the large loss of photoelectron intensity due to inelastic scattering in the ambient atmosphere.

Several instruments available to external users are now in use at the ALS, BESSY, MAXLAB, NSLS... and further instruments will be opened to external users in the future at synchrotron radiation facilities around the world (Soleil, Alba). The one presented here is the NAP-XPS, installed in February 2013, on the soft X-ray TEMPO Beamline of Synchrotron Soleil.

1.2.1 The electron spectrometer: SPECS electron spectrometer PHOIBOS 150 NAP

As the electrons emitted by the sample travel through the gas phase they experience elastic and inelastic collisions with molecules. The mean free path λ , or average distance between collisions depends on their energy and gas pressure. For electrons of 400 eV kinetic energy, λ is about 4 mm when the pressure is 1 mbar. As a result of

scattering, the count rate of detected electrons decreases exponentially with distance (Figure 1.5), indicating the need to shorten the travel distance in the high pressure region as much as possible.[2]

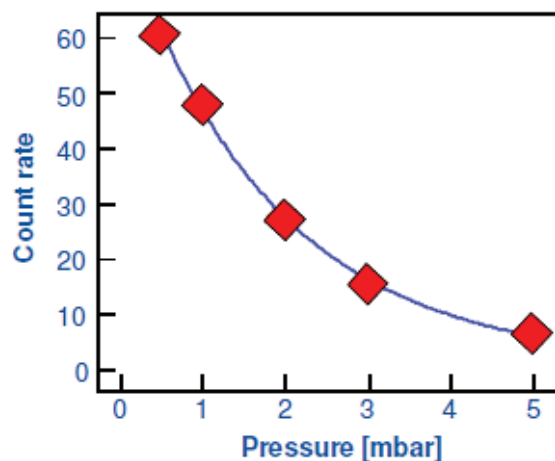


Figure 1.5: Signal vs pressure: The XPS signal decreases exponentially as the pressure increases.

All instruments are developed to make possible electron spectroscopy under environmental gases pressures and to maximize the mean free path of emitted electrons, so they can reach the detector. First, the sample is brought close to a small aperture at a distance equal or less than λ . Then, a differential pumping separate the analyze chamber from the analyzer in order to quickly lower the pressure and decrease the collision rate. As mentioned above, the key feature of the new design approach is the addition of electrostatic lens focusing into the differential pumping scheme. This makes possible the collection of a substantially larger fraction of electrons that would otherwise be lost due to the diverging nature of their trajectories and the small solid angle captured by the apertures separating the pumping stages as schematically illustrated in the diagrams of Figure 1.6.

The analyzer owning the entire characteristic described previously was developed in a collaboration between the Advanced Light Source (Berkley, USA), the Fritz-Haber Institute (Berlin, Germany) and SPECS.

The PHOIBOS 150 NAP consists of a differentially pumped electrostatic pre-lens,

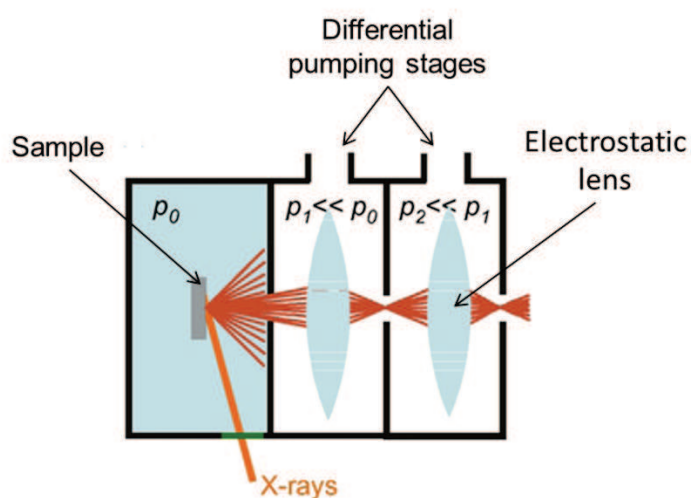


Figure 1.6: Schematic representation of the NAP-XPS analyzer. Electrostatic lenses refocus the electron trajectories into the apertures between the differential pumping stages.[2]

with a three-stage differentially pumped PHOIBOS 150 analyzer.[36] Thus, the design concept provides four stages separated by apertures. The first pumping stage (prelens) is separated from the analytic chamber by a nozzle with a 0.3 mm hole at the tip which maximizes the differential pumping and brings the pressure down to the 10^{-3} mbar range a few millimeter from the sample.

The first and second stages are separated by an aperture with a 4 mm diameter. A valve allows a high-vacuum seal between the stages. This second stage represents the first part of the electrostatic lenses of the PHOIBOS.[36] The front and rear parts of the electrostatic lenses are separated by an iris aperture. The third pumping stage is situated behind the iris. The fourth pumping stage contains the hemispheres and detector. The electron analyzer operates at pressures up to 10^{-7} mbar, making the pressure change from the sample cell to the analyzer approximately seven orders of magnitude.

The analyzer is a true 180° hemispherical energy analyzer with 150 mm mean radius and is equipped with a 3D delay line detector system (one time and two lateral dimensions).

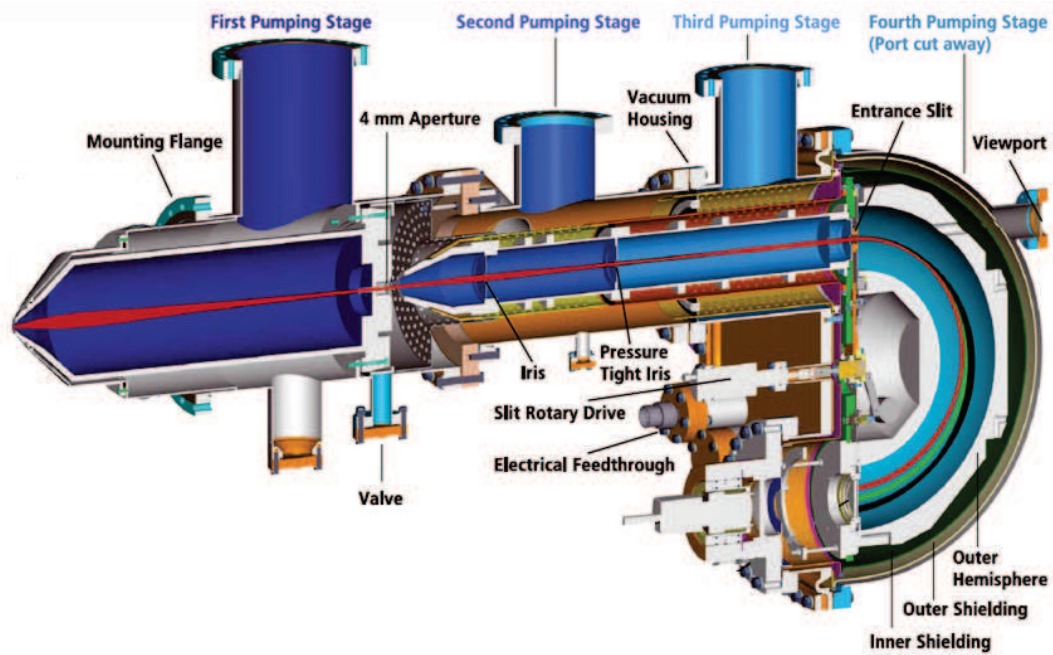


Figure 1.7: The electron spectrometer: SPECS electron spectrometer PHOIBOS 150 NAP.[36]

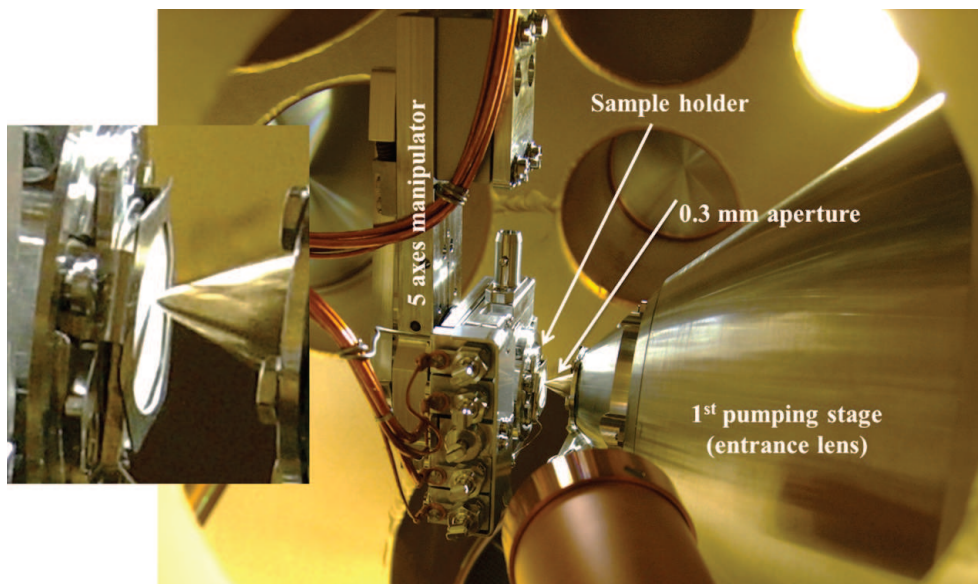


Figure 1.8: Sample holder configuration

1.2.2 Beamline and differential pumping

Several stages of pumping are also essential in order to preserve the vacuum level of the TEMPO beamline. Indeed, to prevent the attenuation of the X-ray beam intensity, the beamline is not protected by a membrane, usually made of Si_3N_4 , Al, or Si, but by four stages of pumping keeping the pressure in the beamline in the low 10^{-9} mbar. The beam, in the analysis chamber, has a diameter of $100 \mu\text{m}$.

1.2.3 The whole NAP-XPS experiment

The system is designed with four chambers separated by gate valves, presented in Figure 1.9. Additionally, a load-lock allows for easy introduction of samples in the transfer chamber with minimal perturbation to the base pressure. The preparation chamber can be optionally equipped with surface science instruments, molecule evaporators, high temperature heating by laser, ion sputtering, LEED, etc. After preparation the sample is moved to the analysis chamber. Two possible manipulators can be installed in this chamber. The first manipulator and sample holder is designed to allow heating in the presence of gases at pressures of several mbar using a laser. The second one comprises a peltier cooler which coldest spot is the sample in order to condensate gases on the sample; for example, in the study of liquid water surface.

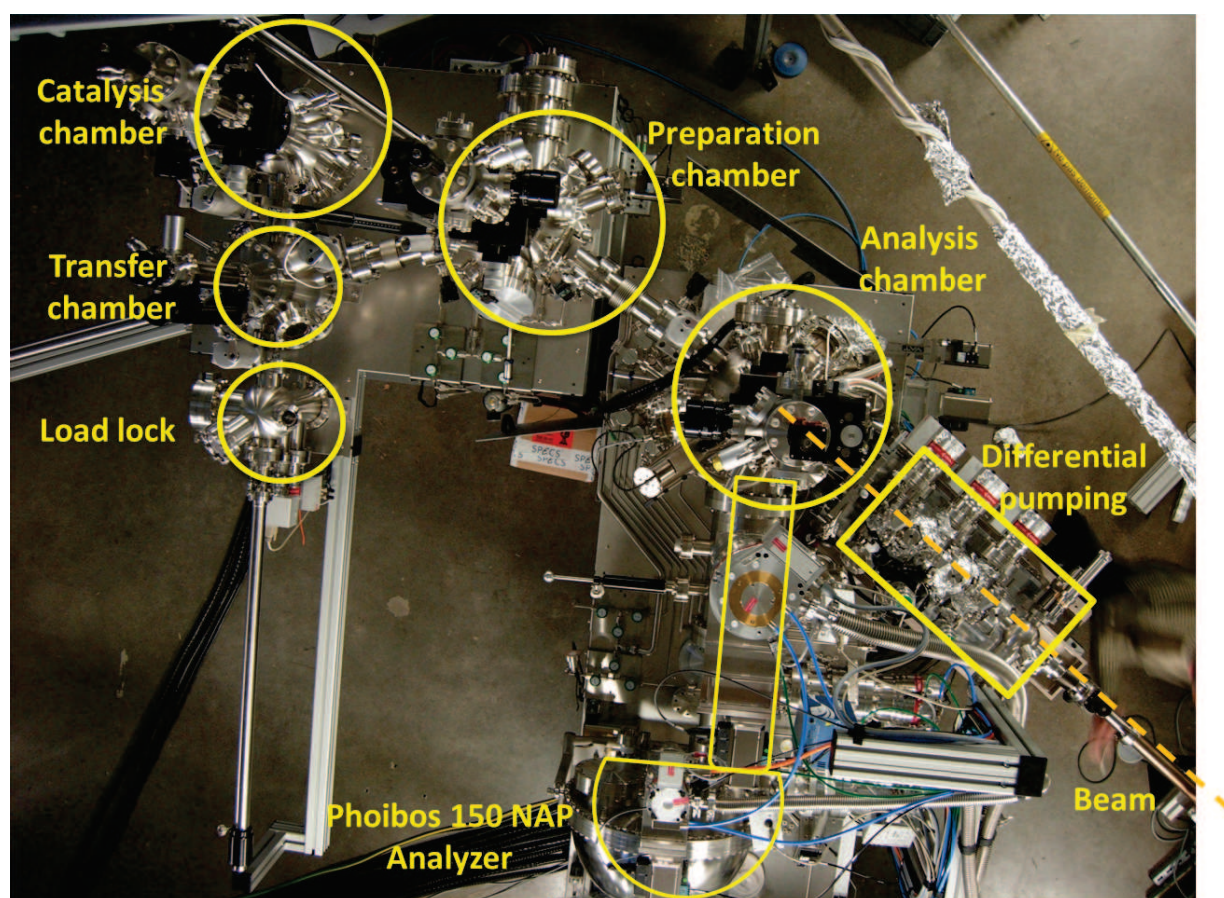


Figure 1.9: Overview of the NAP-XPS experiment

Chapter 2

The clean Si(001)-2×1 surface

As described in the Introduction, the first project, developed during my thesis, deals with TEOS reactivity on the Si(001)-2×1 surface. To make the next chapters easier to understand, we will start by a precise description of this surface.

2.1 Structure of bulk silicon

Silicon is a group IV semiconductor with a bulk crystal structure known as the diamond structure, with a lattice spacing of 5.5 Å and a two-atom basis. The chemical bond is purely covalent, each atom being tetrahedrally coordinated and its valence electrons occupying sp^3 hybrid orbitals. Silicon crystalline structure is presented in Figure 2.1.

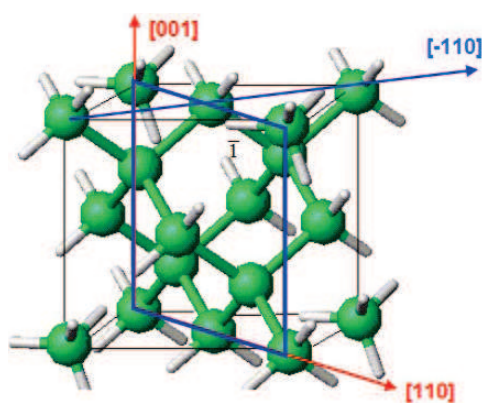


Figure 2.1: Bulk diamond structure of crystalline silicon with each atom tetrahedrally bonded to four nearest neighbors.

2.2 Surface reconstruction

Truncation of the silicon bulk diamond structure along the (001) plan cuts through two Si – Si bonds for each surface silicon atom. Each surface atoms is left with two covalent bonds to the bulk and two dangling bonds holding one electron. Such a structure is thermodynamically unstable; therefore, the surface undergoes a reconstruction to achieve a lower energy state.[37] In order to reduce the dangling bond density, the surface atoms dimerize. The dimers form a 2×1 array, arranged in rows separated by trenches (Figure 2.2).

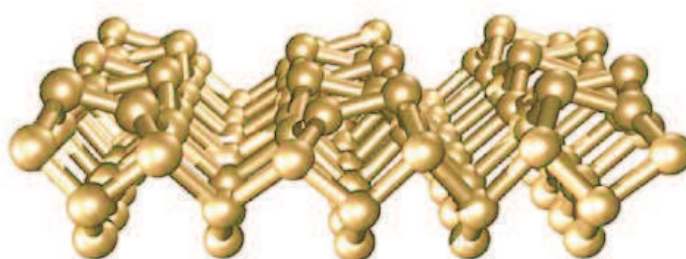


Figure 2.2: Buckling of Si dimers. The dimer bonds make an angle of $\sim 20^\circ$ with the surface.[38]

Dimerization releases energy (the 2×1 dimerization reduces the energy by 2 eV per dimer) because a σ bond is created within each silicon pair. The remaining two broken bonds of the dimer are brought closer to each other to create a weak π bond. The reported energy values of the weak π bond are approximately ~ 28 kcal/mol.[39], [40], [41] It is notable that this bond energy is low compared to the bond energy of traditional alkenes which is reported to be 64 kcal/mol.[42]

Due to electronic effects, the dimers tilt out of the surface plane and make an angle of $\sim 20^\circ$ with it, as shown in Figure 2.2. The “down” atom moves closer to the plane of its three nearest neighbors, so its orbitals become more sp^2 -like. Its dangling orbital acquires more p-character, its energy increases, and its electronegativity decreases. The opposite happens to the “up” atom, which moves away from the plane of its neighbors. Its “dangling” orbital becomes more s-like, its energy decreases and the silicon atom more electronegative. Therefore, the surface Si atoms in the buckled dimer differ chem-

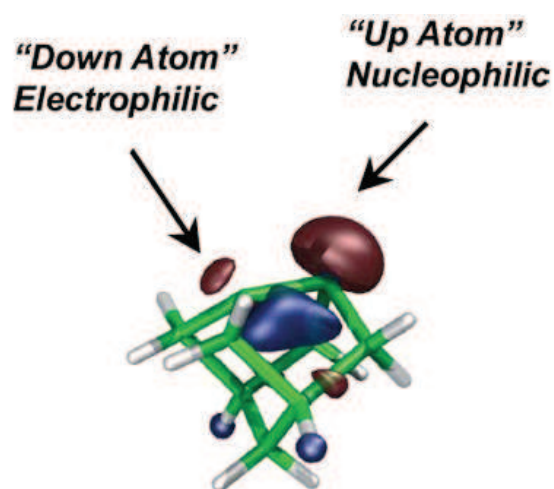


Figure 2.3: The highest occupied molecular orbital of a Si_9H_{12} dimer cluster.[38] The up atom is nucleophilic and possesses the majority of the electronic charge.

ically. The “up” atom is negatively charged (nucleophilic silicon atom) and the “down” atom is electron deficient (electrophilic silicon atom) as shown in Figure 2.3.

2.3 Scanning Tunneling Microscopy investigation of the clean Si(001) surface

Using scanning tunneling microscopy (STM), the surface structure of Si(001) has been investigated in detail. Beyond a certain temperature, thermal motion allows dimers to cross a potential barrier, allowing them to oscillate rapidly between two inclined states. Molecular dynamics simulations demonstrate that silicon dimers tilt on the picosecond timescale at room temperature.[43], [44] Since the time scale of the image collection by STM (millisecond-second) is much slower than the surface dynamics, at room temperature the asymmetry of the dimers is not distinguished as shown in Figure 2.4(a).[45], [46], [44] However, at a temperature of 85 K (Figure 2.4(b)), the dimers movement is frozen and their asymmetry can be observed. It is possible to identify the up (bright protrusions) and down (dark protrusions) silicon atoms.[45], [47]

The number of dangling bonds is reduced by the reconstruction, however, the

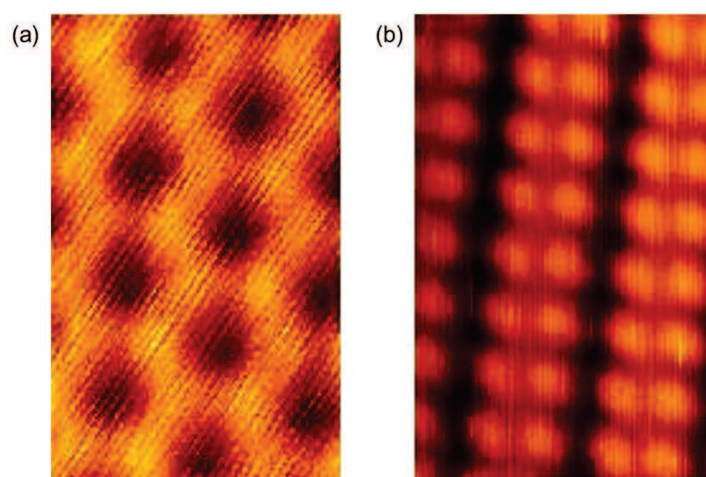


Figure 2.4: Unoccupied-state STM images of Si(001)-c(4×2) at 85 K (left: $V_s = 1.0$ V, $I_t = 0.14$ nA) and Si(001)-2×1 at 300 K (right: $V_s = 1.5$ V, $I_t = 0.12$ nA)[45]

Si(001)-2×1 surface is still highly reactive and sticking probabilities of many organic molecules are near unit at room temperature.[48] In contact with air, a native oxide layer is readily formed on the surface and protects it from any reaction with other species that might be present in the environment. This oxide layer is often used as a masking agent and as a barrier layer to grow molecular thin films on the silicon surface and is also used in metal-semiconductor interfaces.[49]

2.4 XPS studies of clean Si(001)-2×1

2.4.1 Cleaning procedure

The first step, before obtaining a clean Si(001)-2×1, is to remove all the contamination from the substrate and the sample holder. This is achieved by degassing the sample at 600 °C by Joule effect for a period of 8 to 12 hours. This ensures that all contamination on the surface is removed from the surface before the oxide layer is taken off. To remove the native oxide layer, a rapid flash annealing at 1150 °C is performed while staying in the ultra-high vacuum (during this procedure in order to avoid contamination of the sample the base pressure must not exceed 10^{-9} mbar). The sample is then

slowly cooled down to room temperature. The time that a silicon surface requires to cool down under UHV is approximately one hour.[50]

2.4.2 XPS Characterization

Once the silicon surface is flashed it can be characterized by XPS to verify the cleanliness of the surface and to see if the oxide layer has been effectively removed. A photoemission spectrum of Si 2p core level of a clean surface (highly doped (phosphorous) n-type Si(001) wafer with a resistivity of $0.003\Omega \times \text{cm}$) acquired at room temperature is shown in Figure 2.5 (XPS spectrum recorded at TEMPO beamline).

The photoelectrons were detected at 0° from the sample surface normal \vec{n} and at 46° from the polarization vector E). In order to be surface sensitive, photon energy of 150 eV is used (overall resolution 70 meV).

The core-level spectra are fitted by sums of Voigt curves, i.e. the convolution of a Gaussian (of full width at half maximum GW) by a Lorentzian (of full-width at half maximum LW). The chosen LW is 45 meV.[51], [52] The total full-width at half maximum (fwhm) of the Voigt profile is calculated using the formula from Ref.[53]:

$$fwhm = 0.5346 \times LW + \sqrt{0.2169 \times LW^2 + GW^2} \quad (2.1)$$

The fitting of the Si 2p spectra is done using a $2p_{1/2} / 2p_{3/2}$ doublet with a spin-orbit splitting energy of 0.602 eV and an intensity ratio of 0.5 eV.[54] In order to clarify the spectrum deconvolution, the Si $2p_{1/2}$ and Si $2p_{3/2}$ peaks of each components were summed. The choice of the surface components is inspired by previous XPS works on the clean and oxidized surface.[55], [56], [57] The fitting parameters of the Si 2p spectra are collected in Table 2.1.

The attribution of the various Si $2p_{3/2}$ components is based on the preceding Si 2p XPS works: [56], [53], [51], [58]. The main peak (52.4 % of the Si $2p_{3/2}$ spectral weight) is denoted B + SS, as it encompasses both the bulk component B and the positively charged down silicon dimer atom labeled SS. All components BE are referenced to the bulk Si

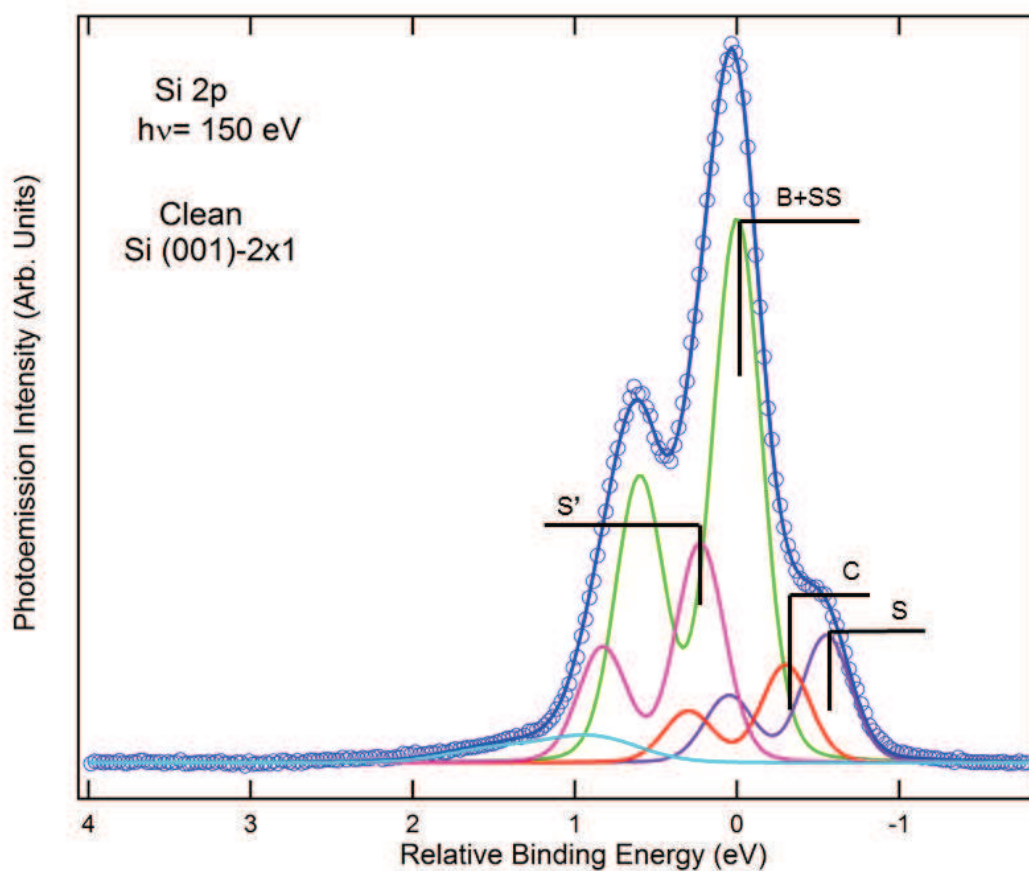


Figure 2.5: XPS Si 2p spectrum ($h\nu = 150$ eV) of the clean Si(001)-2×1 surface. The takeoff angle of the photoelectrons, relative to the surface normal is 0° . The experimental curves (dots) are fitted with sums of Voigt components (blue solid lines). The Si $2p_{3/2}$ (Si $2p_{1/2}$) fitting components colored lines. The fitting parameters are reported in Table 2.1.

$2p_{3/2}$ component. The SS peak presents a surface core-level shift (SCLS) of only +0.06 eV. The peak labeled S, with a SCLS of -0.55 eV (13 % of the Si $2p_{3/2}$ spectral weight), is related to the negatively charged up silicon dimer atom. The structure labeled C with a SCLS of -0.30 eV (9.4 % of the Si $2p_{3/2}$ spectral weight), corresponds to subsurface silicons (3^{rd} plane); and finally the S' peak with a SCLS of +0.23 eV (21.2 % of the Si $2p_{3/2}$ spectral weight), is attributed to the silicon second plane.[56]

The component at highest binding energy, with a SCLS of +0.9 eV (4 % of the Si $2p_{3/2}$ spectral weight), corresponds to a first oxidation degree of silicon and is due to a water contamination in the analysis chamber (some water is always present even after

	Component	SCLS (eV)	fwhm (eV)	Weight (%)	Attribution
Clean Si(001)	S	-0.55	0.35	13.0	Up atom
	C	-0.30	0.35	9.4	Subsurface
	B + SS	0	0.35	52.4	Bulk + Down atom
	S'	0.23	0.35	21.2	2 nd plane
	Water contamination	0.90	0.62	4.0	Si ⁺

Table 2.1: Surface Core Level Shifts (SCLS) referenced to the bulk component binding energy BE = 99.35 eV. Widths and spectral weights of the Voigt components used to fit the Si 2p experimental spectrum shown in Figure 2.5. The Lorentzian width was 0.045 eV for all components.

a bake out). Curve fitting results and attributions are collected in Table 2.1.

Chapter 3

Silicon monomers and self-organization following spontaneous dissociative adsorption of TEOS

Since the beginning of the silicon surface chemistry studies in the mid-1980s, [59] the grafting of organic monomolecular arrays on silicon surfaces via the direct formation of Si – C bonds (both in UHV and wet conditions [60], [38]) has stimulated a considerable interest, essentially because of promising applications in molecular electronics. [10], [11] Silanes are widely used to form self-assembled monolayers on silicon substrates. [7], [8], [9] Within this class of molecules, alkoxysilanes ($R_n\text{Si}(\text{OR})_{4-n}$) are not attached directly to clean silicon surfaces, but rather to native silicon oxide ones, either through the direct reaction of surface Si – OH with the hydrolysable alkoxy terminations of the molecules or via a more complex process involving the participation of molecular water. Fan and Lopinski [61] investigated the reaction of an alkoxysilane, in the absence of molecular water, with the surface hydroxyls of the water-reacted surface (H,OH)-Si(001)- 2×1 . [62] On the other hand, the grafting of alkoxysilanes directly on clean Si(001)- 2×1 is an emerging field of study.

The reaction of n-propyltriethoxysilane (PTES, $\text{Si}[\text{OCH}_2\text{CH}_3]_3[\text{CH}_2\text{CH}_2\text{CH}_3]$) on the clean Si(001)- 2×1 was examined, at room temperature and UHV conditions by our group.[63] Using XPS, we observed that PTES adsorbs dissociatively at room temperature via the scission of Si – O bonds. However, the actual number of broken Si – O bonds in PTES after dissociative adsorption remained elusive due to the presence of

non-identical ligands (one propyl and three ethoxy groups).[63]

The latter issue prompted us to examine how a simpler molecule with four identical ligands, tetraethoxysilane (TEOS, $\text{Si}[\text{OCH}_2\text{CH}_3]_4$) reacts with $\text{Si}(001)\text{-}2\times 1$. Many unknowns remain about the microscopic processes governing the adsorption of TEOS on $\text{Si}(001)\text{-}2\times 1$ at room temperature and under UHV conditions (see e.g. the review by Rauscher [64]). In fact most studies focus on the deposition and electrical/structural characterization of SiO_2 films using TEOS as a precursor.[65], [66], [67] The few published works devoted to the reaction of TEOS with the clean silicon surface date back to almost two decades ago. As an example, Bonzel et al.[68], in a Mg $K\alpha$ XPS and ultraviolet photoelectron spectroscopy (UPS) study, concluded that no adsorbed TEOS could be detected on the $\text{Si}(001)$ surface after its exposure to $10^{-7} - 10^{-3}$ mbar of TEOS at 300 K.

An earlier work, realized by Danner et al. and based on high resolution electron energy loss spectroscopy (HREELS), studied also the deposition of TEOS onto $\text{Si}(001)\text{-}2\times 1$ surface with different deposition conditions.[69] The adsorption of TEOS, made at 90 K, was followed by annealing at room temperature and above. There is a clear indication that TEOS is chemisorbed on the surface, but, in our opinion, the vibrational spectra do not provide a clear information on the nature of the bond breaking (Si – O or C – O bonds), since the Si – C stretching mode is indiscernible from the Si – O one.

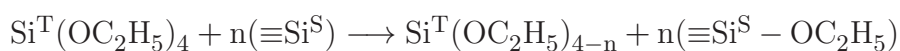
In order to unravel the microscopic mechanisms governing the interaction of TEOS with clean $\text{Si}(001)$, we combine chemical information delivered by synchrotron radiation XPS with structural ones produced by atomically-resolved STM. Electronic structure calculations based on DFT and STM image simulations gave a sound support to understand the experimental STM images.

3.1 XPS results

3.1.1 Si 2p core-level XPS analysis

We start with the determination of the nature of the chemical bonding of TEOS on Si(001), as provided by XPS. The measurements, presented in this chapter were performed at beamline I511 at Max-Lab synchrotron facility (Lund Sweden). In this experiment, the clean reconstructed surface is exposed to TEOS at 120 K and 300 K for doses of 6.75 L and 4.5 L respectively. The core-level spectra are plotted against a BE scale referenced to the Fermi level. The $2p_{3/2}$ BE of the bulk silicon component varies with coverage and substrate temperature. At room temperature, the $2p_{3/2}$ BE of the bulk component is found at 99.35 eV. It shifts to 99.40 eV after TEOS adsorption at 300 K (due to a reduction of the upward band bending) and at 99.55 eV for TEOS physisorbed at 120 K, the increase in BE being largely due to a surface photovoltage effect [56] that flattens the bands at cryogenic temperature.

The determination of the oxidation state of the central atom of the molecule, denoted Si^{T} , is crucial to conclude about the nature and the precise number of broken chemical bonds in the TEOS molecule. If we consider that dissociative chemisorption on the surface occurs via cleavage of Si – O bonds as for PTES,[63] the number of remaining oxygen neighbors around Si^{T} depends on the number of cleaved bonds, according to the scheme:



where $\equiv\text{Si}^{\text{S}}$ is a tri-coordinated silicon of the surface and n an integer less than or equal to 4. The number of oxygen ligands $i = 4 - n$ around the central atom Si^{T} determines its oxidation state, denoted Si^{i+} . On the other hand, the number of oxygen ligands around Si^{T} is not affected if the O – C bond is broken, i.e. the oxidation state of Si^{T} remains Si^{4+} .

Therefore, the key spectroscopic feature of the Si 2p spectra is the BE position of the oxidation states. In the case of the Si/SiO₂ interface, each oxidation state is associated

with a well-defined Si $2p_{3/2}$ surface core-level shifts (SCLS), referenced to the BE of the bulk Si $2p_{3/2}$ component. With i being the oxidation state, the SCLS scales as $\sim 0.9 \times i$ eV, the chemical shifts being additive.[70], [71], [72], [73]

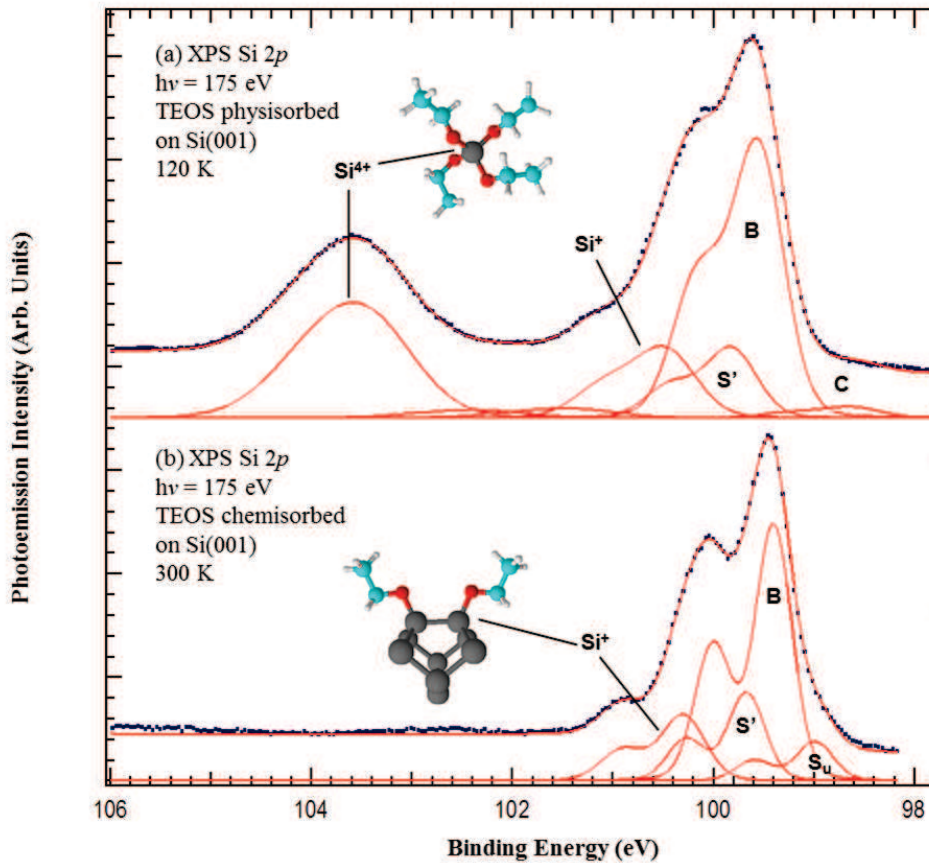


Figure 3.1: (a) Si 2p XPS spectrum ($h\nu = 175$ eV) of TEOS physisorbed on Si(001)- 2×1 surface (n-doped, $0.003 \Omega \times \text{cm}$) (clean surface exposed to 6.75 L of TEOS, 15 min, 10^{-8} mbar, at 120 K). (b) Si 2p XPS spectrum of TEOS chemisorbed on Si(001)- 2×1 surface (surface exposed to 4.5 L of TEOS, 10 min, 10^{-8} mbar, at 300 K). The BE, spectral weights, and attributions of the different components are reported in Table 3.1.

However, in the case of the TEOS molecule, the ethoxy ($-\text{OC}_2\text{H}_5$) ligand may induce a chemical shift different from the one due to oxygen in siloxane bridges (Si – O – Si) in SiO_2 . For instance, the BE shift per ethoxy ligand in gas phase ethoxysilane $\text{Si}[\text{CH}_3]_n[\text{OCH}_2\text{CH}_3]_{4-n}$ is reported to be only $\sim +0.4$ eV,[74] which suggests that the na-

	Component	SCLS (eV)	fwhm (eV)	Weight (%)	Attribution
TEOS physisorbed on Si(001)	B	0.00	0.59	43.9	Bulk
	S'	0.27	0.59	10.9	2 nd plane
	C	-0.93	0.59	1.9	Non-attributed
	Si ⁺	0.92	0.71	12.6	1 st oxidation state
	Si ²⁺	1.80	0.99	2.0	2 nd oxidation state
	Si ³⁺	2.70	0.99	1.7	3 rd oxidation state
	Si ⁴⁺	3.88	1.1	27	4 th oxidation state
TEOS chemisorbed on Si(001)	B	0.00	0.40	56.4	Bulk
	S'	0.27	0.40	18.7	2 nd plane
	Si _u	-0.41	0.40	8.5	Up dimer atoms
	Si ⁺	0.90	0.49	16.4	1 st oxidation state

Table 3.1: Si $2p_{3/2}$ Surface core level shifts (SCLS, relative Si $2p_{3/2}$ BE referenced to the bulk component one), spectral weights, full widths at half maximum (fwhm), and attribution of the Voigt components used to reconstruct the Si 2p XPS experimental spectra shown in Figure 3.1. The BE of the Si $2p_{3/2}$ component (referenced to the Fermi level) is 99.55 eV for the TEOS physisorbed on Si(001) at 120 K, and 99.40 eV for the TEOS chemisorbed on Si(001) at 300 K.

ture of second neighbor atoms (C versus Si) may impact the BE shifts. Therefore, it is crucial to measure the BE shift of the intact TEOS molecule (Si⁴⁺ oxidation state) with respect to the substrate component. Thus, we produced physisorbed TEOS molecules by exposing the surface to the gas at 120 K (6.75 L).

The Si 2p XPS spectrum is shown in Figure 3.1 (a) (the fitting parameters are collected in Table 3.1). We observe a component with SCLS of +3.88 eV, that we ascribe to the intact physisorbed molecule. The SCLS of the intact molecule (a Si⁴⁺ state) is nearly equal to that of the Si⁴⁺ state at the Si/SiO₂ interface (\sim +3.6 eV [70], [71]). Since the second neighbor effect (Si versus C) is not present, as suggested by the gas phase data, we can clearly state that the SCLS of partially decomposed products via Si – O bond breaking should also follow the additivity rule (\sim 0.9 eV/oxygen ligand). Therefore, we

introduce two components in the fitting procedure, with fixed SCLS of $\sim +1.8$ eV (Si^{2+}) and $\sim +2.7$ eV (Si^{3+}). Their overall intensity is almost negligible, below 4% of the total spectral weight, and is within the detectability limit.

On the other hand, we clearly see a Si^{1+} state with a SCLS of $\sim +0.92$ eV. After heating the sample back to room temperature, the Si^{1+} component is the only oxidation state remaining visible. The Si 2p spectrum is then similar to that obtained after TEOS exposure at room temperature (Figure 3.1 (b)). The annealing experiment confirms that no chemisorbed Si^{4+} species is produced at 120 K, and that the Si^{1+} component results from the dissociation of some TEOS molecules on the surface at 120 K, the product being similar to that formed directly at room temperature (see below).

The Si 2p XPS spectrum (Figure 3.1 (b)) of the surface exposed to TEOS at room temperature is characterized by the absence of the Si^{4+} component at $\sim +3.9$ eV. As discussed before, physisorbed molecules cannot remain on the surface at this temperature. Neither chemisorbed molecules, resulting from the breaking of the O – C bonds, are present on the surface, as they should give a Si^{4+} component. This observation calls for the rupture of the Si – O bond. We recall that Si – O bond breaking is also seen in PTES dissociation on Si(001)- 2×1 . [63] Si^{3+} and Si^{2+} states are also absent from the Si 2p XPS spectrum of chemisorbed TEOS.

As Si^{1+} is the only oxidation state observed (SCLS of +0.90 eV), three to four Si – O bonds are necessarily cleaved within the TEOS molecule, leading either to the formation of the $(\text{Si}^{\text{S}})_3\text{Si}^{\text{T}} - \text{OC}_2\text{H}_5$ adduct (plus three $\equiv\text{Si}^{\text{S}} - \text{OC}_2\text{H}_5$ moieties) or to the release of an atomic silicon (plus four $\equiv\text{Si}^{\text{S}} - \text{OC}_2\text{H}_5$). However, the Si^{1+} component, due to $\equiv\text{Si}^{\text{S}} - \text{OC}_2\text{H}_5$ moieties, cannot be distinguished from $(\text{Si}^{\text{S}})_3\text{Si}^{\text{T}} - \text{OC}_2\text{H}_5$ ones, the Si 2p XPS spectra themselves cannot give a definite answer on the extent of the dissociation.

3.1.2 C 1s core-level XPS analysis

The C 1s XPS spectrum ($h\nu = 350$ eV) of TEOS chemisorbed at room temperature, see Figure 3.2, is fitted with five Voigts components (LW is chosen at 80 meV). The very weak peak at lower BE (~ 283.2 eV) can be ascribed to carbonaceous CH_x species likely

due to beam damage.[75]

The BE of the four main components are interpreted based on straightforward initial-state considerations.[63] The substitution of a hydrogen (Pauling electronegativity = 2.20) bonded to a carbon by a more electronegative oxygen (Pauling electronegativity = 3.44) leads to a charge loss and to an increase of the C 1s core-level BE. Therefore, the α peak at 286.54 eV is attributed to carbons bonded to oxygen in ethoxy groups ($\text{Si} - \text{O} - \text{CH}_2 - \text{CH}_3$) and the β peak at 285.23 eV to terminal carbon atoms in those ethoxy groups ($\text{Si} - \text{O} - \text{CH}_2 - \text{CH}_3$). The ethoxy termination corresponds to $\sim 80\%$ of the carbon species on the surface. The detection of surface ethoxy groups, as majority products, is consistent with the observation of a single oxidation component (Si^{1+}) in the Si 2p spectrum, confirming that $\text{Si}^{\text{T}} - \text{O}$ bond breaking is the main dissociation channel.

Similarly, carbons (Pauling electronegativity = 2.55) bonded to silicon atoms (Pauling electronegativity = 1.90) are expected to be slightly more negatively charged than those bonded to other carbon atoms within ethyl groups; therefore the former ones are expected at lower BE. The minority product is the ethyl termination: the γ peak at 284.70 eV is attributed to the terminal carbon ($\text{Si} - \text{CH}_2 - \text{CH}_3$) and the δ peak at 284.07 eV to the carbon atom directly bonded to silicon ($\text{Si} - \text{CH}_2 - \text{CH}_3$). A similar BE shift of 0.6 eV is observed in the C 1s XPS spectrum of cyclopentene di- σ bonded on Si(001) that exhibits two components, at 284.2 eV (C bonded to Si) and at 284.8 eV (C non-bonded to Si).[75] The presence of ethyl groups needs the breaking of the O – C bond.

3.1.3 O 1s core-level XPS analysis

The O 1s XPS spectrum of the Si(001) surface exposed to TEOS at room temperature (4.5 L) is shown in Figure 3.3. It is fitted with a single component, at 532.1 eV (LW = 120 meV, fwhm = 1.1 eV). This BE is between that of surface Si – OH (532.3 eV) and that of Si – O – Si bridges (531.4 eV).[76] We attribute it to Si – O – C bonds, as the ethoxy groups are the main (80 %) carbon containing species at the surface. Oxygen in siloxane bonds cannot be detected.

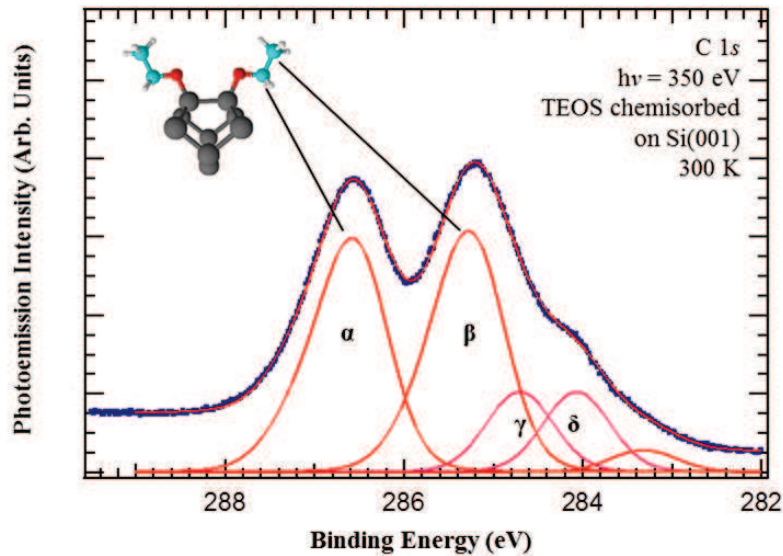


Figure 3.2: C 1s XPS spectrum ($h\nu = 350$ eV) of the TEOS chemisorbed on Si(001)- 2×1 surface (n-doped, $0.003 \Omega \times \text{cm}$) (surface exposed to 4.5 L of TEOS, 10 min, 10^{-8} mbar, at room temperature). The BE is referenced with respect to Fermi level. The Si $2p_{3/2}$ bulk component is 99.40 eV for the 4.5 L TEOS chemisorbed at 300 K. The BE, spectral weights, and attributions of the different components are reported in Table 3.2.

	Component	BE (eV)	fwhm (eV)	Weight (%)	Attribution
TEOS chemisorbed on Si(001)	α	286.54	0.96	38.5	Si – O – CH ₂ – CH ₃
	β	285.23	0.96	38.5	Si – O – CH ₂ – CH ₃
	γ	284.70	0.96	11.5	Si – CH ₂ – CH ₃
	δ	284.07	0.96	11.5	Si – CH ₂ – CH ₃

Table 3.2: Relative BE (C 1s) referenced to the Si $2p_{3/2}$ bulk component, spectral weights, full widths at half maximum (fwhm), and attribution of the Voigt components used to reconstruct the C 1s XPS experimental spectrum shown in Figure 3.2. Si can be either a substrate atom (dimer) $\equiv \text{Si}^{\text{S}}$, or the silicon of the TEOS molecule Si^{T} .

3.2 STM measurements

While XPS proves that the dissociative adsorption of TEOS on Si(001) surface involves (essentially) the cleavage of the $\text{Si}^{\text{T}} - \text{O}$ bonds and the bonding of ethoxy groups

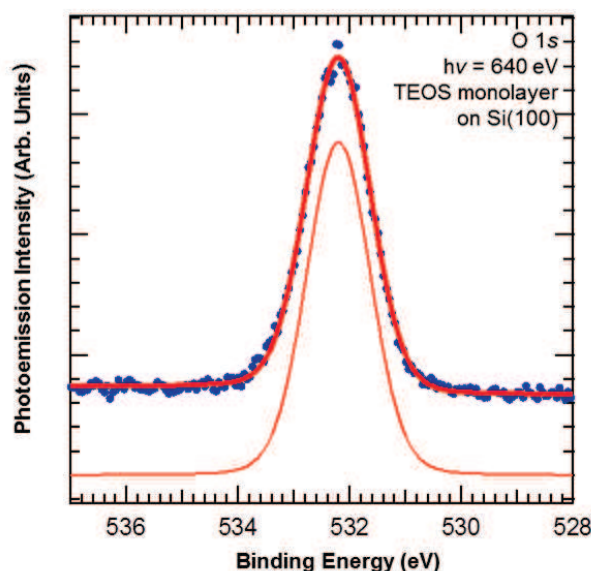


Figure 3.3: O 1s XPS spectrum ($h\nu = 640$ eV) of TEOS chemisorbed on Si(001)- 2×1 surface (n-doped, $0.003 \Omega \times \text{cm}$) (clean surface exposed to 4.5 L of TEOS, 10 min, 10^{-8} mbar, at 300 K). The BE is referenced with respect to Fermi level. The Si $2p_{3/2}$ bulk component is 99.40 eV for the 4.5 L TEOS chemisorbed at 300 K.

to the surface. The nature of the adsorption sites needs to be determined by STM imagery.

STM imagery was performed using the Variable Temperature scanning tunneling microscope STM XA (Omicron NanoTechnology) of the UPMC campus (Paris). The occupied-states STM images were obtained in constant current mode ($I = 100$ pA), at a sample voltage (V_{bias}) of -2 V at room temperature. The chemically-etched tungsten tip was cleaned by heating in UHV prior to STM measurements. The silicon wafer was taken from the same batch as the one used for XPS (n-doped, $0.003 \Omega \times \text{cm}$).

In order to examine the early stage of adsorption at 300 K, the surface was exposed to a low TEOS dose, 0.4 L, that is, an order of magnitude less than the exposure used in XPS. This eased the identification of the adsorption sites, as large portions of the surface remain clean. In Figure 3.4 (a), we show a filled state image of the surface. Two types of bright protrusions sitting on the dimer rows are observed. The minority adsorption feature (30 % of the dissociation products) appears as an isolated protrusion (blue circle

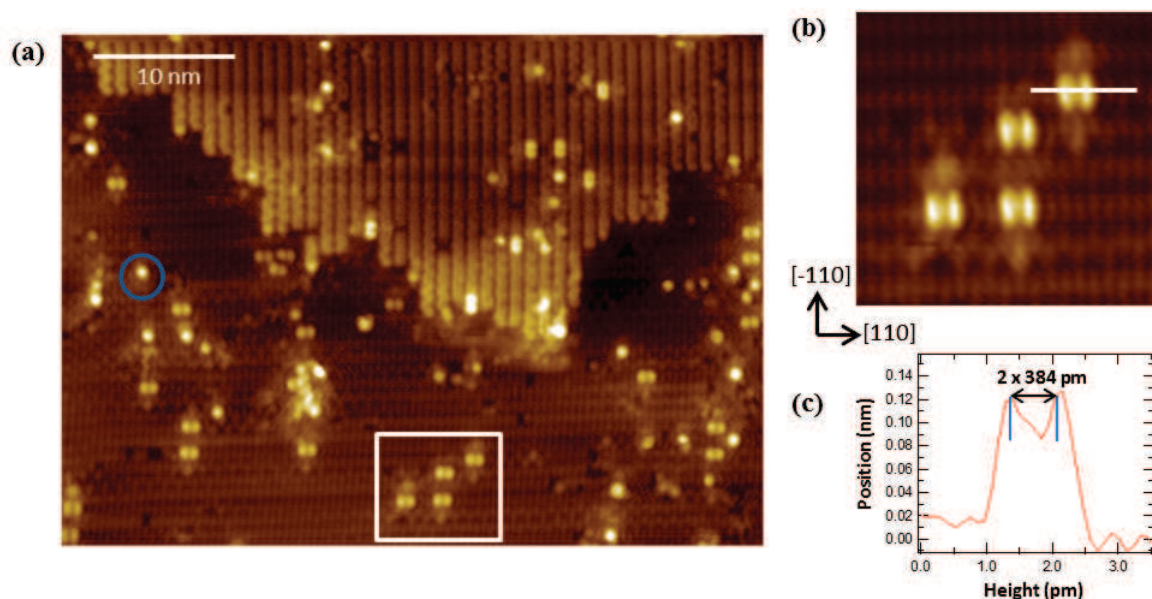


Figure 3.4: (a) Occupied-states STM image ($U = -2.0V$, $I = 100$ pA; $50\text{ nm} \times 33\text{ nm}$) of TEOS adsorbed at room temperature on Si(001)- 2×1 (n-doped, $0.003\ \Omega \times \text{cm}$) after an exposure of 10 min under a pressure of 9×10^{-10} mbar (0.4 L), (b) magnification image of the rectangular area of image (a) ($8\text{ nm} \times 8\text{ nm}$), (c) topographical profile along the line drawn in (b).

Figure 3.4 (a)) of apparent height ~ 130 pm. It seems to encompass two adjacent silicon dimers in a row. We attribute it to a non-fully dissociated molecule.

The majority of adsorption features is a pair of protrusions of height ~ 109 pm (somewhat smaller than that of the preceding one). Four such pairs are enclosed in the white rectangle of Figure 3.4 (a). Each pair extends over three dimers, as the protrusion maxima are separated by 2×384 pm, twice the inter-dimer distance in a row (Figure 3.4 (b) and 3.4 (c)). The symmetry of the pairs of protrusions in the mirror planes $(\bar{1}10)$ and (110) is a signature of the full TEOS dissociation where each bright protrusion is composed of two ethoxy moieties bonded to the same dimer. In contrast, the formation of three $\equiv\text{Si}^{\text{S}} - \text{OC}_2\text{H}_5$ moieties plus one $(\text{Si}^{\text{S}})_3\text{Si}^{\text{T}} - \text{OC}_2\text{H}_5$ adduct would lead to asymmetric footprints. Because of the breaking of all four Si – O bonds, each bright protrusion is indeed composed of two ethoxy moieties bonded to the same dimer. Inasmuch as all Si – O bonds are broken in the TEOS molecule, the fate of the released silicon

atom remains to be determined.

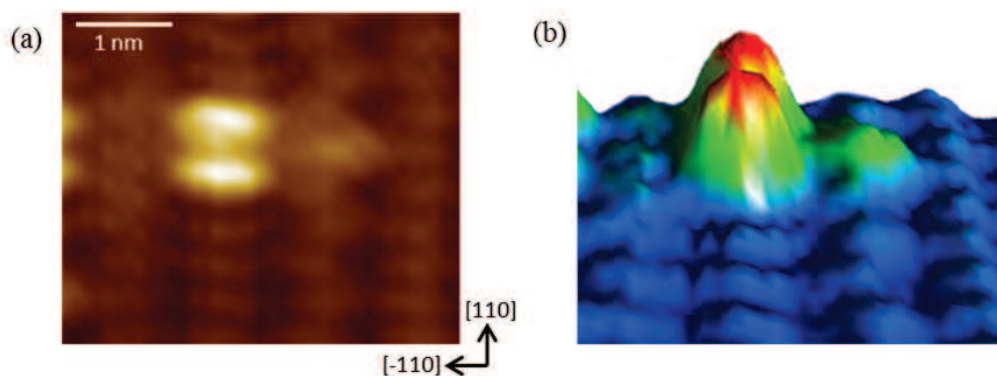


Figure 3.5: (a) Occupied-states STM image ($U = -2.0$ V, $I = 100$ pA; 3.3 nm \times 4 nm) of one TEOS molecule adsorbed at room temperature on Si(001)- 2×1 (n-doped, $0.003 \Omega \times \text{cm}$), (b) 3D representation of the image.

In Figure 3.5 (a), we zoom in on a pair of protrusions from Figure 3.4 (a). The 3D view (Figure 3.5 (b)) helps showing the nature of the adsorption site after molecular breaking. A weaker protrusion can be seen on the row adjacent to the ethoxy-decorated row. Its height is about 34 pm, four times smaller than the protrusions associated to the ethoxy groups. The systematic presence of this protrusion in the vicinity of the four ethoxy groups is indicative of the presence of the released silicon atom trapped on the adjacent row.

The resolution of Figure 3.4 (b) is good enough to observe the influence of TEOS fragments on surface buckling. On the dimer row bearing the ethoxy groups, the dynamic buckling is not affected: the dimer appear symmetric as the STM scanning time (ms to s) is much longer than the flip-flop buckling period (ps).[43], [44]

In contrast, where the silicon monomer sits, a static buckling is observed. The question of static/dynamic dimer buckling upon adsorption was addressed theoretically by Wilson et al.,[77] for the adsorption of phosphine (PH_3) on Si(001). When the two fragments (H and PH_2) decorate the two silicon dangling bonds of a dimer no static buckling occurs. This is a situation similar to the (fully symmetric) bonding of two ethoxy groups

on the same dimer. On the other hand, when PH_3 adsorbs datively (giving its lone pair to a down Si dimer atom), then static buckling is predicted by the calculation. Apparently, the adsorption of the silicon monomer causes a perturbation (e.g. a displacement of the pedestal silicon positions) comparable to the one due to the dative bonding of phosphine.

3.3 DFT calculations

To determine the exact position of the monomer on the surface a theoretical approach is needed.

The electronic structure and the adsorption energies of different adsorption configurations of TEOS on the silicon surface are computed within the Density Functional Theory, adopting the generalized gradient approximation (GGA) to the exchange and correlation energy.[78] The interaction between the ionic cores and the valence electrons was described through ultra-soft pseudo-potentials, as implemented in the VASP code.[79], [80] A Si slab consisting of 8 atomic layers, with lateral dimensions corresponding to a (8×4) two dimensional (2D) unit cell, is adopted in the simulations (Figure 3.6). The lattice parameter was kept fixed at the computed theoretical value $a = 546$ pm. This 2D unit cell makes it possible to study the adsorption in the limit of low coverage. For one TEOS ad-molecule on the $\text{Si}(001)\text{-}8 \times 4$ surface, the interaction energy between periodically repeated ad-molecules is negligible.

The slab is terminated by hydrogen atoms at the bottom side, in order to saturate bonds with unpaired electrons, and then relaxed. In all adsorption geometries, the two Si bottom layers and the H atoms are kept fixed, while all other degrees of freedom (Si atoms in the slab or atoms belonging to the ad-molecules) were relaxed until residual atomic forces do not exceed a few $\text{meV}/\text{\AA}$. At the surface of our slab, the relaxation results in the well-known buckling of the silicon dimers. The slab considered in our calculations comprises eight dimers that exhibit the experimentally observed alternate buckling expected at 0 K.

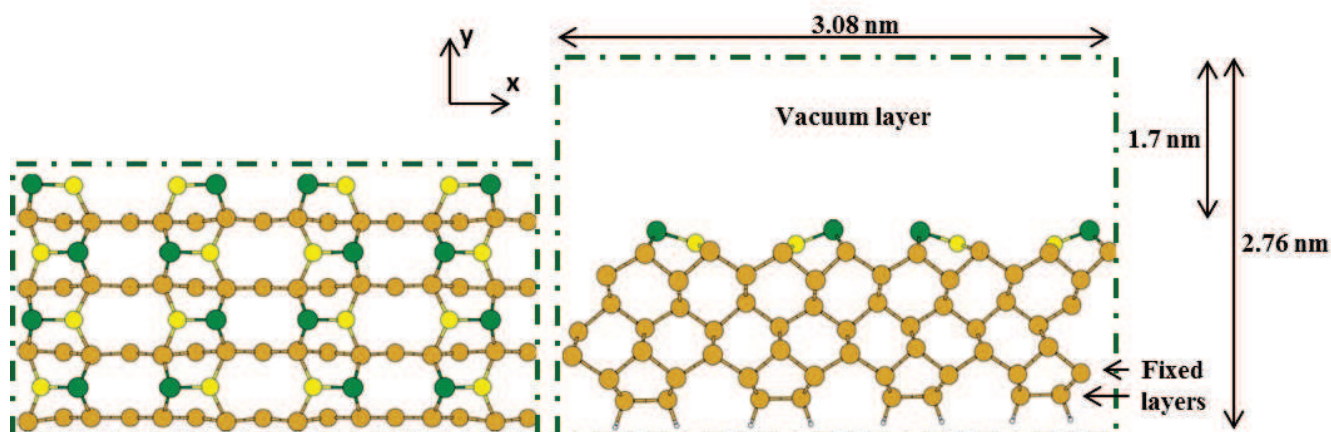


Figure 3.6: The 8×4 slab model within the unit cell used for the calculation.

The proper consideration of the buckling is important, because the reactivity of the Si(001)- 2×1 strongly relies on the non-equivalent positions and charges of the two silicon atoms within the dimer.

A 1.7 nm thick void space separates periodically repeated slabs along the [001] direction, which prevents the adsorption of molecules from being biased by the presence of periodic images. This sampling would correspond to the gamma point in the Brillouin zone of the Si(001)- 8×4 surface, which gives reasonably converged electronic DOS within the 50 meV smearing. Therefore, even if the precision of our calculations regarding the sampling of the Brillouin zone presented herein is not the best available, it offers far enough accuracy to calculate the LDOS and to simulate the STM images within the Tersoff-Hamann approximation.

TEOS fragments were positioned on the surface, four ethoxy groups on two dimers separated by an empty one and an adatom on the adjacent row. The adatom is bonded to two dimers, which belong to the same dimer row and roughly normal to a silicon on the second layer (position M in ref. [81], for more details see chapter 4). After configuration optimization the adatom distance from the two Si atoms within the dimers is 235 pm and from the silicon on the second layer 240 pm (the Si – Si bond length in the bulk is 235 pm), these values are in agreement with the calculated bonds lengths in ref.[81]. As the system is an open-shell system, spin polarized and non-spin polarized calculations

were performed; the resulting adsorption energies showed negligible differences.

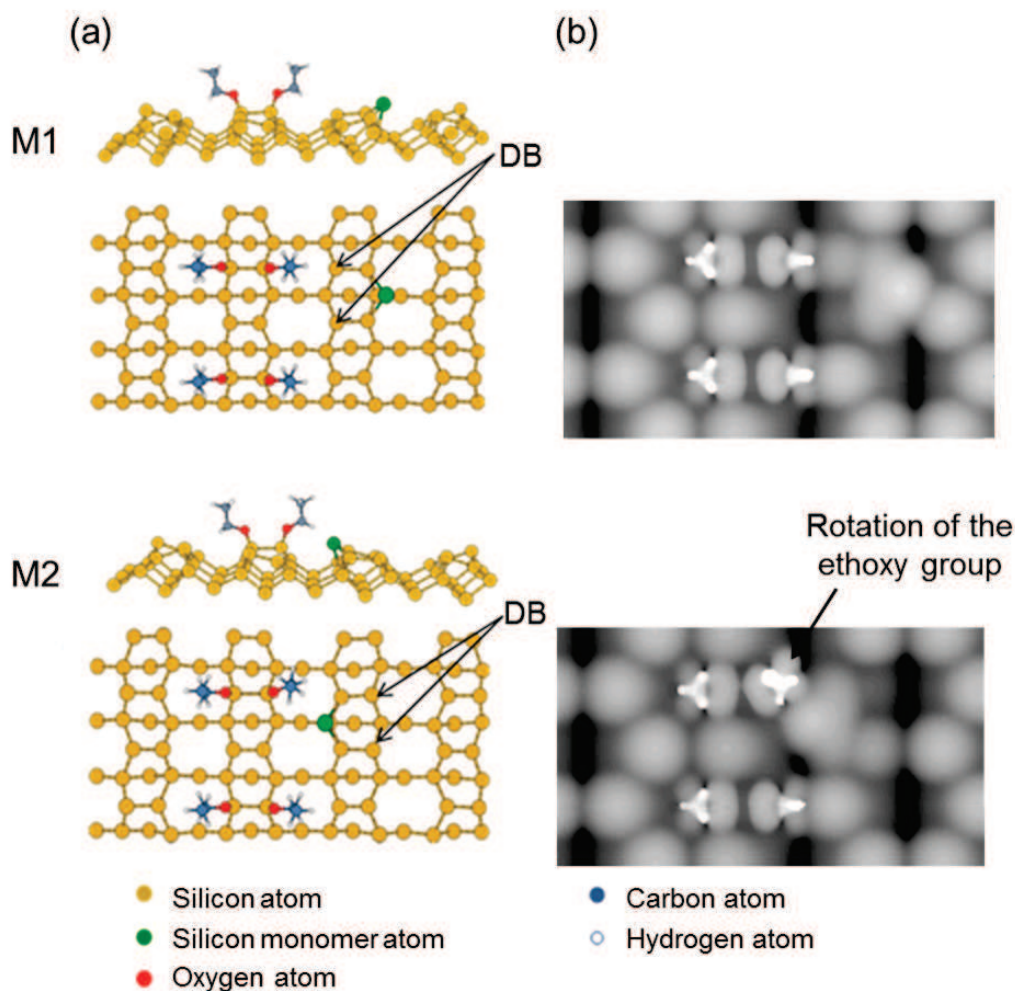


Figure 3.7: (a) Ball-and-stick representation of the adsorbed TEOS fragments obtained via DFT geometry optimization. (M1) corresponds to the configuration in which the monomer is sitting on the dimer side opposite to the ethoxy adsorption site, (M2) the monomer is pointing towards the ethoxy groups. (b) Simulated occupied-state STM images, computed within the Tersoff-Hamann approximation. Dangling bonds are denoted by DB.

Two non-equivalent M-configurations are possible (Figure 3.7): the monomer can bind to the adjacent row pointing away from the ethoxy groups (M1) or towards it (M2). The corresponding adsorption energies were calculated for both configurations. After

geometry optimization, the two configurations were almost degenerated ($E_{ads}(M1) = 1.97$ eV; $E_{ads}(M2) = 2.01$ eV). Apart from the position of the Si adatom, the most striking difference between the two configurations is the rotation of the ethoxy group in configuration M2 (by about 25° around the surface normal from a symmetric configuration, as in M1), due to the effective repulsion between the ethoxy group and the neighboring Si adatom.

Using as an input the M1 and M2 optimized configurations, we computed the corresponding occupied-state STM images in the framework of the Tersoff-Hamann theory.[82] The intensity of the tunnel current is proportional to the integrated density of state in the energy range $[\epsilon_F - \Delta V, \epsilon_F]$, where ϵ_F is the Fermi level and $\Delta V = 2$ eV corresponds to the bias voltage of the experimental measurement. A density threshold ρ_0 was employed, which defines the height of the iso-density contour with respect to the atomic surface. ρ_0 was adjusted to a height of about 450 pm, which is a typical tip-surface distance in an experimental setup. The simulated STM images are presented in Figure 3.7 (b).

As a preamble to any comparative discussion of the experimental and theoretical STM images, firstly, one must emphasize that calculations are carried out at 0 K. The simulated images correspond to an absolute minimum of energy; secondary energy minima that could be accessed at non-zero temperature via rotations of the ethoxy moieties around the Si – O and O – C axes (Figure 3.7) are not taken into account. In our simulation all tunneling currents are considered and represented in an intensity grey scale (the brightest corresponds to the most intense current). Therefore, we focus on the brightest spots in Figure 3.7 (b).

The calculation gives a distinct spot for each ethoxy group, while the two ethoxy groups on a dimer are not resolved in the experimental STM images (Figure 3.7). Rotations, unhindered at 300 K, may explain the difference. The calculation gives also a crucial information: the dangling-bond bearing Si atoms (denoted DB in Figure 3.7 (a)), pertaining to the two adjacent dimers on which the adatom is sitting, give a spot fainter than that of the Si adatom. In the experimental image, the “faint protrusion” (green in the 3D image) is seen away from the ethoxy features (Figures 3.5 (a) and 3.5 (b)).

Therefore, the adatom should sit on an M1 position (and not on M2). However, in the experimental image the “faint protrusion” is aligned with the depression between the two ethoxy-decorated dimers, corresponding to a bare dimer. This symmetric position of the “faint protrusion” is not accounted by the simulated image. In fact, we can hypothesize that the adatom moves back and forth between two equivalent M1 positions, and that the experimental image is time-averaged.

To our knowledge, this is the first time that a silicon monomer is identified by STM on a dimer row at room temperature. Adsorption and diffusion of silicon atoms on Si(001) was widely studied, in order to gain a better knowledge of the initial stages of homoepitaxial growth.[83], [84], [85], [86], [87] On cold enough substrates ($T = 160$ K), the diffusion of the monomer is frozen out,[83] but the precise geometrical configuration of monomers likely trapped in steps, islands, or clusters cannot be obtained precisely.[88], [89], [90], [91] At room temperature, no isolated monomer on a terrace has ever been observed, mainly because its diffusion is so fast that it cannot be imaged and thus remains unnoticed. In our case, we propose that the presence of ethoxy groups helps trapping Si adatoms on the adjacent dimer row.

3.4 Summary

Using XPS and STM experiments in conjunction with DFT calculations and STM image simulations, we have shown that TEOS dissociates on the Si(001)- 2×1 surface at room temperature. For exposures in the langmuir range, XPS shows that the majority dissociation product results from the cleavage of the Si – O bonds of the TEOS molecule. The chemical adsorption sites of the majority species are better identified by STM at low coverage (0.4 L). The four ethoxy fragments decorate two surface dimers separated by an empty one. The remaining Si central atom moves to the adjacent dimer row, where it sits as an adatom.

In our DFT modeling, the adatom rests on three pedestal atoms, two silicon atoms from the top plane and one (hypercoordinated) silicon from the second plane. To ac-

count for the observed symmetries in the STM experimental image, we must assume that the monomer moves back and forth between two equivalent positions. We propose that the detection of the silicon adatom at room temperature is related to its hindered diffusion along the dimer row, due to the presence of ethoxy groups in the adjacent row and we will try to prove it in the next chapter.

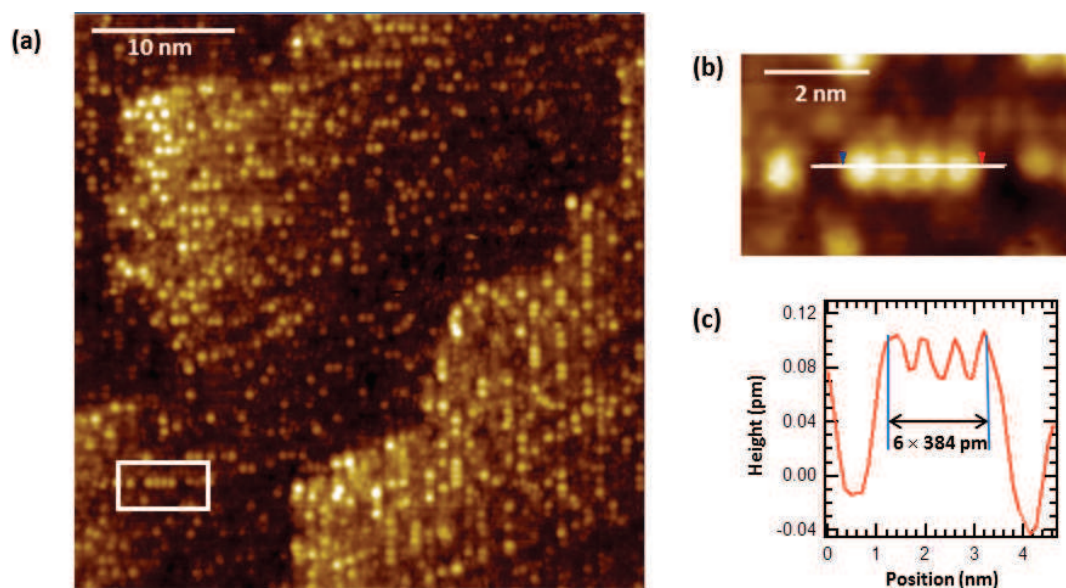


Figure 3.8: (a) Occupied-states STM image ($U = -2.0$ V, $I = 100$ pA; 40 nm \times 40 nm) of a clean Si(001)- 2×1 surface (n-doped, $0.003 \Omega \times$ cm) exposed, at room temperature, to TEOS (30 min, 9×10^{-10} mbar), (b) magnification image of the rectangular area of image (a), (c) topographical profile along the line drawn in (b).

As described in the chapter introduction, TEOS is used to form self-assembled layers. STM images, at higher coverage (1.2 L) compared to those presented in section 3.2, are presented Figure 3.8. The number of paired bright protrusion corresponding to the ethoxy groups has increased significantly. The growth of ethoxy-decorated domains can be observed, their length extends up to ~ 13 dimers. The topographical profile of Figure 3.8 (c) shows that, despite the “crowding”, the distance between ethoxy pairs (two $\langle 110 \rangle$ lattice spacings) does not change with respect to the more diluted case (see Figure 3.4). The ethoxy group adsorption is clearly one-dimensional and occurs along a dimer row and ethoxy-covered dimer rows alternate with ethoxy-free ones. It may be due to the presence of silicon monomers on the adjacent ethoxy-covered row. This inter-

esting pattern could be used to produce self-organized nano-structures on Si(001)- 2×1 .

Chapter 4

Silicon monomer diffusion on the clean and the TEOS covered Si(001)- 2×1 surface

In chapter 3, we presented the observation of an isolated monomer by STM, on the Si(001)- 2×1 surface after TEOS dissociation. In order to understand how TEOS fragments influence the diffusion of the monomer on the silicon surface, we decided to restart from the analysis of the monomer diffusion on the clean surface and afterward to extend our work to the ethoxy-covered surface.

4.1 Overview: Silicon monomer diffusion on the clean Si(001)- 2×1 surface

The diffusion of adatoms on semiconductor surfaces is a fundamental problem in surface physics, in particular, in relation to epitaxial growth. Two important questions to be answered are the identification of the binding sites for adatoms and the determination of the activation energies for surface diffusion. Two main approaches to atomistic simulations in materials science are possible, representing two extremes with respect to computational cost of the simulation.

The first widely used technique is ab-initio methods. They are adapted to reproduce a rich variety of experimentally observed effects. Ab-initio methods are computationally expensive, the largest systems studied so far involve geometry optimization for supercells with up to 600-800 atoms using parallel supercomputers.[92] Due to the

computational cost, dynamic simulations are limited to time scales of 10 to 100 ps.

The second technique is based on the use of empirical or semi-empirical interaction potentials to describe bonding between atoms. These potentials might be of different degrees of sophistication (e.g. two-body or many-body potentials), but they always rely on a specific parametrization of the total energy of the system as a function of atomic positions. Parameters for such schemes are usually selected so as to reproduce chosen experimental properties of the material in question. The advantages and drawbacks of this technique are directly opposite to those of ab-initio methods. This approach has the advantage of computational simplicity which allows large-scale computations to be performed at a relatively low cost and increases the time scale that it is possible to reach for dynamic simulations (1000 times higher than for ab-initio methods). However, these potentials for silicon,[93], [94] fail in reproducing the ground-state structure of the Si(001) surface. The problem can be traced back to the fact that the potentials are constructed to favor four-fold diamond structure coordination and the accuracy of modeling a system with dangling bonds using these potentials was never guaranteed.

In this chapter, we are interested in the electronic structure of the surface as a function of the monomer position and therefore, we decided to use ab-initio methods.

4.1.1 Ab initio methods

First-principles calculations were used to identify the binding position and migration barriers of a single Si adatom on a reconstructed Si(001) surface in order to explain the difficulty to observe silicon monomers by STM and their anisotropic diffusion on the surface. A schematic view of the important positions for the adatom on the Si(001) surface is presented Figure 4.1.

Pioneering work on Si atoms on the Si(001) surface by ab-initio methods was published in 1992 by Brocks et al.[81] They performed calculations within the local-density-functional formalism, using norm-conserving pseudo-potentials and a plane-wave basis set. The Si(001) surface was modeled as a repeated slab, consisting of twelve layers of Si atoms and 9.5 Å of vacuum spacing. Inversion symmetry with respect to the mid-

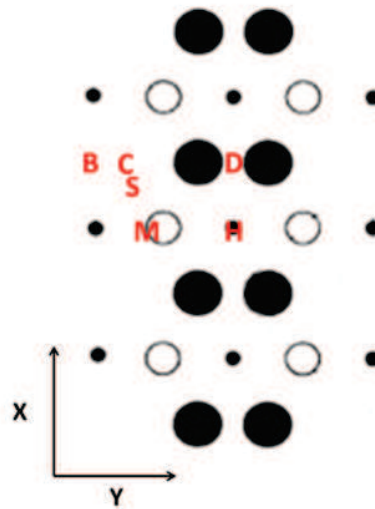


Figure 4.1: Schematic representation of the topmost three layers of the $p(2\times 1)$ symmetric dimer reconstruction Si(001) surface. The large solid circles represent the top-layer atoms, the medium-sized open circles represent the second-layer atoms, and the small solid circles represent the third-layer atoms.

dle of the slab was used to increase the computational efficiency. The authors simulated first the clean surface (without the ad atom) and in agreement with the results obtained by Roberts and Needs, they found that the $p(2\times 2)$ alternating-buckled-dimer surface has the lowest energy.[95] However, the energy difference between the $p(2\times 2)$ and the $p(2\times 1)$ symmetric-dimer reconstruction was small (less than 0.1 eV/dimer); in order to reduce the size and thus the computational time, calculations were carried out on the $p(2\times 1)$ symmetric-dimer reconstructed surface.

The total energy was mapped out as a function of the adatom position (x,y) in order to draw a potential energy surface $E(x,y)$. For each (x,y) position, the z coordinate of the adatom is kept free, in order to determine the position minimizing the system total energy. Figure 4.2 shows the energy surface obtained by Brocks et al.[81]

On the interpolated energy surface, the binding position of the absolute minimum energy is identified to be position M. The geometry of the resulting equilibrium binding configuration of adatom and substrate (shown in Figure 4.3) may be understood in terms of the adatom making as many covalent bonds as possible without disrupting

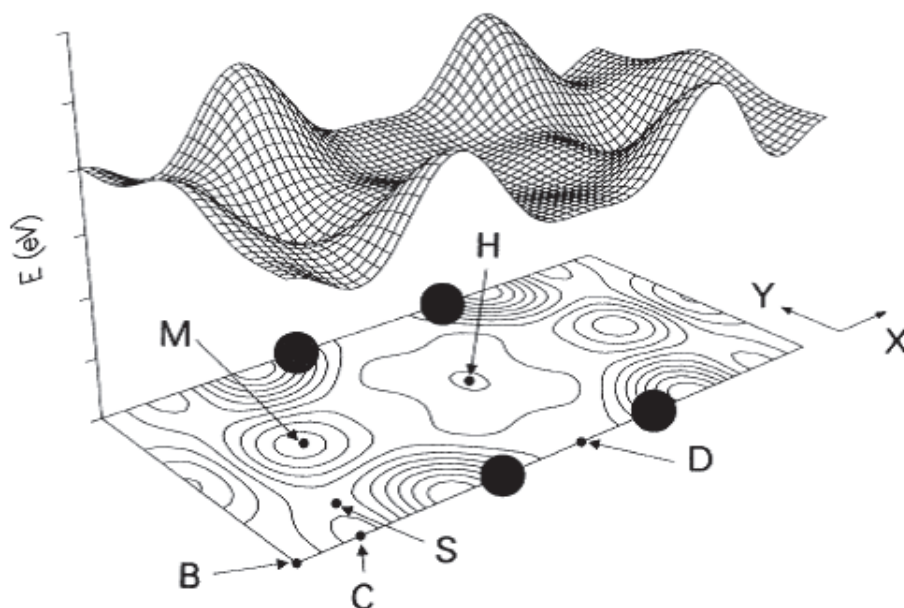


Figure 4.2: Perspective view and contour plot of the total-energy surface $E(x,y)$ obtained by Brocks et al.[81] The first contour is at 0.1 eV with respect to the absolute minimum (M) and the contour spacing is 0.2 eV. The interval on the vertical energy axis is 1 eV and the zero of energy is chosen arbitrarily. The x axis is chosen so as to pass through a dimer.

the underlying substrate. The adatom, in position M, is bonded to two dimers which belong to the same dimer row (bond lengths are 2.35 Å) and to a silicon atom of the second layer substrate (bond lengths are 2.40 Å). In all ab-initio calculations, position M is recognized as the energy absolute minimum.[81] [96]

The quasi-hexagonal site H corresponds to a local minimum on the energy surface.[81] The adatom forms four long bonds of 2.48 Å to the substrate and stretches the dimer bonds to 2.42 Å. The total energy for this site is 0.25 eV higher than the absolute minimum. However, Smith et al.[96] considered, both the uniformly buckled asymmetric $p(2\times 1)$ reconstructed surface and the alternating buckled $p(2\times 2)$ surface; little difference was observed on the total energy map (less than 0.05 eV), except near the H site. For the $p(2\times 2)$ surface, H is a local minimum while in the case of the $p(2\times 1)$ surface it is not; the local minimum is moved toward the M site on the C-M-H line. It shows that the substrate degrees of freedom play a role in the adsorption process, and that

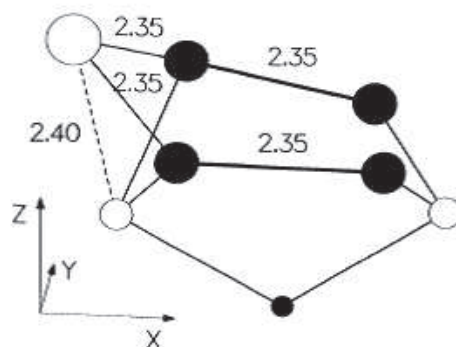


Figure 4.3: Perspective view of the equilibrium binding configuration obtained by Brocks et al.[81] showing the first-, second-, and third-layer substrate atoms as in Figure 4.2, and the bond lengths in angstroms. The adatom is shown as a large open circle.

local minima can depend on the local surface buckling. However, the potential surface is, in the area between two dimers, almost flat and the energy differences between two possible local minimums are small (0.1 eV in ref. [96])

To describe the diffusion of a silicon adatom on the Si(001) surface, it is necessary to determine the activation energy for a jump between two binding sites. Brocks et al.[81] investigated three different pathways; two are parallel and the third is perpendicular to the dimer rows (see Figure 4.2). The first path runs from the absolute energy minimum site M to the local minimum site H and from there to the saddle point position D, its activation energy is 0.6 eV. The second path links the M site to the local minimum C via the saddle point position S and has an activation energy of 0.8 eV. The last one goes over the B site, established as the saddle point configuration for diffusion perpendicular to the dimer rows, and implies an activation energy of 1.0 eV. The authors conclude in favor of the first path to explain the adatom diffusion on the surface observed at room temperature.

Shu et al.[97] also studied the diffusion of adatoms on the $p(2\times 2)$ surface, they showed, similarly to Brocks et al., that H was a local minimum but the activation barrier obtained for the two path parallel to the dimer rows are comparable (0.65 eV for M-H-D and 0.66 eV for M-S-C); the probability for an adatom to diffuse along one of these two path is the same.

Smith et al.[96] also reported closed values for these two path for both p(2×2) and p(2×1) surfaces. The energetic barrier value is modified between these two surface configurations of 0.2 eV from M to H (0.7 eV for the p(2×2) surface and 0.5 eV for the p(2×1) surface); in the reverse direction on the C-M-H line, an adatom in H position see a barrier of 0.2 eV for the p(2×2) surface and no barrier for the p(2×1) surface. For the M-S-C path, the calculated energy barrier is 0.6 eV for both reconstructions.

The comparison of various ab-initio calculations shows that qualitatively similar potential energy surfaces are obtained. There are, however, some quantitative differences. They can be due to the reconstruction surface used, the local configuration of dimers can modify how silicon adatoms are linked to the surface as described previously. A second reason is the various approximations that can be used for the calculation and more precisely the choice of the functional. This aspect will be discussed later.

4.1.2 Empirical or semi-empirical interaction potentials

The second possible approach for the understanding of silicon adatom diffusion is the use of empirical or semi-empirical interaction potentials. Many inter-atomic potentials can be used to obtain a correct description of equilibrium properties and microscopic energies of solids. Several types of such empiric (or semi-empiric) interatomic potentials have been developed for semi-conductors. Some of them correctly describe bulk elastic properties of the material, while others are more suitable for predicting surface properties. Consequently, the choice of the potential needs to take into account the characteristics of the material which are fundamental for the investigation. In particular, diffusion on Si(001) terraces was simulated [98], [99], [100] with the help of the Stillinger-Weber potential,[93] or Tersoff potential;[94] molecular dynamics with the potential of an embedded atom (method MEAM [101]) was also used for simulating individual silicon adatoms and ad-dimers on the Si(001) surface.[102]

Zhang et al.[103] and Smith et al.[96], using the Stillinger-Weber silicon potential, predicted the lowest-energy position to be position B and the second-lowest-energy site

to be site D. With Tersoff potential, Smith et al.[96] gave identical conclusions. These results show that D is a local minimum while, with first-principles calculations, it is a saddle point. Using the modified embedded-atom method MEAM[101], Baskes obtained two energy minimums M and B with close energies. Cai et al.[102] used an empirical potential able to correctly predict asymmetrical buckling of the Si(001) surface and the relative stability between them. They showed, with this potential, that the binding energies gradually decrease for site M, D, H, A, and B, i.e., therefore, site M is predicted to be the lowest-energy site and site D the second-lowest-energy position. The results from these empirical potentials are, therefore, conflicting with each other and also with those from first principles calculations.

Diffusion path can also be compared. Same paths, as for first principle calculation are considered, two parallel to the dimer rows and one perpendicular to them. Zhang et al.,[103] using the Stillinger-Weber silicon potential, found that diffusion parallel to dimers rows occurs with an activation energy of 0.3 eV, and perpendicularly to them with 0.7 eV. Using MEAM [101], the calculated activation energies are respectively 0.74 eV for parallel diffusion and 0.98 eV for normal diffusion. But using Tersoff potential, Simth et al.[96] gave the corresponding energies of 0.7 and 0.3 eV which are in conflict with previous results and first principles calculations. Finally, Cai et al.[102] conclude that the migration of an adatom occurs in parallel to the dimer rows between two rows.

We can conclude that available empirical potentials have been unable to predict, up to now, the most stable position for the adatom on the Si(001) surface and its most probable path for diffusion. These potential have been also unable to predict the asymmetric reconstruction structure of the surface in its ground state. This indicates that there is an intrinsic error in empirical treatment of dangling bonds.[92]

Finally, a different pathway also investigated, by Wang et al.[104] and Ijima et al.,[105], should be mentioned. Si adatom can diffuse along the direction perpendicular to the dimer row, involving exchanges between the adatom and surface atoms. They found that the Si adatom can diffuse on a Si(001) surface by switching position with a surface atom with a non-negligible frequency of occurrence at high temperature (1000 K to 1300 K). The exchange mechanism is not always a simple process, and complex

processes were observed where up to three surface atoms were involved. For diffusion perpendicular D_{\perp} to the dimer row, the exchange events occurred slightly more frequently than hopping did (14 occurrences compared with 11) and reduce the energy barrier of diffusion. In the parallel direction D_{\parallel} , the exchange has only a minor effect as the hopping occurs much more frequently.

4.2 The energy landscape of a Si adatom on the Si(001) surface

Looking at the various results described in the literature for the monomer diffusion on the clean Si(001) surface, and their dependence on the surface reconstruction and the calculation method, we decided to restart the investigation.

The energy surfaces, presented in this chapter, are computed within the Density Functional Theory (DFT), adopting the generalized gradient approximation (GGA) to the exchange and correlation energy.[78] The interaction between the ionic cores and the valence electrons is described through ultra-soft pseudo-potentials, as implemented in the VASP code.[79], [80]

4.2.1 The Si(001)-2×2 surface

The first slab consists of 10 atomic layers, with lateral dimensions corresponding to a (2×2) two dimensional (2D) unit cell. The lattice parameter, which is of 541.5 pm according to the experiment, is kept fixed at the computed theoretical value $a = 546$ pm which minimizes the energy of the Si bulk in the GGA approximation. A 1.7 nm thick void space separates periodically repeated slabs along the [001] direction, which prevents the adsorption of molecules from being biased by the presence of periodic images. The sampling corresponds to two k-points in the Brillouin zone of the Si(001)-2×2 surface (k-points are presented in Table 4.1). However, the energy was also calculated with eight k-points for the monomer in position M and D of the surface, the energy

barrier was unchanged ($\Delta E < 0.05 \text{ eV}$).

Reconstruction	Reciprocal space vectors	Number of k-points	Coordinates of the k-points
2×2	$\vec{b}_1 = \frac{2\pi}{\sqrt{2}a}(1, 0, 0)$	2	$(1/4, 1/4)$ $(1/4, -1/4)$
	$\vec{b}_2 = \frac{2\pi}{\sqrt{2}a}(0, 1, 0)$	8	$(1/8, 1/8)$ $(1/8, 3/8)$ $(3/8, 1/8)$ $(3/8, 3/8)$ $(1/8, -1/8)$ $(1/8, -3/8)$ $(3/8, -1/8)$ $(3/8, -3/8)$

Table 4.1: Description of the k-points used for the 2×2 reconstructed surface calculations (where a is the lattice parameter).

The slab is symmetric and a monomer is present on each side. This approach maintain the symmetry of the cell and avoid the presence of an artificial dipole-dipole interaction between the periodic images in the z direction. In all adsorption geometries, the two central Si layers are kept fixed, while all other degrees of freedom are relaxed until residual atomic forces do not exceed a few $\text{meV}/\text{\AA}$. The slab considered in our calculations comprises two dimers that exhibit an alternate buckling, as expected at 0 K. The energy surface is presented Figure 4.4.

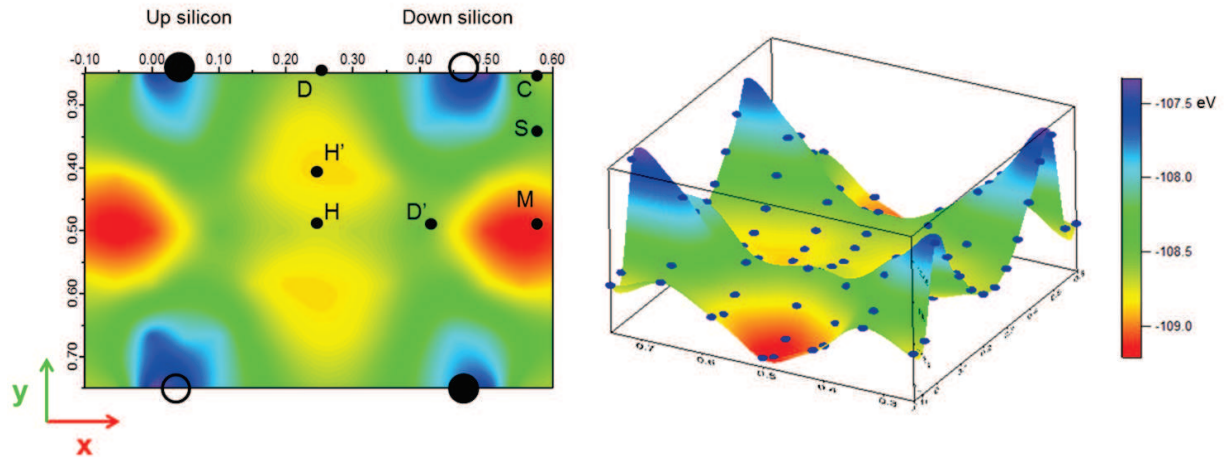


Figure 4.4: Contour plot and perspective view of the 2×2 total energy surface.

The dimer rows on the Si(001) surface are parallel to the y axis, and the direction of the dimer bond is along the x axis. An equidistant grid, with a spacing between the grid

points of 0.24 Å in the x and 0.54 Å in the y direction, was used to represent the surface. The surface was interpolated using the Gaussian interpolation method of Igor Pro.

As shown in the overview, the proper consideration of the buckling is important, because the reactivity of the Si(001)-2×1 surface strongly relies on the non-equivalent positions and charges of the two silicon atoms within the dimer. In order to understand the buckling role, the results, obtained with the 2×2 surface cell, were compared with a 2×1 surface comprising two dimers with the same orientation. Both surfaces have the same dimer density. Negligible modifications are observed between the two surfaces (energy differences lower than 0.1 eV).

The binding position of the adatom at the absolute minimum (site M) can be identified on the interpolated energy surface. It corresponds to the configuration of the monomer described in the previous section and in chapter 3, where the adatom is bonded to two silicon atoms of two neighboring dimers and bonded to a silicon atom of the beneath layer.

Unlike Brocks et al. results, [81] the quasi-hexagonal site (site H) does not correspond to a local minimum on the energy surface. A local minimum is observed in position H', the total energy for this site is 0.14 eV lower than the site H and 0.35 eV higher than the absolute minimum.

Both H and H' adsorption sites are described in Figure 4.5. At the H' site, the monomer can make two bonds (~ 2.3 Å) with two silicon atoms of a dimer. At the H site, only weak bonds are possible (~ 2.55 Å) with the four silicon atoms of two dimers and may explain the obtaining of a less stable configuration.

From the knowledge of the energy landscape, we can figure out how the silicon adatom diffuses. It can diffuse on the surface through two different paths along the x direction. The first path connecting two adjacent cells is the path through the M-S-C line where S is a saddle point and C a local minimum (see Figure 4.6 (a)). The energy barrier is of 0.75 eV. The second path we consider supposes that the monomer in H' position cross a first saddle point in H to reach the second H' site of the cell and then a second saddle point in D to access to the next cell (see Figure 4.6 (b)). The energy

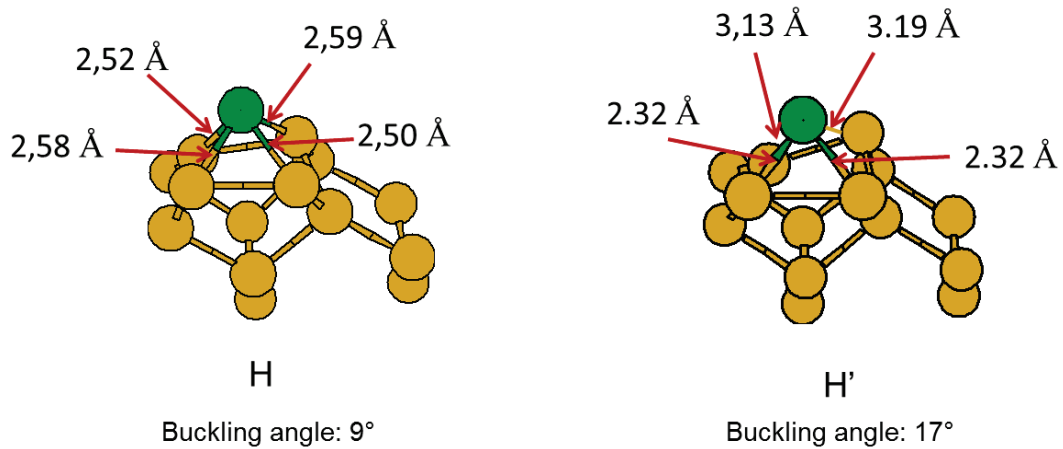


Figure 4.5: Perspective view of the H and H' configurations on the 2×2 reconstructed surface.

barrier between H' and H is of 0.12 eV and between H and D of 0.23 eV. The easiest way for diffusion along the dimer row is thus the second path. However, this second path does not start from the absolute energy minimum M. The energy needed to pass the barrier between M and H is of 0.70 eV. (see Figure 4.6 (c)) However, all the barriers calculated in this chapter are obtained from a static simulation and do not take into account thermal fluctuations.

Except for the H/H' local minimum difference, also raised up by Smith et al., [96] and which is a quite small quantitative difference, the energy surface is similar with the one obtained by Brock et al.. The energy barrier are also comparable, for the M-S-C line we obtain 0.75 eV vs 0.8 eV in ref. [81] and for the M-D' barrier energy 0.6 eV vs 0.7 eV in ref. [81]. The major difference between these two calculations remains the surface buckling, indeed, in ref. [81] the dimers are symmetric while in our calculations they are asymmetric.

4.2.2 The Si(001)- 8×4 surface

A bigger slab was then investigated for two reasons:

- In the previous slabs, all the dimers of the surface are bonded to the monomer and

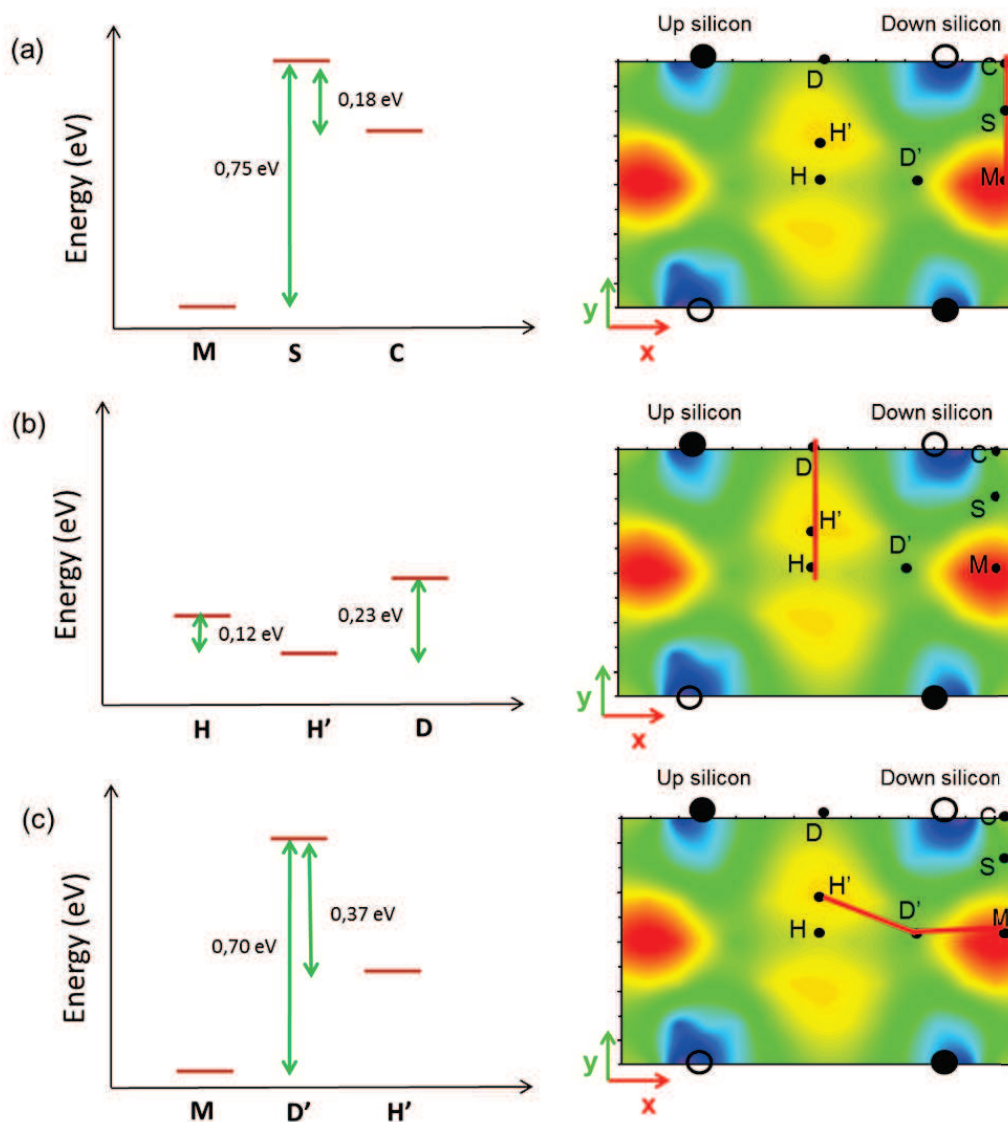


Figure 4.6: Energies along the possible diffusion paths on the 2×2 total energy surface.

this monomer can interact with its periodic images. A more realistic situation with an isolated monomer must be investigated.

- Because a bigger slab will be needed, in the next section, to add ethoxy groups on a clean row and investigate their role in the monomer diffusion. Therefore, to allow a direct comparison between the clean and the ethoxy covered surface, the same slab is used for both systems.

This slab is similar to the one presented in chapter 3 and corresponds to a 8×4 reconstructed surface. It is terminated by hydrogen atoms at the bottom side, in order to saturate bonds with unpaired electrons, and then relaxed.

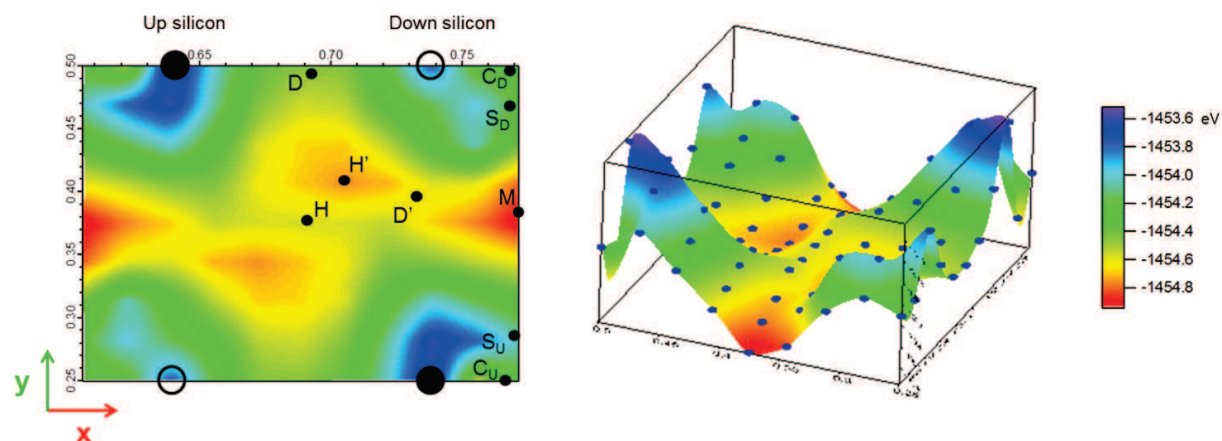


Figure 4.7: Contour plot and perspective view of the 8×4 total energy surface.

In all adsorption geometries, the two Si bottom layers and the H atoms are kept fixed, while all other degrees of freedom (Si atoms in the slab or atoms belonging to the ad-molecules) are relaxed until residual atomic forces do not exceed a few $\text{meV}/\text{\AA}$. An equidistant grid, with a spacing between the grid points of 0.34\AA in the x and 0.43\AA in the y direction, was used to represent the surface.

For the calculation, we used the gamma point in the Brillouin zone of the Si(001)- 8×4 surface which gives a comparable density of k-points in the Brillouin zone relative to the 2×2 cell. We also run some additional test with a different k-point and the energy barriers were varied less than 0.05 eV .

The energy surface is presented in Figure 4.7. The asymmetry of the dimers has more important consequences on this energy surface with respect to the 2×2 surface. The monomer at the vertical position of the upper silicon is less stable than the one at the vertical position of the lower silicon ($\Delta E = 0.25 \text{ eV}$ compared to 0.13 eV on the 2×2 surface). It induces an asymmetry of the energy surface, the axes (MD) and (DH) are not symmetry axes anymore; however, H is still a symmetry center.

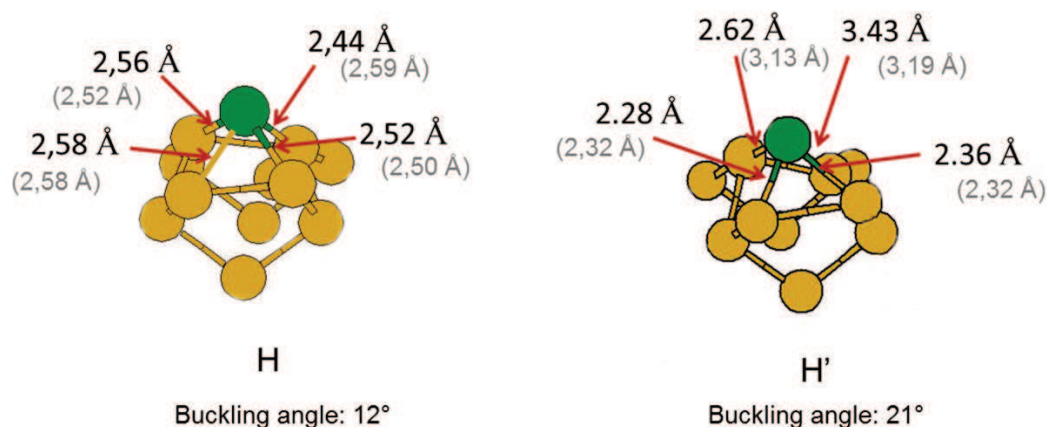


Figure 4.8: Perspective view of the H and H' configurations on the 8×4 reconstructed surface (The values between brackets are the bond length obtained for the clean 2×2 surface).

These changes force us to distinguish between C and S sites placed near an upper or a lower dimer silicon atom. In the following, they will be marked as C_D and S_D if they are close to a lower silicon atom and C_U and S_U if they are close to an upper silicon atom.

Site M is still the absolute minimum and H a saddle point on the energy surface. A minimum is observed in position H'. The monomer configurations on the H and H' positions are given Figure 4.8. The total energy for this site is 0.16 eV higher than the one of the absolute minimum M, this value can be compared to the one obtained for the 2×2 surface, the energy difference between M and H' is of 0.35 eV.

The H' configuration is more stable on the 8×4 surface than on the 2×2 surface. The monomer makes two bonds ($\sim 2.3 \text{ \AA}$) to two silicon atoms of a dimer similarly to the 2×2 surface and additionally, a weaker bond with one silicon atom of a second dimer ($\sim 2.6 \text{ \AA}$), as shown Figure 4.8. This supplementary bond may be responsible for the slight stabilization.

Figure 4.9 (a) presents the energy barrier for the path through the M-S-C line. The energy barriers for the M- S_D - C_D path are similar to the one on the 2×2 surface while

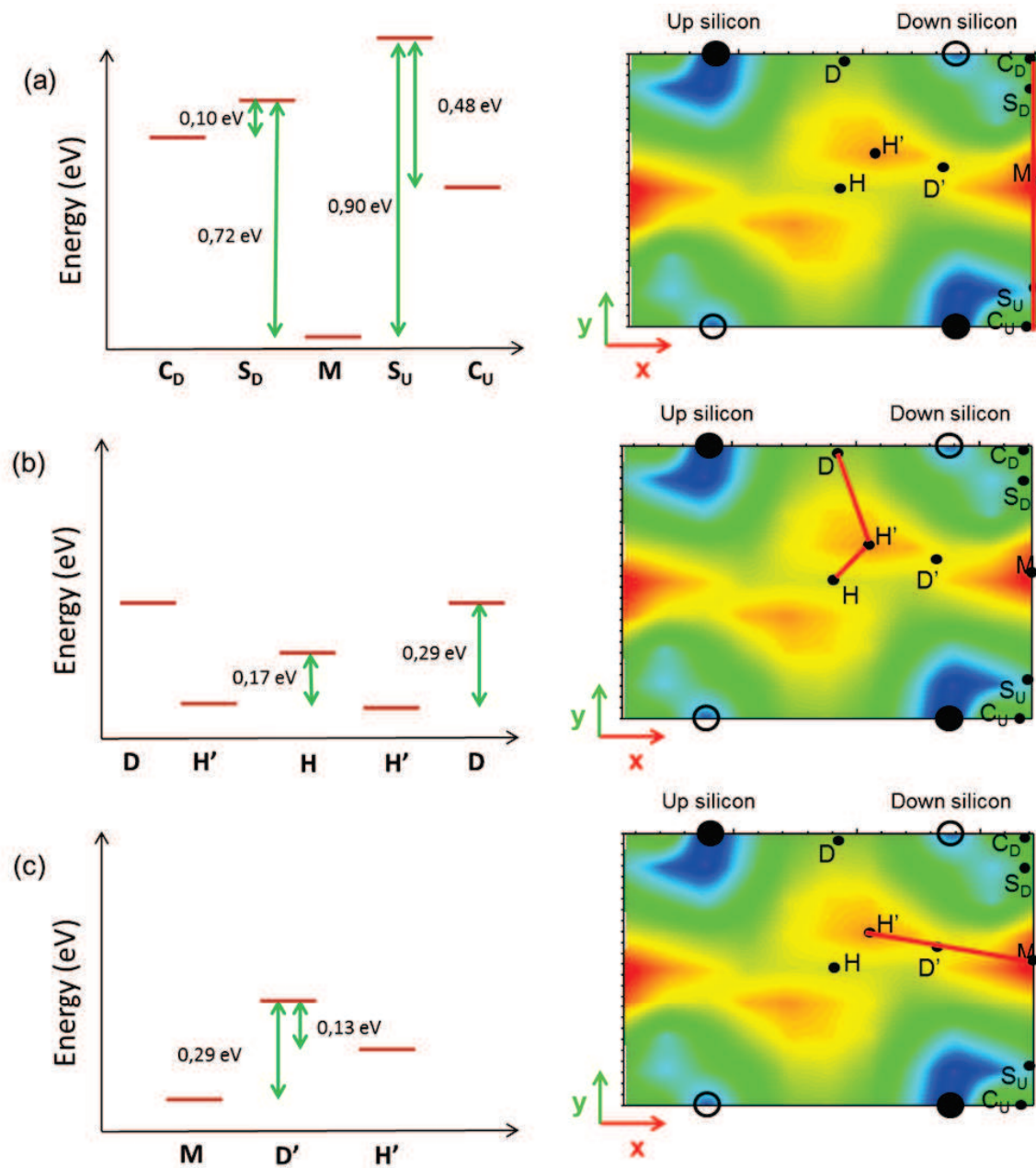


Figure 4.9: Energies along the possible diffusion paths on the 8×4 total energy surface.

for the M - S_U - C_U path they have significantly increased (~ 0.20 eV). This increase can be related to the proximity with the upper silicon atom, which position induces on increase in the z position of the adatom and so, weaker interactions are developed with underneath surface silicon atoms.

The second path we consider is presented Figure 4.9 (b). The energy barrier between H and H is of 0.17 eV and between H and D of 0.29 eV. They are similar to those measured for the 2×2 surface. But the stabilization, observed on H position, is also significant at the transition state between M and H, in position D (see Figure 4.9 (c)), the energy barrier is of 0.29 eV (0.70 eV on the 2×2 surface).

In conclusion, the major difference between the 2×2 and 8×4 surface is the difference in the energy barrier between sites M and H (0.70 eV and 0.29 eV respectively). This modification can considerably modify the possibilities of diffusion for the monomer.

4.2.3 Influence of the slab dimension

To verify that the dimensions of the slab are not responsible for these energy differences, we transformed the 2×2 slab into a 8×4 slab by replicating the 2×2 configuration four times along x and twice along y. In this new slab, only the atoms of one 2×2 cell are kept free during the calculation. The energy of the system was determined for sites M and D, an energy difference between these two sites of 0.74 eV was obtained while, for the 2×2 slab, the barrier is of 0.70 eV.

Therefore, the energy difference is not due to an artifact of the calculation but to a physical effect linked to the slab dimension and to the adatom density on the surface. For the 2×2 slab, there are two dimers on the surface and one monomer between them, consequently, all the dimers of the infinite surface are interacting with a silicon monomer. On the contrary, on the 8×4 surface, there is one monomer for 16 dimers, and more precisely, the two dimers carrying the monomer are surrounded by free dimers. The 8×4 slab simulates conditions that are more directly comparable with experiments, where few monomers are diffusing on the surface. The free dimers may be able to enforce the alternate buckling of a row (it explains the energy difference between sites C_D and C_U) and to counterbalance the effect of the monomer. The comparison of the buckling angle for H and H positions between the 2×2 and 8×4 surfaces (Figure 4.5 and Figure 4.8 respectively) shows that it is slightly more significant ($\sim 5^\circ$) on the 8×4 surface.

4.2.4 GGA vs LDA

A delicate problem with DFT is the choice of the functional for exchange and correlation. The most widely used approximations are the local-density approximation (LDA), where the functional depends only on the density at the coordinate where it is evaluated and the generalized gradient approximation (GGA) which takes into account the gradient of the density at the same coordinate.

In order to control the impact of the functional choice on the potential surface, the energy barriers between several important monomer positions on the surface were calculated for both LDA and GGA functionals. The results are presented Table 4.2. We observe that the barriers are slightly higher in the GGA than in the LDA; however, the energy differences are small ≤ 0.5 eV and these differences do not modify the interpretation of the results.

Energy difference	GGA	LDA
M-D	0.74 eV	0.69 eV
M-H	0.48 eV	0.42 eV
M-S	0.75 eV	0.75 eV

Table 4.2: Energy difference between two sites of the surface obtained for two different approximations for exchange and correlation.

Another parameter must be discussed, in these two cases we used the theoretical value of the lattice parameter obtained by minimization of the silicon crystal structure energy. For the LDA calculation $a = 540.6$ pm and for the GGA $a = 546$ pm while the experimental value is of 541.6 pm. The choice of the theoretical lattice parameter seemed to us the most adapted as it minimizes the structure energy and avoid tensions on surface bonds.

Other functionals can also be used as Meta-GGA functional (includes the second derivative of the electron density, the Laplacian) or hybrid functional corresponding to non local-density approximations (NLDA) (include a component of the exact exchange energy calculated from Hartree–Fock theory). These functionals have been used in sev-

eral studies on the monomer diffusion on the Si(001) surface and some differences were observed compared to LDA and GGA functionals. [96], [106], [107]

4.3 The energy landscape of a Si adatom on the ethoxy-covered Si(001) surface

In this section, the slab is similar to the previous one, it is a 8×4 reconstructed surface but four ethoxy groups are present on it, as it is the case after the dissociation of a TEOS molecule. Their positions are similar to the ones described in chapter 3, the four ethoxy groups are shared among two dimers of a row separated by a clean one. The monomer is then positioned on the neighboring row in the area delimited by the red rectangle shown Figure 4.10.

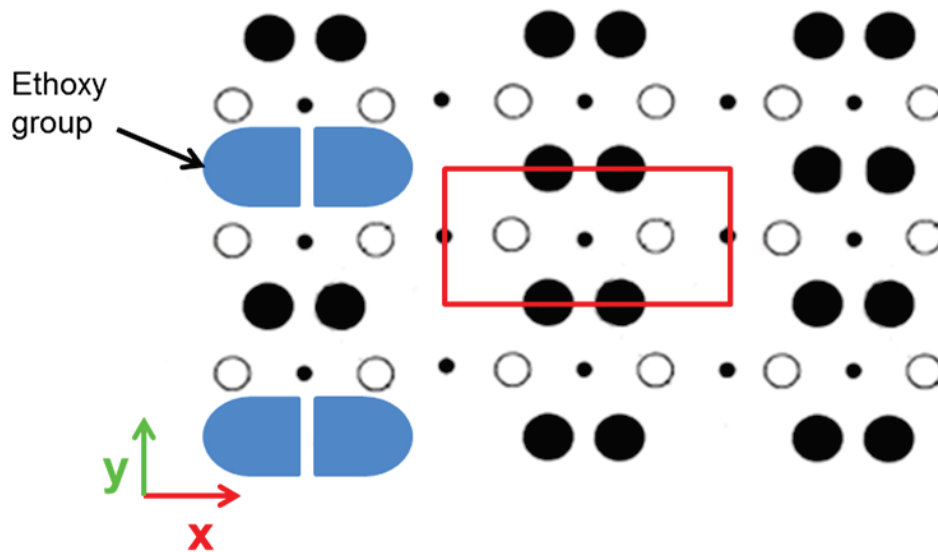


Figure 4.10: Schematic representation of the ethoxy-covered Si(001)- 8×4 surface.

The presence of the ethoxy groups modifies the symmetry of the surface, in particular, H is not a symmetry center anymore. This increases the number of points needed to draw a precise potential surface. Consequently, we limited our self to the determination of the main energy barrier. The results are collected Figure 4.11 and 4.12.

Figure 4.11 compares the energy barriers for the adatom diffusion between two dimer rows. The energy barriers are similar to the ones of the 8×4 clean surface. However, the energy barrier the monomer has to cross to reach sites C_1 or C_2 from M_1 are higher than the ones to reach C_3 or C_4 from M_2 , certainly due to the presence of the ethoxy groups.

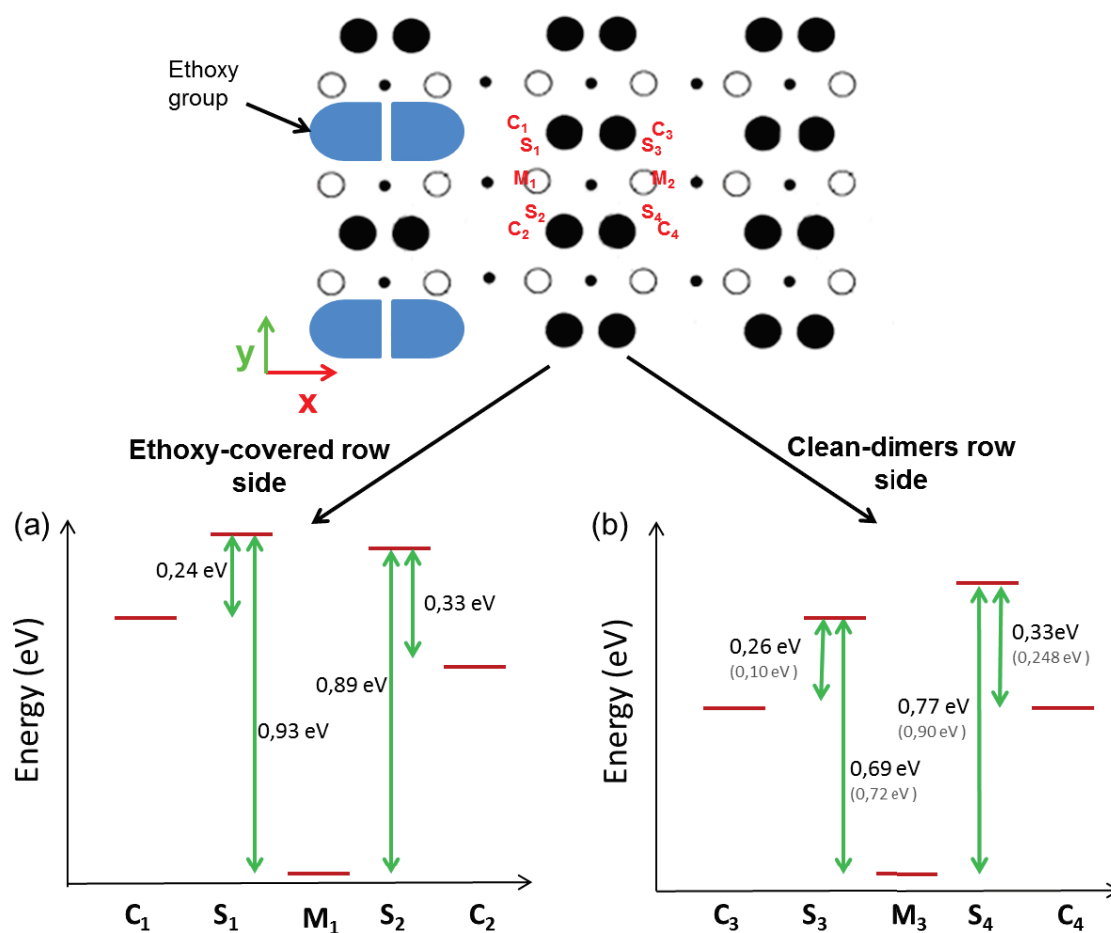


Figure 4.11: Energies along the possible diffusion paths on a clean dimer row neighboring the ethoxy-covered row of the 8×4 ethoxy-covered energy surface. (The values between brackets are the energies obtained for the clean 8×4 surface)

Figure 4.12 presents the results obtained for the positions situated on the silicon row, similarly to the previous sections, diffusion can occur in parallel to the dimer row (Figure 4.12 (a)) or perpendicularly to it (Figure 4.12 (b)). If we compare the energy differences between two positions of the monomer on this surface to the ones obtained

previously on the clean 8×4 surface (values in grey between brackets) they are not significant.

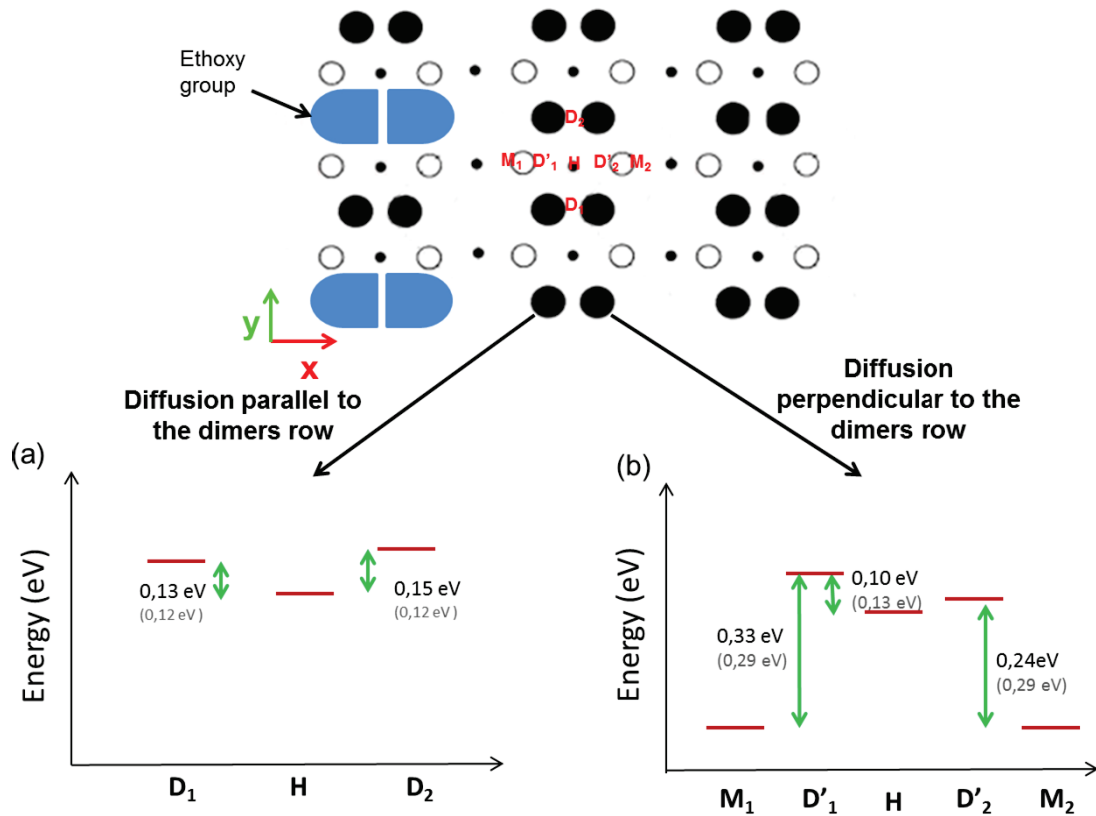


Figure 4.12: Energies along two possible diffusion paths (a) parallel to the dimer row, (b) perpendicular to the dimer row. (The values between brackets are the energies obtained for the clean 8×4 surface)

Consequently, the energy barriers, obtained for the ethoxy-covered surface, are very similar to those of the clean surface. Therefore, the observation of the monomer on the ethoxy-covered surface, which was not observed up to now on the clean surface, can not be simply explained by relying on the difference between static barriers.

An explanation can be proposed. The simulations performed in this chapter do not take into account the dynamic aspect of the dimers buckling. In contrast, the comparison of the 2×2 and the 8×4 surface have shown that the dimer configuration can have important consequences on the energy barriers. On the clean silicon surface, there is a dynamic buckling of the dimers on each row; while, on the ethoxy-covered one, the

TEOS dissociation fragments may modify the buckling dynamic of the adjacent rows and may create a trap for the monomer.

4.4 Summary

The analysis of the clean surface have shown the importance of the surface buckling for the determination of the energy landscape of a silicon monomer on the Si(001) surface. All calculations presented in the literature, using ab-initio methods, are similar to our results with the 2×2 slab. However, we have shown, using a bigger slab (8×4 surface), more directly comparable with experiments, that the dimensions of the 2×2 slab do not allow to account for the role of neighboring free silicon dimers which tend to maintain the alternate buckling. This effect lowers significantly the required static barrier for the monomer to escape from its absolute minimum energy position (from 0.70 eV to 0.29 eV).

The surface buckling may also explain the absence of differences between the clean and the ethoxy covered surface, as the calculation is performed at 0 K the influence of the ethoxy groups on the dimer buckling dynamic of the ethoxy covered row and its neighboring rows can not be analyzed. Therefore, DFT-based molecular dynamics simulation could provide an answer to this question but would be computationally expensive for this type of large systems.

Chapter 5

Dissociation of Ethoxysilane on Si(001)-2×1 and Si(111)-7×7 at Room Temperature

In chapter 3, we examined the dissociation of TEOS on Si(001)-2×1 in the low coverage limit (~ 1 L), combining STM, with XPS and periodic slab DFT calculations. [108] We found that the full dissociation of TEOS via Si – O bond cleavage is the majority channel. As shown in Figure 5.1, the ethoxy fragments attach to the four dangling bonds of two surface dimers, separated by a bare one, while the liberated Si atom (Si^{T}) moves to the dimer row adjacent to the ethoxy-decorated one. There, it sits as a triply coordinated adatom (a monomer), making two bonds with two adjacent silicon atoms and a third one with a silicon atom of the second layer. The release of silicon monomers leads to self-organized structures, with possible nano-patterning applications. Indeed, ethoxy-decorated rows alternate with Si adatom-occupied ones, non-reactive (or much less reactive), when compared to bare dimer rows (Figure 3.8).

However the reaction scheme is likely more complicated. Minority dissociation products are also detected by STM, probably non-fully dissociated molecules. Then, the XPS C 1s spectrum exhibits a weak component attributed to a Si – C bond, implying a C – O bond rupture (Figure 5.2), as it is believed to be the case for the TEOS/Si(111)-7×7 system.[109], [64] A possible non-selectivity in the products certainly impacts the patterning issue, and is crucial for the formation and quality of the interface in, e.g., an ALD (TEOS/water) process.

As different reaction channels, via Si – O and/or C – O bond cleavage (see Figure 5.2), could be opened as a function of molecular coverage, we wished to extend our

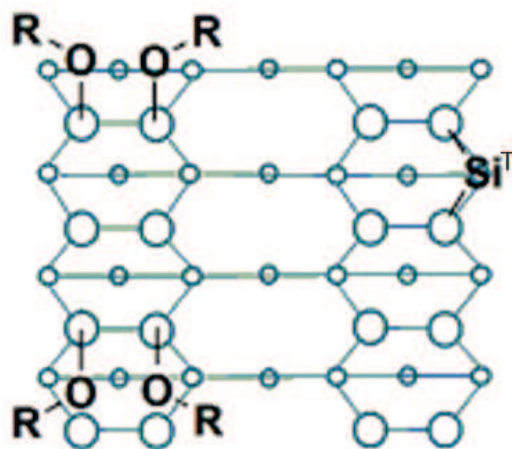


Figure 5.1: TEOS fragments position ($R = \text{CH}_2\text{CH}_3$) after dissociation on the Si(001)-2×1 surface at low coverage ($\sim 1 \text{ L}$). The Si^{T} denotes the silicon atom pertaining to the TEOS molecule.

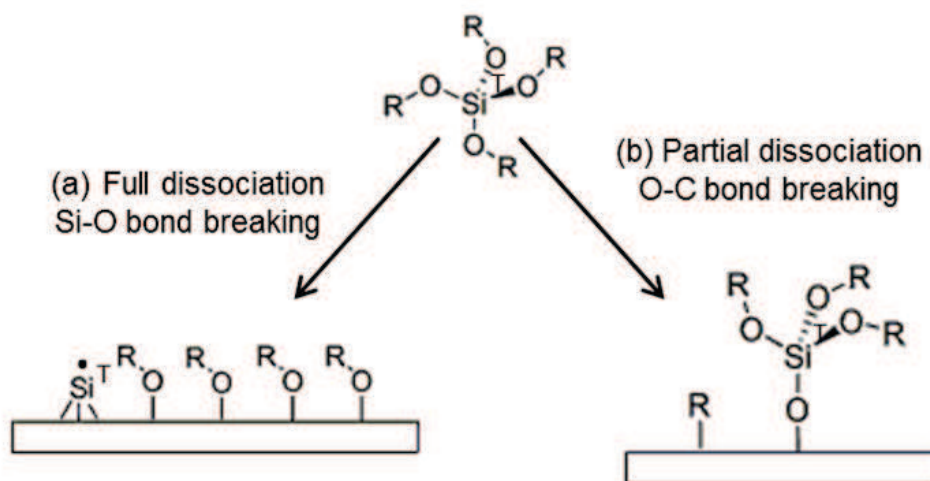


Figure 5.2: Possible dissociation channels of alkoxy silanes on silicon surfaces. The Si^{T} denotes the silicon atom pertaining to the alkoxy silane molecule.

preceding study on the TEOS/Si(001)-2×1 system to much larger exposures (tens of langmuirs). We present, in this chapter, synchrotron radiation XPS measurements performed at TEMPO Beamline, SOLEIL synchrotron facility (St Aubin, France)[110] and at beamline I511 at Max-Lab synchrotron facility (Lund Sweden).[111]

Because the ethoxy (or ethyl) ligands bear two non-equivalent carbons, the spec-

tral interpretation becomes complicated when various products with overlapping XPS components are present on the surface. Therefore, the TEOS adsorption experiments on the clean silicon surfaces were systematically duplicated by using tetramethoxysilane (TMOS, $\text{Si}(\text{OCH}_3)_4$). As the methoxy (or methyl) ligands present only one carbon, this leads to a considerable simplification of the C 1s spectral reconstruction and interpretation. This is of great help to interpret the C 1s spectrum of TEOS-covered silicon surfaces, assuming that the reactivity of both molecules is not affected by steric effects. To our knowledge, no surface study of the dissociation of TMOS on silicon surfaces has ever been published.

The combined TMOS/TEOS study was extended to the Si(111)- 7×7 surface. The reason was twofold.

- We believed that the pioneering works of Rauscher and coworkers needed to be reexamined in the light of photoemission measurements using synchrotron radiation.[64] Indeed these authors used non-monochromatized Al $K\alpha$ /Mg $K\alpha$ XPS, whose major weakness with respect to synchrotron radiation XPS, besides a low spectral resolution, is the insufficient surface sensitivity that makes the observation of the interfacial oxidation states in the Si 2p spectrum practically impossible.
- The second point is related to the differences and similarities between the Si(111)- 7×7 and the Si(001)- 2×1 surfaces. The clean Si(111)- 7×7 surface forms a well-characterized 7×7 reconstruction with fully occupied dangling bond on the restatom and partially filled dangling bond on adatom reactive sites; they are basically similar to the up (electron-rich) and down (electron-deficient) silicon atoms of the silicon dimer on the Si(001)- 2×1 surface, respectively.[112] However the surface topology is different, especially the distance and layout of the dangling bonds, which can affect the nature of the reaction products, as it has been shown e.g. for acetonitrile.[76], For instance, pairs of silicon dangling bonds are at shorter distances on Si(001)- 2×1 than on Si(111)- 7×7 . Moreover, for Si(001)- 2×1 , the reaction site on which TEOS fully dissociates encompasses six dimers of two adjacent

dimer rows,[108] while nothing such exists on Si(111)-7×7, due to the different surface symmetries (see Figure 5.11

5.1 TMOS and TEOS reaction on Si(001)-2×1 at room temperature

5.1.1 Si 2p core-level XPS analysis

The Si 2p spectra of the Si(001)-2×1 surface exposed to TMOS (4.5 L and 67.5 L) and TEOS (4.5 L and 13.5 L) at room temperature are presented in Figure 5.3. For each spectrum, the Si 2p line shapes are reconstructed by sums of Voigt components.

A dose of 4.5 L of TEOS and TMOS on the Si(001)-2×1 surface lead to the disappearance of the surface states (that have a SCLS of ~ -0.5 eV with respect to the bulk peak B). The structure labeled *S* (SCLS of ~ 0.3 eV) remains, attributed to the second plane atoms.[113] The first oxidation state Si^+ grows at a SCLS of $\sim +0.90$ eV. It corresponds, for TMOS, to a silicon atom linked to a methoxy in a $(\text{Si})_3\text{Si} - \text{O} - \text{CH}_3$ unit (the ionized Si is underscored) and for TEOS to a silicon atom linked to an ethoxy groups in a $(\text{Si})_3\text{Si} - \text{O} - \text{CH}_2 - \text{CH}_3$ unit.

The Si^+ structure represents 15.5 % of the spectral weight for TMOS and 13.2 % for TEOS. To estimate their surface area, we can make a comparison with the Si 2p spectra of the water-saturated surface (measured with same kinetic energy). Half the surface silicon atoms are Si – OH species and the Si^+ peak weight represents 15 % of the spectral area. Therefore, a coverage of ~ 0.5 ML for TMOS dosage and of ~ 0.45 % for TEOS dosage can be deduced. Note the absence of measurable oxidation states higher than Si^+ , in particular the Si^{4+} component. The majority species are fully dissociated. By analogy with the TEOS case for which STM shows that the ethoxy fragments of one dissociated molecule occupy four dimers (Figure 5.1), the dissociation pattern of TMOS should be alike at this same coverage.

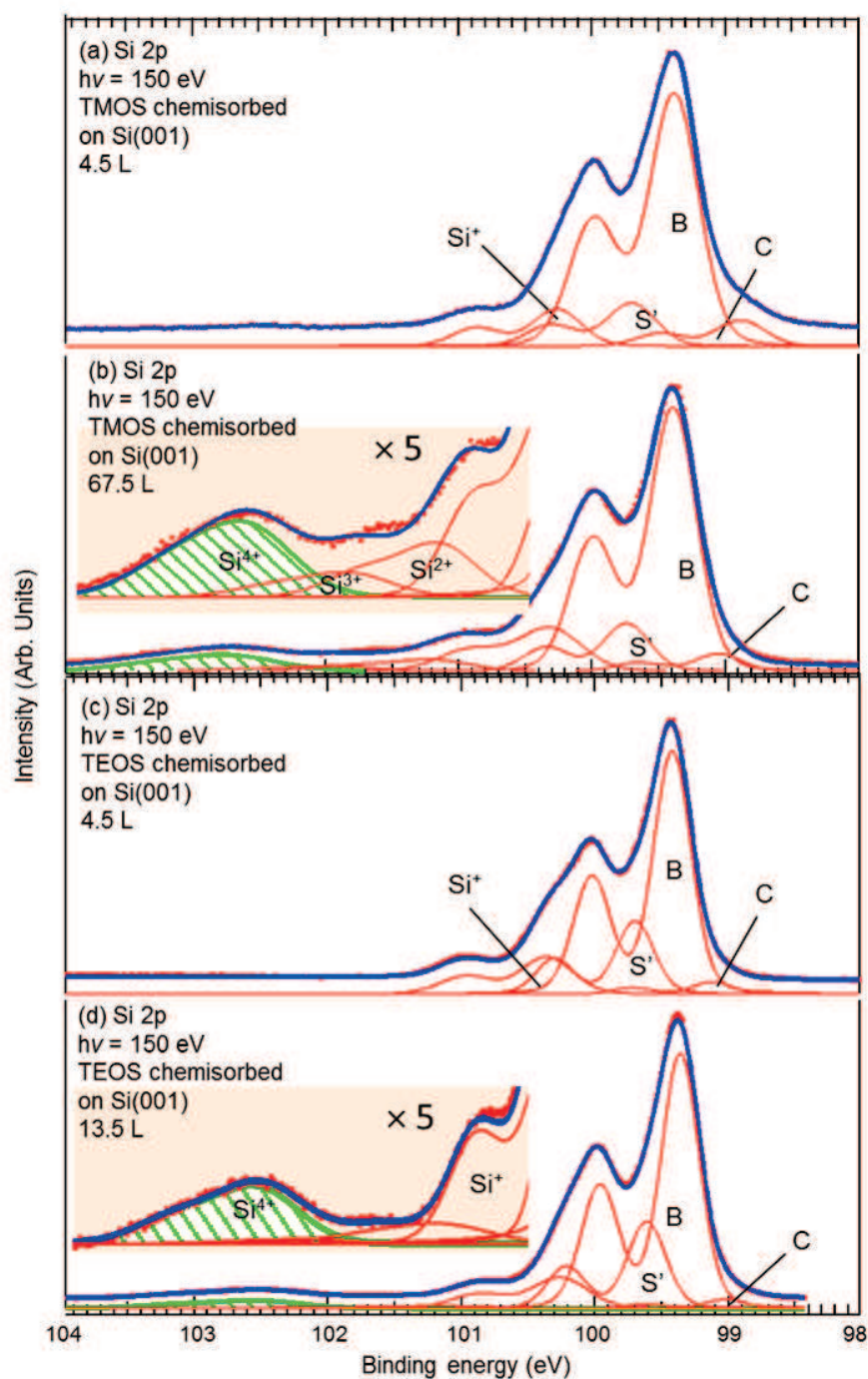


Figure 5.3: Si 2p XPS spectra ($h\nu = 150$ eV) of Si(001)-2×1 surface (n-doped, $0.003 \Omega \times \text{cm}$) (a) exposed to TMOS for a coverage of 4.5 L (10 min, 10^{-8} mbar); (b) of 67.5 L (15 min, 10^{-7} mbar) (c) exposed to TEOS for a coverage of 4.5 L (10 min, 10^{-8} mbar); (d) of 13.5 L (30 min, 10^{-8} mbar). The BE is referenced with respect to the Fermi level. Fitting parameters are collected in Table 5.1

	Component	SCLS (eV)	fwhm (eV)	Weight (%)	Attribution
TMOS chemisorbed on Si(001) 4.5 L	B	0.00	0.40	68.3	Bulk
	S	0.32	0.40	15.9	2 nd plane
	C	-0.50	0.40	7.3	Non-attributed
	Si ⁺	0.90	0.48	15.5	1 st oxidation state
TMOS chemisorbed on Si(001) 67.5 L	B	0.00	0.40	59.5	Bulk
	S	0.35	0.40	10.8	2 nd plane
	C	-0.34	0.40	4.0	Non-attributed
	Si ⁺	0.93	0.55	13.2	1 st oxidation state
	Si ²⁺	1.81	0.67	4.0	2 nd oxidation state
	Si ³⁺	2.59	0.74	1.9	3 rd oxidation state
TEOS chemisorbed on Si(001) 4.5 L	B	0.00	0.35	64.3	Bulk
	S	0.28	0.35	19.2	2 nd plane
	Si _u	-0.30	0.35	3.1	Non-attributed
	Si ⁺	0.94	0.46	13.2	1 st oxidation state
TEOS chemisorbed on Si(001) 13.5 L	B	0.00	0.35	61.5	Bulk
	S	0.25	0.35	21.0	2 nd plane
	C	-0.34	0.35	2.2	Non-attributed
	Si ⁺	0.90	0.48	10.5	1 st oxidation state
	Si ²⁺	1.80	0.65	j 1	2 nd oxidation state
	Si ³⁺	2.65	0.68	j 0.5	3 rd oxidation state
	Si ⁴⁺	3.20	0.80	3.8	4 th oxidation state

Table 5.1: Si 2p_{3/2} Surface core level shifts (SCLS, relative Si 2p_{3/2} BE referenced to the bulk component one), spectral weights, full widths at half maximum (fwhm), and attribution of the Voigt components used to reconstruct the Si 2p XPS experimental spectra shown in Figure 5.3. The BE of the Si 2p_{3/2} component (referenced to the Fermi level) is 99.40 eV.

For large exposures, new peaks corresponding to oxidation states higher than Si^+ appear in the Si 2p spectrum of TMOS and TEOS. In particular, we see an oxide state peak with a SCLS of +3.22 eV (6.6 % of spectral weight) for TMOS (67.5 L) and a SCLS of \sim +3.18 eV (3.8 % of spectral weight) for TEOS (13.5 L) and a fwhm \sim 0.80 eV. We attribute this peak to a Si^{4+} state. Similar SCLS (+3.2 eV) and fwhm (0.88 eV) were observed in the Si 2p spectrum of Si(111)-7×7 exposed to water at room temperature,[71] where the reaction of adatoms with water leads to $(\text{O}_3)\text{Si} - \text{OH}$ units.[71], [85] The observed fwhm is much smaller than the typical value of the thermally oxidized surfaces, \sim 1.0 eV. As the SCLS is a function of the Si – O bond-length,[57] the narrow width associated to the alkoxy silane suggests a greater static order than that of SiO_4 units in thermal amorphous silica.[71] The Si^{4+} state spectral weight corresponds to a surface coverage of \sim 0.22 ML for TMOS and \sim 0.13 ML for TEOS. The appearance of a Si^{4+} state means that the C – O bond breaks and that $\text{Si}^{\text{T}}\text{O}_4$ species are left on the surface according to reaction path (b), depicted in Figure 5.2.

For both molecules, intermediate states, Si^{2+} and Si^{3+} , are seen at \sim +1.8 eV and \sim +2.6 eV For TMOS, the Si^{3+} and Si^{2+} states represent 4.0 % and 1.9 % of the spectrum area. For TEOS, the sum of these two components represents less than 1.5 % of the whole spectrum. They could be attributed to partially dissociated molecules via Si – O bond breaking.

5.1.2 O 1s core-level XPS analysis

The corresponding O 1s spectra are given in Figure 5.4. The fitting parameters are collected in Table 5.2.

For low exposures to TMOS and TEOS, the spectra are essentially constituted by one component centered at a BE of 531.9 eV, that we attribute to an oxygen atom in a $(\text{Si}_3)\text{Si} - \text{O} - \text{C}$ unit, resulting from the full dissociation of TMOS and TEOS, according to the path (a) on Figure 5.2. A smaller component is seen at higher BE, 532.6 eV (about 18 % of the spectral weight for TMOS and TEOS). When the exposure increases, it leads, for both molecules, to an increase of the high BE component that reaches \sim 34 % of

the spectral weight for TMOS and $\sim 26\%$ for TEOS. This increase is correlated to the appearance of the Si^{4+} state in the Si 2p spectra due to the C – O bond rupture (path (b) in Figure 5.2). Therefore, we attribute the high BE peak to oxygen atoms in a $\text{Si}^{\text{T}}\text{O}_4$ tetrahedron.

5.1.3 C 1s core-level XPS analysis

The C 1s spectra of both molecules after reaction of the molecules on Si(001)-2×1 surface are given in Figure 5.5. The fitting parameters are collected in Table 5.2.

First, we will start with the analysis of the TMOS spectra which is simpler, as discussed earlier. In Figure 5.5 (a), the C 1s spectrum after the 4.5 L exposure is fitted by three components, at 284.10 eV, 286.73 eV and 287.28 eV. A fourth, weak component at 283.3 eV is attributable to beam damage.[108], [75] The small component 284.1 eV, corresponds to $(\text{Si}_3)\text{Si} - \text{CH}_3$. This suggests that the C – O bond can break. On the other hand, the main structures at higher BE, are related to a C – O bond, resulting from Si – O bond breaking. For the 4.5 L spectrum (low coverage limit), the main C – O component is at 286.73 eV and corresponds to an $(\text{Si}_3) - \text{O} - \text{Si} - \text{CH}_3$ unit.

However, for the longest exposure (67.5 L), we need to introduce a component at 287.20 eV to fit properly the spectrum shown in Figure 5.5(b): the width of the C – O component, ~ 1.6 eV becomes much wider than the fwhm of a single C 1s component (0.92 eV). The peak at 287.20 eV is attributed to $(\text{O}_3)\text{Si} - \text{O} - \text{CH}_3$ on the basis of a second-neighbor effect chemical shift. Assuming that initial state effects dominate BE shifts, in a $(\text{O}_3)\text{Si} - \text{O} - \text{CH}_3$ unit, the liganding of the silicon atom to four O atoms increases the charge loss of the carbon with respect to the $(\text{Si}_3)\text{Si} - \text{O} - \text{CH}_3$ case, explaining the +0.6 eV BE shift. Note that Jolly and Bomben report a ionization potential shift of 0.67 eV between gaseous $\text{H}_3\text{C} - \text{SiH}_3$ and $\text{H}_3\text{C} - \text{SiCl}_3$. [74] Such second second-neighbor effect in the BE shifts is not screened out by the presence of the silicon substrate, despite its high dielectric permittivity.

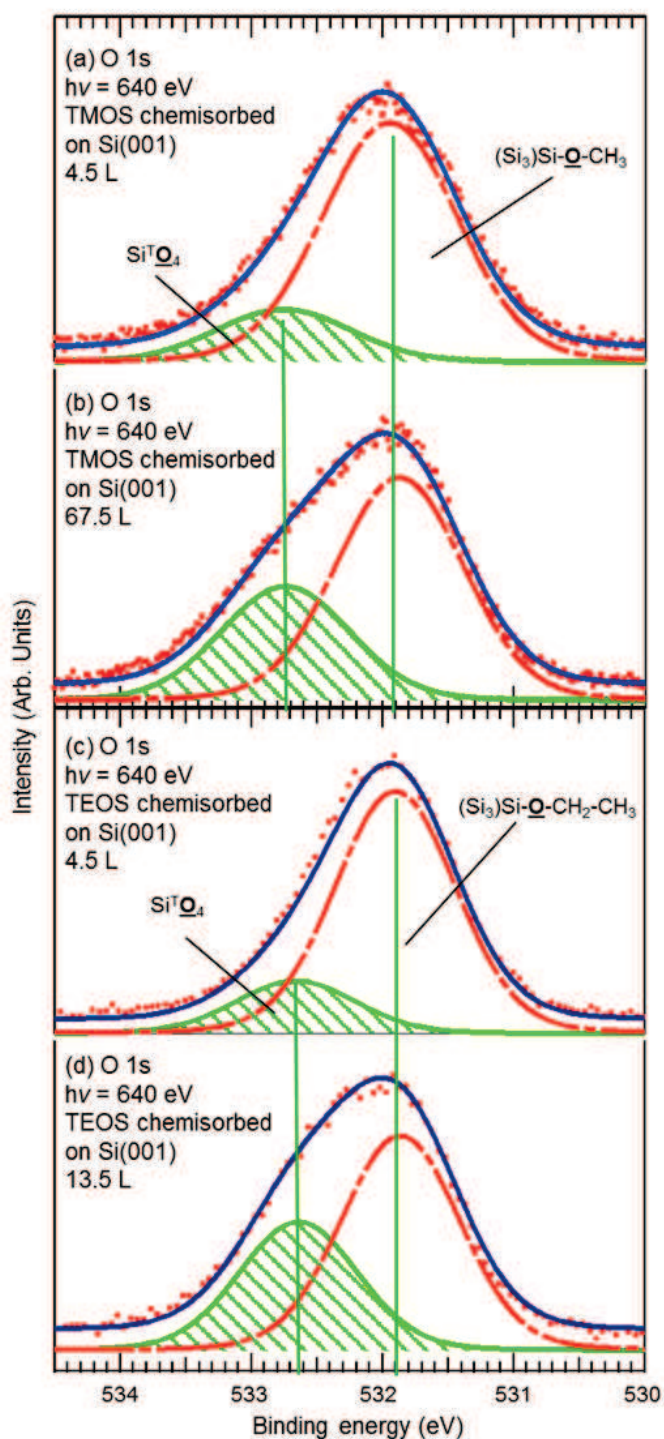


Figure 5.4: O 1s XPS spectra ($h\nu = 640$ eV) of Si(001)-2×1 surface (n-doped, $0.003 \Omega \times \text{cm}$) (a) exposed to TMOS for a coverage of 4.5 L (10 min, 10^{-8} mbar); (b) of 67.5 L (15 min, 10^{-7} mbar) (c) exposed to TEOS for a coverage of 4.5 L (10 min, 10^{-8} mbar); (d) of 13.5 L (30 min, 10^{-8} mbar). The BE is referenced with respect to the Fermi level. Fitting parameters are collected in Table 5.2

	BE (eV)	fwhm (eV)	Weight (%)	Attribution
TMOS chemisorbed on Si(001), 4.5 L	531.94	1.2	82.0	(Si ₃)Si – O – CH ₃
	532.75	1.2	18.0	Si ^T O ₄
TMOS chemisorbed on Si(001), 67.5 L	531.88	1.2	65.9	(Si ₃)Si – O – CH ₃
	532.74	1.2	34.1	Si ^T O ₄
TEOS chemisorbed on Si(001), 4.5 L	531.90	1.1	82.2	(Si ₃)Si – O – CH ₂ – CH ₃
	532.66	1.1	17.8	Si ^T O ₄
TEOS chemisorbed on Si(001), 13.5 L	531.94	1.2	73.9	(Si ₃)Si – O – CH ₂ – CH ₃
	532.67	1.2	26.1	Si ^T O ₄

Table 5.2: Si $2p_{3/2}$ Surface core level shifts (SCLS, relative Si $2p_{3/2}$ BE referenced to the bulk component one), spectral weights, full widths at half maximum (fwhm), and attribution of the Voigt components used to reconstruct the Si 2p XPS experimental spectra shown in Figure 5.4. The BE of the Si $2p_{3/2}$ component (referenced to the Fermi level) is 99.40 eV.

Naturally the $(\text{O}_3)\text{Si} - \text{O} - \text{CH}_3$ component correlates with the appearance of the Si^{4+} state in the Si 2p spectra, associated to species grafted after C – O bond rupture (path (b) in Figure 5.2). When one C – O bond is broken, one $\text{Si} - \text{O} - \text{Si}^{\text{T}}(\text{OCH}_3)_3$ group and one $\text{Si} - \text{CH}_3$ group are formed. In such a case, the $(\text{O}_3)\text{Si} - \text{O} - \text{CH}_3 / (\text{Si}_3)\text{Si} - \text{O} - \text{CH}_3$ intensity ratio is 3:1. On the other hand, when two C – O bonds are broken, one $(\text{Si} - \text{O})_2 - \text{Si}^{\text{T}}(\text{OCH}_3)_2$ and two methyl groups are formed on the surface. Then the $(\text{O}_3)\text{Si} - \text{O} - \text{CH}_3 / (\text{Si}_3)\text{Si} - \text{O} - \text{CH}_3$ ratio is 1:1.

At low coverage, the $(\text{Si}_3)\text{Si} - \text{CH}_3$ component represents 15 % of the spectral weight and the $(\text{O}_3)\text{Si} - \text{O} - \text{CH}_3$ component 18.7 %, corresponding approximately to a ratio of 1:1. We deduce that two C – O bonds are broken. When the exposure increases, the $(\text{Si}_3)\text{Si} - \text{CH}_3$ component represents 12.4 % of the spectral weight and the $(\text{O}_3)\text{Si} - \text{O} - \text{CH}_3$ component 34.5 %, this ratio decreases to 3:1, pointing to the breaking of only one C – O bond. This coverage dependence can be explained by an increasing difficulty in finding free silicon dangling bonds on the surface as more and more adsorption sites are occupied.

The C 1s spectra of TEOS shown in Figures 5.5 (c) and 5.5 (d) are more complex than that of TMOS because of the two non-equivalent carbons in the ethoxy. Besides a weak structure at 283.2 eV due to beam damage, we see three broad structures at ~ 286.8 eV, ~ 285 eV and ~ 284 eV. The structures at ~ 286.8 eV and ~ 284 eV are related to carbon atoms bonded to oxygen and to silicon, respectively, as in the case of TMOS. With respect to TMOS, the additional feature at ~ 285 eV is related to the terminal CH_3 of the ethoxy group. The low coverage (4.5 L) spectrum (Figure 5.5 (c)), for which ethoxy fragments directly grafted on the substrate dominate,[108] gives us the BE position of the two non-equivalent carbons, $(\text{Si}_3)\text{Si} - \text{O} - \text{CH}_2 - \text{CH}_3$, at 286.58 eV (close to the $(\text{Si}_3)\text{Si} - \text{O} - \text{CH}_3$ component at 286.7 eV) and $(\text{Si}_3)\text{Si} - \text{O} - \text{CH}_2 - \text{CH}_3$ at 285.23 eV. Note that these two components have the same width and intensity. The BE difference between the two non-equivalent carbons is ~ 1.4 eV.

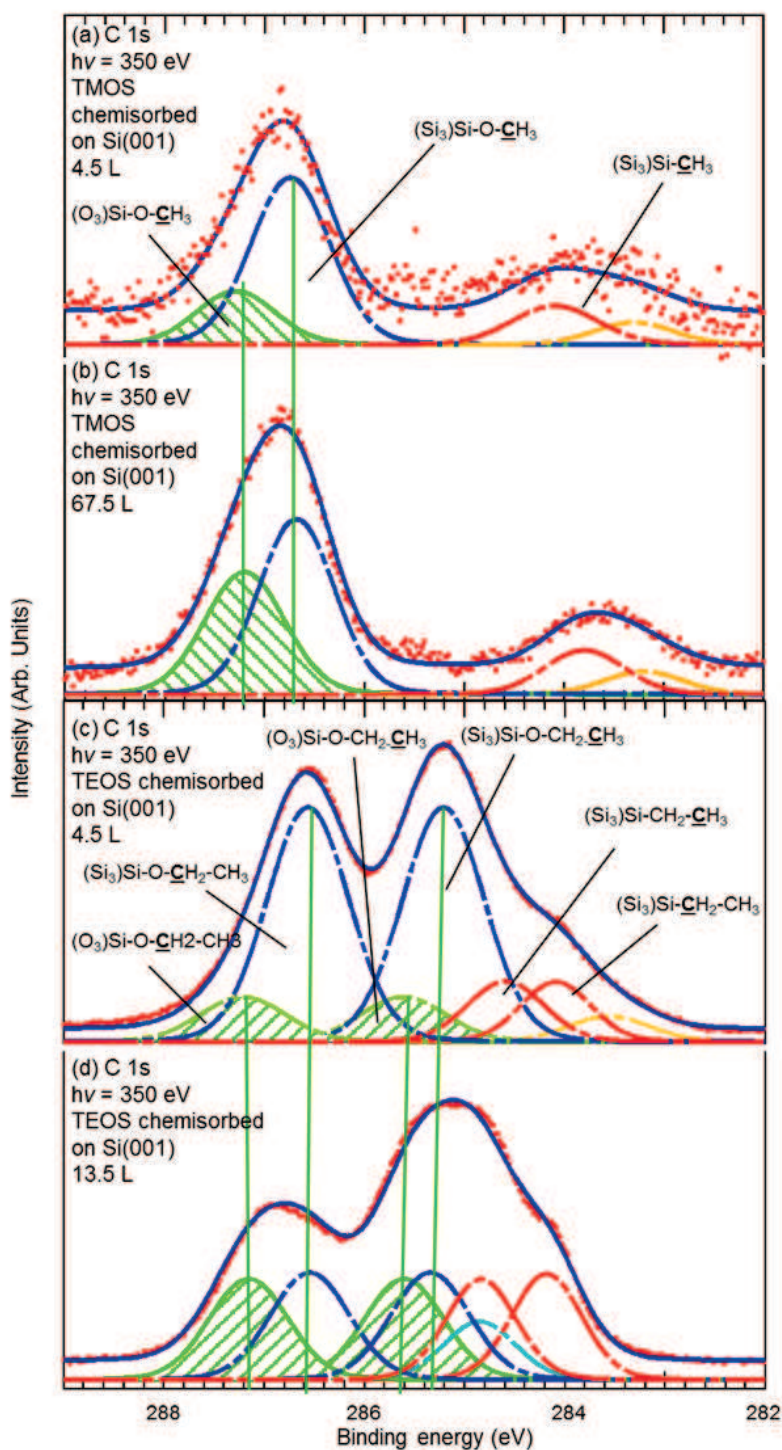


Figure 5.5: C 1s XPS spectra ($h\nu = 350$ eV) of Si(001)-2×1 surface (n-doped, $0.003 \Omega \times \text{cm}$) (a) exposed to TMOS for a coverage of 4.5 L (10 min, 10^{-8} mbar); (b) of 67.5 L (15 min, 10^{-7} mbar) (c) exposed to TEOS for a coverage of 4.5 L (10 min, 10^{-8} mbar); (d) of 13.5 L (30 min, 10^{-8} mbar). The BE is referenced with respect to the Fermi level. Fitting parameters are collected in Table 5.3

	BE (eV)	fwhm (eV)	Weight (%)	Attribution
TMOS chemisorbed on Si(001) 4.5 L	287.28	0.92	18.7	(O ₃)Si – O – CH ₃
	286.73	0.92	58.6	(Si ₃)Si – O – CH ₃
	284.10	0.92	15.0	(Si ₃)Si – CH ₃
	283.3.	0.92	7.7	–CH _x
TMOS chemisorbed on Si(001) 67.5 L	287.20	0.92	34.5	(O ₃)Si – O – CH ₃
	286.68	0.92	46.8	(Si ₃)Si – O – CH ₃
	284.01	0.92	12.4	(Si ₃)Si – CH ₃
	283.20	0.92	6.4	CH _x
TEOS chemisorbed on Si(001) 4.5 L	287.40	0.92	5.0	(O ₃)Si – O – CH ₂ – CH ₃
	286.58	0.92	34.9	(Si ₃)Si – O – CH ₂ – CH ₃
	285.74	0.92	5.0	(O ₃)Si – O – CH ₂ – CH ₃
	285.23	0.92	34.9	(Si ₃)Si – O – CH ₂ – CH ₃
	284.66	0.92	8.3	(Si ₃)Si – CH ₂ – CH ₃
	284.13	0.92	7.7	(Si ₃)Si – CH ₂ – CH ₃
TEOS chemisorbed on Si(001) 13.5 L	287.16	0.90	15.5	(O ₃)Si – O – CH ₂ – CH ₃
	286.55	0.90	16.4	(Si ₃)Si – O – CH ₂ – CH ₃
	285.61	0.90	15.5	(O ₃)Si – O – CH ₂ – CH ₃
	285.34	0.90	16.4	(Si ₃)Si – O – CH ₂ – CH ₃
	284.82	0.90	13.8	(Si ₃)Si – CH ₂ – CH ₃
	284.18	0.90	14.3	(Si ₃)Si – CH ₂ – CH ₃
	284.85	0.90	8.1	X

Table 5.3: C 1s Surface core level shifts (SCLS, relative Si 2p_{3/2} BE referenced to the bulk component one), spectral weights, full widths at half maximum (fwhm), and attribution of the Voigt components used to reconstruct the Si 2p XPS experimental spectra shown in Figure 5.5.

For the longest dose (13.5 L, Figure 5.5 (d)), the TEOS C 1s spectral shape is strongly modified. We need to introduce a component at 287.16 eV we attribute to $(\text{O}_3)\text{Si} - \text{O} - \text{CH}_2 - \text{CH}_3$. Indeed, the BE is practically the same as that $(\text{O}_3)\text{Si} - \text{O} - \text{CH}_3$ in TMOS (287.20 eV). To ensure self-consistency, a second component corresponding to $(\text{O}_3)\text{Si} - \text{O} - \text{CH}_2 - \text{CH}_3$ is added at BE of 285.74 eV with the same width and intensity as those of $(\text{O}_3)\text{Si} - \text{O} - \text{CH}_2 - \text{CH}_3$. The BE shift between the two non-equivalent carbons is ~ 1.5 eV, in accordance with the one observed for the non-equivalent carbons in $(\text{Si}_3)\text{Si} - \text{O} - \text{CH}_2 - \text{CH}_3$ units. Therefore, as for TMOS, higher doses lead to the appearance of a second dissociation mode of TEOS, via C – O bond breaking (path (b) in Figure 5.2). In the BE energy window 284 eV-285 eV, we see contributions from the ethyl moieties directly attached to the silicon substrate. We use a doublet of components, of equal widths and intensities for the sake of consistency, separated by ~ 0.6 eV, $(\text{Si}_3)\text{Si} - \text{CH}_2 - \text{CH}_3$ (at ~ 284.15 eV) and $(\text{Si}_3)\text{Si} - \text{CH}_2 - \text{CH}_3$ (at ~ 284.75 eV).[108], [75] A supplementary component X, also at ~ 285 eV, is introduced to improve curve fitting and is related to beam damage. Comparing Figure 5.5 (c) and 5.5 (d), we see that the increase of the $(\text{O}_3)\text{Si} - \text{CH}_2 - \text{CH}_3$ components is correlated to the increase of the $(\text{Si}_3)\text{Si} - \text{CH}_2 - \text{CH}_3$ components, which is expected when the number of dissociated fragments via C – O bond breaking increases.

5.2 TMOS and TEOS reaction on Si(111)-7×7 at room temperature

5.2.1 Si 2p core-level XPS analysis

We present, in Figure 5.6, the Si 2p spectra of the Si(111)-7×7 surface after exposures to TMOS and TEOS. The fitting parameters are collected in Table 5.4.

In Figure 5.6 (a) and 5.6 (c), we present the Si 2p spectra after a short exposure to TMOS (0.11 L) and TEOS (4.5 L), respectively. On the clean surface, components S, C and SS, are attributed to the adatoms, the pedestal atoms and the restatoms, respec-

tively. [114] In particular, after the 0.11 L dose, we still observe the restatom component (SS). Similarly to the Si(001)-2×1 surface case, a first oxidation state Si⁺ grows with a SCLS of $\sim +0.90$ eV. It is attributed to (Si₃)Si – O – CH₃ (TMOS) and (Si₃)Si – O – CH₂ – CH₃ (TEOS). The Si⁺ structure represents 12.5 % (10%) of the spectrum area for TMOS (TEOS). It corresponds to an estimated Si¹⁺ coverage of 0.42 ML (0.33 ML) for TMOS (TEOS).

For the longest exposures, new peaks corresponding to higher oxidation state appear, see Figure 5.6 (b) and 5.6 (c). For TMOS, the Si⁴⁺ state has a SCLS of $\sim +3.26$ eV and a spectral weight of 4.1% (corresponding to a surface area of ~ 0.17 ML). The intermediate states Si³⁺ and Si²⁺, with SCLS of $\sim +1.89$ eV and $\sim +2.60$ eV, respectively, have also emerged. As a whole their spectral weight is 4.8 %. For TEOS, the Si⁴⁺ state has a SCLS of $\sim +3.25$ eV and a spectral weight of 7.1 % (corresponding to a Si⁴⁺ areal density of 0.25 ML). The intermediate states Si³⁺ and Si²⁺ at $\sim +1.8$ eV and $\sim +2.70$ eV as a whole have a spectral weight less than 1.5 %. As for the Si(001)-2×1 surface, the appearance of a Si⁴⁺ state means that the Si – O bond breaks and that SiO₄ species are left on the surface according to the reaction path (b) of Figure 5.2. As discussed earlier, the Si³⁺ and Si²⁺ states may be due to an incomplete dissociation via Si – O bond breaking.

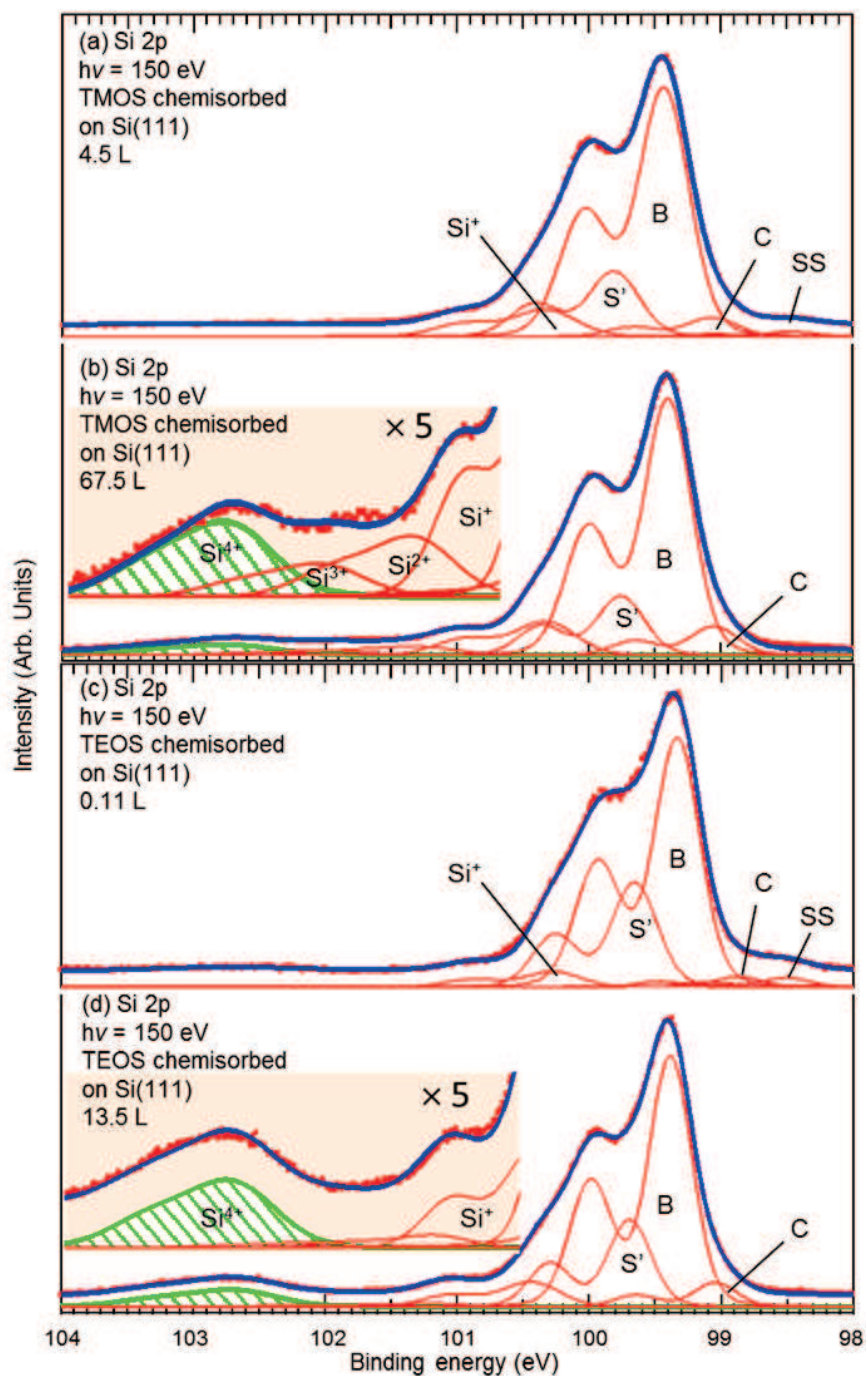


Figure 5.6: Si 2p XPS spectra ($h\nu = 150$ eV) of Si(111)-7×7 surface (n-doped, $0.003 \Omega \times \text{cm}$) (a) exposed to TMOS for a coverage of 4.5 L (10 min, 10^{-8} mbar); (b) of 67.5 L (15 min, 10^{-7} mbar) (c) exposed to TEOS for a coverage of 0.11 L (30 min, 5×10^{-9} mbar); (d) of 4.5 L (10 min, 10^{-8} mbar). The BE is referenced with respect to the Fermi level. Fitting parameters are collected in Table 5.4

	Component	SCLS (eV)	fwhm (eV)	Weight (%)	Attribution
TMOS chemisorbed on Si(111) 4.5 L	B	0.00	0.40	64.3	Bulk
	S'	0.36	0.40	16.2	Adatoms
	SS	-0.80	0.40	1.0	Restatoms
	C	-0.34	0.40	6.0	Pedestal
	Si ⁺	0.95	0.48	12.5	1 st oxidation state
TMOS chemisorbed on Si(111) 67.5 L	B	0.00	0.40	60.5	Bulk
	S'	0.36	0.40	13.9	Adatoms
	C	-0.35	0.40	6.8	Pedestal
	Si ⁺	0.93	0.55	9.9	1 st oxidation state
	Si ²⁺	1.89	0.66	3.1	2 nd oxidation state
	Si ³⁺	2.60	0.72	1.7	3 rd oxidation state
TEOS chemisorbed on Si(111) 4.5 L	B	0.00	0.35	62.5	Bulk
	S'	0.32	0.35	26.3	Adatoms
	SS	-0.83	0.35	2.5	Restatoms
	C	-0.23	0.35	2.9	Pedestal
	Si ⁺	0.94	0.46	4.8	1 st oxidation state
TEOS chemisorbed on Si(111) 67.5 L	B	0.00	0.35	57.5	Bulk
	S'	0.30	0.35	21.3	Adatoms
	C	-0.34	0.35	5.1	Pedestal
	Si ⁺	1.08	0.48	8.2	1 st oxidation state
	Si ²⁺	1.80	0.65	1	2 nd oxidation state
	Si ³⁺	2.70	0.69	0.5	3 rd oxidation state
	Si ⁴⁺	3.25	0.72	7.1	4 th oxidation state

Table 5.4: Si $2p_{3/2}$ Surface core level shifts (SCLS, relative Si $2p_{3/2}$ BE referenced to the bulk component one), spectral weights, full widths at half maximum (fwhm), and attribution of the Voigt components used to reconstruct the Si 2p XPS experimental spectra shown in Figure 5.6. The BE of the Si $2p_{3/2}$ component (referenced to the Fermi level) is 99.40 eV.

5.2.2 O 1s core-level XPS analysis

The O 1s spectra are given in Figure 5.7. Similarly to the Si(001)-2×1 surface, the spectra measured for low TMOS/TEOS exposures, are constituted by one main component centered at 531.9 eV, that we attribute to $(\text{Si}_3)\text{Si} - \text{O} - \text{C}$ species resulting from the full dissociation of TMOS and TEOS, according to the path (a) of Figure 5.2. A smaller component is seen at higher BE, i.e. 532.6 eV, with a spectral weight of about 23 % for TMOS and 36 % for TEOS. Longer exposures, lead, for both molecules, to an increase of the high BE component intensity whose spectral weight reaches ~ 39 % for TMOS and ~ 68 % for TEOS. This increase is correlated to the appearance of the Si^{4+} state in the Si 2p spectra, attributed to the C – O bond rupture mechanism (path (b) of Figure 5.2). We reach the same conclusion as that drawn in the Si(001)-2×1 case: the high BE peak in the O 1s spectra is due to oxygen atoms in $\text{Si}^{\text{T}}\text{O}_4$ tetrahedra.

5.2.3 C 1s core-level XPS analysis

The C 1s spectra are given in Figure 5.8. The Fitting parameters are collected in Table 5.6. The spectra of TMOS, shown in Figure 5.8 (a) and 5.8 (b), are fitted with the same components as the spectra of TMOS on Si(001)-2×1, see Figure 5.5 (a) and 5.5 (b). Similarly, the peak at 287.25 eV, corresponding to $(\text{O}_3)\text{Si} - \text{O} - \text{CH}_3$, increases for higher coverage and is correlated, to the appearance of the Si^{4+} state in the Si 2p spectra due to the C – O bond rupture according to scheme (b) Figure 5.2.

At low coverage, the spectral weight of the $(\text{Si}_3)\text{Si} - \text{CH}_3$ component is 33 % and that of the $(\text{O}_3)\text{Si} - \text{O} - \text{CH}_3$ component is 29 %. With an intensity ratio of about 1:1, we deduce that two C – O bonds are broken. When the exposure increases, the weight of the $(\text{O}_3)\text{Si} - \text{O} - \text{CH}_3$ component is 42 % and that of the $(\text{Si}_3)\text{Si} - \text{CH}_3$ component 17 %. The ratio between these two components is $\sim 2:1$. This situation corresponds to the scission of only one C – O bond.

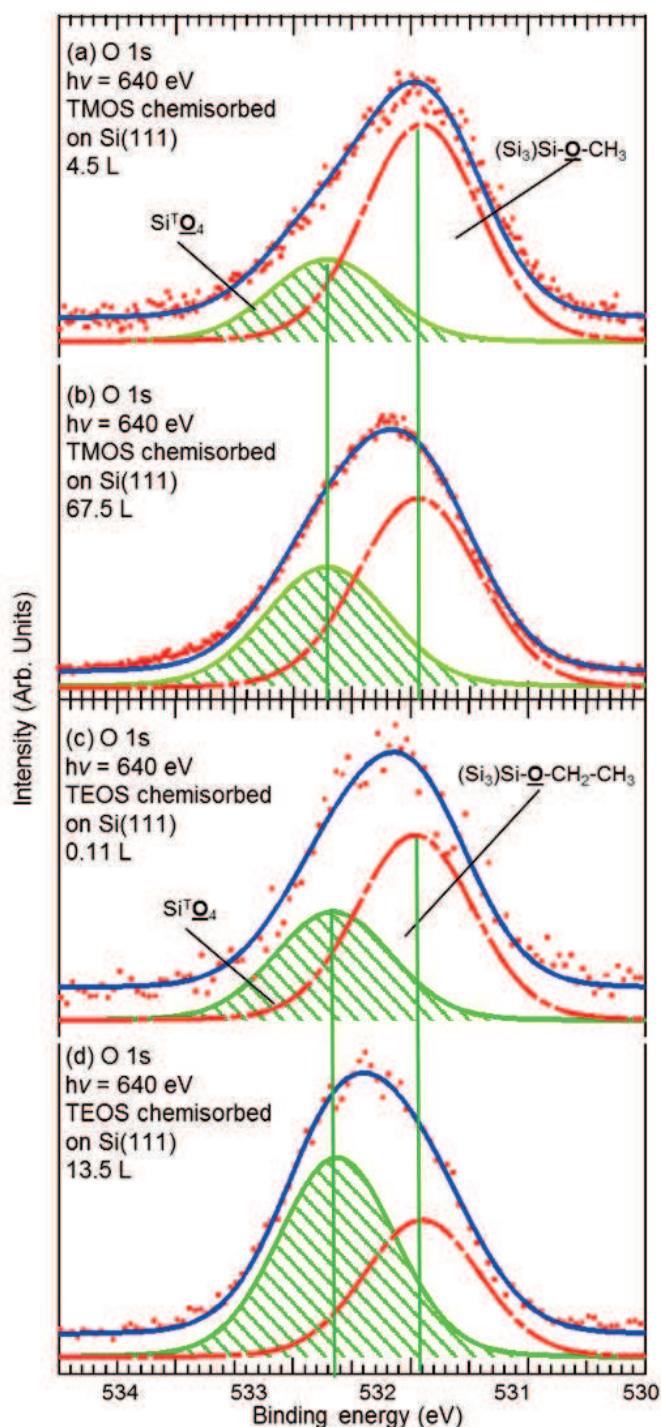


Figure 5.7: O 1s XPS spectra ($h\nu = 640$ eV) of Si(111)-7×7 surface (n-doped, $0.003 \Omega \times \text{cm}$) (a) exposed to TMOS for a coverage of 4.5 L (10 min, 10^{-8} mbar); (b) of 67.5 L (15 min, 10^{-7} mbar) (c) exposed to TEOS for a coverage of 0.11 L (30 min, 5×10^{-9} mbar); (d) of 4.5 L (10 min, 10^{-8} mbar). The BE is referenced with respect to the Fermi level. Fitting parameters are collected in Table 5.6

	BE (eV)	fwhm (eV)	Weight (%)	Attribution
TMOS chemisorbed on Si(111), 4.5 L	531.85	1.2	76.7	(Si ₃)Si – O – CH ₃
	532.76	1.2	23.3	Si ^T O ₄
TMOS chemisorbed on Si(111), 67.5 L	531.90	1.2	61.4	(Si ₃)Si – O – CH ₃
	532.73	1.2	38.6	Si ^T O ₄
TEOS chemisorbed on Si(111), 0.11 L	531.96	1.2	63.0	(Si ₃)Si – O – CH ₂ – CH ₃
	532.66	1.2	36.0	Si ^T O ₄
TEOS chemisorbed on Si(111), 13.5 L	531.96	1.2	32.0	(Si ₃)Si – O – CH ₂ – CH ₃
	532.67	1.2	68.0	Si ^T O ₄

Table 5.5: Si $2p_{3/2}$ Surface core level shifts (SCLS, relative Si $2p_{3/2}$ BE referenced to the bulk component one), spectral weights, full widths at half maximum (fwhm), and attribution of the Voigt components used to reconstruct the Si 2p XPS experimental spectra shown in Figure 5.7. The BE of the Si $2p_{3/2}$ component (referenced to the Fermi level) is 99.40 eV.

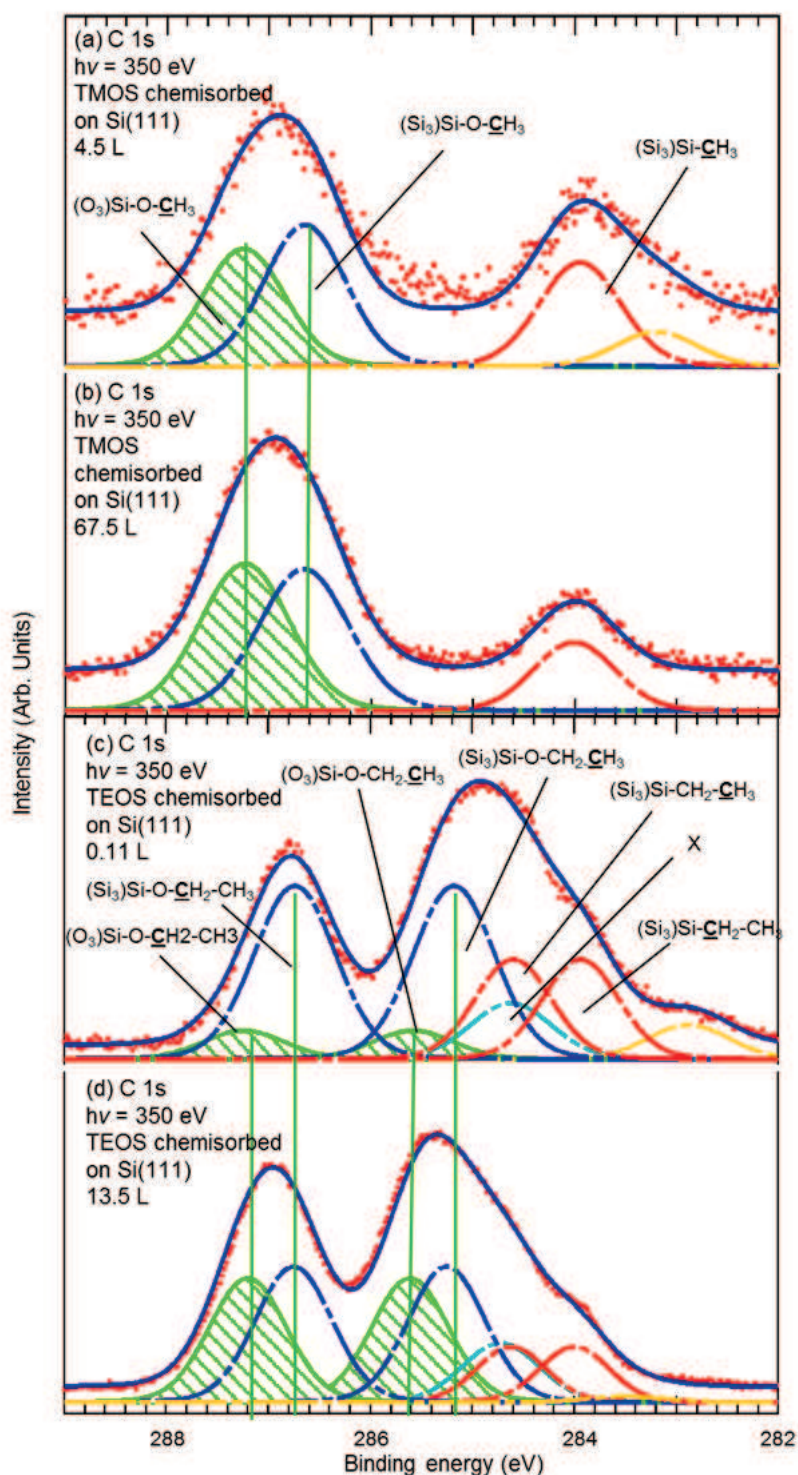


Figure 5.8: C 1s XPS spectra ($h\nu = 350$ eV) of Si(111)-7×7 surface (n-doped, $0.003 \Omega \times \text{cm}$) (a) exposed to TMOS for a coverage of 4.5 L (10 min, 10^{-8} mbar); (b) of 67.5 L (15 min, 10^{-7} mbar) (c) exposed to TEOS for a coverage of 0.11 L (30 min, 5×10^{-9} mbar); (d) of 4.5 L (10 min, 10^{-8} mbar). The BE is referenced with respect to the Fermi level. Fitting parameters are collected in Table 5.6

	BE (eV)	fwhm (eV)	Weight (%)	Attribution
TMOS chemisorbed on Si(111) 4.5 L	287.26	0.92	29.2	(O ₃)Si – O – CH ₃
	286.69	0.92	37.8	(Si ₃)Si – O – CH ₃
	283.89	0.92	33.0	(Si ₃)Si – CH ₃
TMOS chemisorbed on Si(111) 67.5 L	287.25	0.91	42.2	(O ₃)Si – O – CH ₃
	286.67	0.91	40.2	(Si ₃)Si – O – CH ₃
	284.01	0.91	17.6	(Si ₃)Si – CH ₃
TEOS chemisorbed on Si(111) 0.11 L	287.24	0.92	4.2	(O ₃)Si – O – CH ₂ – CH ₃
	286.74	0.92	25.5	(Si ₃)Si – O – CH ₂ – CH ₃
	285.58	0.92	4.2	(O ₃)Si – O – CH ₂ – CH ₃
	285.18	0.92	25.5	(Si ₃)Si – O – CH ₂ – CH ₃
	284.60	0.92	13.7	(Si ₃)Si – CH ₂ – CH ₃
	283.95	0.92	13.7	(Si ₃)Si – CH ₂ – CH ₃
	284.62	0.92	8.2	X
TEOS chemisorbed on Si(111) 13.5 L	287.20	0.89	18.1	(O ₃)Si – O – CH ₂ – CH ₃
	286.75	0.89	19.8	(Si ₃)Si – O – CH ₂ – CH ₃
	285.61	0.89	18.1	(O ₃)Si – O – CH ₂ – CH ₃
	285.26	0.89	19.8	(Si ₃)Si – O – CH ₂ – CH ₃
	284.62	0.89	7.4	(Si ₃)Si – CH ₂ – CH ₃
	283.99	0.89	7.4	(Si ₃)Si – CH ₂ – CH ₃
	284.70	0.89	8.7	X
	282.90	0.89	0.9	CH _x

Table 5.6: C 1s Surface core level shifts (SCLS, relative Si 2p_{3/2} BE referenced to the bulk component one), spectral weights, full widths at half maximum (fwhm), and attribution of the Voigt components used to reconstruct the Si 2p XPS experimental spectra shown in Figure 5.8.

Similar trends are found for the C 1s spectra of TEOS shown in Figure 5.8 (c) and 5.8 (d). The fit procedure is similar to that used for the Si(001)-2×1. We see that the $(\text{O}_3)\text{Si} - \text{CH}_2 - \text{CH}_3$ peak intensity increases relatively to that of the $(\text{Si}_3)\text{Si} - \text{CH}_2 - \text{CH}_3$ component from short to long exposures, in accord with a full dissociation via Si – O bond breaking (path (a) in Figure 5.2) at low coverage, and with C – O bond breaking (path (b)) at higher coverage. The weighing of the $(\text{Si}_3)\text{Si} - \text{CH}_2 - \text{CH}_3$ is obscured by the component X related to beam damage.

5.3 Reactions mechanisms of alkoxysilanes on silicon surfaces

As shown in the previous section, the studied alkoxysilane molecules are decomposed on Si(001)-2×1 surface via two reaction channels presented Figure 5.2. One involving the breaking of all four Si – O bonds (also clearly observed at low exposures by STM for TEOS), and one involving the rupture of the C – O bond (observed at large exposures).

Si – O bond breaking of alkoxysilane was considered by Eng and Raghavachari. [115] They performed DFT calculations on trimethoxysilane ($\text{SiH}(\text{OCH}_3)_3$) reaction over a Si dimer of the Si(001)-2×1 surface. The key feature is the zwitterionic nature of the silicon dimer, with a down electron-poor atom and an up electron-rich one.[45] In an “on-dimer” reaction (Si – Si distance of 2.35 Å), the molecule is first adsorbed (without activation barrier) via a dative bond between one oxygen lone-pair (electron-rich) and the down Si dimer atom (electron-poor). The resulting intermediate species is found -0.6 eV below the separated reactant energy. Then, Si – O dissociation occurs via a four center transition state (see Figure 5.9), involving the central Si atom of the molecule (electron-poor) and the up Si dimer atom. The activation barrier is only 0.15 eV (from the datively bonded intermediate species).

These theoretical results, obtained for the scission of one alkoxysilane Si – O bond, can be used to propose a plausible reaction path, shown in Figure 5.10, for the scission

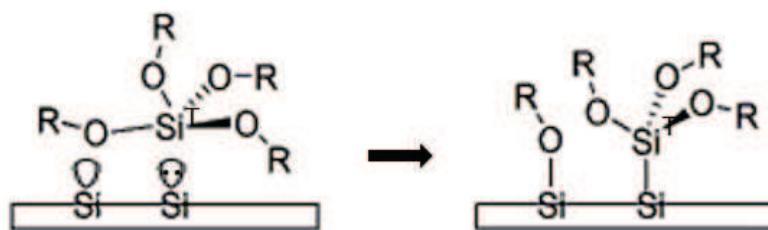


Figure 5.9: Possible mechanism by Si – O bond breaking of $\text{Si}(\text{OR})_4$ molecule on a zwitterionic Si pair of Si(001)-2×1. Si^{T} denotes the alkoxy silane Si atom.

of all TEOS Si – O bonds observed on the Si(001)-2×1 surface at low coverage. On Si(001)-2×1, the distance between two silicon dimers is of 3.84 Å; therefore, several dimers can be involved in the reaction mechanism. A concerted mechanism involving the simultaneous breaking of two (or more) Si – O can be envisaged, it involves three consecutive dimers in a row, and two dimers in the adjacent row on which the expelled monomer sits.

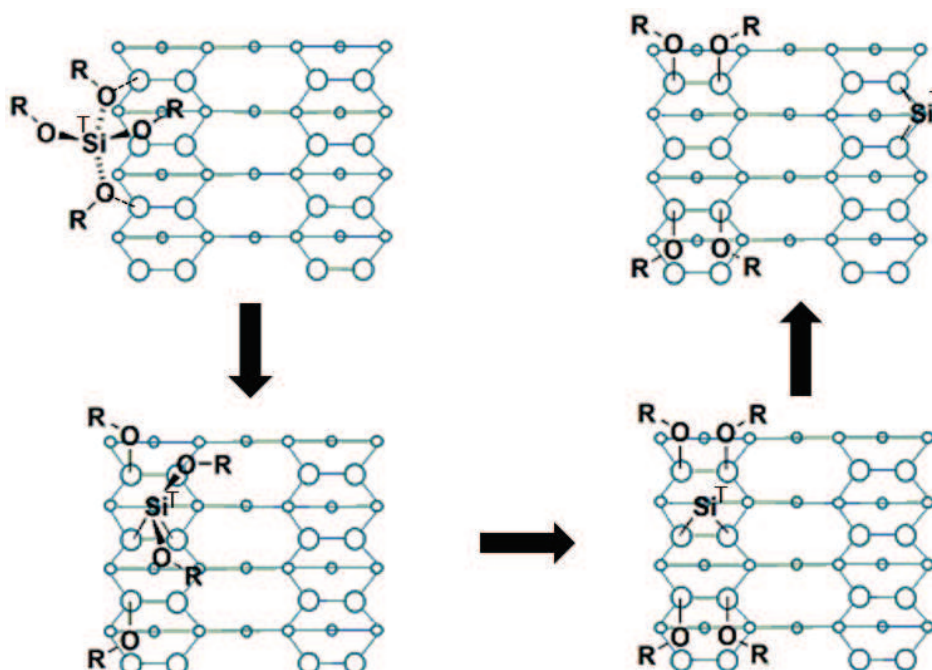


Figure 5.10: Possible reaction path on Si(001)-2×1 leading to the full dissociation of a $\text{Si}(\text{OR})_4$ molecule. Si^{T} denotes the alkoxy silane Si atom.

The modeling of C – O bond breaking on Si(001)-2×1 was not examined theoretically. But many theoretical works were devoted to the decomposition of alcohols on Si(001)-2×1, considering both O – H and C – O bond rupture over a silicon dimer. In all cases the pre-dissociation intermediate species is datively bonded to a down Si dimer atom. The activation barrier for C – O breaking is always very high, 1.2 eV range for methanol according to the cluster calculation of Ref. [116] and 1.0 eV for ethanol according to the Car-Parinello calculation of Ref. [117]. Therefore by transposing these results to alkoxysilanes, it is expected that Si – O bond breaking over a silicon dimer is preferred to C – O bond breaking.

Consequently, where could alkoxysilane react via C – O bond breaking on Si(001)-2×1 as observed at large exposures?

Our results can be compared to the experimental ones obtained by Casaletto et al.[118] and Carbone et al.[119] for the deposition of ethanol on the Si(001)-2×1 and the Si(111)-7×7 surface respectively. Ethanol dissociate on both surfaces by scission of the O – H bond creating Si – O – CH₂ – CH₃ and Si – H units. Compared to TEOS, ethanol do not contain a silicon atom which could be expelled and create an adatom on the surface. On the Si(001)-2×1 surface, the C 1s spectrum is constituted by two peaks of same intensity separated by 1.2 eV, the peak at high BE is attributed to Si – O – CH₂ – CH₃ and the one at low BE to Si – O – CH₂ – CH₃. No further decomposition is observed. On the contrary, for the Si(111)-7×7 surface, there is still two peaks but their intensities are different; the one attributed to Si – O – CH₂ – CH₃ is asymmetric and has a larger area than the other peak suggesting the presence of other fragments as ethyl groups. These observations suggest that C – O bond scission mechanism cannot occur on the silicon dimers of the clean Si(001)-2×1 surface but need the presence of the triply coordinated monomer on the surface, similar to those present on the Si(111)-7×7 surface.

On the Si(111)-7×7, we observed that TEOS dissociates by Si – O bond scission in the initial regime. However, in order to observe only Si⁺ oxidation state on the surface the pressure and duration of exposure were decreased compare to the one on the Si(001)-2×1 surface, from 4.5 L to 0.11 L. Indeed, the apparition of the Si⁴⁺ oxidation state

occurs quicker than for the Si(001)-2×1 surface, certainly due to the presence, since the beginning of the reaction, of adatoms, tricoordinated to the surface, allowing the mechanism by C – O bond scission.

In fact, as for the Si(001)-2×1, the Si(111)-7×7 surface presents a reaction site constituted by pair of atoms, the electron-rich restatom and the electron-poor adatom, respectively (distant by $\sim 4.5 \text{ \AA}$, distances are indicated Figure 5.11). This pair could lead to Si – O bond breaking via a four-center transient species similar to that depicted in Figure 5.9 for the Si(001)-2×1 surface. The –OR moiety could go to the adatom, while the silicon atom of the (electrophilic) alkoxy silane molecule could form a bond with the restatom. Given that, two other adatoms are at a distance of $\sim 4.5 \text{ \AA}$, two more Si – O bonds could break (the reaction could also be concerted), releasing a Si – OR species that could move away to further react (the nearest adatom on the half cell, a center adatom, is at $\sim 9 \text{ \AA}$). This would lead to the attachment of three –OR moieties to three middle adatoms and to one corner adatom. For a full dissociation (4 Si – O broken bonds) the released silicon atom could move to a restatom site (in another half-cell) surrounded by three bare adatoms (making there four formal bonds). This adsorption site for a monomer was indeed observed by STM.[120] Therefore in the initial regime the dissociation of Si(OR)₄ molecules is similar to that of SiCl₄ that leads to the rupture of three to four Si – Cl bonds at room temperature.[121]

Consequently, we propose that alkoxy silane dissociation by C – O bond breaking channel occurs on the adatoms already present on the Si(111)-7×7 surface. The adatom backbonds are indeed strained, weakened single bonds. They break under exposure to hydrogen,[122] ammonia[123] and water.[71] The other reaction sites for C – O bond breaking could be the silicon atoms released by the Si – O dissociation channel.

5.4 Summary

Synchrotron radiation XPS study gives crucial information on the reactivity of alkoxy silane molecules (TMOS and TEOS) on the Si(001)-2×1 and the Si(111)-7×7 surface at

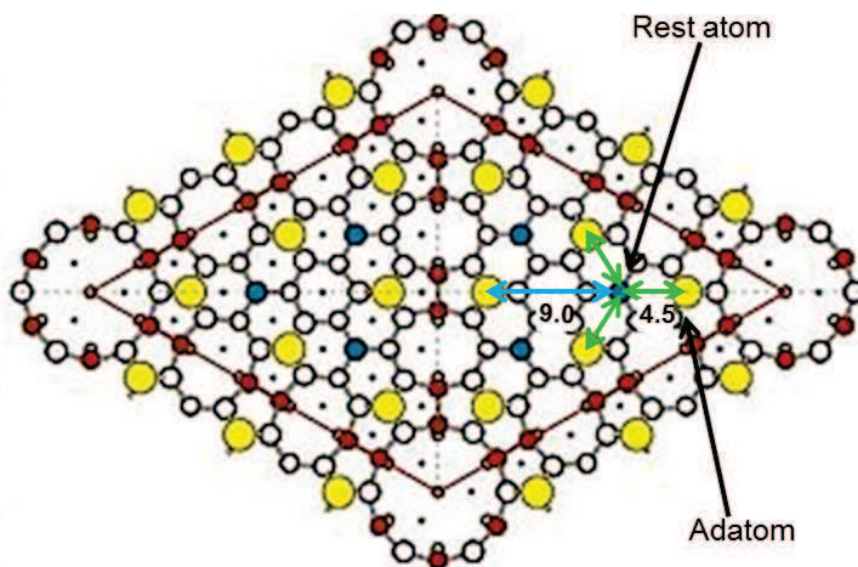


Figure 5.11: Scheme of the Si(111)-7 \times 7 surface with its characteristic distances (\AA)

room temperature. Si 2p core-levels (measured with high surface sensitivity at a sub-monolayer level) together with O 1s and C 1s core-levels give an insight on the dissociation reactions.

On Si(001)-2 \times 1, an initial regime corresponding to the full dissociation of the molecule, via Si – O bond breaking and emission of a silicon monomer, is in competition with a second regime involving the breaking of the C – O bond. We propose that the latter reaction occurs on the monomers produced by Si – O bond breaking. As the exposure to tetraethoxysilane is a promising route to nano-pattern the Si(001)-2 \times 1 surface, with alternating ethoxy-covered and monomer-covered dimer rows, the present study indicates that large exposures to the molecule may be detrimental to the chemical order.

On Si(111)-7 \times 7, Si – O bond breaking also occurs, in contrast to preceding reports, that favored C – O bond breaking at low coverage; [109], [64] however, C – O bond is also observed. We also speculate that adatoms, and monomers possibly released by Si – O bond breaking can be involved in C – O bond breaking.

The presence of surface alkyl surface species, besides the expected alkoxy species,

has profound consequences for ALD deposition of silica on a clean silicon substrate. While alkoxy species can be hydrolyzed to silanols by exposure to water, surface ethyls species will remain unaltered. Therefore, if the presence of Si – C bonds is not desired at the surface/interface, a first exposure of the clean surface to alkoxy silane molecules should be avoided. Instead, the silicon surface could be water-reacted first, to form surface silanols, [124], [62] and the chemisorption of alkoxy silane molecules, via an alcohol-elimination reaction with surface silanols, [61] could be explored. This reaction path will be investigated in the next chapter.

Chapter 6

Atomic layer deposition on Si(001) surface using TEOS as a precursor and monitored by NAP-XPS

In the previous chapters, we attempt to describe the dissociation mechanism of TEOS on the clean Si(001)- 2×1 surface. We explore different aspects of its reactivity, the dissociation mechanism and the distribution of fragments on the clean surface at low coverage (chapter 3), the future of the silicon monomer released on the surface (chapter 4), possible dissociation channels at high coverage and their probable link with the presence of the silicon monomer (chapter 5).

In this chapter, we will focus on one of the main application of TEOS: its use as a precursor in ALD process for the deposition of thin silicon oxide layer on the silicon surface.

6.1 Atomic layer deposition (ALD)

Several processes can be used to deposit silicon dioxide on a clean silicon surface, the most common are Chemical Vapor Deposition (CVD), Molecular Beam Epitaxy (MBE) or Atomic Layer Deposition (ALD). These techniques use gases as silane (dichlorosilane SiCl_2H_2 or TEOS) and oxygen. [14], [15] Silane is used between 300 and 500 °C, dichlorosilane at around 900 °C, and TEOS between 650 and 750 °C. CVD oxides may contain impurities and byproducts of the deposition; indeed, TEOS produces a relatively pure oxide, whereas silane and dichlorosilane introduces hydrogen and chlorine

impurities respectively. [16]

In this chapter, we will focus on ALD. Interest in ALD has increased in the mid-1990s and 2000s, in conjunction with the development of silicon-based microelectronics. ALD is considered one deposition method with great potential for producing very thin, conformal films with control of the thickness and composition of the films possible at the atomic level. A major driving force for the recent interest is the perspective of using ALD in scaling down microelectronic devices.[12], [13]

ALD, a variant of CVD, is a repeated sequence of self-limited surface reaction. The main difference with CVD is that ALD uses chemical precursors that are introduced one at a time and separated by inert gas purging in order to avoid gas phase reactions. By repeating the process of growing individual layers, thin films can be applied to surfaces. Some advantages of a self-limiting film include uniform surfaces, high conformity to surface features, high control and accuracy of atomic level thickness, and high reproducibility. ALD may have some drawbacks, such as incomplete surface reaction and slow rate. Surface science is summoned up to get a more in-depth knowledge of the surface reaction mechanisms, in order to improve the technological processes.

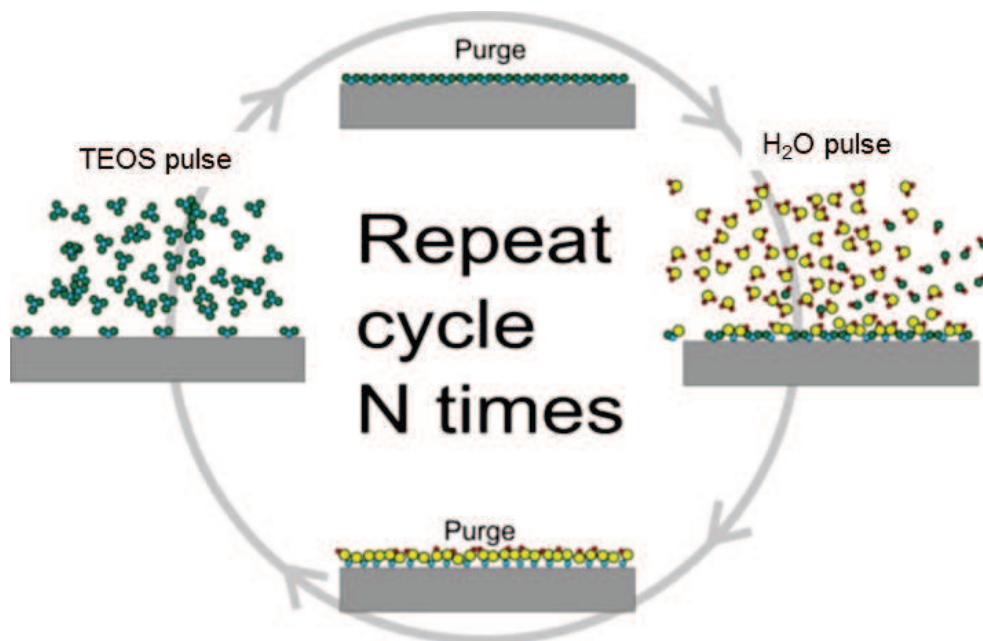


Figure 6.1: Schematic representation of the Atomic Layer Deposition (ALD) process.

A schematic presentation of the ALD process is presented Figure 6.1.[12] The precursor, which will be TEOS in our case, is added to the reaction chamber containing the water-covered Si(001) surface to be coated by ALD. A possible reaction path for this step is presented in Figure 6.2 (a), we suppose a reaction between the surface hydroxyl groups and TEOS. It creates a $(\text{Si}^{\text{S}} - \text{O})_n \text{Si}^{\text{T}}(\text{OC}_2\text{H}_5)_{4-n}$ adduct (where Si^{S} indicates a surface silicon atom, Si^{T} the silicon atom of the TEOS molecule and n the number of bonds created by one TEOS molecule with the surface) by the elimination of an ethanol molecule. On Figure 6.2 (a), n is arbitrary chosen equal to 2.

After the TEOS adsorption on the surface, any excess of the molecule is removed from the reaction chamber by pumping it down. Then, water is added and hydrolyzes the ethoxy groups resulting from TEOS dissociation on the surface. The hydrolysis transforms them in hydroxyl groups as shown in Figure 6.2 (b). Similarly to TEOS, water is then cleared from the reaction chamber and the freshly created hydroxyl groups are ready to react with TEOS again.

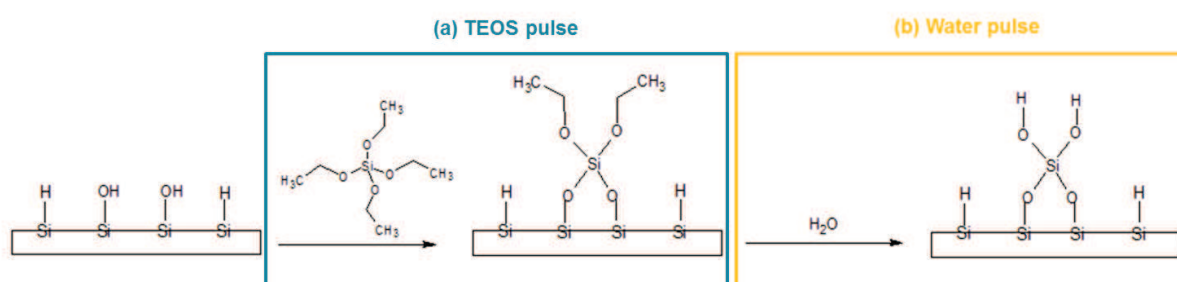


Figure 6.2: Possible reaction path for the ALD process on the water-covered Si(001)- 2×1 surface, (a) TEOS pulse and (b) Water pulse.

6.2 ALD process monitored by NAP-XPS

The ALD process is the alternance of the two steps described in the previous section, a TEOS pulse and a water pulse. To study this process with the NAP-XPS, we started from a water-covered silicon surface. A Si(001) sample (n-doped, $0.003 \Omega \times \text{cm}$) was flashed into the preparation chamber ($P = 1 \times 10^{-9}$ mbar) and exposed to water

(1×10^{-8} mbar, 30 min, 13.5 L) in this same chamber to avoid carbon contamination during the transfer to the analysis chamber.

Due to the use of high pressures (mbar range) of water and TEOS in the analysis chamber during the acquisition, it was not possible to recover a good vacuum ($\sim 1 \times 10^{-8}$ mbar) between two exposures. In these conditions, starting the study in the analysis chamber with an already water-covered silicon sample was the cleanest way to proceed.

6.2.1 First step: Exposure to TEOS

For the TEOS exposure, the pressure was increased to 1 mbar and kept at this value for 120 min (5.4×10^9 L). In the following section, we present the Si 2p, C 1s and O 1s core-level spectra acquired during the exposure and after the remove of the gas.

Influence of the gas phase on the Si 2p core-level position:

We present in Figure 6.3, the evolution of the Si 2p bulk peak as a function of TEOS pressure. We observe an increase of its BE of ~ 0.2 eV between $P = 2 \times 10^{-8}$ mbar and $P = 0.5$ mbar. After removing the gas from the chamber, the Si 2p bulk peak goes back to a position close to its initial one; the phenomenon is reversible.

On the clean Si(001)- 2×1 surface, water dissociates into $-H$ and $-OH$ fragments that react with two silicon dangling bonds and then decorate these silicon atoms.[125], [62] However, not all dangling bonds are capped with OH/H fragments. A few of them, amounting to 0.01 ML, remain unreacted. These isolated silicon dangling bonds are negatively charged (the dangling bond is doubly occupied) on highly doped n wafers. The transfer of electrons from the bulk to the surface (due to the alignment of the bulk and surface Fermi levels) is accompanied by an upward band bending. Any change of the surface charge density involves a change in the band bending. When the electrically active surface dangling bonds are passivated, the band bending diminishes (i.e. the bands go flatter). The BE changes of the Si 2p core-level reflect changes in the po-

sition of the Fermi level at the surface. For a n-type wafer, the increase in BE indicates that the band bending decreases and that the density of electrically active sites at the surface decreases.[126], [127] We tentatively propose that the TEOS molecules interact with the silicon dangling bonds, pushing up in energy the acceptor level. Hence the TEOS-Si dangling bond complex would be neutral. Interaction between oxygen lone-pairs and silicon dangling bonds are expected (see for instance the case of aldehydes in ref. [128]) These defects may interact with a lone electrons pair of oxygen atoms present in the TEOS molecule; the non-dissociation of TEOS, in this case, would explain the reversibility of the phenomenon.

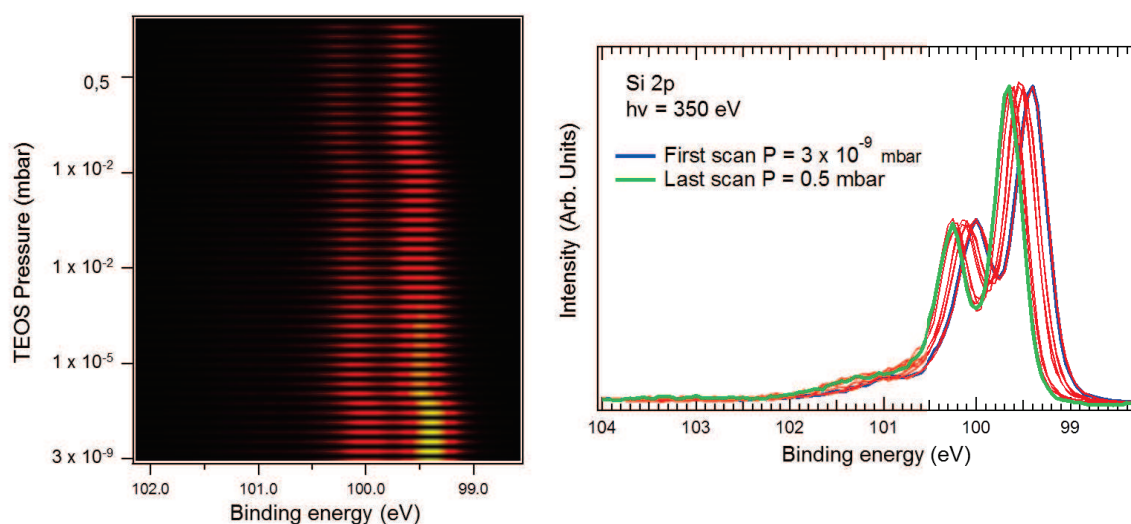


Figure 6.3: Si 2p bulk position as a function the exposure of the water-covered Si(001) surface (n-doped, $0.003 \Omega \times \text{cm}$) to TEOS (from $P = 2 \times 10^{-8}$ mbar to $P = 1 \times 10^{-2}$ mbar).

Evolution of the C 1s and the Si 2p core-level spectra during exposure

Figure 6.4 and 6.5 present the Si 2p and C 1s spectra respectively, before, during and after TEOS exposure. Si 2p and C 1s spectra are calibrated in energy relative to the position of the Fermi level.

The Si 2p spectra was fitted using the same components than those chosen in previous chapters. B is related to bulk component and S to second layer silicon atoms. Before

filling the chamber with TEOS, we observe on the Si 2p spectra (Figure 6.4 (a)) a first oxidation state at + 0.9 eV (fwhm = 0.9 eV) and a fourth oxidation state at + 3.6 eV (fwhm = 3.2 eV) relative to the bulk component (at 99.62 eV) and corresponding to a spectral weight of 13.6 % and 0.9 % respectively.

To estimate the TEOS coverage of the surface, we can compare the intensity of the Si⁺ and Si⁴⁺ peak. On the water-saturated surface, half of the surface silicon atoms are Si – OH species, corresponding to a coverage of ~ 0.5 ML can be deduced. During the reaction with TEOS, the number of Si⁺ species on the surface is supposed to be constant; the comparison of the Si⁺ and Si⁴⁺ spectral weights gives a TEOS coverage of 0.03 ML.

On the C 1s (Figure 6.4 (b)), four components are used for the fit, two corresponding to ethoxy groups at ~ 287.1 eV and ~ 285.5 eV (fwhm = 1.2 eV) attributed to Si – O – CH₂ – CH₃ and Si – O – CH₂ – CH₃ respectively and two related to ethyl groups at ~ 285.3 eV and ~ 284.8 eV (fwhm = 0.9 eV) attributed to Si – CH₂ – CH₃ and Si – CH₂ – CH₃ respectively. A small component at ~ 283 eV can be ascribed to carbonaceous CH_x species likely due to beam damage. As mentioned previously, the pressure of TEOS is already of ~ 10⁻⁸ mbar in the chamber (which corresponds to pressures used for TEOS exposure in previous chapters) and, therefore, the reaction has already started.

During the exposure, we observe an increase of the Si⁴⁺ component (+ 3.6 eV, fwhm = 0.9 eV and spectral weight = 3.6 %) on the Si 2p spectrum (Figure 6.4 (b)) associated with TEOS dissociation and oxide growth. However, this component also contains a contribution of the silicon atom from TEOS molecules of the gas phase or physisorbed on the surface. On the C 1s (Figure 6.5 (b)), the components relative to ethoxy and ethyl groups are unchanged, but two new components associated to carbon atoms of TEOS molecules in the gas phase or physisorbed on the surface are present on the spectrum at higher energy (at ~ 288.31 eV and ~ 286.74 eV, fwhm = 0.7 eV).

After the exposure, the C 1s spectrum (Figure 6.5 (c)) is similar to the one of the starting point; however, on the Si 2p spectrum (Figure 6.4 (c)) the oxide component (at + 3.6 eV, fwhm = 0.92 eV, spectral weight = 2.4 %) has slightly increased compared to the one of the starting point spectrum (at + 3.6 eV, fwhm = 0.90 eV, spectral weight = 0.9 %) and the TEOS coverage can be estimated at 0.09 ML.

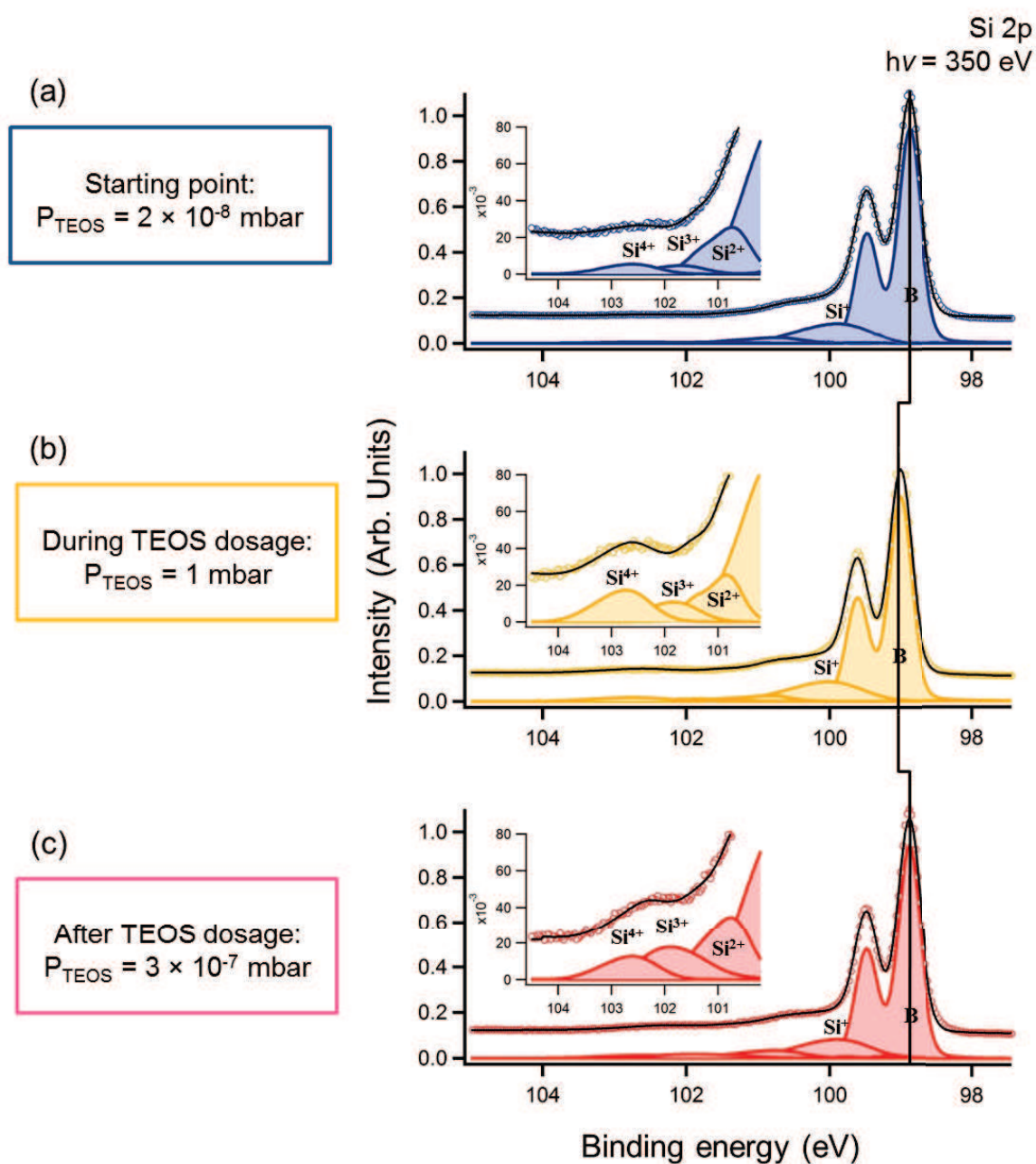


Figure 6.4: Si 2p XPS spectrum ($h\nu = 350$ eV) of the water-covered Si(001) surface (n-doped, $0.003 \Omega \times \text{cm}$) (a) at the starting point, (b) during the exposure to TEOS (120 min, up to 1 mbar, at room temperature), (c) after TEOS exposure. The BE is referenced with respect to the Fermi level.

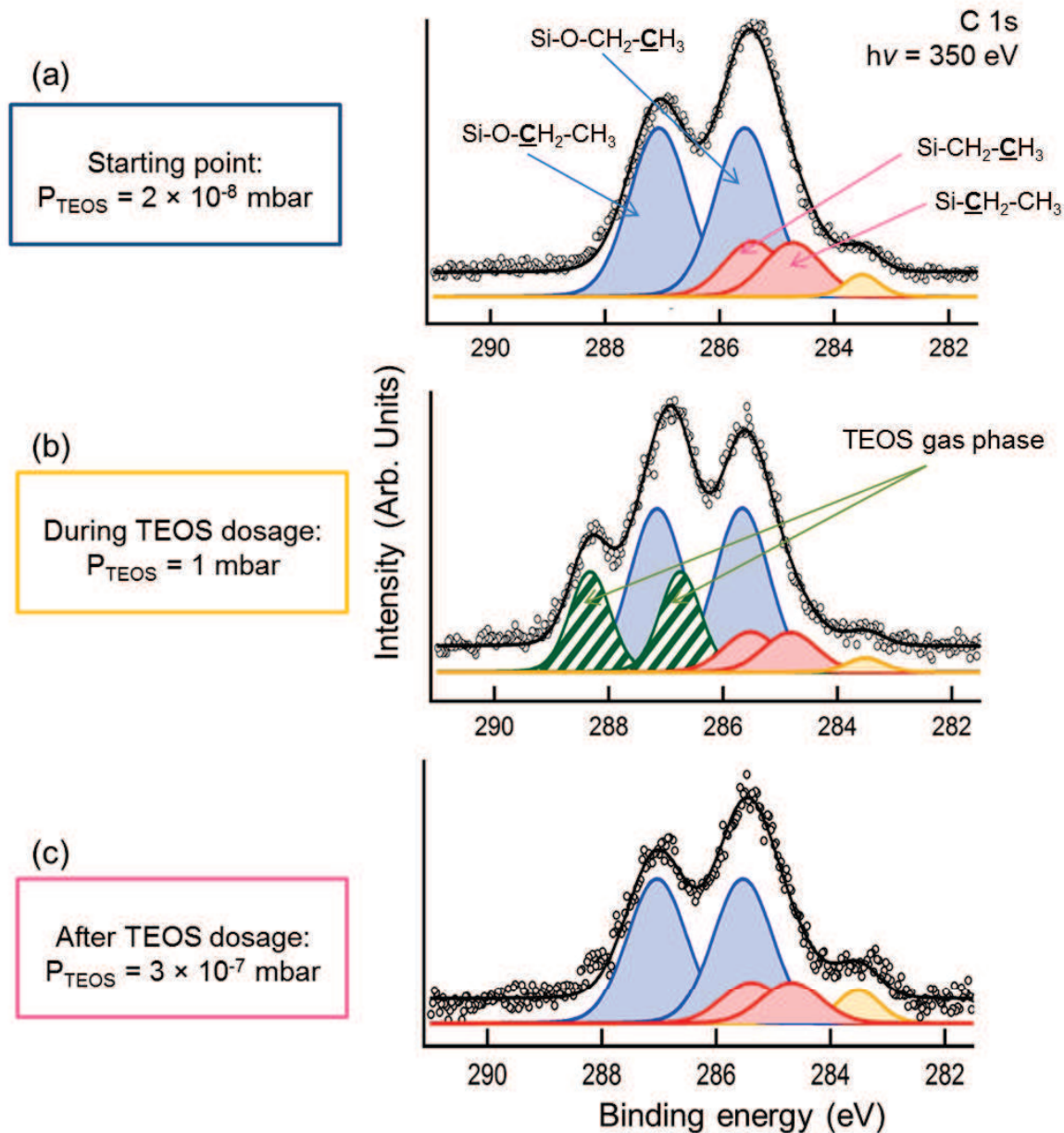


Figure 6.5: C 1s XPS spectrum ($h\nu = 350$ eV) of the water-covered Si(001) surface (n-doped, $0.003 \Omega \times \text{cm}$) (a) at the starting point, (b) during the exposure to TEOS (120 min, up to 1 mbar, at room temperature), (c) after TEOS exposure. The BE is referenced with respect to the Fermi level.

During this first step, we observe mainly the appearance of ethoxy groups and an increase of the fourth oxidation state of silicon in agreement with the mechanism proposed in Figure 6.2, however it is not possible to determine how many bonds of the TEOS molecule are broken and replaced by a bond with surface hydroxyl groups. The origin of the Si – C bonds as minority species (pink components in Figure 6.5) remains unclear.

6.2.2 Second step: Exposure to water

The second step of ALD process consists in the introduction of water. During the exposure to water (120 min, up to 2 mbar, 1.1×10^{10} L), we followed the evolution of C 1s and O 1s at $h\nu = 640$ eV, the spectra are presented in Figure 6.6 and Figure 6.7 respectively. After the remove of the water vapor, the Si 2p was measured at $h\nu = 350$ eV (to be compared with the Si 2p spectrum of Figure 6.4 (c)) and is presented in Figure 6.9.

The C 1s spectra are fitted similarly than previous ones, no modification of the spectra are observed during the increase of pressure, only a global decrease of the intensity due to the inelastic scattering of the photoelectron in the gas phase. (The component at ~ 283 eV, ascribed to carbonaceous CH_x species in the bulk, seems more intense than Figure 6.5, it is due to the photon energy. We choose to follow simultaneously the C 1s and O 1s spectra during exposure to water; indeed, at $h\nu = 640$ eV we are more sensitive to the bulk than at $h\nu = 350$ eV which exacerbate the peak associated to bulk contamination). The ratio between the ethoxy and ethyl groups components area remains constant. In presence of water, ethoxy groups may be hydrolyzed by water molecules, but no reaction can occur with ethyl groups. In consequence, the ratio between the ethoxy and ethyl groups components area should change. It is not the case here and no reaction are affecting the ethoxy groups of the silicon surface.

On the O 1s spectra Figure 6.7, we observe the emergence of a peak related to the water gas phase (at ~ 536.2 eV and $\text{fwhm} = 0.3$ eV), the second peak at ~ 532.7 eV, attributed to surface oxygen, is a very large structure ($\text{fwhm} = 2.0$ eV) containing

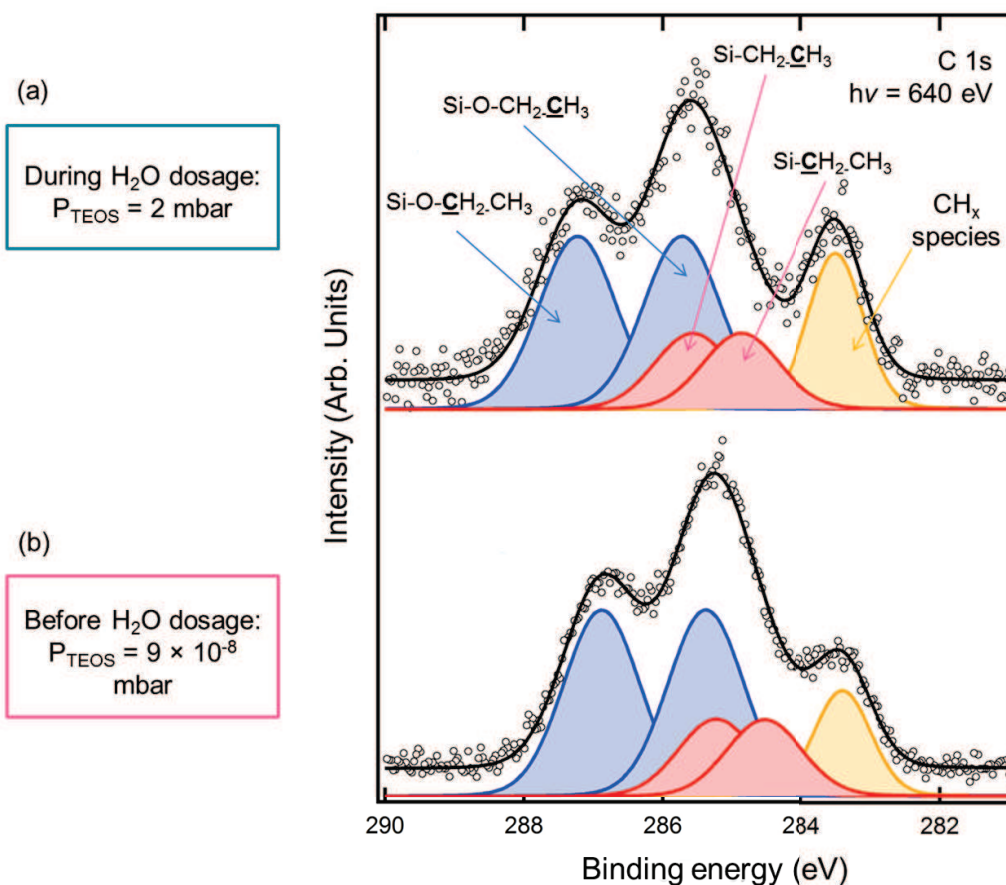


Figure 6.6: C 1s XPS spectra evolution ($h\nu = 640$ eV) before and during the exposure of the TEOS-covered silicon surface (n-doped, $0.003 \Omega \times \text{cm}$) to water (120 min, up to 2 mbar, at room temperature). The BE is referenced with respect to the Fermi level.

various components and is, therefore, difficult to analyze. However, the shape and the fwhm of this peak do not change when RH increases from RH = 0 % ($P \sim 10^{-8}$ mbar and $T = 293$ K) to 10 % ($P \sim 2$ mbar and $T = 293$ K). In particular, we do not observe the emergence of a peak at ~ 534 eV that could be attributed to liquid water on the surface. Therefore, with a RH of 10 %, no water films are found on the (H,OH)-Si(001) surface. This is at odds with what is observed on the silica surface, for which NAP-XPS showed that a 1 nm thick film forms.[129]

Figure 6.8 presents the O 1s spectra before and after the water dose. The spectra are normalized on the silicon auger LVV in order to evaluate the variation of oxygen quantities on the surface. The ratio between the area of the two O 1s peak measured

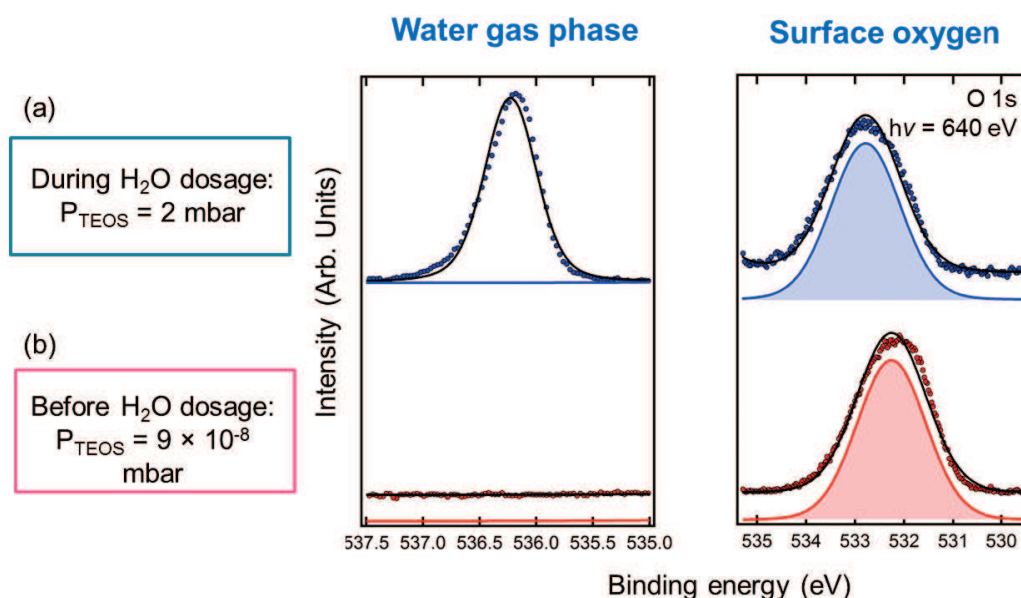


Figure 6.7: O 1s XPS spectra evolution ($h\nu = 640$ eV) before and during the exposure of the TEOS-covered silicon surface (n-doped, $0.003 \Omega \times \text{cm}$) to water (120 min, up to 2 mbar, at room temperature). The BE is referenced with respect to the Fermi level.

after and before the water dose is about 3.

This observation implies that, despite the fact that the C 1s is not modified by the water exposure, some oxygen has been inserted into the surface. This is confirmed by the Si 2p spectrum presented Figure 6.9 where an increase of the Si^{4+} component (at + 3.6 eV, fwhm = 0.9 eV, spectral weight after water dose = 6.2 %).

Therefore, the expected hydrolysis of the surface ethoxy group does not occur. As NAP-XPS demonstrates that at 2 mbar no liquid water is present on the surface, this suggests humidity ratios higher than 10 % should be explored. The presence of liquid water may be determining in the hydroxylation process; this point should be explored in the future. Nevertheless, the substrate undergoes an oxidation in presence of water molecules. It means that, in the present conditions, the direct oxidation of the substrate by water molecules is more favorable than an oxidation mechanism involving the hydrolysis of surface ethoxy groups by water molecules of the gas phase. As silicon wafer oxidation is an undesirable process, this interesting observation suggests

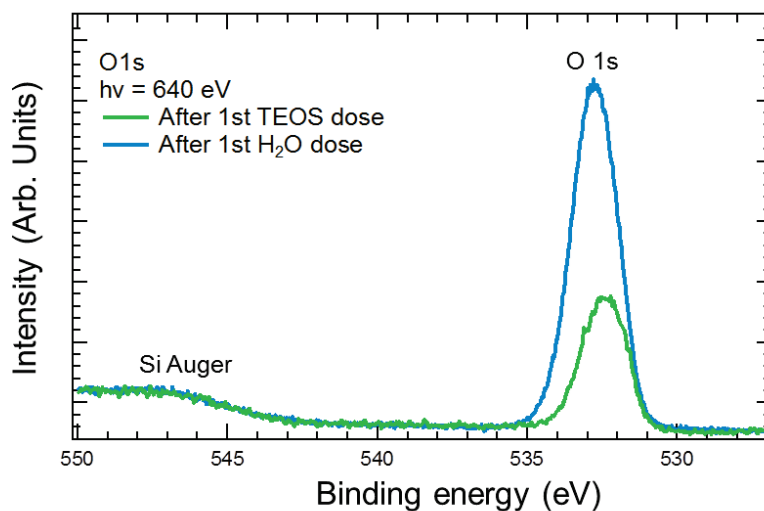


Figure 6.8: Si Auger LVV and O 1s core level peak recorded at $h\nu = 640$ eV from both the TEOS-covered silicon surface (n-doped, $0.003 \Omega \times \text{cm}$) and the same surface after exposure to water. ($P \sim 10^{-8}$ mbar)

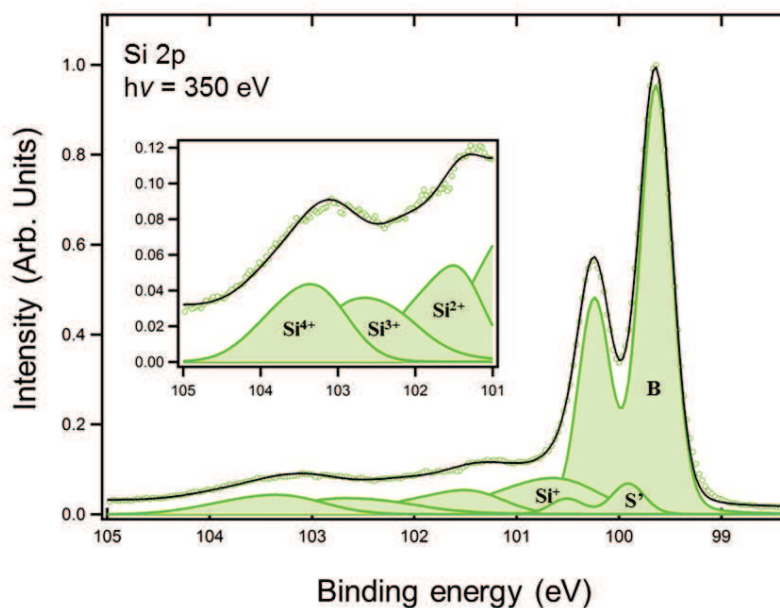


Figure 6.9: Si 2p XPS spectrum ($h\nu = 350$ eV) of the water-covered Si(001) surface (n-doped, $0.003 \Omega \times \text{cm}$) after exposure to TEOS and water. The BE is referenced with respect to the Fermi level. ($P \sim 10^{-8}$ mbar)

that other molecular species, less oxidative than water such as alcohols, ethers, or metal alkoxides should be used. Rauwel et al. studied thin film deposition using carboxylic acids and metal alkoxides and showed that the ALD process takes place via an ester elimination condensation step.[130], [131]

6.3 Beam damage on the silicon surface

During these experiments, we observed damages on our samples due to the X-ray beam. Similarly to UHV experiments, the sample was continuously moved during the acquisition to avoid damages induced by the X-ray beam on the surface. However, unlike UHV measurements, the damages directly induced by the beam on the surface are not the only one we have to take into account, the gas phase is also concerned. We present in this section two experiments illustrating beam induced reactions in the gas phase and their consequences on material deposition.

First experiment:

The water-covered surface was exposed to a TEOS pressure of 1 mbar during 30 min at room temperature. During the exposure, the Si 2p spectrum was continuously acquired at $h\nu = 640$ eV and the sample was scanned along x for a z value corresponding to position 1 on the sample scheme Figure 6.10. Then, the chamber was emptied and the Si 2p spectrum was acquired on several points of the surface. Three of them are presented Figure 6.10:

- The spectra acquired on position 1 (this position was exposed directly to the beam during the dosage) presents a huge oxide peak, unusual after TEOS dissociation.
- On position 2 (this position was not hit by the beam during the TEOS exposure), the spectrum contains very small component for the oxide, this spectra is similar to the ones presented in previous sections and chapters and shows what we should expect on the surface after reaction of TEOS in absence of the X-ray beam.

Consequently, scanning the surface during the acquisition is not sufficient, indeed, beam damage occurs rapidly ($t \leq$ spectrum acquisition duration ~ 30 s) (We also observe during our experiments that this phenomenon was significant for a photon energy higher than the O 1s threshold at 530 eV as it is the case here.)

- On position 3, the spectrum contains a component relative to the oxide, smaller than on position 1 but still more significant than for position 2. This position is located 1 mm from position 1 while the beam has a diameter of 100 μm . It means that damages do not occur only where the X-ray beam strikes the surface but that TEOS fragments created by the beam in the gas phase are responsible for the oxidation of the surface on a large area.

The thickness of silicon oxide can be evaluated for positions 1 and 3, using the following equation:

$$\frac{I_{\text{SiO}_2}}{I_{\text{Si}}} = \frac{n_{\text{SiO}_2} \sigma_{\text{SiO}_2} \lambda_{\text{SiO}_2}}{n_{\text{Si}} \sigma_{\text{Si}} \lambda_{\text{Si}}} \left(\exp\left(\frac{d}{\lambda_{\text{SiO}_2}}\right) - 1 \right) = \frac{I_{\infty}}{I_0} \left(\exp\left(\frac{d}{\lambda_{\text{SiO}_2}}\right) - 1 \right) \quad (6.1)$$

where:

- I_{SiO_2} and I_{Si} are the intensity of the oxide and the bulk peak respectively,
- n_{SiO_2} and n_{Si} are the density of silicon atoms of SiO_2 and Si respectively,
- σ_{SiO_2} and σ_{Si} are the atomic photoionization cross sections of SiO_2 and Si respectively,
- λ_{SiO_2} and λ_{Si} are the escape depths of SiO_2 and Si respectively,
- and d the oxide layer thickness.

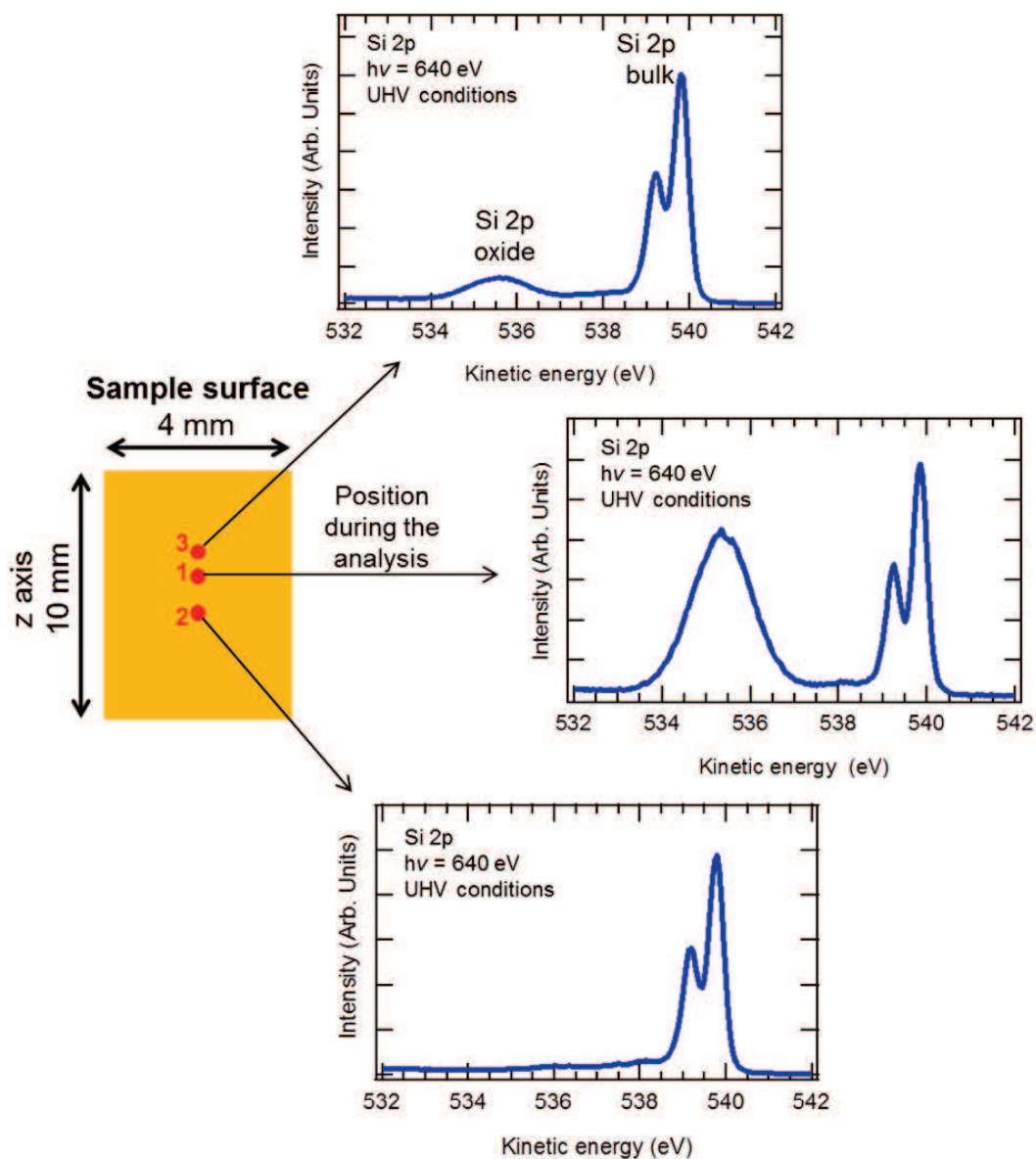


Figure 6.10: Si 2p XPS spectra ($h\nu = 640$ eV) of the water-covered surface (n-doped, $0.003 \Omega \times \text{cm}$) after exposure to TEOS (30 min, $P = 5$ mbar), acquired on several position of the sample.

The values of the different parameters are chosen in agreement with the work of Himpsel et al. [132], $\frac{I_{\infty}}{I_0} = 0.69$ and $\lambda_{SiO_2} = 11 \text{ \AA}$.

For position 1, $\frac{I_{SiO_2}}{I_{Si}} = 1.8$ and gives a value of d equal to 14.2 \AA ; for position 2, $\frac{I_{SiO_2}}{I_{Si}} = 0.23$ and $d = 3.2 \text{ \AA}$.

Second experiment:

The water-covered surface was exposed to a pressure of water of 5 mbar at room temperature. During the exposure the Si 2p spectrum was acquired at $h\nu = 150 \text{ eV}$ using a detuned gap. Figure 6.11 (a) shows the Si 2p spectra obtained in these conditions, the silicon oxide peak is present but small and there is no evolution of its shape with time. The gap was then tuned in order to increase the photon flux, modifications appear immediately as shown Figure 6.11 (b), the oxide peak increases gradually with time relative to the silicon bulk component.

To conclude, the sample analysis, in presence of a gas phase must be done with prudence, damages in the gas phase can not be neglected and may have huge consequences on the surface structure. In particular, we must be aware that damages may be not localized on the scanned area, that low photon flux should be used and that photon energies should be lower than important absorption threshold of elements present into the gas phase.

6.4 Summary

During the first step of the ALD process, we observe mainly the appearance of ethoxy groups and an increase of the fourth oxidation state of silicon due to the dissociation of TEOS on the water-covered Si(001) surface in agreement with the mechanism proposed in Figure 6.2, however it is not possible to determine how many bonds of the TEOS molecule are broken and replaced by a bond with surface hydroxyl groups. During the second step, the expected hydrolysis of the surface ethoxy group does not occur. As NAP-XPS demonstrates that at 2 mbar no liquid water is present on the surface, this

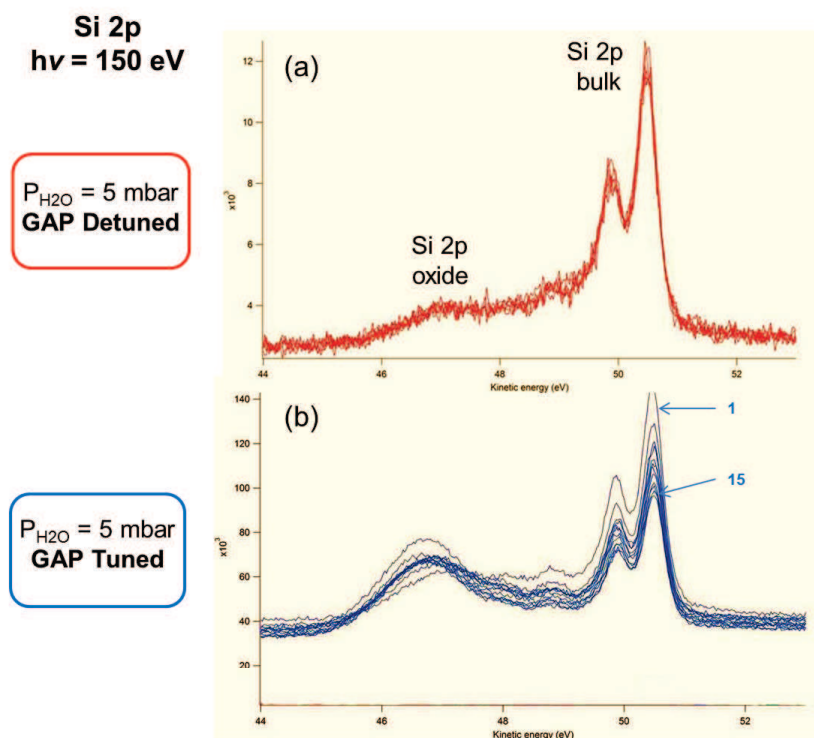


Figure 6.11: Si 2p XPS spectra ($h\nu = 150$ eV) of the water-covered Si(001) surface (n-doped, $0.003 \Omega \times \text{cm}$) during exposition to water $P = 5$ mbar, acquired using (a) a low flux by detuning the gap, (b) a higher flux by tuning the undulator gap.

suggests humidity ratios higher than 10 % should be explored. Nevertheless, the substrate undergoes an oxidation at this RH. It means that, in the present conditions, the direct oxidation of the substrate by water molecules is more favorable than an oxidation mechanism involving the hydrolysis of surface ethoxy groups by the water vapor.

NAP-XPS allows to follow the ALD process in conditions similar to those used in industrial processes. However, we observe that the expected ethoxy group hydrolysis by water molecules does not occur and that direct oxidation of the substrate seems more favorable.

To come closer to industrial conditions, three experiments could be tried:

- the RH, during the second step of the ALD process, should be increased to higher values. To do that, the sample must be cooled down to reduce the water pressure needed for the analysis.

- the temperature, as mentioned in the introduction could be increased to $\sim 700^\circ\text{C}$ during the exposure to gases, the increase of temperature may allow the reaction of water on surface ethoxy groups.
- the use of a catalyst should be tried. Indeed, amine bases can catalyze the SiCl_4 and H_2O reactions during SiO_2 ALD. With the amine base catalyst, the reaction requires much smaller reactant exposures and the reaction temperature can be lowered to ~ 300 K. However, a problem with catalyzed SiO_2 ALD is that the amine catalysts readily react with the HCl reaction product to form a salt. For example, ammonium chloride forms when using NH_3 as the catalyst. Salt formation could be eliminated by using TEOS and would form ethanol instead of HCl and avoid salt formation. [133]

Chapter 7

Ion segregation at liquid water/gas interface

The NAP-XPS set up allows to increase the pressure in the analysis chamber to ~ 20 mbar; it also permits, thanks to the Peltier cooler, to cool down the sample (as described in Chapter 1). In these conditions, solid/gas interface are no longer the only interface that it is possible to investigate. In particular, water droplets can be created in front of the electron analyzer at 283 K and ~ 10 mbar. Therefore, the analysis of their surface is within reach.

In this chapter, we are interested in a particular aspect of the liquid/vapor interface, the behavior of ions at the liquid water surface. We present results obtained on saturated sodium-halide water solutions. For instance, ionic species, present at the surface water droplet, are involved, in key chemical reactions in the troposphere. Chlorine atoms can significantly affect the tropospheric ozone balance in marine atmosphere and react, in atmospheric sea salt particles, with nitrogen oxides. Their behavior into the liquid and the possible interactions with the gas phase at the liquid surface need to be understood.[17]

The structure and chemistry of liquid water/air interface is, therefore, a topic of fundamental interest. Many questions remain open. How are ions distributed? How do the water molecules rearrange at the water/vapor interface? Are anions and cations separated at the interface? What are the conditions for the formation of an electric double layer? How are ions accommodated in the solvent network, and what is the range of influence on the water network?

7.1 The liquid water/ vapor interface

7.1.1 Liquid water surface structure

To understand the behavior of ions near the liquid water surface, we need first to look at its own structure. Indeed, the vapor/water interface has properties different from that of the bulk. Its structure was investigated using dedicated surface-sensitive techniques and molecular dynamics studies which will be briefly discussed in this section.

An early infrared-visible SFG study [134] concluded that 20 % of the surface molecules are orientated with one free OH bond pointing out of the liquid, at about 38° relative to the surface. The second OH extending into the bulk, is involved in an hydrogen bond. In this configuration, the permanent water dipoles are nearly contained within the surface plane which is consistent with the very small surface potential of water. [135]

More recent Vibrational Sum-Frequency Generation (VSFG) work indicates the presence of several types of species, at different depths. [136], [137] The topmost one is similar to the one previously mentioned. The other type of interfacial species are assumed to be completely surrounded by other water molecules (although not necessarily fully symmetrically tetrahedrally bonded), and are located a few angstroms from the top of the surface. [136], [137]

A slightly different picture of water surface arises from XAS studies [138]. An additional interfacial water species was identified, the "acceptor-only" configuration, where both OH bonds are directed towards the vacuum, and both electron lone pairs act as a hydrogen-bond donor, in agreement with ab-initio molecular dynamic studies by Kuo and Mundy.[139].

Photoelectron spectroscopy (PES) studies, using the liquid-water microjet technique, were reported for valence [140] and core [141] electron emission. Ref. [140] discusses the energy shifts and the broadening of the valence orbitals with respect to the gas phase when using 60-120 eV photon energies. A shift of about 1.4 eV is observed between the water vapor peak and the liquid one due to an increase of the relaxation

energy in the liquid. Indeed, the screening contribution of the core-hole between the gas and the liquid phase is modified by an increase of the relative permittivity. The peak broadening is related to the statistical distribution of H-bonding configurations in the liquid.

The inner-shell PES [141] uses photon energies up to 1200 eV to probe the water O 1s core photoelectron emission. Depending on the photon wavelength the electrons are emitted either predominantly from H₂O molecules at the surface or in bulk water, corresponding to about 6 Å or 20 Å probing depths. O 1s electron BE are identical in the two cases, equal to 538.1 eV, but a small additional peak at 536.6 eV appears when probing more in depth. The 536.6 eV peak was assigned to distorted tetrahedral configurations with an elongated hydrogen bond at one of the H-accepting sites.[141]

7.1.2 Ions behavior at liquid water/ vapor interface

The traditional view of electrolytes surfaces is essentially an ion-free surface and is similar to the surface of neat water. However molecular simulations [142] and various spectroscopic techniques [140], [143], [144], [145] show a very different picture of these electrolytes surfaces. They suppose a segregation of ions to the surface. Small hard ions, such as alkali cations are repelled from the aqueous surface while large polarizable anions can be found (and even enhanced) at the surface.

Indeed, ions can be divided into two classes, kosmotropes and chaotropes, based on their binding strength with water molecules and their effect on water molecules organization. Generally, ionic behavior parallels the Hofmeister series which is a qualitative ordering of ions based originally on their propensity to salt-out proteins from aqueous solution.[146] Large, polarizable, singly charged ions, with low charge density are chaotropes (for example, SCN⁻, I⁻, Cl⁻, NO₃⁻, NH₄⁺, Cs⁺, K⁺ ions). They exhibit weaker interactions with water than water with itself and thus they interfere little in the hydrogen bonding of the surrounding water. Small or multiply-charged ions, with high charge density, are kosmotropes (for example, SO₄²⁻, Mg²⁺, Ca²⁺, Li⁺, Na⁺, H⁺, OH⁻ ions). They create stronger interactions with water molecules than water with itself

and therefore are able to break water-water hydrogen bonds. Therefore, kosmotropes remain hydrated near the water surface, while chaotropes lose their hydration sheath [147].

In this chapter, we will focus on sodium halide salts behavior in water solution. Na^+ is kosmotrope, it should create interactions with water and find its place into the water molecules network. Cl^- , Br^- and I^- are chaotropes, furthermore their polarizability increases from Cl^- to I^- which may turn interactions with water increasingly difficult.

The results of MD slab simulations of 1.2 M aqueous solutions of the sodium halide series are presented Figure 7.1.[145], [148] In NaF solution, both ions are repelled from the air/water interface, leaving an almost ion-free top layer while chloride penetrates all the way to the interface and bromide and iodide even exhibit a surface concentration peak followed by subsurface depletion. Anions in the topmost layer are not completely solvated, but they do maintain a substantial solvation shell. They showed that in terms of getting an anion to the surface of a solution, polarizability seems to be the most important factor. The surface neutrality requires that for the more polarizable halide solutions, the sodium cations are dragged by the anions toward the interface and, consequently, exhibit a subsurface peak.

Liu et al. used vibrational sum frequency generation spectroscopy (SFG) to examine the liquid/vapor interface of sodium halide solutions and their results indicated that water structure at the interface of sodium bromide or sodium iodide is distorted more strongly than that of sodium chloride or sodium fluoride, suggesting that the role of halide anions at the interface increases with respect to increasing size and polarizability.[149]

The surface activity of the heavier halogen anions was the subject of several recent photoelectron spectroscopic studies. Weber et al. reported valence band photoemission data on liquid microjets of alkali metal iodide solutions spanning a wide range of concentration (0.5-12 M).[143] Their data were consistent with a surface excess of the anion for NaI, but only one component is observed on the spectrum of all anions and no cation selectivity is shown. The absence of chloride and bromide enhancement on the surface

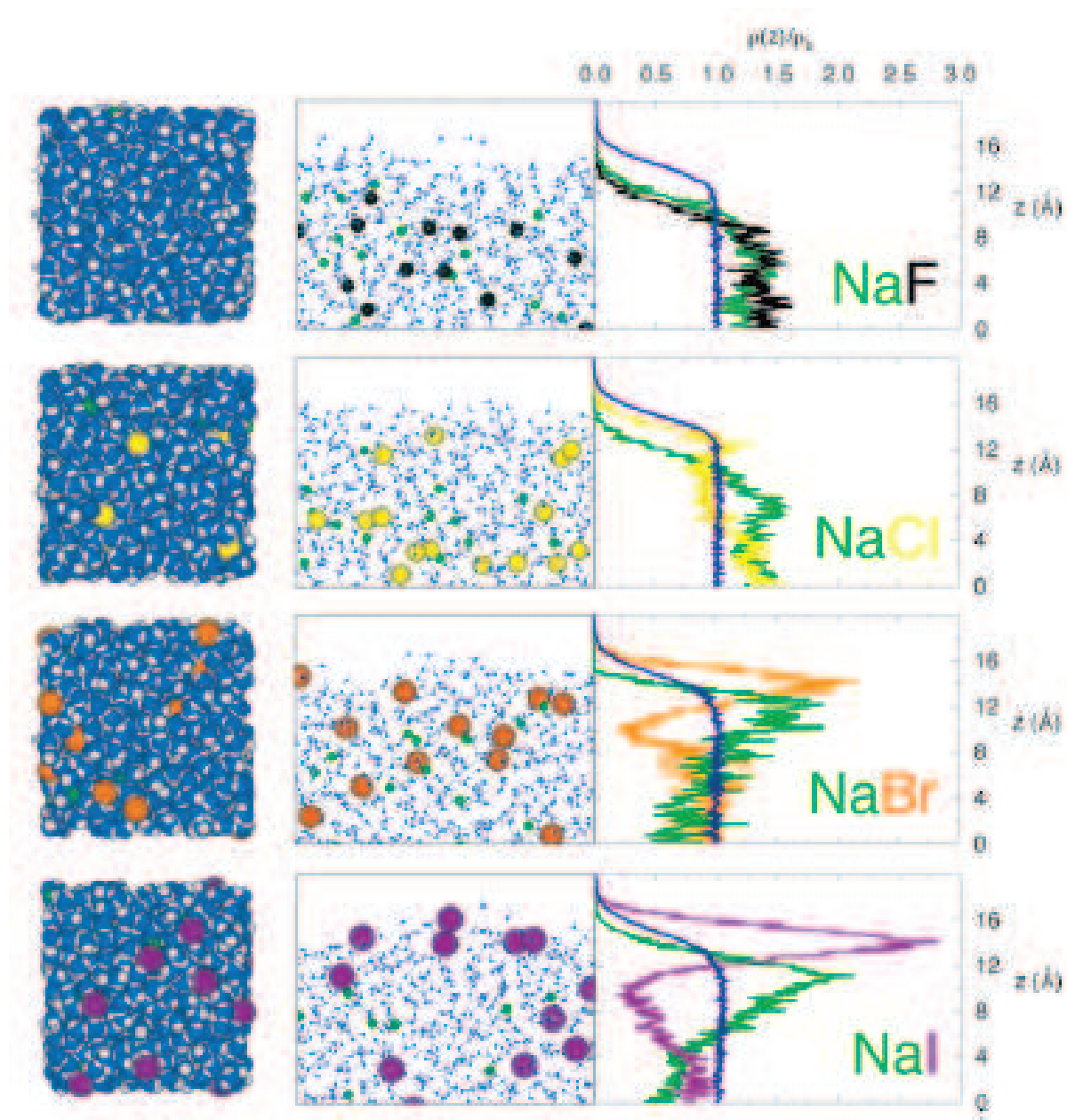


Figure 7.1: Snapshots (top and side views) of the solution/air interfaces of 1.2 M aqueous sodium halides from the molecular dynamics simulations and density profiles (number densities) of water oxygen atoms and ions plotted vs distance from the center of the slabs in the direction normal to the interface, normalized by the bulk water density.[145]

appears to contradict the predictions of MD simulations.[150]

Using X-ray photoelectron spectroscopy operating at near ambient pressure, Ghosal

et al. measured the composition of the liquid/vapor interface for deliquesced samples of potassium bromide and potassium iodide.[151] In both cases, the surface composition of the saturated solution is enhanced in the halide anion compared with the bulk of the solution. The enhancement of anion concentration is more dramatic for the larger, more polarizable iodide anion. Cheng et al. also presented the Br 3d and Cl 2p XPS spectra for saturated solutions in surface and bulk sensitive conditions, two components are observed and attributed to symmetric solvation in the bulk and asymmetric solvation of the anion on the water surface. Only one peak is observed for the cation.[152] However, its behavior relative to anion segregation is not investigated; how are cations distributed below the surface to compensate the negative charge induced by anion segregation?

7.2 NAP-XPS analysis of the water surface: the ions behavior

7.2.1 Analysis conditions

Salts of high purity (99.9% – 99.999%) purchased from Sigma-Aldrich were used. NaCl and NaBr salts were roasted overnight before using them. A saturated salt solution was prepared with ultra pure water ($18\text{ M}\Omega \times \text{cm}$). Samples were, then, prepared by evaporation of the saturated salt water solution on a gold coated silicon surface. XPS measurements were performed between 278 K and 283 K and at a pressure between 8 mbar and 12 mbar, corresponding to $\text{RH} = 100\%$ ($P_{\text{sat}}(\text{water}) = 12\text{ mbar}$ at 283 K)

Lowering the temperature of the sample was achieved by using a circulating chiller and a Peltier block attached to the sample holder. The salt solution on the sample surface could be visually observed, as shown Figure 7.2. Because the sample surface is the lowest temperature point in the sample chamber and that salts are hygroscopic, water vapor condenses on the salt first. (The concentration of saturated NaCl, NaBr and NaI solutions are of 35.8 g/100mL (6.1 mol/L), 85.2 g/100mL (8.2 mol/L) and 170 g/100mL (11.3 mol/L) respectively at 283 K.)

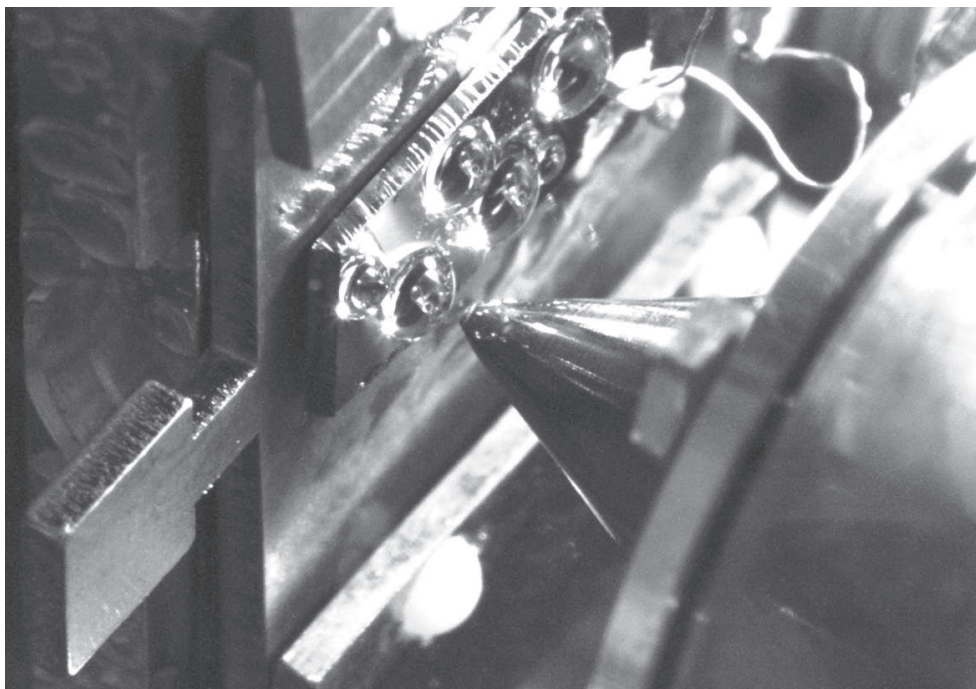


Figure 7.2: Water droplets on the gold coated silicon surface in the analysis chamber during the acquisition (RH = 95 %, P = 12 mbar, T = 283 K).

For XPS measurement, the Au 4f peak was used as an energy reference. Indeed, no charge effects are observed on the water droplet which can be explained by the low resistance of the salt saturated solution. For example, a saturated sodium chloride solution has a resistivity of $\sim 5 \Omega \times cm$. [153]

7.2.2 Carbon contamination

Carbon contamination is a recurring problem in the analysis of this type of sample. Organic molecules may come from the gold surface or the salt despite the fact that they were cleaned before use or from the chamber walls and the gas line.

Overall, the carbon contamination induces a C 1s XPS spectrum similar to the one presented in Figure 7.3 (b) and (c) which correspond to the C 1s spectrum of NaBr and NaI solutions taken at $h\nu = 500$ eV. The spectra are constituted by two peaks, a main one at ~ 284.8 eV associated to alkyl chains and a second one at ~ 286.2 eV corresponding

to $\sim 15\%$ of the spectral weight.

However, for the NaCl solution, we obtained a very different C 1s spectrum (see Figure 7.3 (a)). It contains components at high BE that can be associated to carboxylic acids. We suppose that this contamination comes from the salt as Aldrich uses organic molecules to purify it. To clean it, the salt was roasted before use but it was not enough to purify it entirely.

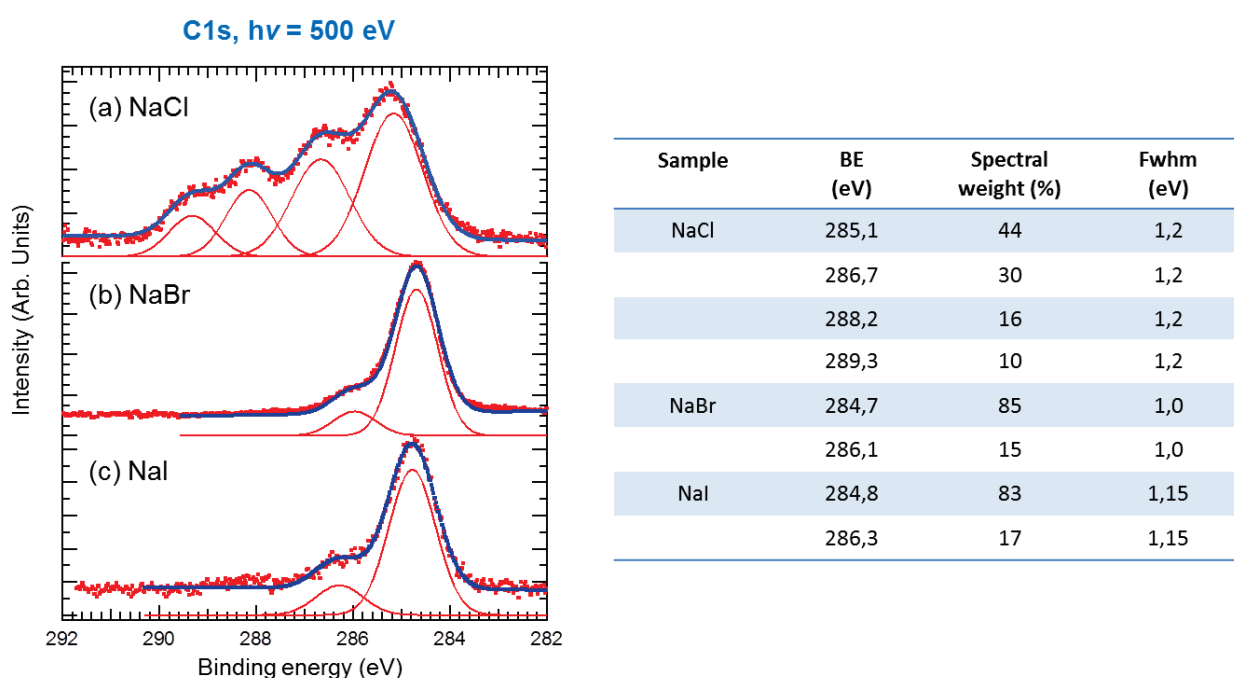


Figure 7.3: C 1s XPS spectra of saturated sodium chloride, sodium bromide and sodium iodide solutions surfaces measured with a photon energy of 500 eV at RH = 95 % ($P = 8$ mbar, $T = 278$ K). The BE is referenced with respect to Fermi level measured on the gold substrate.

7.2.3 Cation behavior

If the behavior of the anion near the surface is known, there are still interrogations about the position of the counterion. Molecular dynamics shows that a cation plane should be present below the anion one near the liquid surface (see Figure 7.1).[145]

Thanks to the surface sensitivity of XPS, it is possible to investigate precisely the behavior of the cation in saturated salt solutions.

We acquired the Na 2s XPS spectra for the three saturated salt solutions. They are presented for two different photon energies in Figure 7.4. For each solution, one spectrum is acquired at a photon energy of 1200 eV corresponding to bulk sensitive conditions ($E_k \approx 1140$ eV, $\lambda \approx 40$ Å) and one at 360 eV to surface sensitive conditions ($E_k \approx 300$ eV, $\lambda \approx 12$ Å).[149] The Na 2s BE is measured at 63.15 eV for all samples and for both photon energies, showing that the nature of the anion does not have influence on the Na 2s BE. The spectra are constituted by only one component attributed to the cation in a spherical solvation state into the bulk; therefore, no sodium cation is localized on the liquid water surface in direct interaction with the gas phase (it would induce the apparition of a second peak at higher energy similar to the one observe in the case of the anion as it will be discussed in the next section).

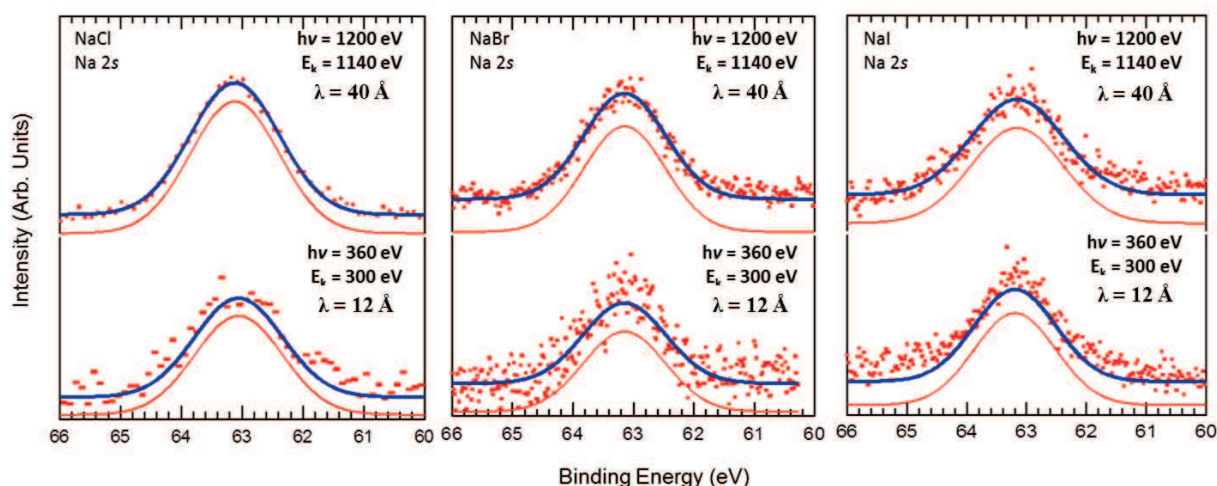


Figure 7.4: Na 2s XPS spectra of saturated sodium chloride, sodium bromide and sodium iodide solutions surfaces measured with a photon energy of 1200 eV and 360 eV at RH = 95 % (P = 8 mbar, T = 278 K). The BE is referenced with respect to Fermi level measured on the gold substrate.

For each electron KE, a probing depth is given in Figure 7.4. However, the evaluation of the probed thickness as a function of the electron KE is a sensitive issue. The inelastic mean free path (IMFP), which is the distance that photoelectrons travel before

they lose energy from inelastic collisions, depends upon the KE of the photoelectron: photoelectrons with higher KE can reach the detector from deeper in solution than photoelectrons with lower KE. However, the relation between the absolute IMFP values and photoelectron KE in aqueous solutions is still a subject of on-going current research and, for the analysis of aqueous solution surface, a source of error in the determination of concentration profiles from XPS data. At present, minimum IMFP range values for liquid water are accessible by calculation only. A minimum for the IMFP curve as a function of photoelectron KE is observed near 1.2 nm when different theoretical models are applied as shown in Figure 7.5. [149], [154], [155]

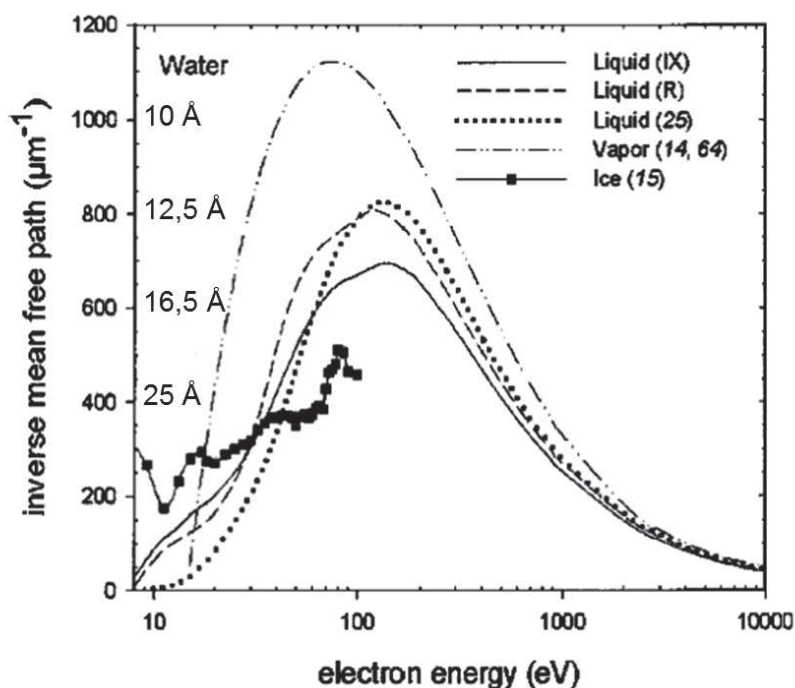


Figure 7.5: Inelastic inverse mean free path of electrons in water in different phases calculated using different theoretical models. The squares are experimental data for amorphous ice.[155]

The Na 2p core-level was also investigated for the three saturated salt solutions. The Na 2p core-level is closed to the O 2s one; however, the O 2s peak contains two contributions, one from the gas phase and one from the liquid phase. In order to separate these two peaks, the sample was polarized of 40 eV as illustrated for NaI sample in figure 7.6. The polarization of the sample induces an increase of of 40 eV of the ki-

netic energy of all photoelectrons coming from the sample surface (which confirms the absence of charge effect at the solution surface) and allows to exclude the O 2s peak of the vapor from the acquisition window.

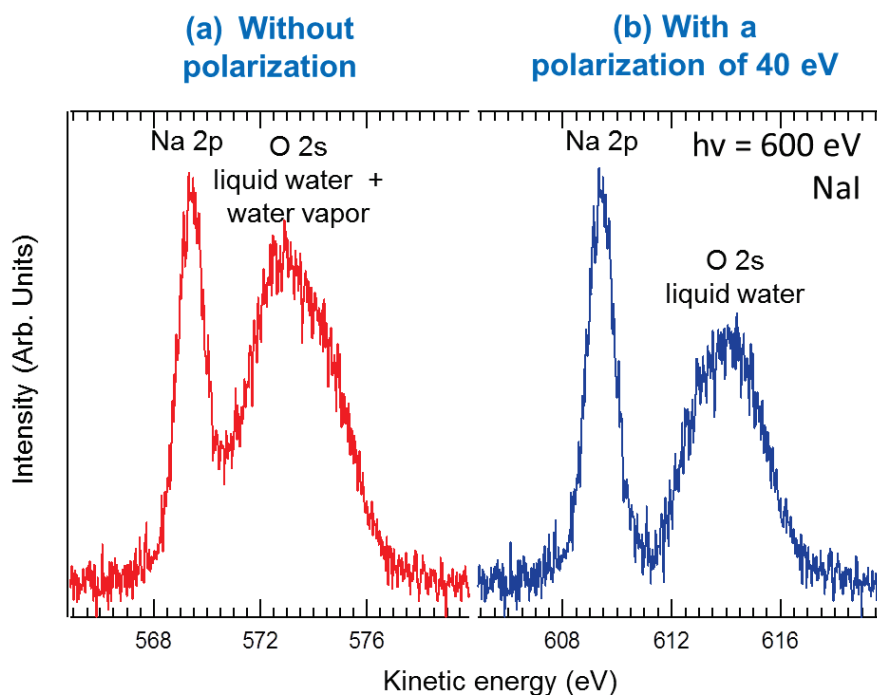


Figure 7.6: Na 2p and O 2s XPS spectra of a saturated sodium iodide solution surface measured at $h\nu = 600$ eV (a) in the absence of polarization (b) with a polarization of 40 eV at RH = 95 % (P = 8 mbar, T = 278 K).

The Na 2p and O 2s spectra of the NaI are presented in Figure 7.7 sample for different photon energies and with a polarization of 40 eV. The Na 2p position is measured at a BE of 30.7 eV, its position remains constant, with depth, similarly to the Na 2s. The O 2s peak corresponding only to liquid water has a BE of 25.8 eV. Na 2p core-level is interesting due to its proximity with the O 2s core-level (BE = 26 eV). The advantage of this situation is that photoelectron coming from both core-hole have the same kinetic energy and will suffer the same attenuation by the gas phase; therefore, their intensity can be directly compared after correction by the cross section. Indeed, cross section decrease dramatically between photon energies from 200 and 1200 eV, O 2s and Na 2p cross section evolution are presented Figure 7.8.

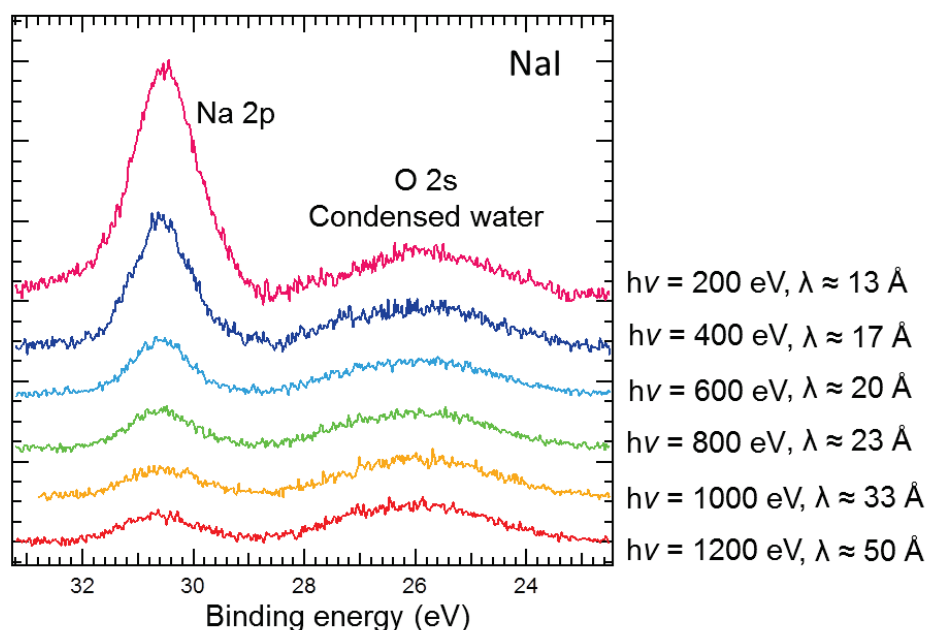


Figure 7.7: Na 2p and O 2s XPS spectra of a saturated sodium iodide solution surface measured at several photon energies with a polarization of 40 eV at RH = 95 % ($P = 8$ mbar, $T = 278$ K). The BE is referenced with respect to Fermi level measured on the gold substrate.

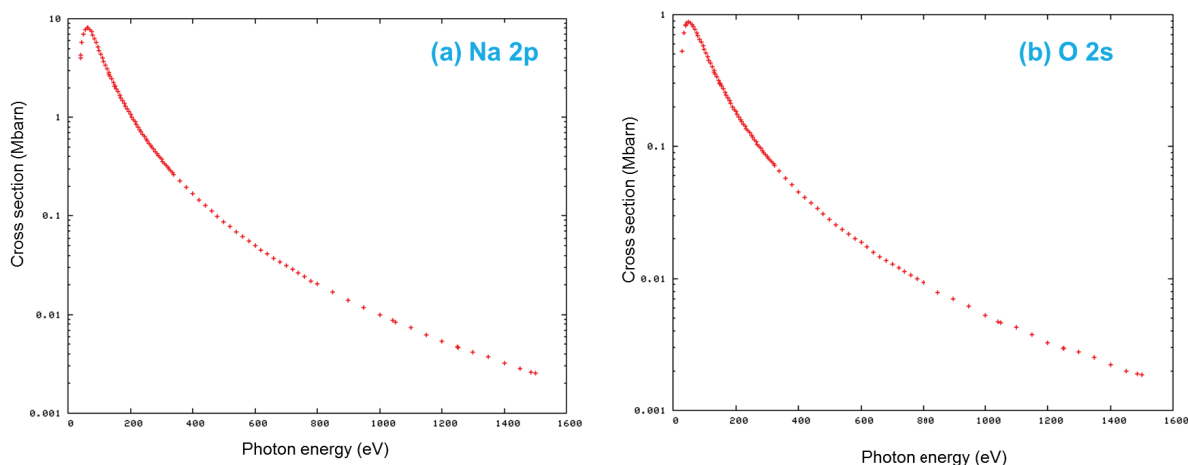


Figure 7.8: Atomic calculation of cross section for (a) Na 2p and (b) O 2s as a function of photon energy.[156]

The evolution of the ratio between Na 2p peak area and O 2s peak area after the correction by the cross sections is presented in Figure 7.9 for the three salts. These ratios

are given as a function of the photoelectron KE which is characteristic of the probed depth. The ratio between Na 2s and O 2s peak area, corrected by cross sections, was also calculated in order to verify the accuracy of the cross section values. The same ratio was obtained ($\Delta(\text{Na}/\text{O ratio}) \leq 0.03$).

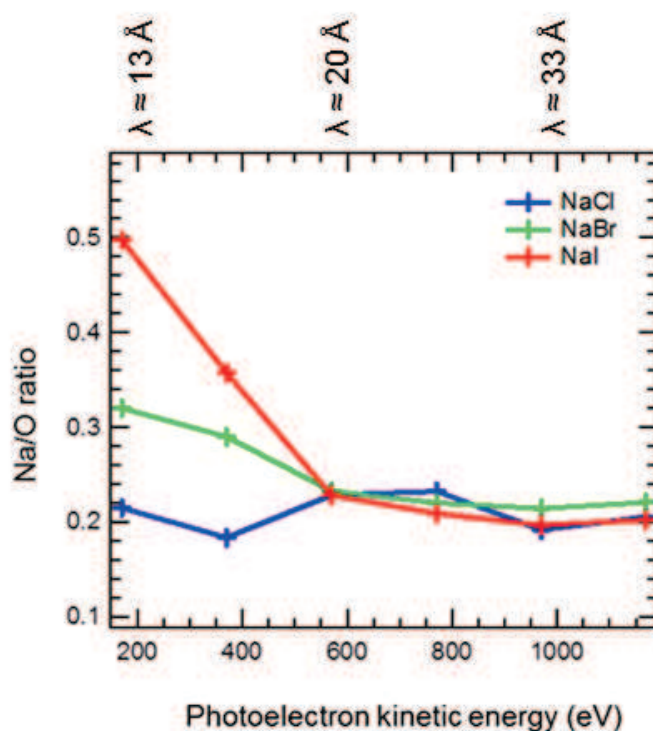


Figure 7.9: Na/O ratio as a function of depth after correction by the cross sections.

The depth profiles show that for NaCl, the concentration of Na relative to water is constant with depth. This is in agreement with density profiles presented Figure 7.1; for NaCl, the curve of the sodium follows the oxygen one. For NaBr and NaI, the behavior is different, the ratio with oxygen increases close to the surface, specially for NaI for which this ratio is multiplied by two between the bulk and the surface. These observations are in agreement with theoretical simulations which suppose the presence of an cation plan just below the surface. However, this is the first time that it is proved by an experimental measurement.

7.2.4 Anion behavior

The anion behavior analysis and more precisely the anion/cation ratio as a function of depth was already investigated for alkali halides, [143], [143], [157], [151] and will be discussed in this section.

The first spectra, presented in this section Figure 7.10, shows the valence band of the three saturated salt solutions acquired for $h\nu = 500$ eV. The energetic positions of the characteristic water valence orbitals are marked at the top of the Figure. The narrow-width gas phase b1 (denoted b1gas) line appears at a BE of 7.6 eV, about 1.6-2 eV below the broad liquid water b1 (HOMO) line which is found at ~ 5.8 eV below the Fermi level. Anion related features are found above the liquid water HOMO.[149] The I 5p appears as a doublet at 2.6 and 3.4 eV. Br 4p is seen at about 4.1 eV, and Cl 3p at 4.9 eV. The intensity of these peak relative to oxygen peaks present in the valence band confirms the high concentration of salt into the solution.

Figure 7.11 presents Cl 2p and I 4d XPS spectra of sodium chloride and sodium iodide solutions. In fact the 2p and 4d core-levels are spin-orbit split doublets, the energy difference between Cl $2p_{3/2}$ and Cl $2p_{1/2}$ is of 1.6 eV and between I $4d_{5/2}$ and I $4d_{3/2}$ of 1.7 eV [158]. For both solutions, two doublets are necessary to fit the spectra properly, in agreement with the findings of Cheng et al..[151] The majority species (Cl $2p_{3/2}$ at 197.6 eV and I $4d_{5/2}$ at 49.0 eV) are attributed to anions in bulk water with a symmetrical solvation shell. The minority species found at higher BE (Cl $2p_{3/2}$ at 199.8 eV and I $4d_{5/2}$ at 50.6 eV) is assigned to anions having an asymmetrical solvation shell (i.e. surface anions). It can be expected that the relaxation energy is smaller for the anions at the very surface than for those in the bulk (shift of ~ 1.5 eV).[151] Both core-levels spectra are presented for two different photon energies, one sensitive to the bulk ($E_k \approx 1100$ eV, $\lambda \approx 40$ Å) and one in surface sensitive conditions ($E_k \approx 300$ eV, $\lambda \approx 12$ Å). In bulk sensitive conditions, the component at higher energy has almost disappeared while in surface sensitive conditions the ratio between the high energy peak area and the low energy peak area is of 0.54 in both cases. It confirms the presence of anions on the surface while only one cation environment attributed to the entirely solvated situation is

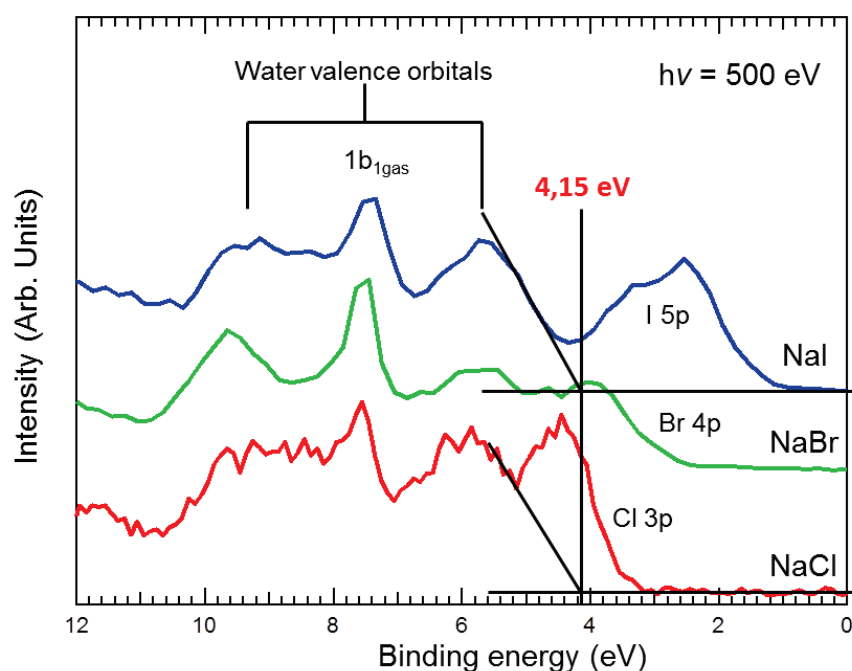


Figure 7.10: Valence band of the three saturated salt solutions measured at $h\nu = 500$ eV at RH = 95 % ($P = 8$ mbar, $T = 278$ K). The BE is referenced with respect to Fermi level measured on the gold substrate.

observed.

A second interpretation of the two observed peaks must be considered. Due to the presence of organic molecules on the surface, as demonstrated in a previous section by the analysis of the C 1s spectrum, the peak at high energy may be attributed to an anion not only surrounded by water molecules but also by organic ones close to the surface. Figure 7.12 presents the Cl 2p and C 1s spectra acquired at $h\nu = 500$ eV for three different saturated NaCl solutions prepared in the same manner but containing, at the end, different quantities of carbon. The shape of the Cl 2p remains the same between these three different samples and seems independent of the carbon one; however, the carbon contamination amount are not very different between the three samples.

The Br 3d XPS spectra are also presented in Figure 7.13 and 7.14. Figure 7.13 shows the five scans of the Br 3d XPS spectrum acquired at $h\nu = 200$ eV, a significant decrease of the peak intensity with time is observed. The shape of the spectrum is also modified,

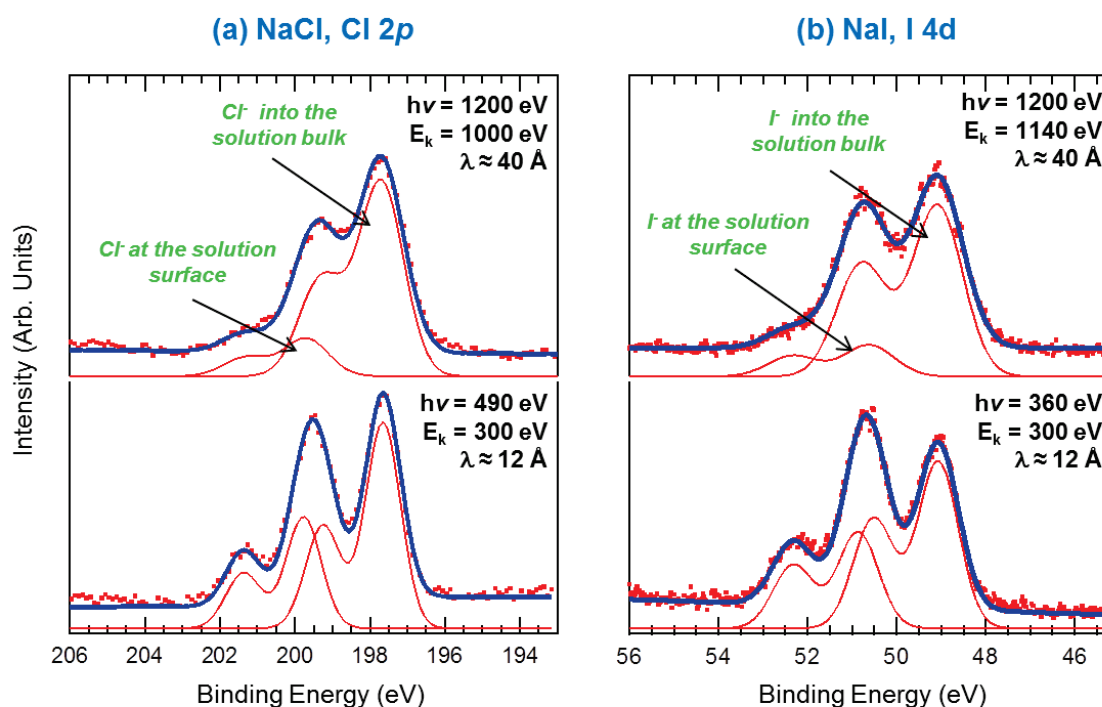


Figure 7.11: (a) Cl 2p spectra of a saturated NaCl solution surface and (b) I 4d spectra of a saturated NaI solution surface measured with two photon energies at RH = 95 % ($P = 8$ mbar, $T = 278$ K). The BE is referenced with respect to Fermi level measured on the gold substrate.

the five scans are fitted in Figure 7.14. 3d core-level is spin-orbit split doublet, the energy difference between Br $3d_{5/2}$ and Br $3d_{3/2}$ is of 1.05 eV. [158] On the first scan, the peak corresponding to the surface bromine represents 2.5 times the area of the bulk peak, then this ratio decreases with time to reach a value of 0.5 after ~ 120 s. These observations are in agreement with an extraction of surface bromide by the photon beam.

The loss of halides in dry conditions has already been observed under X-ray irradiation; defects, such as anion vacancies, interstitials and color center in alkali halide may be created.[159], [160], [161] Further experiments, using bulk crystals in presence of water vapor have reported an anion/cation average ratio of about 0.85 (for RHs below the deliquescence point).[150] In particular, the work of Arima et al. [143] described significant damages at the surface of a potassium bromide surface in presence of water. An important decrease of the Br 3d peak intensity as a function of exposure time to the

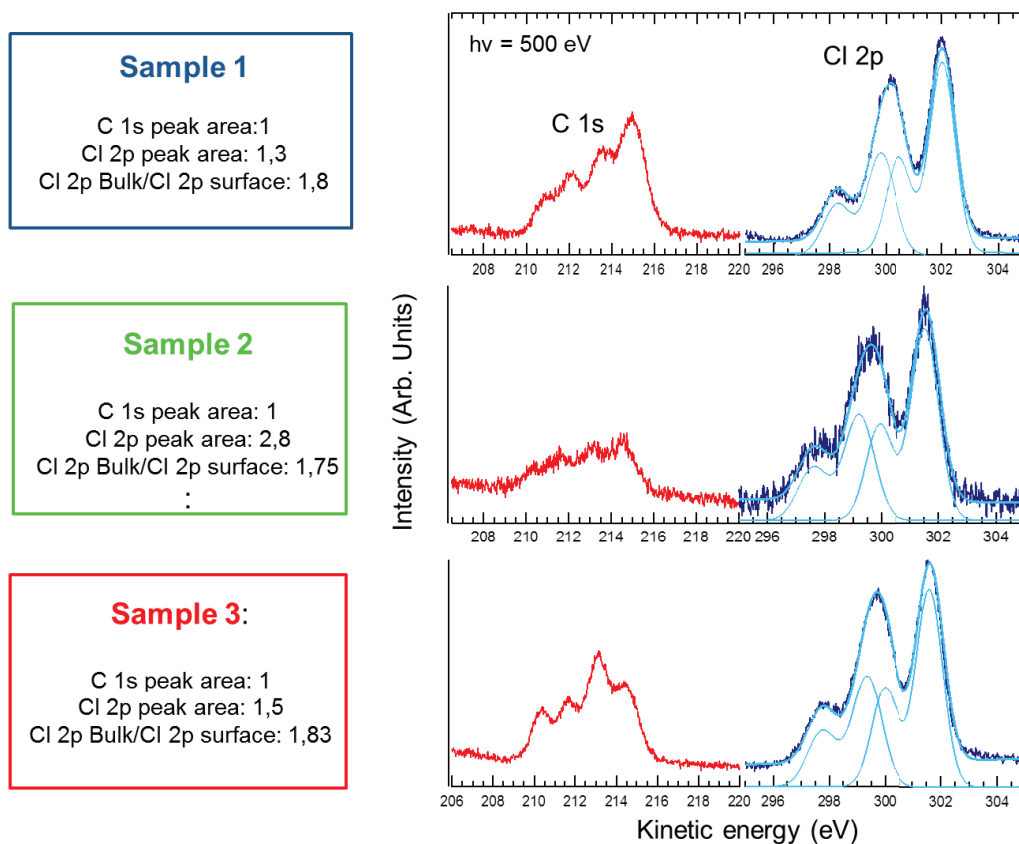


Figure 7.12: C 1s and Cl 2p spectra of three different sodium chloride solutions prepared in the same manner, measured for $h\nu = 500$ eV at RH = 95 % ($P = 8$ mbar, $T = 278$ K).

X-ray beam is presented in reference [143] and the measured Br/Na ratio presents important variation when RH increases. It reaches a minimum of 0.2 for RH = 80 % and then increases to achieve almost 1 at RH = 100 %. The apparently lower loss of Br at higher humidity values is interpreted by an increased mobility of solvated Br^- , which partially refills the irradiated spot by diffusing from the surrounding areas. Beam damage was found to be negligible for other elements, particularly for the counterion.

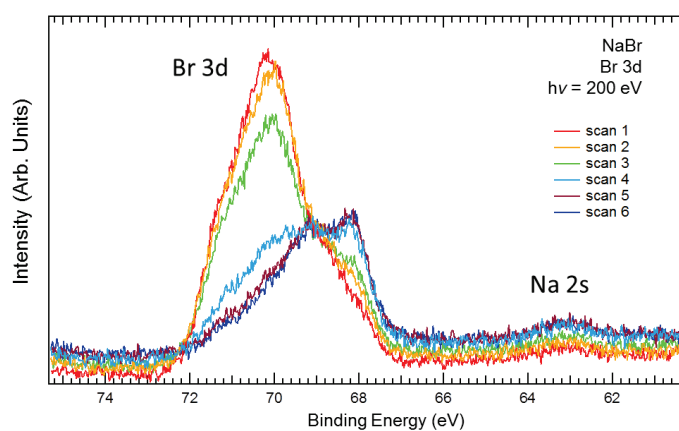


Figure 7.13: Br 3d spectrum evolution with time measured for $h\nu = 200$ eV at RH = 95 % ($P = 8$ mbar, $T = 278$ K). The BE is referenced with respect to Fermi level measured on the gold substrate.

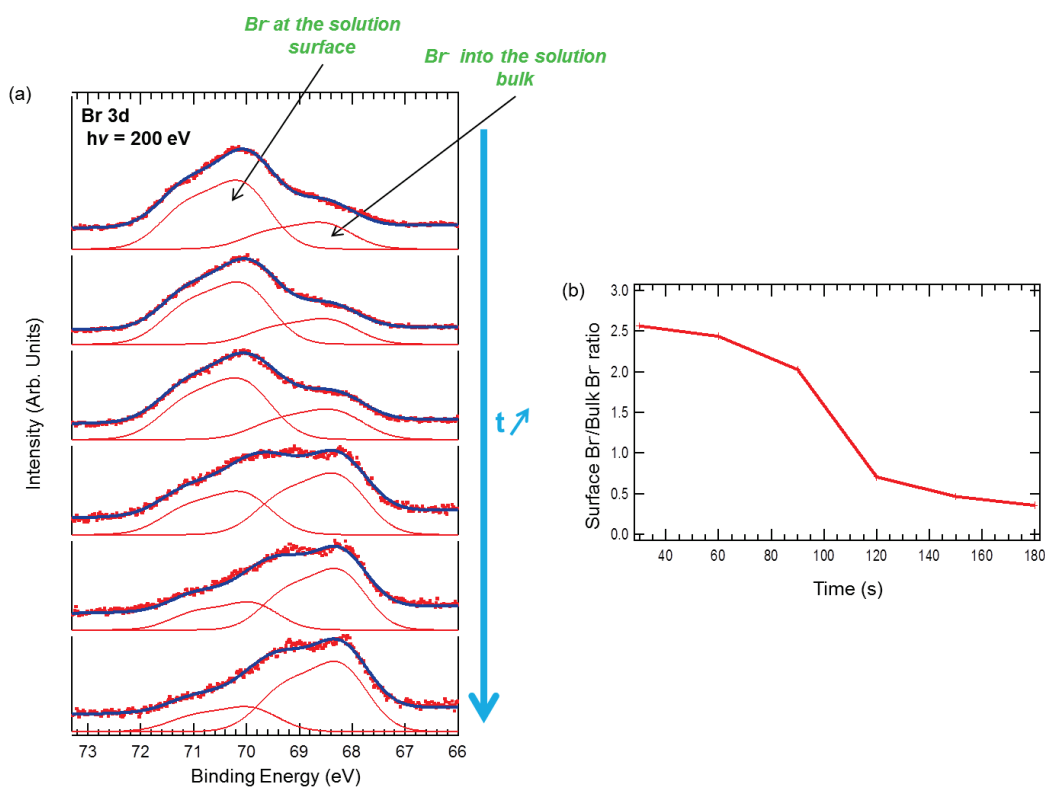


Figure 7.14: Br 3d spectrum fit evolution with time measured for $h\nu = 200$ eV at RH = 95 % ($P = 8$ mbar, $T = 278$ K). The BE is referenced with respect to Fermi level measured on the gold substrate.

This damage can be due to photochemical reactions involving water molecules. Soft X-ray photons can decompose water molecules in the gas phase or at the surface layer to create radicals, such as hydroxyl $\text{OH}\cdot$, atomic oxygen $\text{O}\cdot$, and hydroperoxyl $\text{O}_2\text{H}\cdot$ which may oxidize aqueous anions to form molecular dianion, [162], [163] and desorbs from the sample. This phenomenon may be significant in our experiment due to the high water vapor pressure present in the chamber (~ 10 mbar compared to ~ 1 mbar in reference [143], [150], [151])

To evaluate the anion segregation near the surface, we attempt to determine the anion/cation ratio as a function of depth. Due to the shape and intensity evolution of the Br 3d with time, it was impossible to determine this ratio for NaBr solutions. However, Figure 7.16 shows the I/Na ratio determined from the peak areas of I 4d and Na 2s spectra as a function of RH. Both peak are present on the same spectra and emitted electron have a similar KE, measured areas are corrected by cross sections (the cross section evolutions as a function of photon energy for I 4d and Na 2s are given Figure 7.15). The I/Na ratio is found to be constant and equal to 0.6 which means that, for the minimum depth region we are able to probe (~ 17 Å) the behavior of the anion is similar to the one of the cation.

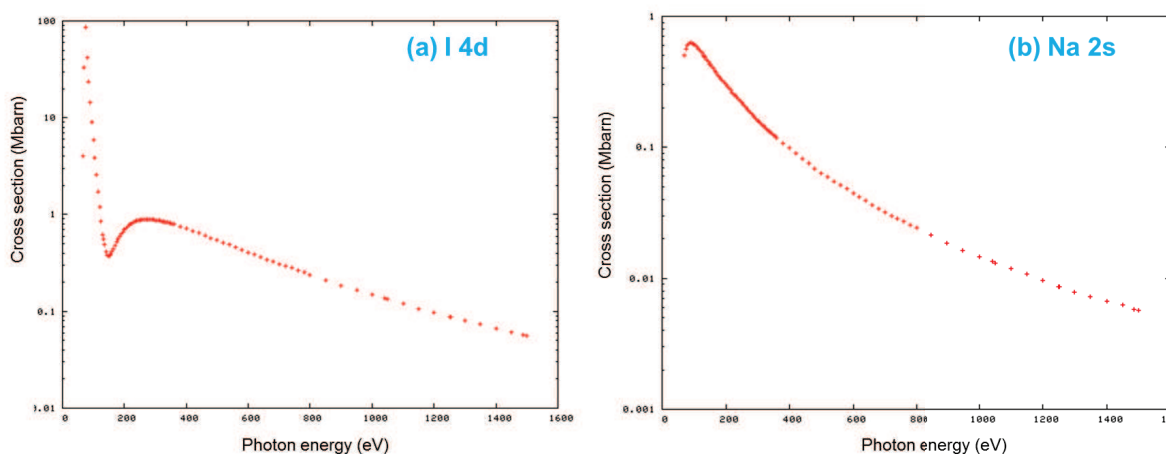


Figure 7.15: Atomic calculation of cross section for (a) I 4d and (b) Na 2s as a function of photon energy.[156]

The ratio value is lower than the stoichiometric ratio of 1.0. A possible explanation

for the larger deviations from the expected value in the present experiments is a loss of I atoms due to beam damage at the solution surface as already guessed for the NaBr solution. However, the difference with stoichiometric ratio is small and the difference can also be attributed to the imprecision of the cross sections used for the ratio calculation.

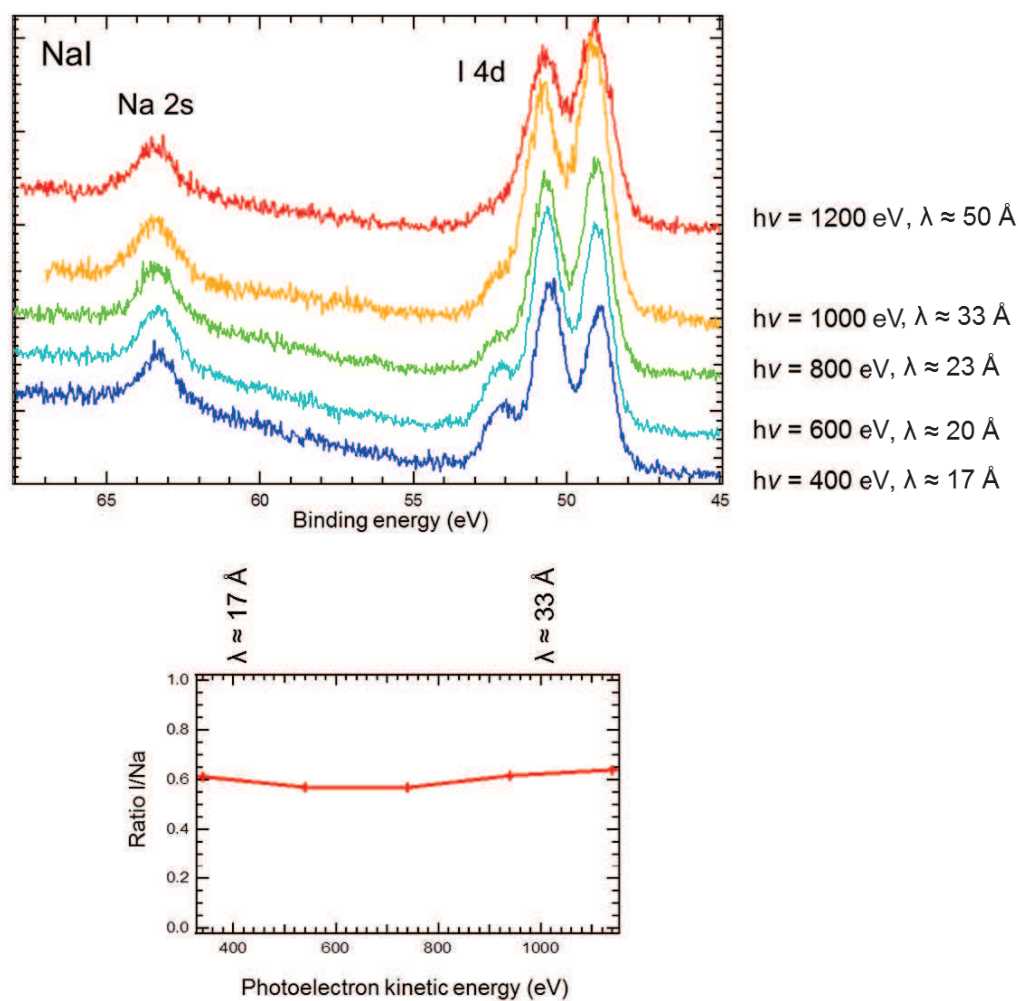


Figure 7.16: (a) Na 2s and I 4d XPS spectra of a saturated sodium iodide solution surface measured with several photon energies at RH = 95 % (P = 8 mbar, T = 278 K). The BE is referenced with respect to Fermi level measured on the gold substrate. (b) I/Na ratio as a function of depth after correction by the cross sections.

7.3 Work function measurements and electronic level diagrams

The fundamental characteristic of our set up, with respect to liquid jet experiments, is the fact that the conductive electrolyte solution is connected to the ground via the gold electrode. No charging effects are observed, and we expect the alignment of the Fermi levels of the gold substrate and of the electrolyte. This permits the measurement of the valence band energy levels (in particular the HOMO of liquid water) referenced to the Fermi level.

As the sample can be polarized with respect to the ground, the work function can be measured via the KE cutoff of the secondary electron (i.e. the electrons with the slowest energy escaping from the liquid surface). Adding together the BE and the work function, we obtain the vertical ionization potentials (IP) of the valence level of liquid water and solutes core-levels (Na 2s, Cl 2p, Br 3d, I 4d).

7.3.1 Measurement of the secondary electron cutoff and determination of the work function

By polarizing the sample by a negative voltage V_{bias} , we increase the KE of the photoelectrons by $+e |V_{bias}|$ ($e > 0$) entering into the analyzer. The bias is used to increase the energy of the photoelectrons above the vacuum level of the analyzer and to get a better separation of the secondary electrons of liquid water from the background due to the gas phase.

Knowing the exact photon energy $h\nu$, the KE of the cutoff, and the KE of the gold Fermi level E_K^F (pushed up in energy by $e |V_{bias}|$) one obtains the work function $WF = h\nu - (E_K^F - E_K^{cutoff})$. The procedure is illustrated by the NaBr solution case, see Figure 7.17. V_{bias} was measured precisely (40.1 eV) via the KE change (polarized vs non-polarized) of the halogen core-levels. The photon energy was measured by making the difference between the 2nd and 1st order of Au 4f kinetic energies ($h\nu = 500$ eV).

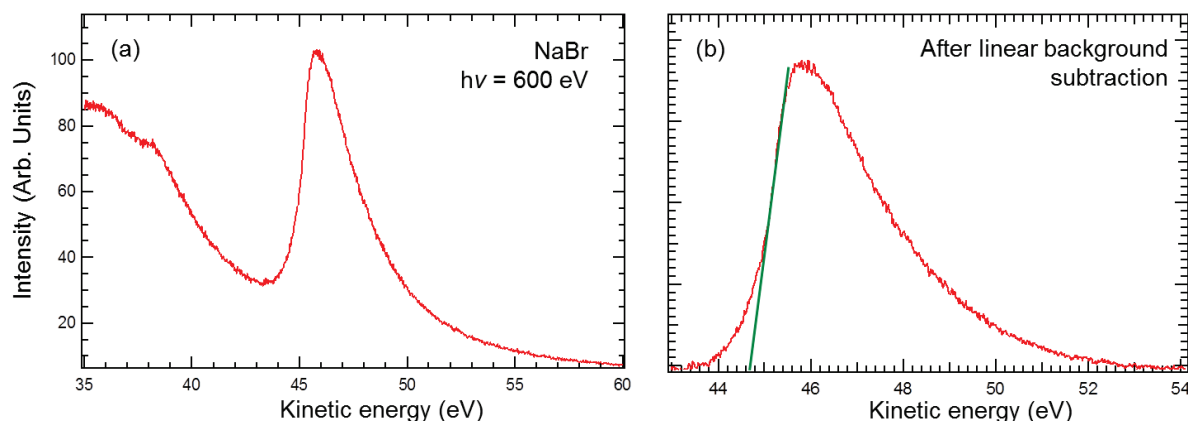


Figure 7.17: Secondary electron cut off measured at $h\nu = 500$ eV for the saturated NaBr solution with a polarization of 40 eV at RH = 95 % ($P = 8$ mbar, $T = 278$ K). (a) raw data spectrum, (b) spectrum after subtraction of a background.

The cutoff of the secondary electrons from the liquid water is observed at a KE of ~ 45 eV, over a strong background corresponding to secondary electrons from the gas phase (Figure 7.17 (a)). After a linear background subtraction, the liquid water secondary electron peak is presented in Figure 7.17 (b). For solid surfaces, it is a common practice to determine the cutoff by extrapolation, drawing a line on the step edge. We adopt also this method for liquid water, and the cutoff is determined as the intersection point of the horizontal baseline and the tangent to the step (green line in Figure 7.17 (b)). Note that the edge is much steeper for the clean gold case than for the electrolyte solution, as shown in Figure 7.18. We can attribute this to the fact that the liquid/vapor interface is not that sharp, as it extends over $\sim 3 - 4$ Å, according to the simulated density profiles calculated by Jungwirth et al.[145] Therefore, the tangent method introduces for liquid an uncertainty in the cutoff determination estimated to ± 0.4 eV (while, for the gold surface it is < 0.1 eV)

Note that the low energy secondary electron peaks of NaI and NaCl solutions are practically superimposable (the 0.02 eV difference could be accounted by a mere background subtraction effect). The NaBr solution work function is found ~ 0.2 eV greater than for NaI and NaCl solutions. We note that the step edge is also broader than that of the NaCl and NaI solutions, making a precise determination more difficult. In any

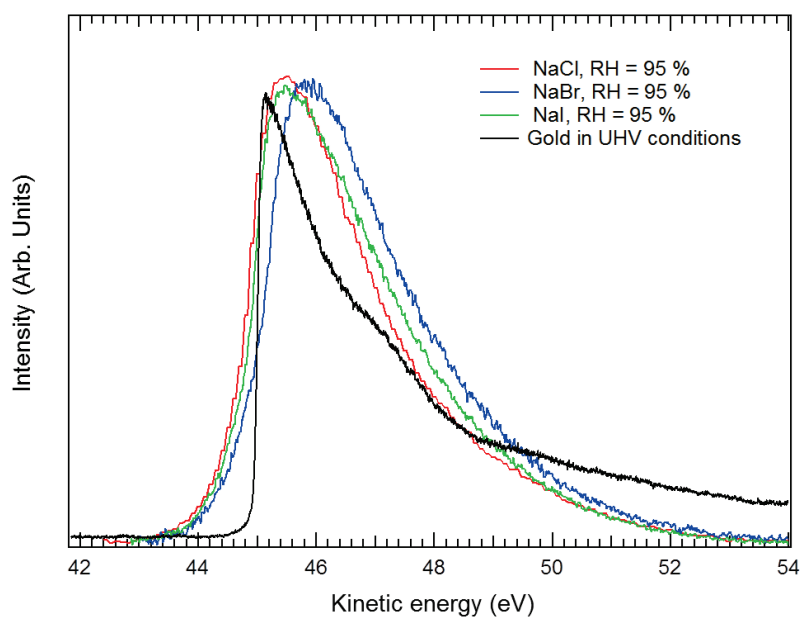


Figure 7.18: Secondary electron cut off measured at $h\nu = 500$ eV for the saturated NaCl, NaBr, NaI solutions and for the gold surface with a polarization of 40 eV at RH = 95 % ($P = 8$ mbar, $T = 278$ K).

Sample	Work function (eV)
NaCl solution RH = 95 %	4.20
NaBr solution RH = 95 %	4.43
NaI solution RH = 95 %	4.22
Clean gold in UHV conditions	4.95

Table 7.1: Work function measured for NaCl, NaBr and NaI saturated solutions, and Ar sputtered (non-annealed) polycrystalline gold

case, we can conclude that for the two extreme cases (with respect to the anion size) the work-function is practically the same.

Jungwirth et al.[164] calculated variations in surface potentials for KCl, KBr and KI solutions up to molalities of 2 mol/kg with respect to neat water. The trend is an increase of the surface potential (i.e. of the work function) with respect to that of pure water, in the order $KCl < KBr < KI$ (big anions segregate more at the surface). Up to

$m = 2 \text{ mol/kg}$ the effect is relatively small (0.04 V for KI, less than 0.005 V for KCl). Unfortunately, the surface potentials are not calculated at saturation concentrations. Different surface organic contamination, with different molecular dipoles, may also affect the surface potential. The NaCl and NaI solutions (see Figure 7.3) contain different organic contamination on their surfaces, however the work functions are practically the same.

We would also add a comment on the concept of vacuum level. Through work function measurements, we measure the position of vacuum level VL, referenced to the Fermi level, “just outside the surface”. [26], [165], [166] This corresponds to a distance such that the image potential of the electron is zero, but this distance is much smaller than the size of the macroscopic sample. The work function we measure here is that of the metal/solution/vacuum system. Importantly, a link can be established with electrochemistry. For redox solutions in the standard state (infinite dilution), this quantity is equivalent to the absolute electrode potential, defined by Trasatti [165] as “the difference in electronic energy between a point inside the metal (Fermi level) and a point outside the solution”. This quantity is calculable by the (periodic) methods of computational surface science. [166]

The vacuum level VL (that depends on the surface dipoles present at the surface) should be distinguished from the vacuum level at infinity VL^∞ , i.e. the ultimate reference level. VL is distinct from VL^∞ as it depends on the surface dipole barrier.

This discussion is necessary because of comparisons with liquid jet experiments, [167], [149] where VL^∞ is the reference level used to calibrate the BE scale, via the measurement of the KE position of the b1(gas) line, of known ionization potential (12.60 eV). In Ref. [167], [149] (pure water) as in Figure 7.10 of the present work, the b1(gas) line is found at lower BE than the HOMO of liquid water, 1.44 eV in Ref. [167], [149] and 1.6-1.7 eV here. However, in contrast to the liquid jet case, in our experimental configuration, the sample and the spectrometer are in electrical contact, distant by $\sim 1 \text{ mm}$. The alignment of the Fermi levels of the two dissimilar materials (with different work functions) implies a charge transfer between the sample and the spectrometer, that leads to the appearance of a contact potential difference (CPD), [26] in which the gaseous molecules are plunged (see Figure 7.19 (a) and (b)). This CPD induces a shift in the KE of the gas

phase photoelectrons, which is absent in the liquid jet configuration, as the $b_1(\text{gas})$ KE does not change when the beam is moved away from the jet surface.[149]

The CPD effect on the gas-phase BE was studied more in detail with the O 1s core-level of the water vapor. The gas phase core-level BE changes as the sample-nozzle distance is modified (as the irradiated volume is at different electrostatic potentials, according to the distance). We have measured the O 1s energy position, referenced to the Fermi level of the sample/analyzer, for increasing nozzle-sample distances d_{ns} . At the optimized working distance $d_{ns} \sim 1$ mm (see Figure 7.19 (c)), the O 1s BE of the vapor is 535.30 eV (liquid water O 1s BE is at 533.20 eV). By retracting the sample several cm away from the nozzle (when the sample contribution vanishes) the gas phase O 1s BE is found at 535.84 eV. This BE (KE) energy increase (decrease) of 0.5 eV when d_{ns} varies from ~ 1 mm to “infinity” gives an estimate of the CPD. It indicates that electron charge is transferred from the analyzer to the sample (see Figure 7.19 (d)).

In fact VL^∞ should be measured with a sample freely floating in space, and initially electrically neutral,[26] which in practice cannot be achieved, because of charging. Subtracting the “infinite” d_{ns} O 1s BE to the gas phase IP of 539.79 eV [168] gives 3.95 eV (this is the value close to the negatively charged sample surface). Subtracting the O 1s BE at $d_{ns} \sim 1$ mm, gives 4.49 eV (this is the value close to the positively charged analyzer), see Figures 7.19 (c) and (d). Therefore $3.95 \text{ eV} < VL^\infty(\text{O } 1s) - E_F < 4.49 \text{ eV}$. We note that $VL(\text{cutoff}) - E_F$ value of 4.2 eV is bracketed by these two values. VL and VL^∞ are expected to be close for pure water, as the surface dipole contribution should be of the order of 0.1 eV.

We consider now the use of the $b_1(\text{gas})$ line in the valence band to position the vacuum level. For now, we neglect the CPD effect. In fact we note that the $b_1(\text{gas}) - b_1(\text{liq})$ BE difference we find, only differs by 0.2 - 0.3 eV from the value obtained by the Winter-Faubel group. Using the $b_1(\text{gas})$ IP of 12.6 eV, and the $b_1(\text{gas})$ BE of 7.4 - 7.6 eV (see Figure 7.10), we find a $VL^\infty(b_1(\text{gas})) - E_F$ value of 5.0 - 5.2 eV, about 1 eV larger than $VL(\text{cutoff}) - E_F$. The discrepancy is large, contrary to the vacuum level determinations using the gas phase O 1s ionization energies and secondary cutoff that gave close values. At present we cannot provide any explanation.

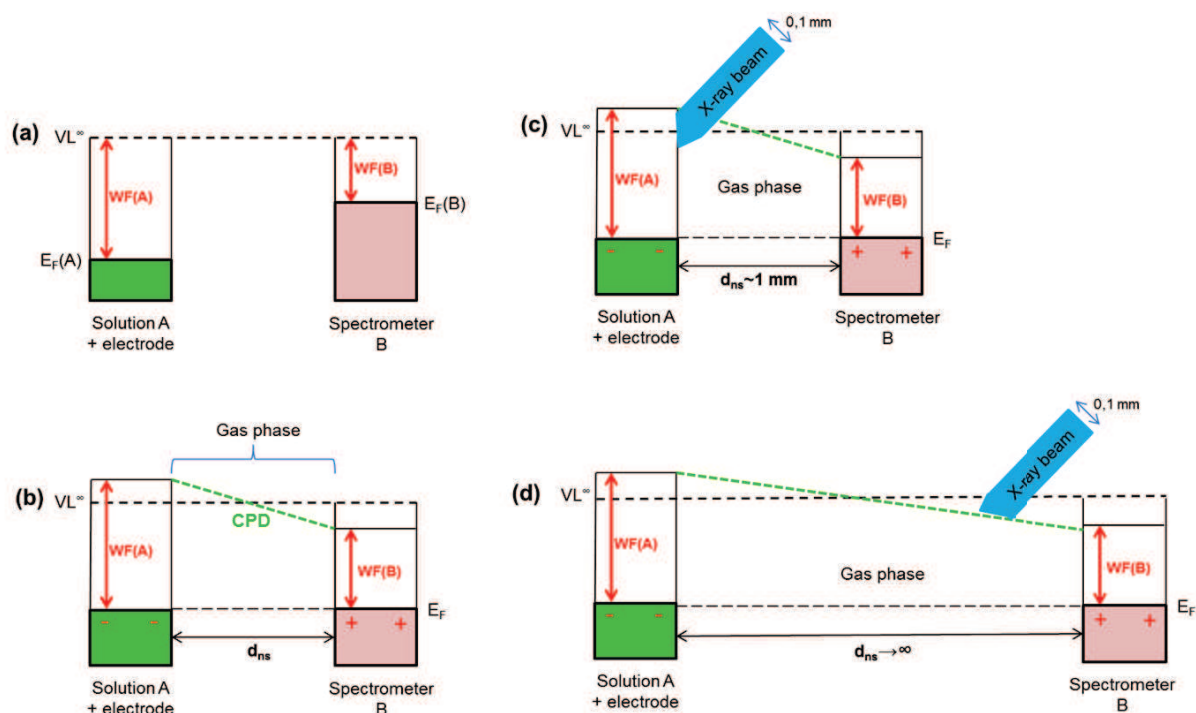


Figure 7.19: Illustration of how electrons flow to the larger work function material A (a) when dissimilar conductive materials (A and B) are put into electrical contact (b), to establish the contact potential difference CPD. The sample A (spectrometer B) is negatively (positively) charged. At nozzle-spectrometer distances d_{ns} of ~ 1 mm, the ~ 0.1 mm diameter X-ray beam probes the solution A and the gas phase above it (c), hence the higher bound KE for gas phase O 1s. At very large d_{ns} values, the beam probes the gas phase molecules that see practically the same potential as that close to the spectrometer, hence the lower bound KE for gas phase O 1s. The absolute $VL^\infty - E_F$ is bracketed by the two extreme values deduced from the O 1s gas phase at d_{ns} equal to ~ 1 mm and “infinity”.

7.3.2 Work function measurements and electronic level diagrams

Looking to the valence bands of Figure 7.10, one can obtain the valence band maximum position of liquid water (VBM_w) by linear extrapolation of the rising low BE. This can be clearly obtained in the case of the NaI solution, as the water b_1 HOMO is well separated from the I 5p level. VBM_w is found at a BE of ~ 4.15 eV.

In Figure 7.20, the positions of the electronic levels in NaCl and NaI saturated solutions are summarized in an energy level diagram, taking either the Fermi level and the

vacuum level VL (“just outside the solution”) as a reference.

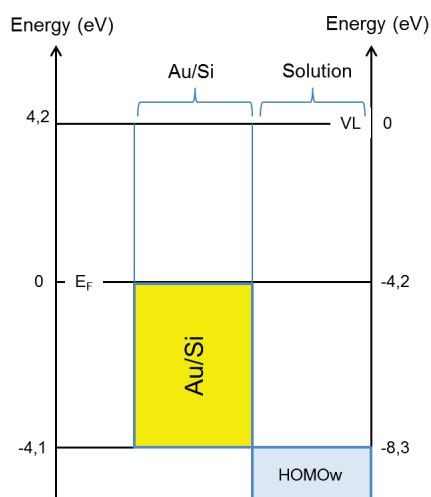


Figure 7.20: Schematic energy diagram of the gold substrate/solution/vacuum system, referenced to the E_F (left) and to VL(cutoff) (right). Note that the energies correspond to vertical transitions.

The energy scheme shows that VBMw is ~ 8.3 eV below the vacuum level (VL(cutoff)). Our findings are different from the reported values for neat liquid water, determined by the Winter-Faubel group [149] (9.9 eV), who used a different vacuum level reference (VL^∞), see above. The BE and vertical detachment energies (VDE) of the anion valence orbitals (peak maximum and linear extrapolation of the rising low-binding energies), see Figure 7.10 are collected in Table 7.2, and compared to photoemission thresholds [169] already published.

Delahay[169] measured photoelectron thresholds making plots of the photoelectron yield Y^n (with $n = 0.4$ or 0.5) against $h\nu$. As discussed by Coe, the onset of the photoelectron yield should occur at photon energies smaller than the vertical transitions (optimized overlap of the excited and ground-state wave-functions, according to the Franck-Condon principle). For the anionic series we do not discuss the absolute VDE (should we use the peak maximum or the low BE rising edge?) and the photoemission threshold values. We note simply that the trend and the energy differences are coherent for the two experiments.

Anion (bulk water)	Cl 3p	Br 4p	I 5p
BE (peak maximum)	~ 4.9	~ 4.1	~ 2.6
VDE (peak maximum)	~ 9.1	~ 8.3	~ 6.8
BE (low BE rising edge)	~ 3.4	~ 3.0	~ 1.4
VDE (low BE rising edge)	~ 7.6	~ 7.2	~ 5.8
Photoemission threshold[169]	8.81	8.05	7.19

Table 7.2: BE (Fermi level) and VDE (VL(cutoff)) of the anions valence levels. Comparison with photoemission thresholds from Ref. [169].

If we consider now the core level BE, we note that the Na 2s BE in NaCl, NaBr, and NaI are identical for the three solutions. This can be understood if the Fermi level in the solutions does not depend on the nature of the anion. Considering the VL(cutoff), the IP of the cation Na^+ in the solution (67.35 eV for NaCl and NaI, 67.45 eV for NaBr) can be compared with those found with the liquid jet technique, 68.00 ± 0.15 eV.[149] The difference can be ascribed to the choice of the vacuum level reference, as for the determination of the VBMw IP. In any case it is significantly smaller than the gas phase IP of Na^+ (80.07 eV[149]), due to the solvation effect.

The O 1s BE of liquid water of 533.2 eV gives an IP (VL(cutoff)) of ~ 537.4 eV, to be compared with the gas phase value of 539.79 eV. The 2.4 eV difference is also accounted by condensation. An illuminating discussion of solvation and condensation effects on the vertical IP/BE is given in Ref. [149]. This point will be reexamined in Chapter 8 devoted to insertion of water in clays.

7.3.3 Electronic level alignments

At this point of the discussion a question should be raised. What fixes the Fermi level in the electrolyte solution at about 4.2 eV below VL(cutoff)? According to Trasatti [165] and others, [170] E_F in the solution is determined by redox couples. The redox level of the standard hydrogen electrode (SHE) H^+/H_2 (standard electrode potential $E^0 = 0$ V) is positioned 4.44 eV below the vacuum level (at pH = 0). Therefore, the

energy positioning (with respect to the vacuum level) of the other redox couples can be obtained via the following equation $VL - E_F(\text{redox}) = 4.44 + E^0$, with E^0 expressed in V.

In the present electrolytes, the ionic species are H_3O^+ (H^+), OH^- (at a concentration of 10^{-7} mol/L), Na^+ and the anions. Therefore we can consider the following redox couples: Na^+/Na , H^+/H_2 , the halogen redox couples, to which we can add $\text{H}_2\text{O}_2/\text{H}_2\text{O}$. In fact X-ray induced radiolysis of the water layer can produce H_2 and H_2O_2 . [171], [172] In Table 7.3, we give the corresponding standard electrode potentials E^0 referred to the SHE, and the deduced $VL - E_F$ values.

Redox couple	E^0	$VL - E_F$
Na^+/Na	-2.7	1.74
H^+/H_2	0	4.44
I_3^-/I^-	0.53	4.97
Br_2/Br^-	1.09	5.53
Cl_2/Cl^-	1.36	5.8
$\text{H}_2\text{O}_2/\text{H}_2\text{O}$	1.78	6.22
Work function of gold (sputtered clean polycrystalline, 5×10^{-10} mbar)		4.95
Work function of the gold/Si substrate on which droplets are formed (degreased, 6×10^{-9} mbar)		4.0

Table 7.3: Values of standard potentials (E^0), $VL - E_F$ values for redox couples and gold metal surfaces (work function).

A simple reasoning [173], [174] (assimilating work functions and redox potentials to the electrochemical potential) considers that the substrate (the solution) will transfer electrons to the solution (substrate) if $(VL - E_F)_{Au}$ is smaller (greater) than $(VL - E_F)_{\text{redox}}$ before contacting the two phases. The equilibrium will be reached when the two Fermi layers in the solid and the electrolyte align. Table 7.3 suggests that the electron transfer from the substrate to the solution to reduce Na^+ is merely impossible. Also, the oxidation of Cl^- into Cl_2 and of Br^- into Br_2 via electron transfer from the so-

lution to the substrate is a priori not feasible. On the other hand, the reduction of H_2O_2 (if present) to H_2O could be envisaged. The reduction of H^+ is “on the border line” considering the metal substrate work functions (note the relatively low work function found for the degreased gold/Si substrate, likely due to surface contamination). This is also true for the oxidation of I^- , but noticing that the NaCl and NaI solutions have practically the same work function, iodine redox couples should be excluded.

In fact the work function of ~ 4.2 eV is a value very close to the $VL - E_F$ of the H^+ / H_2 in standard conditions (4.44 eV). In fact the equilibrium value of the Fermi level depends on the pH and H_2 concentration (or partial pressure in the gas phase), according to Nernst law:

$$VL - E_F = 4.44 + \frac{0.058}{2} \left(2pH + \log\left(\frac{[\text{H}_2]}{[\text{H}_2]_{\text{SHE}}}\right) \right) \quad (7.1)$$

Using the Q-pole inserted in the 2nd stage of the differential pumping, we have measured the partial pressures of H_2O , H_2 and O_2 of the sampled gas, in two cases: (i) for the residual gas (6×10^{-9} mbar in the analysis chamber), (ii) for 5 mbar of water vapor in the analysis chamber. The data are collected in Table 7.4.

Total pressure in analysis chamber	Q-pole partial pressures (mbar)		
	H_2O	H_2	O_2
6×10^{-9} mbar (residual)	5×10^{-11}	6.5×10^{-10}	$< 10^{-13}$
5 mbar (H_2O)	2×10^{-8}	3×10^{-9}	2×10^{-10}

Table 7.4: Partial pressures measured by the Q-pole in the second stage of the differential pumping system of the analyzer

Table 7.4 shows that H_2 gives the major contribution in the residual gas. H_2 is also the main pollutant in the water gas. The increase jump in H_2 pressure measured by the Q-pole by increasing the analysis chamber pressure from 6×10^{-9} mbar to 5 mbar is 2.25×10^{-9} mbar, about 1/10 of the H_2O pressure. Assuming that the partial pressures measured by the Q-pole in the sampled gas are proportional to those in the

analysis chamber (no preferential pumping), the partial pressure of H_2 would be ~ 0.5 mbar (5×10^{-4} bar). This value seems very large, and we shall take it as an upper bound. A lower bound would be 6×10^{-9} mbar, considering that almost all the residual is H_2 (see Table 7.4), and that no supplementary H_2 is brought by introducing H_2O . With $pH = 7$ and $5 \times 10^{-4} > \frac{[H_2]}{[H_2]_{SHE}} > 6 \times 10^{-12}$, the Nernst equation gives $4.13 \text{ eV} < VL - E_F < 4.35 \text{ eV}$. High concentrations of H_2 in the water layer could also be produced by radiolysis, but we have no direct visual indication, like bubbling,[172] that it occurs. Therefore with the considered range of H_2 concentrations of hydrogen in the solution, it is possible that electron exchange between the metal substrate and the water layer is governed by the H^+ / H_2 redox reaction.

In conclusion, by growing macroscopic alkali halide droplets at saturation concentration onto a metallic substrate we have been able to draw the electronic diagram level of the solution, assuming that the Fermi levels of the metal and of the electrolyte are aligned. In particular we have estimated the position of the water valence band edge with respect to E_F , and we have demonstrated that the measurement of the work function (“just outside the surface of the electrolyte solution”) is feasible via the secondary cutoff method. We have examined what could pin the Fermi level in the solution, and considered the H^+ / H_2 redox couple. The fact that electron energy level diagrams at metal/electrolyte interfaces are obtainable via NAP-XPS is of prime importance in fields related to electrochemistry,[166], [173] and photo-electrochemistry.[175], [176]

7.4 Summary

In this chapter, we presented the first results we obtained, using the NAP-XPS instrument at the TEMPO beamline, on ion segregation at water solution surfaces.

Our results confirm a preferential presence of anions at the liquid water surface as suggested by previous experimental work and theoretical simulations.[145] However, if we are sure of their presence due to the surface component observed on the anion core-level spectra, the reason of this presence is less clear. Indeed, this peak can be

attributed to a pure asymmetric water solvation shell of the anion or to an interaction with organic molecules (surface contamination). Furthermore, beam damage makes the analysis delicate.

For the cation the story is easier, particularly because beam damage was not observed. In agreement with Molecular dynamics results,[145] cations are not present on the water surface (which may protect them from beam damage). But, when the anion polarizability increases, a cation plane is formed below the anion one near the liquid surface, to recover the electroneutrality of the solution. This is an important result, this is the first time that an experimental measurement proves the existence of an increase of cation concentration below the surface.

To clarify the role of carbon contamination on the surface, the use of surfactant that will create a layer on it, may be interesting. The influence of the chemical function (carboxylic acid, amine...) present on the surfactant skeleton on the ions behavior should be investigated. The interaction between anions and octadecylamine at a water droplet surface was already studied using Vibrational Sum Frequency Spectroscopy (VSFS).[144] The vibrational spectra collected in the CH stretch range showed dramatic differences in the degree of ordering in the alkyl chains as a function of the anion nature in the subphase. This ordering seems to be modified by the ability of some anions to penetrate into the alkyl chain portion of the monolayer, thereby disrupting the hydrocarbon packing.

Furthermore, ions behavior is also fundamental at the liquid water/hydrophobic interface, for example at the interface with polymers and proteins. These interfaces, similarly to liquid water/vapor ones, are submitted to a reorganization of ions. Depending on the ion nature, this reorganization can be responsible for the solubility and stability of polymers and proteins in aqueous solutions (Hofmeister series [146]). [152]

Chapter 8

The swelling properties of clays monitored by NAP-XPS

Clay minerals, rich in silicon and aluminum, are breakdown products of minerals formed in greater depths of the Earth's crust or mantle. At the Earth's surface, they come into contact with an acidic environment (carbon dioxide dissolved in water), active atmosphere and temperature fluctuations. This so-called weathering process is the main source of sediments and soils on the Earth's surface, on which the biosphere heavily relies. Clays, as layered, fine-grained (high surface area) materials with water retention and ionic exchange capacities, have crucial role in nutrient (both organic and inorganic) retention and pH buffering of soil. Furthermore, a vast number of applications of clays has been developed, beginning with their use in ceramic ware, paper-making, removal of impurities, decolorizing and more recently as molecular sieves, in catalysis, CO₂ sequestration and geological storage of long half-time radioactive waste. [19], [20], [21], [22], [23]

With respect to these issues, it is crucial to establish a bridge between the microscopic scale (chemical bonding, ionic exchange, ion solvation, ion and matter transport) and the macroscopic scale (swelling, retention capacities). Clays are composed of micrometric particles formed by stacks of negatively charged alumina-silicate layers compensated by counterions such as Na⁺ and Ca²⁺ in between them, in the so called interlayer. The origin of water adsorption and retention by clays lies in the hydration of these compensating interlayer cations and depends on the alumina-silicate layer negative charge and the nature of the counterions (charge, size).

The hydration of clays has already been studied by several techniques: X-ray diffraction, infrared spectroscopy, several neutron induced techniques (neutron spin echo, Neutron Time of Flight and Backscattering).[177], [178] X-ray diffraction (XRD) provides information about the effects of relative humidity (RH) on the interlayer spacing. However, due to static and dynamic disorder in the interlayer, XRD does not allow to determine the specific atomic positions needed for detailed structural analysis, particularly with respect to the hydrogen positions, and gives essentially no information about dynamics. Neutron scattering also probes interlayer structure and water diffusion and has been recently used to study interlayer water diffusion in smectites.[21]

While much is known on the crystallographic, thermodynamic and dynamic aspects, very little is known about the electronic structure of these materials. The organization of water molecules around the interlayer cations must have a strong impact on their core-level ionization energy (BE), as suggested by recent NAP-XPS experiments on saline solutions.[167] As natural clays are often complex non-homogenous systems (see below), the philosophy of our approach was to study the penetration of water molecules in a well defined, synthetic smectite, the hectorite, by monitoring the BE shifts of the counterions core-levels and of the silicate layer atoms. Besides its novelty as an application of NAP-XPS to clay minerals, our work enabled to establish a link between the BE of the counterion and the presence of water molecules around it. This can be considered as a first attempt to examine the electronic structure of ions in confined water via XPS.

This chapter is organized as follows, it starts by a short presentation of clay structural characteristics and gradually zoom onto smectites and more precisely onto hectorite, highlighting their behavior under conditions of increased relative humidity (RH). Then, we present the NAP-XPS results obtained for three hectorites containing different counterions and therefore, different behaviors relative to water sorption.

8.1 Clay Minerals

8.1.1 Clay layers: atomic structure and charge

The atomic structure of clay minerals, determined mainly from detailed X-ray studies beginning in mid-20th century ([179]) and more recently from electron microscopy and solid state NMR, [22] has a number of general features that span the entire clay family. At the same time, a continuum of possible atomic substitutions of the general structure exists and results in blurred boundaries in any attempt to classify clays. Gradual changes in atomic structure are an excellent framework for scientific purposes where the influence of a single parameter (e.g. clay layer charge density) and the resulting properties can be investigated. However, occurrence and purification down to strictly stoichiometric phases in natural clays is impossible and most often we deal with mixtures.

To get a good control of the sample, we have examined a synthetic swelling clay, the hectorite, member of the smectite clay group (details of its preparation in section 1.2). Its general molecular formula is $\text{Cat}_{0.4/z}[\text{Mg}_{2.6}\text{Li}_{0.4}][\text{Si}_4]\text{O}_{10}\text{F}_4$, where Cat stands for a counterion carrying a charge $z+$.

The basic building block of clays is an SiO_4 tetrahedron (the corners of the tetrahedron correspond to O atoms, while the center can be occupied by an Si or an Al atom). These tetrahedra are arranged in a hexagonal pattern sharing three of the four corners (O atoms) to form a planar structure referred to as a clay sheet (see Figure 8.1 (a)). In 2:1 clays (e.g. smectites), as opposed to 1:1 (e.g. kaolinite) and 2:1:1 (e.g. chlorites) clays, two of such sheets come together, with the unshared O atoms facing, to form a clay layer. In the mid-region of the clay layer, a sheet of octahedra is generated by the two planes of the unshared O atoms and, usually, additional hydroxyl groups (OH). The hectorite we used is fluorinated meaning that the structural hydroxyl groups are replaced by F^- atoms (see Figure 8.1 (b)). The centers of the generated octahedra can be occupied by different ions as Al^{3+} , Fe^{2+} , Mg^{2+} , Li^+ ... These cations have different charges, in order to preserve the electroneutrality, Al^{3+} occupies only 2/3 of the octahedra (dioctahedral

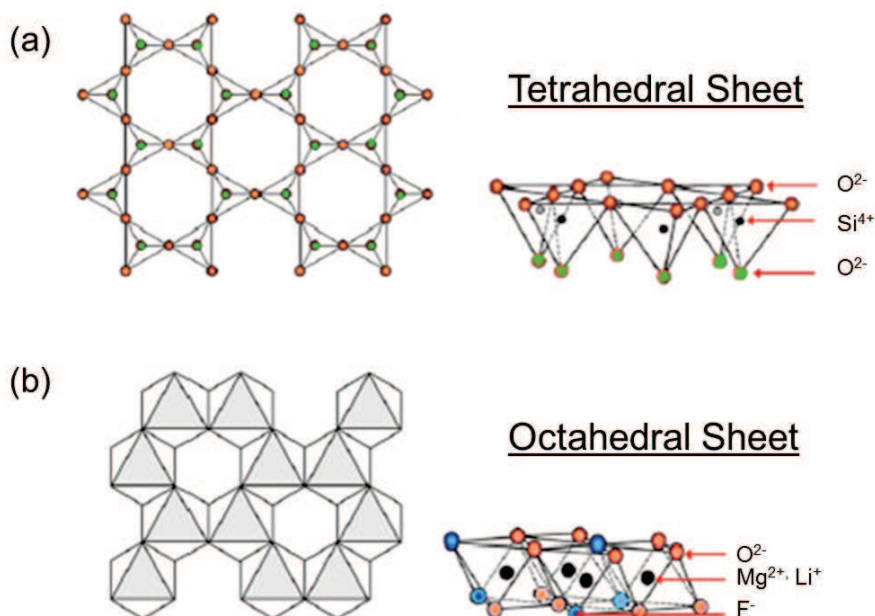


Figure 8.1: (a) Tetrahedral sheet (b) Octahedral sheet of a fluorinated hectorite layer.

2:1 clays) while Mg^{2+} occupies all of them (trioctahedral 2:1 clays).

In the case of hectorite, the tetrahedra formed by oxygen atoms are occupied by Si atoms and octahedra by Mg^{2+} . But some Mg^{2+} ions are substituted by Li^+ creating a negatively charged clay layer. The charge is compensated by cationic species (counterions) on the layer surface or between two adjacent layers (interlayer region), see Figure 8.2. The density and location of these substitutions together with the nature of the counterion are crucial factors. They determine the layer stacking within a clay particle, the response of the particle to increased humidity, the mobility and the potential exchange of counterions with an external system. In other words, charged clay layers, with compensating mobile cations in-between, are the key for all the widely-exploited clay properties such as swelling and water/ion retention.

The direct link between swelling and ion exchange with the layer charge is confirmed Table 8.1.[21]

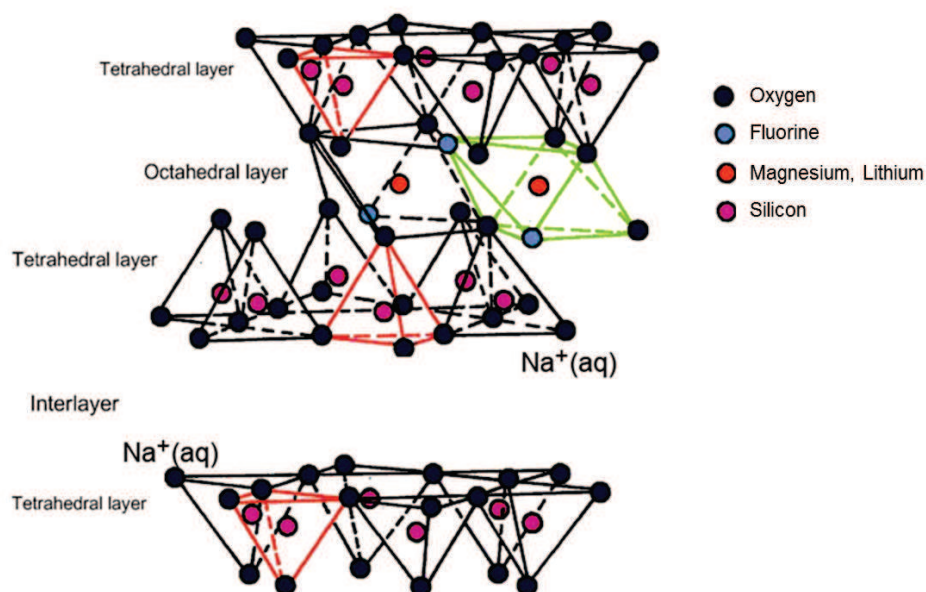


Figure 8.2: Schematic representation of fluorinated Na-hectorite structure.

- For high tetrahedral layer charge (micas), the attraction between layers and abundant counterions is too strong for water to penetrate and for ions to become mobile and exchangeable.
- For zero-layer charge (pyrophyllites), particles do not absorb water. No counterions are present, the only forces holding the layers together are of Van der Waals type. It is thought to be due to the hydrophobicity of the uncharged layers and their large lateral size compared to their thickness. (The lateral size of clay particles ranges from $0.1 \mu\text{m}$ for smectites up to the macroscopic scale, order of cm for vermiculite and order of m for mica. There is a trend in the formation of laterally larger particles with increasing layer charge.)
- For the intermediate charge case (vermiculites, smectites), the swelling can occur.

Clay layers are highly anisotropic (thickness 1 nm, lateral size from nm to m). Hectorite platelets have been studied by Atomic Force Microscopy (AFM), their shape are irregular and the typical lateral dimension of a particle is about $\sim 1 \mu\text{m}$ as observed on

Name	Charge (per unit cell)	Type of substitution	Counterion	Swelling, ion exchange
pyrophyllite	0	none	none	none
smectites	0.4-1.2	TET, OCT	Ca ²⁺ , Mg ²⁺ , Na ⁺	yes
vermiculites	1.2-1.8	TET, OCT	Mg ²⁺	yes
micas	2.0-4.0	TET	K ⁺ (Ca ²⁺)	none

Table 8.1: Classification of dioctahedral 2:1 clays as a function of layer charge. TET- referred to tetrahedral substitutions and OCT- to octahedral substitutions

Figure 8.3. The thickness of the platelets seen by AFM is approximately of 10-15 Å, in good agreement with the value expected for an isolated clay platelet.

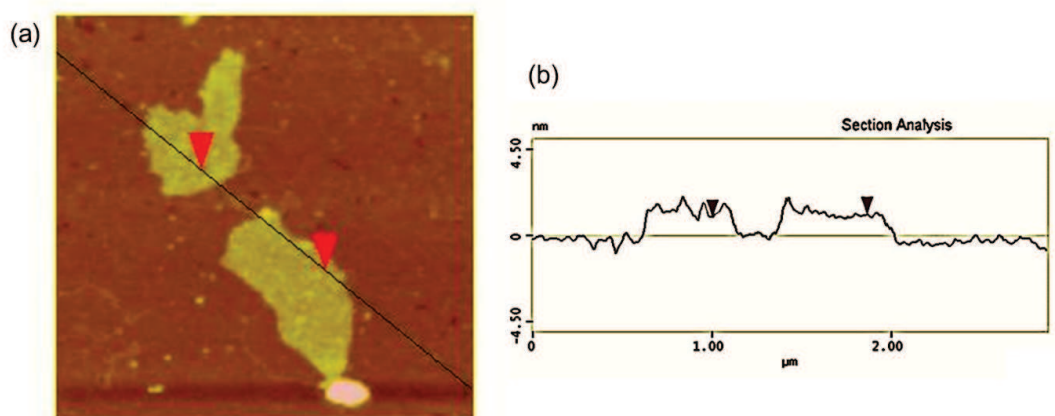


Figure 8.3: (a) AFM image of dissociated hectorite platelets. A dilute solution of hectorite particles was deposited on a mica substrate and evaporated. The vertical (color) scale ranges from 0 to 10 nm. (b) Topological profile along the line drawn on the AFM image

They have a strong tendency to stack into clay particles, adjacent layers are held by the weaker Van der Waals forces but above all, electrostatic interactions are important when individual layers possess an overall electrostatic charge. At the mesoscopic scale, these particles form aggregates. Therefore, during hydration, water can enter into the interlayer or into interparticle and interaggregate pores (Figure 8.4).

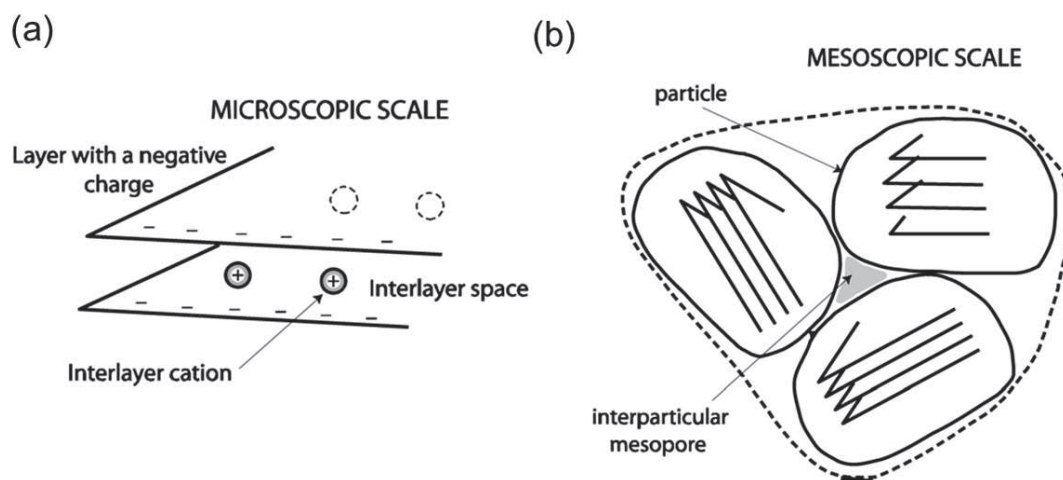


Figure 8.4: Water adsorption phenomenon (a) at the microscopic scale and (b) at the mesoscopic scale.

8.1.2 Clay swelling/hydration

Swelling properties of clays and structure and dynamics of water and counterions confined between clay layers has been a subject of numerous investigations, [180] beginning with experimental techniques such as X-ray diffraction combined with water adsorption gravimetry [181], [182], [183], NMR [184], [185], infrared spectroscopy [186] and more recently microscopic simulation. [187], [188], [189], [190]

For routine characterization of the hydration state of a clay sample, the combination of X-ray diffraction and water adsorption gravimetry has been widely used [181], [182], [183]. X-ray diffraction gives direct access to the layer spacing as a function of RH. Coupled with water adsorption gravimetry, the amount of adsorbed water for a given layer spacing can thus be determined. This approach is, however, subject to the following complications arising from the nature of real clay systems: inhomogeneity in the stacking of the clay layers, difficulty of distinguishing water adsorbed on internal (interlayer) and external surfaces of the clay particles, multiple porosities in the system (interlayer, mesopores, macropores etc... [191]

The swelling characteristics of a clay, with a given charge location and density, is strongly dependent on the nature of the counterion. Na^+ , Cs^+ and Sr^{2+} characteris-

tics (size, charge and hydration enthalpy) are given table 8.2. Cs^+ and Na^+ have the same charge but Cs^+ has a bigger radius and its hydration enthalpy is, in absolute value, lower than for Na^+ . Sr^{2+} has a radius close to the one of Na^+ and a double charge which increases its affinity for water, indeed, its hydration enthalpy is significantly higher. Consequently, the NAP-XPS experiments will be presented starting from the Cs-hectorite which should have the less affinity for water and then Na-hectorite and Sr-hectorite which should be easier to hydrate.

However, we should note that these enthalpies are bulk water thermodynamic constant and it is a clear evidence that the structure and dynamics of water are modified when water molecules are close to interfaces or confined in porous spaces.[192] Salles et al. have shown that hydration energies for various interlayer cations, compare to bulk conditions, parallel well with the hydration energy of these cations in aqueous solutions, although the hydration energies for these cations are systematically smaller than those obtained in bulk water. Two effects may be invoked to explain the difference. First, the number of water molecules surrounding a cation in its hydration shell is smaller when it is located in the interlayer space compared to the situation in bulk water due to the confinement by the quasi 2D porosity. Secondly, an additional amount of energy is necessary to eventually separate the cation from the clay surface.[193] In any case such effect cannot be quantified without the use of techniques such as conductivity measurements.[194]

Cation	charge	Ionic radii	Hydration enthalpy of gaseous ion
Na^+	1+	116 pm	- 406 kJ/mol
Cs^+	1+	181 pm	- 264 kJ/mol
Sr^{2+}	2+	132 pm	- 1446 kJ/mol

Table 8.2: Cation properties

The ambient temperature water adsorption and desorption isotherm for Cs-hectorite, Na-hectorite and Sr-hectorite clay are presented in Figure 8.5, Figure 8.6 and Figure 8.9 respectively.

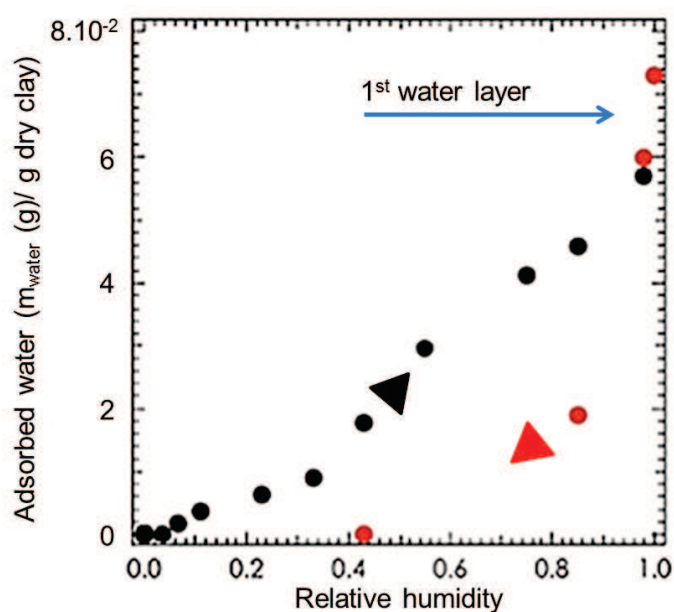


Figure 8.5: Water adsorption and desorption isotherm as a function of RH of Cs-hectorite

For Cs-hectorite, at RH = 100 %, there is less than one water layer in the clay interlayer space. Indeed, first stages of swelling are very sensitive to the balance of ion-water and ion-clay interactions. The dry to monolayer transition involves the replacement of part of ion-clay interactions by water ion interactions. With its larger radius, its higher polarizability, lower charge density and thus lower hydration enthalpy, this transition is not favorable for Cs⁺ ion and the monolayer state is formed with difficulties. [190], [195]

The ambient temperature water adsorption and desorption isotherm for Na-hectorite clay (Figure 8.6) between its dry state (starting and final point of the sorption-desorption cycle) and 100 % RH shows distinctly two plateaus (in both branches) corresponding to the appearance of a pure monolayer and bilayer of water in the Na-hectorite interlayer space.

- For one water layer in the interlayer, cations are not residing in the middle of the interlayer space but are displaced towards the tetrahedral sheet enclosing the

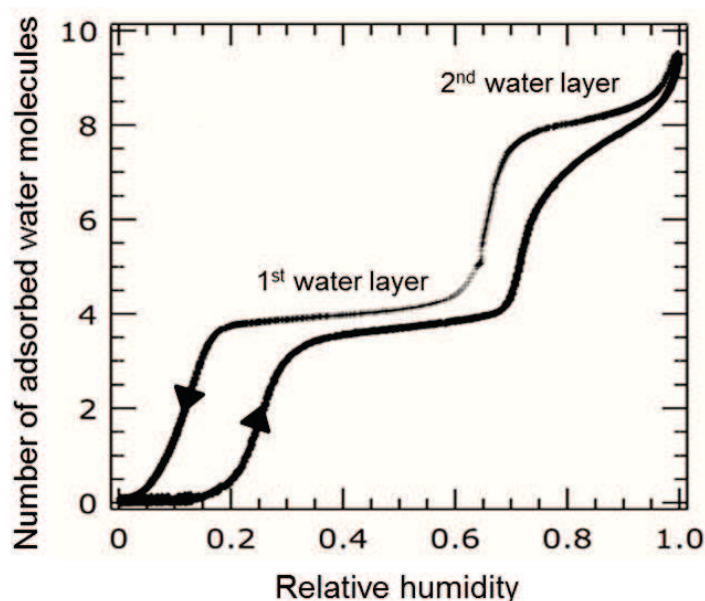


Figure 8.6: Water adsorption and desorption isotherm as a function of RH of Na-hectorite.[21]

interlayer space as shown in Figure 8.7 (a). The coordination observed for Na^+ involves both basal oxygen atoms of the tetrahedral sheet and the interlayer water occupying the center plane of the interlayer. The cation resides above the hexagonal cavity of the tetrahedral sheet and is coordinated by six basal oxygen with distances $\sim 3.23 \text{ \AA}$ and three water molecules of the interlayer.

- For two water layers, the interlayer cation resides at the central plane of the interlayer space as observed Figure 8.7 (b). Each Na^+ is coordinated by six oxygen atoms belonging to water molecules. The coordinating oxygen atoms are located on two planes above and below the plane containing the cations and the stacking order of adjacent layers is assured by well defined hydrogen bonding motifs. Each coordinated water molecule is also able to connect to one basal oxygen atom of the tetrahedral sheet via hydrogen bonding.

The fluorinated hectorite presents a substantial advantage with respect to its hydroxyl form that justifies its use. The isotherm sorption curve of the fluorinated Na-

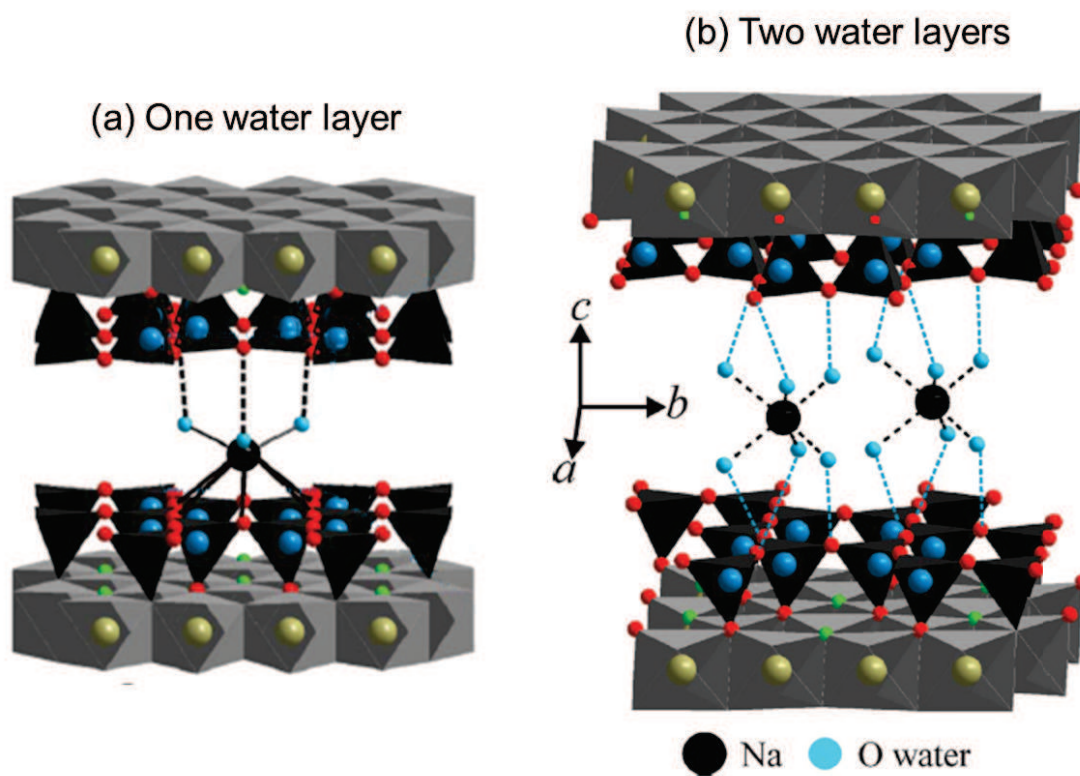


Figure 8.7: Schematic representation of the Na-hectorite structure after sorption of (a) one water layer and (b) two water layers into the interlayer.[196]

hectorite (F-hect) and of the hydroxylated one (OH-hect) are presented in Figure 8.8. The fluorinated hectorite shows two clear plateaus which are not so well defined for the hydroxy-form and the transitions between the different domains are much sharper. F-hect also contains less water than their hydroxylated equivalent possibly due to the hydrophobicity of basal surfaces; therefore, the water sorption lies only on the hydration of charge-compensating cations.[197]

The ambient temperature water adsorption and desorption isotherm for Sr-hectorite clay (Figure 8.9) between its dry state (starting and final point of the sorption-desorption cycle) and 100 % RH shows a plateau from RH = 20 % and RH = 80 % corresponding to the presence of a bilayer of water in the Sr-hectorite interlayer space. The presence of a water bilayer since low relative humidity is in agreement with the high affinity of water

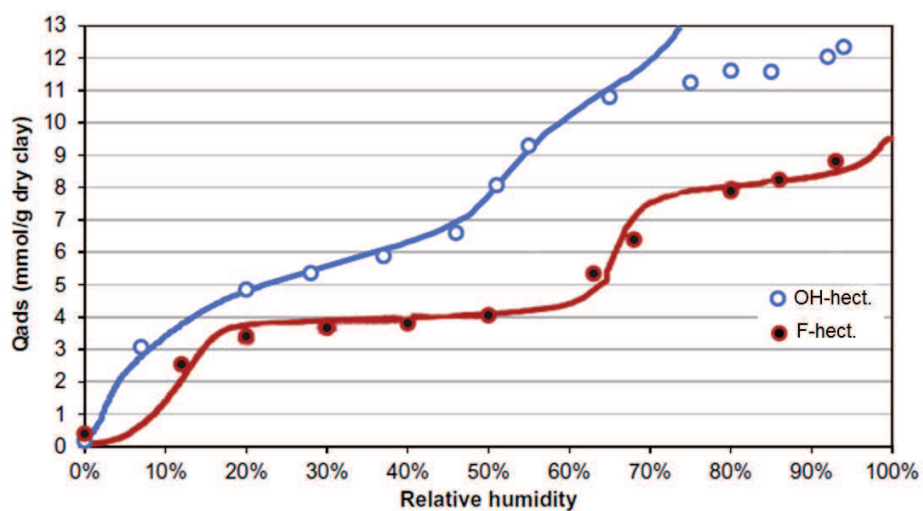


Figure 8.8: Comparison of the sorption isotherms of hydroxylated and fluorinated Na-hectorite.[197]

for Sr^{2+} ions.

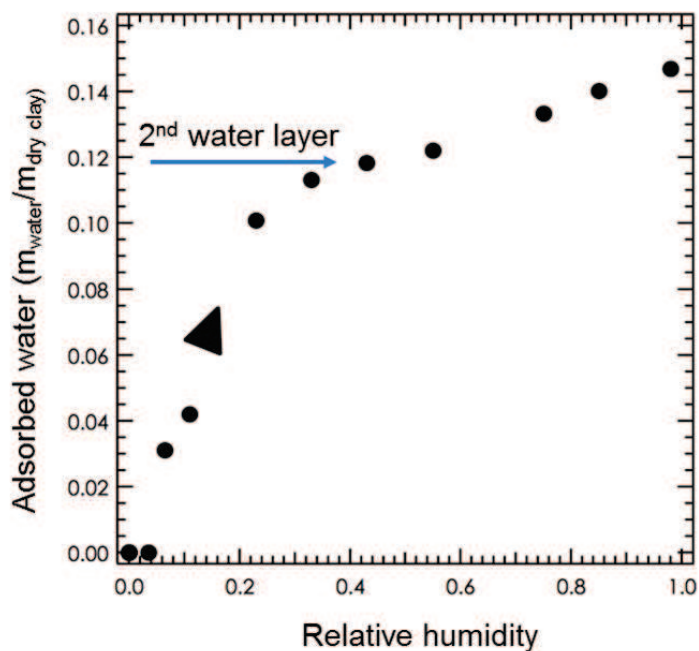


Figure 8.9: Water adsorption and desorption isotherm as a function of RH of Sr-hectorite

8.2 Sample preparation

The fluorinated hectorite was synthesized from gel precursors at high temperature as described elsewhere,[197] leading to a material with very high homogeneity of layer composition and charge density. All samples were initially sodium-saturated at room temperature by contact with aqueous solutions of NaCl. Cs-hectorite and Sr-hectorite were obtained by cation exchange in presence of the corresponding saline solution.

For XPS analysis, clays are deposited in thin layers on a gold coated silicon surface to limit the charge effect during the photoemission acquisition. The deposition is done by evaporation of a water solution containing clay platelets on the gold surface.

8.3 NAP-XPS measurements

The analysis of an insulating material as clays by XPS induces an important charge effect on the surface which weakens when the water pressure increases.[2] Charging is observed as the conductivity of hectorite is too low to replenish the photoemitted electrons. The core-levels shift to lower KE is due to a dynamic equilibrium depending on the X-ray flux and on the stray electrons collected by the positively charged sample surface. In the NAP-XPS case, negative species (secondary electrons, anions resulting from the dissociation of water by the beam) coming from the gas phase participate to the compensation of the positive charge surface. Figure 8.10 presents the evolution of the C 1s peak position referenced to the gold one. The clean gold is grounded and therefore, does not charge, while the carbon contamination attached on the insulating clay platelets suffers the charging effect. Therefore, the variation of the C 1s BE position allows quantifying the charge effect on the sample surface as a function of RH. When RH increases in the chamber, the charge effect decreases and the BE moves towards a limit value of 285.20 eV. Moreover, the distance between the Si 2p and the C 1s, measured for different RH, remains constant. It confirms that both the carbon contamination and the clay platelets experience the same charge effect.

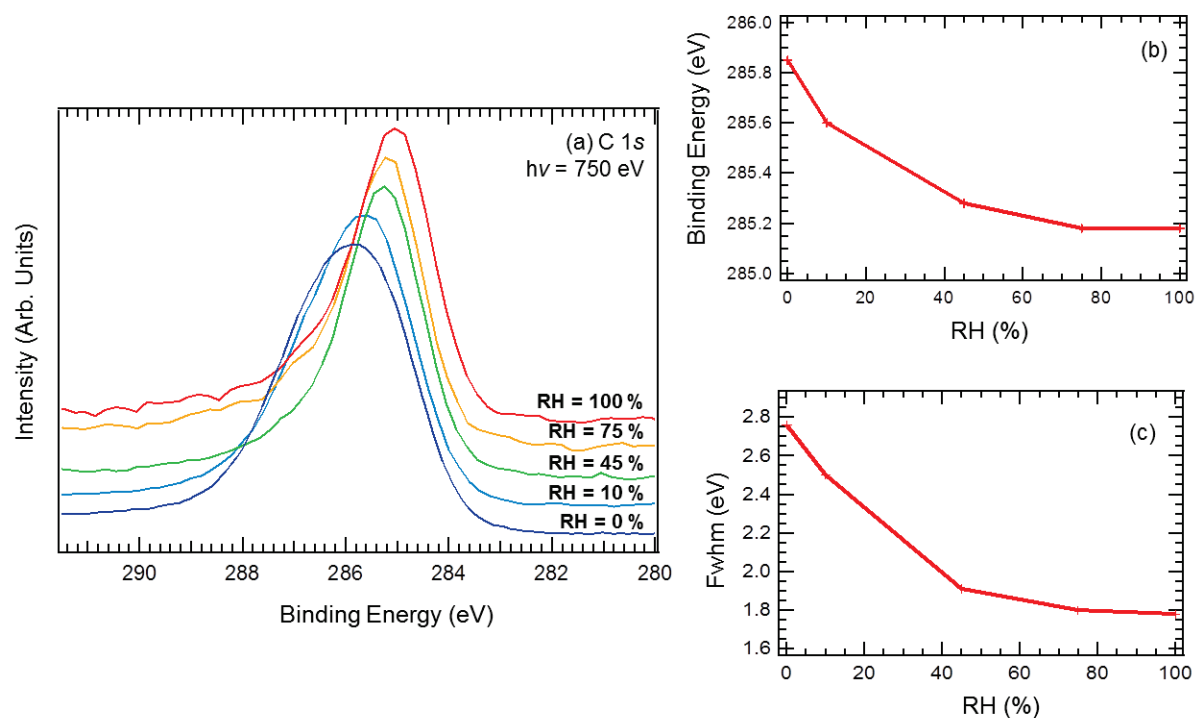


Figure 8.10: (a) C 1s XPS spectra ($h\nu = 750$ eV) of Cs-hectorite for several RH at $T = 283$ K. (b) C 1s BE position evolution with RH. (c) FWHM evolution with RH.

Consequently, the peak of C 1s was used as a reference for the energy calibration for all the spectra presented here. Its BE is fixed at 285.20 eV, corresponding to carbon in alkyl chains. [153] This reference was chosen in order to ease the comparison between samples.

The choice of this reference value is confirmed by the measurements of the C 1s spectrum of the adventitious carbon at the surface of a conductive sodium chloride solution ($\sim 5 \Omega \times cm$), its BE is also found at 285.2 eV, as described in the previous chapter.

Inhomogeneities in the surface potential (or work function according to Egelhoff) of the clay surface can appear when the surface state electronic population varies from place to place. This in turn induces a dispersion of the KE values of the photoelectrons generated at different locations of the surface, leading to peak broadening. These inhomogeneities disappear as soon as water adsorbs on the surface, [143], [198] as illustrated

in Figure 8.10 (c), where the C 1s fwhm, exhibits a monotonic decrease when water pressure increases. The same effect is observed for the core-levels of the other elements present in the clay.

8.4 Cs-hectorite

We present, in this section, the results obtained with Cs-hectorite. XPS measurements were performed at 283 K and at pressures up to 12 mbar, corresponding to different RH values between 0 % and 100 % ($P_{sat}(water) = 12$ mbar at 283 K). Hectorite swelling properties vary strongly with RH, however Tolbert et al. have shown that it is independent of the temperature, therefore, the comparison with the room temperature isotherms is relevant.[178]

Cs 4d XPS spectra evolution with RH is given in Figure 8.11. All Cs 4d XPS spectra can be fitted with a single d-orbital doublet at ~ 76.2 eV (spin-orbit splitting energy of 2.31 eV and an intensity ratio of 0.66 eV). The absence of modification of both shape and BE of Cs 4d core-level peaks suggests that the Cs^+ chemical environment does not change when RH increases and so, that there is no water insertion into the clay interlayer. It is in agreement with the Cs-hectorite isotherm for which at RH = 100 %, less than one water layer is present in the clay interlayer.

The O 1s XPS spectra evolution with RH is shown in Figure 8.12. At RH = 0 %, only one peak is present at 532.7 eV attributed to the clay structure oxygen. When RH increases, the emergence and the increase of two peaks is observed, one at 533.6 eV attributed to condensed water, and a second one at 535.5 ± 0.1 eV (fwhm = 1.1 eV,) corresponding to water vapor. The position of the water vapor peak and its fwhm depends strongly on the distance between the analyzer and the sample. It is due to a variation of the gradient between the surface potential (vacuum level) of the material and the one of the analyzer. When the distance decreases the water vapor peak becomes larger and its BE increases.

The ratio between the clay structure oxygen peak, at 532.7 eV and the condensed

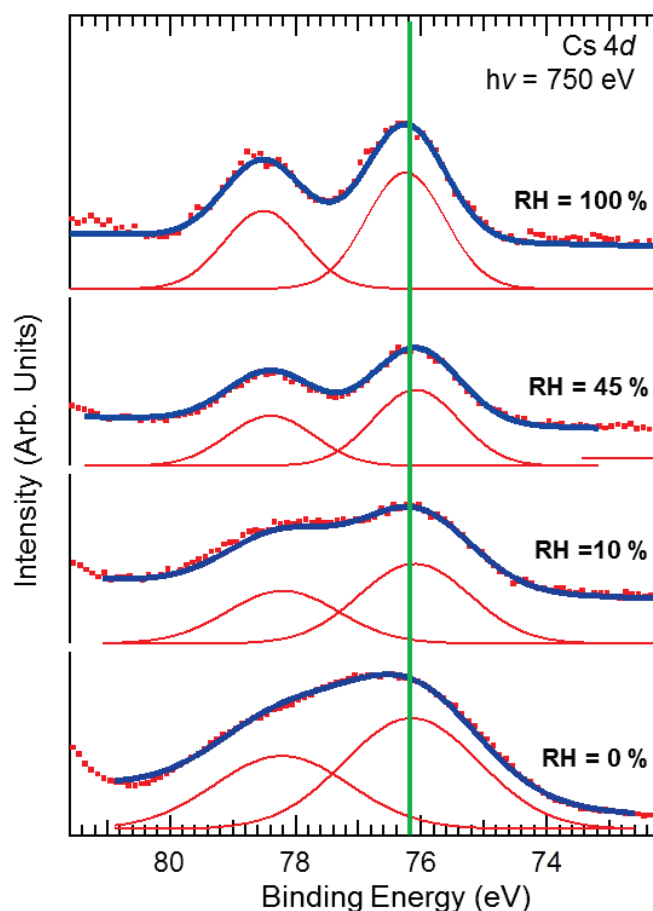


Figure 8.11: Cs 4d XPS spectra ($h\nu = 750$ eV) of Cs-hectorite for RH = 0 % (UHV conditions), 10 % ($P = 1.3$ mbar, $T = 283$ K), 45 % ($P = 5.4$ mbar, $T = 283$ K) and 100 % ($P = 12$ mbar, $T = 283$ K). To overcome the charging of the sample, the C 1s peak at 285.20 eV was chosen as energy reference.

water oxygen one, at 533.6 eV, remains sensibly constant when RH increases. As described previously, water molecules can interact with counterions in the clay interlayer leading to water swelling, or with hydroxyl groups terminating silicate platelet leading to the occupation of interparticle and interaggregates holes. Therefore, the liquid water observed on the O 1s spectrum corresponds to water occupying hectorite interparticle and interaggregates holes and shows that these holes are filled out for $RH < 10\%$, the amount of water is then constant when RH increases.

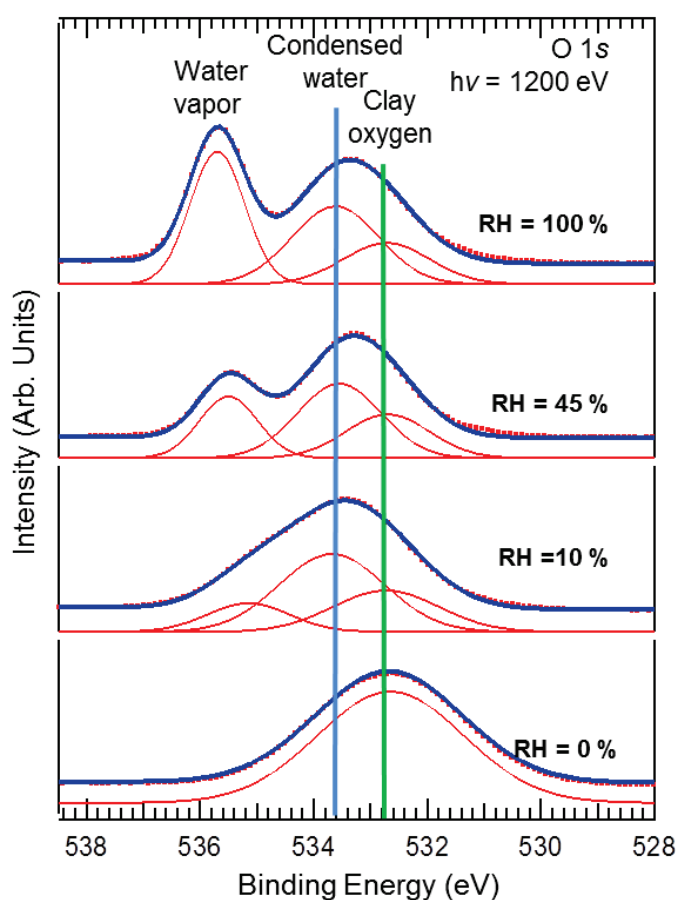


Figure 8.12: O 1s XPS spectra ($h\nu = 1200$ eV) of Cs-hectorite for RH = 0 % (UHV conditions), 10 % ($P = 1.3$ mbar, $T = 283$ K), 45 % ($P = 5.4$ mbar, $T = 283$ K) and 100 % ($P = 12$ mbar, $T = 283$ K). To overcome the charging of the sample, the C 1s peak at 285.20 eV was chosen as energy reference.

8.5 Na-hectorite

8.5.1 NAP-XPS measurements on Na-hectorite

The O 1s XPS spectra evolution with RH is shown in Figure 8.13. At RH = 0 %, similarly to Cs-hectorite, the O 1s spectrum contains only one peak at 532.7 eV attributed to the clay structure oxygen. When RH increases, two peaks are observed, one at 533.6 eV related to condensed water, [143], [199], [200] and a second one at 535.5 ± 0.1 eV (fwhm = 1.1 eV,) corresponding to water vapor.

The intensity of the condensed water oxygen peak relative to the clay structure oxygen peak slightly increases with RH; the ratio is of 1.2 at RH = 10 % and 1.35 at RH = 50 %. According to the water isotherm, there is no water into the interlayer at RH = 10 %, the peak of condensed water measured represents the condensed water in interaggregates holes. The increase of the ratio at higher RH corresponds to the insertion of water into the interlayer.

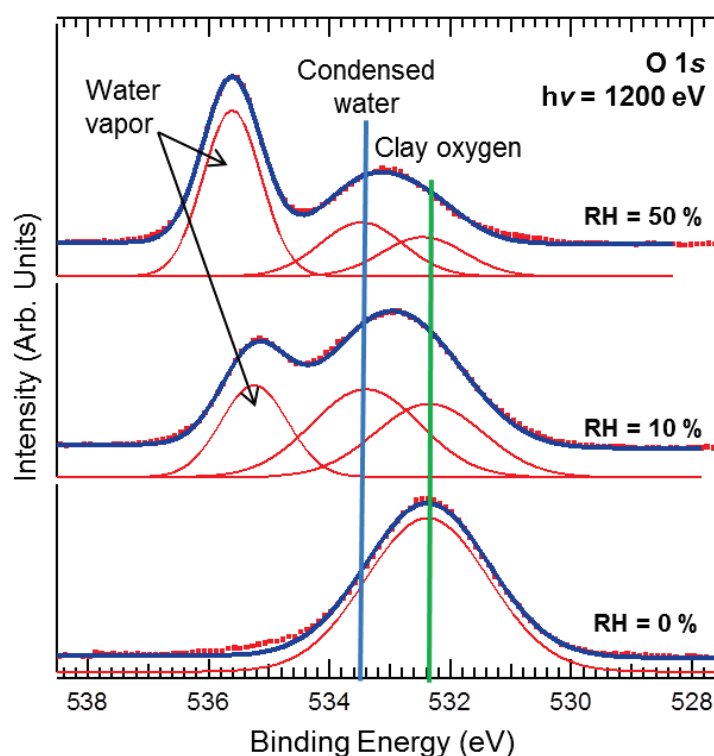


Figure 8.13: O 1s XPS spectra ($h\nu = 1200$ eV) of Na-hectorite for RH = 0 % (UHV conditions), 10 % ($P = 1.3$ mbar, $T = 283$ K) and 50 % ($P = 6$ mbar, $T = 283$ K). To overcome the charging of the sample, the C 1s peak at 285.20 eV was chosen as energy reference.

Figure 8.14 presents the evolution of Na 2s core-level BE as a function of RH. When RH increases from 0 % to 10 %, a shift of ~ -0.1 eV of the Na 2s core-level is observed, then between 10 % to 50 %, the peak shift of -0.89 eV (relative to RH = 0 %). On the contrary, Mg 2p peak BE stays constant when RH increases; indeed, magnesium is located in the middle of a silica lamella and do not interact with water molecules. It confirms that the shift, observed for the Na 2s peak BE, is due to a modification of sodium cation

environment by the presence of water molecules. Their insertion in clay interlayers is in agreement with the water adsorption and desorption isotherm of Na-hectorite (see Figure 8.6), which shows that at RH = 50 % one water layer is already present in the clay interlayer. Unfortunately, the small photoionization cross section of Na 2s core-level makes the acquisition of a spectrum for two water layers in the interlayer impossible (at 283 K a pressure of 11 mbar should be reached to reach a RH close to 100 %).

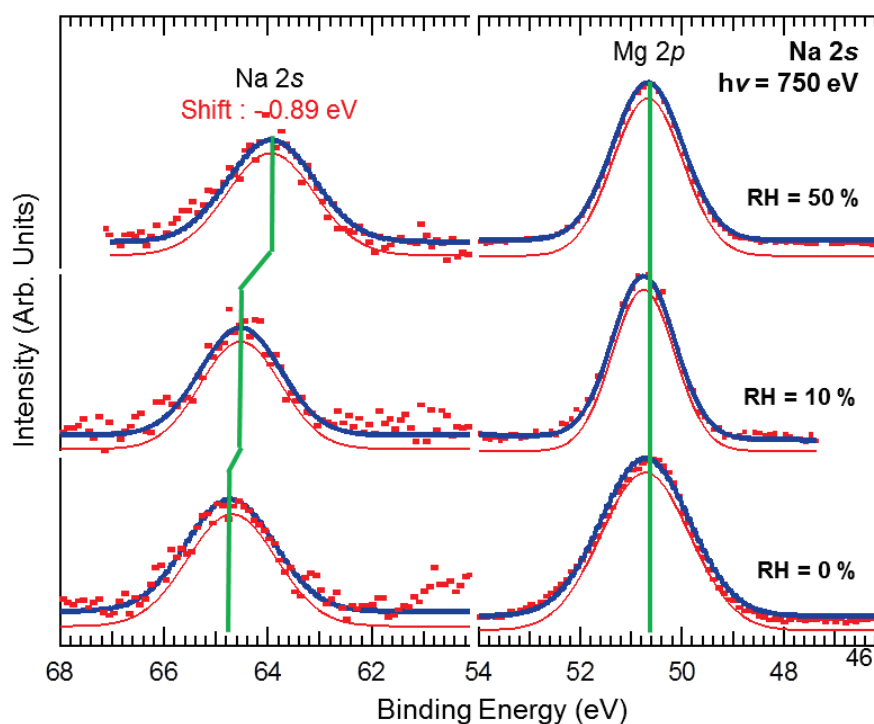


Figure 8.14: Na 2s and Mg 2p XPS spectra ($h\nu = 750$ eV) of Na-hectorite for RH = 0 % (UHV conditions), 10 % ($P = 1.3$ mbar, $T = 283$ K) and 50 % ($P = 6$ mbar, $T = 283$ K). To overcome the charging of the sample, the C 1s peak at 285.20 eV was chosen as energy reference.

8.5.2 Binding energy shift interpretation

The Na 2s peak shift to lower BE can be due to a variation of initial state effect and final state effect. The variation of the BE for the core-level i , also called chemical shift $\Delta\zeta_i$, can be decomposed into the sum of an initial state contribution, $\Delta\epsilon_i$ equals to the

difference between final and initial Hartree-Fock total energies of the system, and a final state contribution corresponding to the total relaxation energy ΔE^R (see chapter 1).[26]

$$\Delta\zeta = -\Delta\epsilon_i - \Delta E^R \quad (8.1)$$

Initial state considerations:

Initial state effects are related to a change in the electrostatic potential felt by the core-level of the cation. Briefly, clays, formed of alternately positive and negative infinite charged planes, can be considered as condensers. The inter-lamellar hydration obviously changes the relative permittivity with respect to that of the dry case. The distance between the charged planes also increases. This in turn changes the capacitance, and affects the electrostatic potential within the clay platelets.

Simulations by classical molecular dynamic are underway at the PHENIX laboratory of the the Pierre et Marie Curie University (V. Marry and E. Dubois) in order to evaluate initial state effects on the cation between the dry and the hydrated state.

Final state considerations:

Final state effect corresponds to a modification of the relaxation energy of the core hole, recorded as ΔE^R , between the dry and the hydrated clay case. The relaxation energy variation can be estimated by measuring the Auger parameter. The Auger parameter α is the sum of the auger KE with the photoelectron core-level BE.[201] Its numerical value is unique to each chemical state and is independent of the charge referencing operation. It is related to the difference in extra atomic relaxation energy between the two chemical states. The variation of the Auger parameter was calculated between Na-hectorite in UHV conditions and RH = 50 %, its value is $\Delta\alpha = 0.70$ eV. Wagner et al. showed that $\Delta\alpha \approx 2 \times \Delta E^R$. [202] Consequently, $\Delta E^R \approx 0.35$ eV.

The energy associated with extra-atomic screening of a core hole is assumed to be given by the classical equation for the electrostatic polarization of a dielectric medium,

treated as a continuum, by a point charge,

$$E^R = \frac{1}{4\pi\epsilon_0} \frac{(1 - \epsilon^{-1})e^2}{2r_o}, \quad (8.2)$$

where e is the point charge, r_o (an adjustable parameter corresponding to the radius of minimum screening distance) is the radius of the effective electron screening distance, and ϵ is the dielectric constant.[26] Since the photoelectron emission process is much faster than the time scale required to reorganize the initial solvation shell (the relaxation of the atomic positions surrounding the photoexisted atom does not have to be considered because relaxation times involved in such a process are of the order of the atomic vibration frequencies ($\sim 10^{-13}$ s). This is several orders of magnitude larger than the time involved in the photoemission process ($\sim 10^{-16}$ to 10^{-17} s), the optical relative permittivity should be used.[203]

However, for sodium cation solvated in the interlayer of hectorite and into water solution, we used for the interpretation of the BE shift, the static relative permittivity. This choice is motivated by the theoretical observations made by Winter et al..[203] They showed that, although the photoionization process is faster than the relaxation of the solvent dipoles, the favorable pre-orientation of water molecules around a cation allows using the static relative permittivity. Indeed, the cation presents a positive charge before and after ionization, which is not true for anionic ionization where the final state is neutral. Consequently, the static relative permittivity is adapted to cation relaxation while optical relative permittivity should be used for anion relaxation.

In absence of water, $\epsilon = \epsilon_{clay}\epsilon_0$ (with ϵ_0 the vacuum permittivity) with $\epsilon_{clay} \approx 2$ (optical dielectric constant of silica)[57]; after hydration $\epsilon = \epsilon_{water}\epsilon_0$, for one water layer with $\epsilon_{water} > \epsilon_{clay}$ (the static dielectric constant of one water layer can be estimated at ~ 20 using the relation between the basal spacing and the dielectric constant described by Laird et al.[204]). The dielectric constant of the sodium cation environment increases with RH, according to equation 8.2, $\Delta E^R > 0$. Consequently we expect that the relaxation energy increases when water is inserted within the lamellae and that the BE decreases.

Simulations by DFT are underway at the PHENIX laboratory of the Pierre et Marie Curie University (V. Marry and E. Dubois) in collaboration with the theoretical chemistry group of the Ecole Normale Supérieure (R. Vuilleumier) in order to determine the BE difference of core-electrons of the cation between the dry and the hydrated state.

8.5.3 Sodium chloride solution

In order to confirm the final state effect interpretation of the Na 2s core-level BE shift, the results can be compared with those obtained for the saturated sodium chloride solution described in the previous chapter, where the BE of Na 2s entirely solvated in a sodium chloride water droplet was measured.

Sample	Na 2s BE (eV)
Na-hectorite, UHV conditions	64.80
Na-hectorite, RH = 50 %	63.90
NaCl, RH = 95 % (liquid water solution)	63.15

Table 8.3: Na 2s BE for both Na-hectorite and NaCl solution samples.

Table 8.3 summarizes the Na 2s BE for different environments. Na 2s BE in Na-hectorite at RH = 50 % is intermediate between the Na 2s BE in dry hectorite and Na 2s BE in sodium chloride solution. Compared to the Na-hectorite with one water layer in the interlayer, in the case of the sodium chloride solution, the relative permittivity of the cation environment has increased, in the water solution $\epsilon_{water} = 80$. Consequently, the relaxation energy increases and the Na 2s BE decreases in agreement with final state effect interpretation.

8.6 Sr-hectorite

In the studied serie (Cs^+ , Na^+ , Sr^{2+}) Sr^{2+} has a the highest hydration energy in bulk water. Thus, it is expected that it will be easily hydrated in hectorite as confirmed by the sorption curves.

The Sr 3d XPS spectra evolution with RH is presented in Figure 8.15. For RH = 0 %, the spectrum was fitted with two d-orbital doublet (spin-orbit splitting energy of 1.8 eV and an intensity ratio of 0.66 eV) at 134.7 eV and 136.5 eV (fwhm = 2.1 eV). The presence of two components in UHV conditions is surprising since only one peak was observed for both Na^+ and Cs^+ counterions.

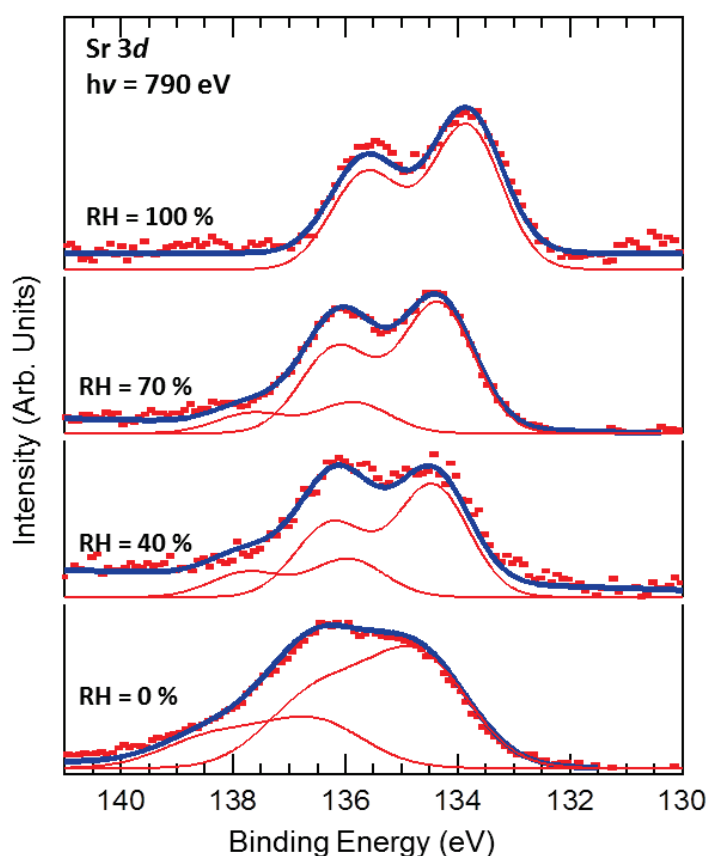


Figure 8.15: Sr 3d XPS spectra ($h\nu = 790$ eV) of Sr-hectorite for RH = 0 % (UHV conditions), 40 % (P = 4.8 mbar, T = 283 K), 70 % (P = 8.4 mbar, T = 283 K) and 100 % (P = 12 mbar, T = 283 K). To overcome the charging of the sample, the C 1s peak at 285.20 eV was chosen as energy reference.

Two different interpretations can be considered:

- The low BE component at 134.7 eV may be attributed to inter-lamella Sr^{2+} , and the one at high BE to Sr^{2+} at the surface of the stack of platelets, where the core-hole is less well screened. To verify this hypothesis, a depth analysis was done varying the photon energy from 400 eV (surface sensitive conditions) to 1200 eV (bulk sensitive conditions) but slight modifications were observed due to the non-oriented clays particles deposition.
- An alternative explanation could be the following, the component at high BE 136.5 eV could be attributed to a counterion placed into the hexagonal cavity, and the component at 134.7 eV to Sr^{2+} ions already surrounded by a few water molecules.

When RH increases to 45 %, two components are still observed at 134.4 eV and 135.9 eV (fwhm = 1.5 eV). It confirms the interaction of Sr^{2+} with water molecules and similarly to the results obtained with Na-hectorite, the peak shifts to lower BE when RH increases.

At RH = 70 %, the BE of both peaks is constant, in agreement with the Sr-hectorite isotherm, the region from 20 % to 80 % corresponds to a bilayer configuration. If the hypothesis of two Sr^{2+} , one in an hexagonal cavity and one partially hydrated at RH = 0 % was true, we should already observe, in this range of RH, only one component corresponding to the cation between two water layers into the interlayer.

Finally at RH = 100 %, we observe a second step in the clay hydration, only one component is present on the spectrum at 133.8 eV (fwhm = 1.4 eV). All Sr^{2+} cations have an equivalent chemical environment due to the presence of several water layers.

We present, Figure 8.16, the O 1s XPS spectra evolution with RH. At RH = 0 %, only one peak is present at 532.7 eV corresponding to clay structure oxygen. In the same way as in Cs-hectorite case, when RH increases to 40 % and 70 %, the emergence of two peaks is observed, one at \sim 536.2 eV corresponding to water vapor and a second one at 533.9 eV to liquid water. At RH = 100 %, the spectrum can also be fitted by three components but a shift of + 0.04 eV of the liquid water peak is observed and has a BE of

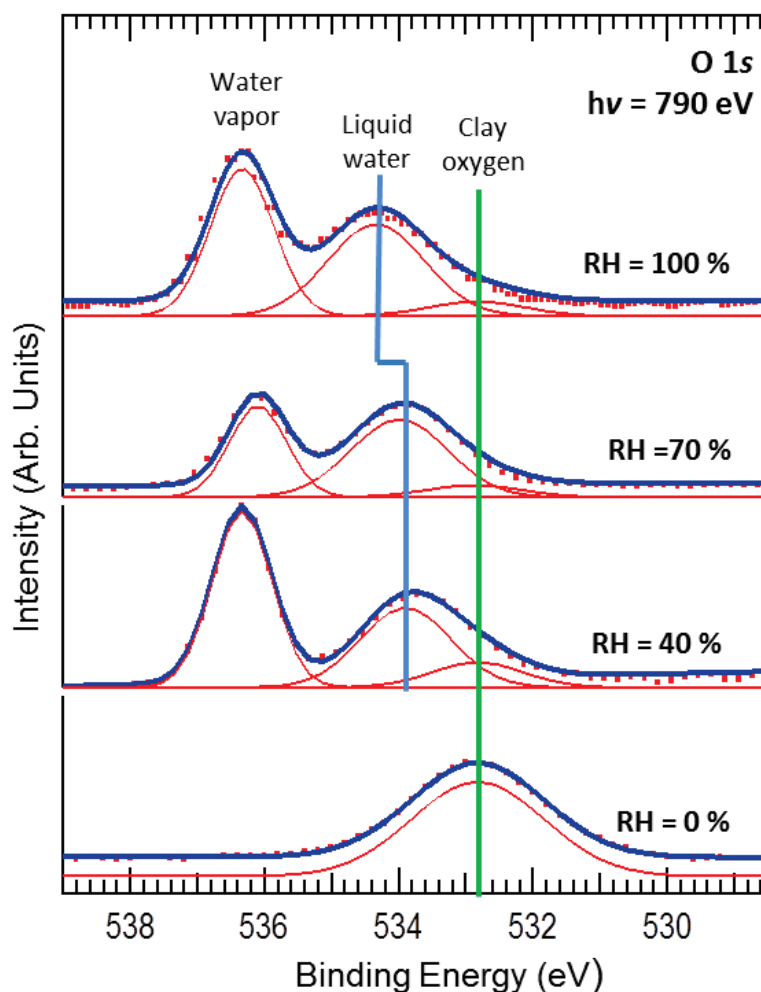


Figure 8.16: O 1s XPS spectra ($h\nu = 790$ eV) of Sr-hectorite for RH = 0 % (UHV conditions), 40 % (P = 4.8 mbar, T = 283 K), 70 % (P = 8.4 mbar, T = 283 K) and 100 % (P = 12 mbar, T = 283 K). To overcome the charging of the sample, the C 1s peak at 285.20 eV was chosen as energy reference.

534.3 eV. The shift can be due to a modification of the water structure in the interlayer due to an increase of the number of water layers.

Sr^{2+} has an enthalpy of hydration in bulk water higher (in absolute value) than the one of sodium (see Table 8.2) due to its double charge. It makes the insertion of water molecules possible and easier than with sodium. Water molecules are inserted into clay interlayer and solvate Sr^{2+} additionally to the occupation of interaggregates holes. The ratio between liquid water and clay oxygen on the O 1s XPS spectrum has

strongly increased comparing to the Cs-hectorite and confirms the adsorption of several water layers in the Sr-hectorite interlayer.

8.7 Solvation energies

In this section, we will consider the relation between the vertical ionization or detachment energies we measure and solution thermodynamics. Indeed, the difference in electron BE of the Na 2s core level between liquid (E_{aq}) and gas-phase water (E_g) correlate with the free energy penalty for disrupting the local solvent structure, known as the solvent reorganization energy.[205]

In order to extract, from XPS data, information concerning the solvation energy of sodium, we will use the Born model which treats the ion-solvent interaction. [205], [206], [207], [167] In this model, presented in Figure 8.17 (a), the cation is modeled by a spherical cavity with a charge ze and a radius R . This cavity is transferred from the vacuum (ϵ_0) to a medium placed into a dielectric medium (ϵ) representing the solvent.

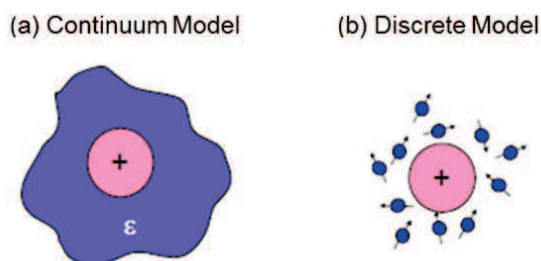


Figure 8.17: Possible models

For the present discussion, the numerical choice of R is not as relevant since we will relate electron BE, measured by photoemission, to experimental (thermochemical) values of the solvation free energy, as we will see below.

The free energy of solvation ΔG^{cav} is:

$$\Delta G^{cav} = -\left(\frac{z^2 e^2}{8\pi\epsilon_0 R}\right)\left(1 - \frac{1}{\epsilon}\right) \quad (8.3)$$

In any case, the continuum model used here does not assume any microscopic details of the solvation shell structure (discrete model Figure 8.17 (b)), and strictly speaking, the cavity (Born) model is applicable only for distances considerably larger than the ion radius. A microscopic description has to account for the specific interactions of a water molecule with ions. For cationic solvation, the O – H groups point away from the ion (then the oxygen atom points to the ion) in order to form hydrogen bonds with bulk water molecules at the solvation shell boundary.

Furthermore, equation 8.3 will be used to link measured vertical ionization energies and thermodynamic quantities in a simple and convenient manner in order to allow for a rough comparison with our experimental data.

To properly apply Equation 8.3 to the present experiment the relevant photoionization processes need to be considered in detail:

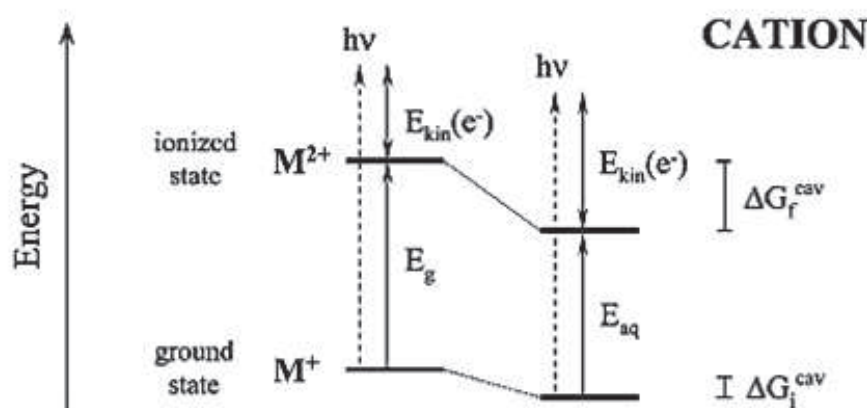


Figure 8.18: Schematic energy level diagrams illustrating the liquid-phase BE shifts in terms of the solvation free energy.[203]

The energies required for the process involved in equation 8.4 are the vertical ionization energies, which are measured by XPS. Since the photoemission process is much faster than the time scale required to reorganize the initial solvation shell, the photoelectron carries only the information on the original solvation configuration; it does not

sense reorientational changes of the solvent molecules. Consequently, the static permittivity may be used in Equation 8.3. Furthermore, entropy changes may be neglected on the time scale of photoionization. Therefore, the experimental value for the electron binding energy of a given ion in solution, E_{aq} contains electron binding energies as well as free energies.

According to equation 8.4, the solvation energies of both the initial (M^+) and final state (M^{2+}) of a given cation in solution, ΔG_i^{cav} and ΔG_f^{cav} , yield to $\Delta G = \Delta G_f^{cav} - \Delta G_i^{cav}$. Hence, with equation 8.4, one derives expressions for ΔG :

$$\Delta G(cation) = E_{aq} - E_g = \Delta G_f^{cav} - \Delta G_i^{cav} \quad (8.5)$$

$$\Delta G(cation) = (-e^2z^2 - (-e^21^2))\frac{1}{8\pi\epsilon_0R}\left(1 - \frac{1}{\epsilon}\right) = -3\left(\frac{e^2}{8\pi\epsilon_0R}\right)\left(1 - \frac{1}{\epsilon}\right) = -3\Delta G^{cav} \quad (8.6)$$

In the sodium photoemission process, z changes from +1 to +2. According to equation 8.5, the modification of z leads to two different solvation energies for Na^+ and Na^{2+} . This situation, depicting the energies of the respective species involved, is illustrated Figure 8.18. Schematic energy level diagrams illustrates the liquid-phase BE shifts in terms of the solvation free energy, $\Delta G^{i,f}$ (for initial and final state), relative to the respective gaseous ion. E_g and E_{aq} are the electron BE of the gas-phase species and the hydrated species, respectively.

The literature gives $E_g(\text{Na}^+(2s)) = 80.07$ eV (from NIST atomic spectra database) and $E_{aq}(\text{Na}^+(2s)) = 67.1$ eV (taking the work function approximately equal to 4 eV). We deduce that $\Delta G^{cav}(\text{Na}^+) = -4.32$ eV ≈ -416.82 kJ/mol. This value can be compared to the tabulated solvation free energy of $\text{Na}^+(2s)$ which is -406 kJ/mol. A similar calculation can be done for the Na^+ surrounded by one water layer in the clay interlayer, we obtain a free energy solvation of 391.9 kJ/mol.

The calculated solvation free energy, obtained by this model, is in agreement with the tabulated value and reflect the fact that orientation changes of the solvation shell

are only small for ionization of a cation; in this case both the initial and final state corresponds to cationic solvation.

8.8 Summary

NAP-XPS brings a new approach with a surface sensitive technique on the adsorption of water by clays. We have compared the behavior of three hectorites containing Na^+ , Cs^+ or Sr^{2+} counterions relative to water adsorption. O 1s XPS spectra analysis combined with counterion core-level XPS spectra analysis have shown that water adsorbs for Cs-hectorite only between clays particles while water is inserted into clay interlayer for Na-hectorite and Sr-hectorite. Indeed, for Cs-hectorite no modification is observed on the counterion core-level XPS spectrum while for Na-hectorite and Sr-hectorite, the counterion core-level peak shifts to lower BE.

However, in the case of Sr-hectorite, the behavior of the Sr^{2+} is not clear, the presence of two components on the Sr 3d spectra in UHV conditions and until RH = 70 % remains misunderstood. To verify the hypothesis of a bulk and a surface Sr^{2+} component on the spectra, we need to synthesize a sample where platelets will form a stack a flat layer and proceed to a depth analysis varying the photon energy in UHV conditions and in presence of water vapor.

The next step is the interpretation of this BE shift observed for both Na-hectorite and Sr-hectorite, classical molecular dynamics and DFT calculations are underway in collaboration with V. Marry and E. Dubois at the PHENIX laboratory of the the Pierre et Marie Curie University (UPMC) and R. Vuilleumier from the theoretical chemistry group of Ecole Normale Supérieure (ENS).

Conclusion

This thesis highlights the contribution of photoelectron spectroscopy in the analysis of various interfaces. The first case study concerns the reactivity of the TEOS molecule with clean and water-covered Si(001) surfaces. It illustrates the transition from XPS used in UHV to XPS at near-ambient pressures. This project presents the precious information that can be obtained with UHV XPS, mainly when it is combined with STM and DFT calculations; and the new point of view introduced by the increase of pressure linked to the possibility to come closer to industrial conditions. We also describe the unusual difficulties, compared to UHV conditions, we met during the sample analysis and how we tried to avoid them.

The two following case studies do need the use of NAP-XPS, as we need to get high humidity ratios, up to 100 %, to form liquid water/vapor and solid/liquid interfaces. In all these experiments the use of NAP-XPS allows to perform experiments impracticable with conventional XPS such as the monitoring of clay hydration in situ or the analysis of a water droplet surface placed just in front of the analyzer's nose.

All the results we obtained for these three interfaces are summarized in the following lines.

The first chapters are devoted to TEOS reactivity on the Si(001)-2×1 surface. In chapter 3, using XPS and STM experiments in conjunction with DFT calculations and STM image simulations, we show that TEOS dissociates on the Si(001) surface at low coverage (~ 1 L) via the cleavage of all its four Si – O bonds on a silicon dimer row, losing its Si central atom to form an adatom on the adjacent dimer row. This mechanism gives rise to ethoxy group pairs occupying a dimer out of two and to a structure alternating ethoxy-covered and Si adatom-occupied dimer-rows; therefore, TEOS could be used to produce self-organized nano-structures on Si(001)-2×1 .

The Si adatom position, identified on the STM images at room temperature, coincides with the one theoretically predicted more than two decades ago for the clean Si(001)-2×1 surface,[81] providing an experimental confirmation which has been lacking so far. Our theoretical analysis of the monomer diffusion have shown the importance of the surface buckling for the determination of the energy landscape of a silicon monomer on the Si(001) surface. We have demonstrated, in chapter 4, that the dimensions of the slab surface are crucial for the understanding of the monomer surface diffusion. The Si(001)-8×4 surface provide results more directly comparable with experiments, than a smaller slab surface (Si(001)-2×2) which neglects the role played by neighboring free silicon dimers. However, our work does not answer the following question: why is the monomer observed on the ethoxy covered surface and not on the clean one?

At high TEOS coverage (~ 10 L), the initial regime corresponding to the full dissociation of the molecule, via Si – O bond breaking and emission of a silicon monomer, is in competition with a second regime involving the scission of the C – O bond. We proposed, in chapter 5, that the latter reaction occurs on the monomers produced by Si – O bond breaking. The consequence of this second reaction path is the creation of ethyl groups on the surface. The presence of surface alkyl surface species, besides the expected alkoxy species, has profound consequences for ALD deposition of silica on a clean silicon substrate. While alkoxy species can be hydrolyzed to silanols by exposure to water, surface ethyls species will remain unaltered.

The ALD process is investigated using the NAP-XPS instrument in chapter 6. How-

ever, the expected hydrolysis of the surface ethoxy group, that should occur during the second step of the ALD process when water is introduced, is not observed. Moreover, the substrate undergoes an oxidation in presence of water molecules. It means that, in a sequential exposure scheme, water is inefficient to form hydroxyls from ethoxy groups, and too oxidative as it reacts strongly with the substrate.

To understand the reasons why this reaction was not observed, several experiments should be performed. The RH, during the second step of the ALD process, should be increased to higher values, the temperature of the surface should be increased to $\sim 700^{\circ}\text{C}$ during the exposure to gases (the increase of temperature may allow the reaction of water on surface ethoxy groups); finally, the use of a catalyst should be tried (amine bases can catalyze the reaction and the reaction mechanism would be interesting to understand).

The second project was related to ion solvation into liquid solutions and confined systems as clays.

Unlike previous works (experimental work and theoretical simulations.[145], [143], [151], [208]) on ion segregation at liquid/vapor interface which describe the behavior of anions at the liquid water surface and their propensity to segregate through the surface when their size and polarizability increases; our studies (chapter 7) are focused on the cation behavior. In agreement with Molecular dynamics results,[145] cation are not present on the water surface. But, when the anion polarizability increases, a cation plane is formed below the anion one near the liquid surface, to recover the electroneutrality of the solution. This is an important result, this is the first time that an experimental measurement prove the existence of an increase of cation concentration below the surface.

As the solution droplets are formed on a metallic electrode, and as the conductivity is sufficiently large to avoid charging under the beam, we have been able to refer the BE with respect to the Fermi level of the metallic substrate and to the vacuum level of the solution. Interesting, but thorny questions are raised by our measurements. Two of them, are unescapable: what is the Fermi level of the saline solution? and what are the relationships between the vertical ionization or detachment energies we measure and solution thermodynamics?

The behavior of cations was also investigated in a confined environment, we studied the hydration of counterion into clay interlayers in chapter 8. We proved that it is possible to follow the hydration of an hectorite system through counterion core-level XPS spectrum analysis and more precisely through its BE shift. The next step is the interpretation of this BE shift observed for both Na-hectorite and Sr-hectorite, classical molecular dynamics and DFT calculations are underway in collaboration with V. Marry and E. Dubois at the PHENIX laboratory of the the Pierre et Marie Curie University (UPMC) and R. Vuilleumier from the theoretical chemistry group of Ecole Normale Supérieure (ENS).

Bibliography

- [1] H. Bluhm, "Photoelectron spectroscopy of surfaces under humid conditions," *Journal of Electron Spectroscopy and Related Phenomena*, vol. 177, no. 2-3, pp. 71–84, Mar. 2010.
- [2] M. Salmeron and R. Schlogl, "Ambient pressure photoelectron spectroscopy: A new tool for surface science and nanotechnology," *Surface Science Reports*, vol. 63, no. 4, pp. 169–199, Apr. 2008.
- [3] D. Ogletree, H. Bluhm, E. D. Hebenstreit, and M. Salmeron, "Photoelectron spectroscopy under ambient pressure and temperature conditions," *Nuclear Instruments and Methods in Physics Research Section A: Accelerators, Spectrometers, Detectors and Associated Equipment*, vol. 601, no. 1-2, pp. 151–160, Mar. 2009.
- [4] D. F. Ogletree, H. Bluhm, G. Lebedev, C. S. Fadley, Z. Hussain, and M. Salmeron, "A differentially pumped electrostatic lens system for photoemission studies in the millibar range," *Review of Scientific Instruments*, vol. 73, no. 11, p. 3872, Oct. 2002.
- [5] J. Pantforder, S. Pollmann, J. F. Zhu, D. Borgmann, R. Denecke, and H.-P. Stein-

- ruck, "New setup for in situ X-ray photoelectron spectroscopy from ultrahigh vacuum to 1 mbar," *Review of Scientific Instruments*, vol. 76, no. 1, p. 014102, Dec. 2005.
- [6] A. Shavorskiy, O. Karslioglu, I. Zegkinoglou, and H. Bluhm, "Synchrotron-based ambient pressure X-ray photoelectron spectroscopy," *Synchrotron Radiation News*, vol. 27, no. 2, pp. 14–23, Mar. 2014.
- [7] A. Ulman, *An Introduction to Ultrathin Organic Films From Langmuir-Blodgett to Self-Assembly*. Boston: Academic Press, 1991.
- [8] J. Sagiv, "Organized monolayers by adsorption. 1. Formation and structure of oleophobic mixed monolayers on solid surfaces," *Journal of the American Chemical Society*, vol. 102, no. 1, pp. 92–98, Jan. 1980.
- [9] H. Sugimura, A. Hozumi, T. Kameyama, and O. Takai, "Organosilane self-assembled monolayers formed at the vapor/solid interface." *Surface and Interface Analysis*, vol. 34, pp. 550–554, 2002.
- [10] M. Hersam, N. Guisinger, and J. Lyding, "Silicon-based molecular nanotechnology," *Nanotechnology*, vol. 11, no. 2, pp. 70–76, 2000.
- [11] A. Vilan, O. Yaffe, A. Biller, A. Salomon, A. Kahn, and D. Cahen, "Molecules on Si: electronics with chemistry." *Advanced materials*, vol. 22, no. 2, pp. 140–59, Jan. 2010.
- [12] M. Leskela, J. Niinisto, and M. Ritala, *Comprehensive Materials Processing. Atomic-Layer-Deposited Thin Films for Silicon Nanophotonics*. Elsevier, 2014.
- [13] S. M. George, "Atomic layer deposition: an overview." *Chemical reviews*, vol. 110, no. 1, pp. 111–31, Jan. 2010.
- [14] I. T. Emesh, "Plasma-enhanced chemical vapor deposition of silicon dioxide using tetraethylorthosilicate (TEOS)," *Journal of The Electrochemical Society*, vol. 136, no. 11, p. 3404, Nov. 1989.

- [15] K. Fujino, "Silicon dioxide deposition by atmospheric pressure and Low-temperature CVD using TEOS and ozone," *Journal of The Electrochemical Society*, vol. 137, no. 9, p. 2883, Sep. 1990.
- [16] J. W. Klaus, O. Sneh, A. W. Ott, and S. M. George, "Atomic layer deposition of SiO_2 using catalyzed self-limiting surface reactions," *Surface Review and Letters*, vol. 06, no. 03n04, pp. 435–448, Jun. 1999.
- [17] S. Ghosal and J. C. Hemminger, "Effect of water on the HNO_3 pressure dependence of the reaction between gas-phase HNO_3 and NaCl surfaces," *The Journal of Physical Chemistry Aournal of physical chemistry A*, vol. 103, no. 25, pp. 6–10, 1999.
- [18] E. K. Frinak, "Infrared characterization of water uptake by low-temperature Namontmorillonite: Implications for Earth and Mars," *Journal of Geophysical Research*, vol. 110, no. D9, p. D09308, 2005.
- [19] M. Bradbury and B. Baeyens, "Near-field sorption data bases for compacted MX-80 bentonite for performance assessment of a high-level radioactive waste repository in opalinus clay host rock," *Technical report, Paul Scherrer Institut*, no. March, 2003.
- [20] I. Gaus, "Role and impact of CO_2 rock interactions during CO_2 storage in sedimentary rocks," *International Journal of Greenhouse Gas Control*, vol. 4, no. 1, pp. 73–89, 2010.
- [21] N. Malikova, "Dynamique de l'eau et des ions dans les argiles de type montmorillonite par simulation microscopique et diffusion quasi-elatique des neutrons," Ph.D. dissertation, Université Pierre et Marie Curie, Paris 6, 2005.
- [22] L. Fowden, R. M. Barrer, and P. B. Tinker, *Clay Minerals: Their structure, behavior and use*. Royal Society - London, 1984.
- [23] B. Velde, *Introduction to clay minerals*, C. and Hall, Ed., 1992.
- [24] C. Berglund and W. Spicer, "Photoemission studies of copper and silver: theory," *Physical Review*, vol. 136, no. 4A, pp. A1030–A1044, Nov. 1964.

- [25] M. P. Seah and W. A. Dench, "Quantitative electron spectroscopy of surfaces: A standard data base for electron inelastic mean free paths in solids," *Surface and Interface Analysis*, vol. 1, no. 1, pp. 2–11, Feb. 1979.
- [26] W. F. Egelhoff, "Core-level binding-energy shift at surface and in solids," *Surface Science Reports*, vol. 6, pp. 253–415, 1987.
- [27] S. Siegbahn, C. Nordling, G. Johansson, J. Hedman, P. F. Heden, K. Hamrin, U. Gelius, T. Bergmark, L. O. Werme, R. Manne, and Y. Baer, *ESCA Applied to Free Molecules*. Amsterdam: North-Holland., 1969.
- [28] H. Siegbahn and K. Siegbahn, "ESCA applied to liquids," *Journal of Electron Spectroscopy and Related Phenomena*, vol. 2, no. 3, pp. 319–325, Jan. 1973.
- [29] R. W. Joyner, M. Roberts, and K. Yates, "A "high-pressure" electron spectrometer for surface studies," *Surface Science*, vol. 87, no. 2, pp. 501–509, Aug. 1979.
- [30] H. Siegbahn, "Electron spectroscopy for chemical analysis of liquids and solutions," *The Journal of Physical Chemistry*, vol. 89, no. 6, pp. 897–909, Mar. 1985.
- [31] D. M. Littrell and B. J. Tatarchuk, "Hydrazine reduction of transition metal oxides: In situ characterization using x-ray photoelectron spectroscopy," *Journal of Vacuum Science and Technology A: Vacuum, Surfaces, and Films*, vol. 4, no. 3, p. 1608, May 1986.
- [32] H. J. Ruppender, M. Grunze, C. W. Kong, and M. Wilmers, "In situ X-ray photoelectron spectroscopy of surfaces at pressures up to 1 mbar," *Surface and Interface Analysis*, vol. 15, no. 4, pp. 245–253, Apr. 1990.
- [33] Grunze M., Dwyer Daniel J., Nassir M., and Tsai Y., *Surface Science of Catalysis*, ser. ACS Symposium Series, D. J. Dwyer and F. M. Hoffmann, Eds. Washington, DC: American Chemical Society, Jan. 1992, vol. 482.
- [34] D. F. Ogletree, H. Bluhm, G. Lebedev, C. S. Fadley, Z. Hussain, and M. Salmeron, "A differentially pumped electrostatic lens system for photoemission studies in

- the millibar range," *Review of Scientific Instruments*, vol. 73, no. 11, p. 3872, Oct. 2002.
- [35] H. Bluhm, M. Havecker, A. Knop-Gericke, E. Kleimenov, R. Schlogl, D. Teschner, V. I. Bukhtiyarov, D. F. Ogletree, and M. Salmeron, "Methanol oxidation on a copper catalyst investigated using in situ X-ray photoelectron spectroscopy," *The Journal of Physical Chemistry B*, vol. 108, no. 38, pp. 14 340–14 347, Sep. 2004.
- [36] SPECS, "Phoibos 150 NAP. Near ambient pressure hemispherical energy analyzer." pp. 1–7, 2010.
- [37] C. B. Duke, "Semiconductor surface reconstruction: The structural chemistry of two-dimensional surface compounds," *Chemical Reviews*, vol. 96, no. 4, pp. 1237–1260, Jan. 1996.
- [38] M. a. Filler and S. F. Bent, "The surface as molecular reagent: organic chemistry at the semiconductor interface," *Progress in Surface Science*, vol. 73, no. 1-3, pp. 1–56, Sep. 2003.
- [39] C. J. Wu and E. A. Carter, "Adsorption of hydrogen atoms on the Si(100)-2x1 surface: implications for the H_2 desorption mechanism." *Chemical Physics Letters*, pp. 172–178, 1991.
- [40] M. P. D'Evelyn, Y. L. Yang, and L. F. Sutcu, " π -bonded dimers, preferential pairing, and first-order desorption kinetics of hydrogen on Si(100)-(2x1)." *The Journal of Chemical Physics*, vol. 96, no. 852, 1993.
- [41] P. Nachtigall, K. D. Jordan, and C. Sosa, "Ab initio calculation of the energy of recombinative hydrogen desorption from the monohydride phase of silicon (100)." *The Journal of Physical Chemistry*, pp. 11 666–11 672, 1993.
- [42] F. A. Carey and R. J. Sundberg, *Advanced Organic Chemistry*, 5th ed. Springer, 2007.

- [43] P. C. Weakliem and E. A. Carter, "Constant temperature molecular dynamics simulation of Si(001) and Ge(100): Equilibrium structure and short-time behavior." *Journal of Chemical Physics*, vol. 96, pp. 3240–3250, 1992.
- [44] R. J. Hamers and Y. Wang, "Atomically-resolved studies of the chemistry and bonding at silicon surfaces." *Chemical Reviews*, vol. 96, pp. 1261–1290, 1996.
- [45] J. Yoshinobu, "Physical properties and chemical reactivity of the buckled dimer on Si(100)," *Progress in Surface Science*, vol. 77, no. 1-2, pp. 37–70, Nov. 2004.
- [46] R. J. Hamers, R. M. Tromp, and J. E. Demuth, "Scanning tunneling microscopy of Si(001)," *Physical Review B*, vol. 34, pp. 5343–5347, 1986.
- [47] R. A. Wolkow, "Direct observation of an increase in buckled dimers on Si(001) at low temperature." *Physical Review Letters*, vol. 68, pp. 2636–2639, 1992.
- [48] S. F. Bent, "Organic functionalization of group IV semiconductor surfaces: principles, examples, applications, and prospects," *Surface Science*, vol. 500, no. 1-3, pp. 879–903, Mar. 2002.
- [49] S. Kollakowski, "Silicon dioxide passivation of InP/InGaAs metal-semiconductor-metal photodetectors." *Journal of Vacuum Science and Technology B: Microelectronics and Nanometer Structures*, vol. 14, no. 1712, 1996.
- [50] A. Khaliq, "Interface chemistry and energy level alignment of silicon/organic semiconductor heterostructures studied with Synchrotron Radiation X-ray Photoelectron Spectroscopy and Near Edge X-ray Absorption Fine structure." Université Pierre et Marie Curie, Tech. Rep. September 2012, 2012.
- [51] J. D. Bozek, G. M. Bancroft, J. N. Cutler, and K. H. Tan, "Vibrationally resolved core-level photoelectron spectroscopy: Si 2p Levels of SiH_4 and SiF_4 molecules," *Physical review letters*, vol. 65, no. 22, pp. 2757–2760, 1990.
- [52] K. Prince, M. Vondracek, J. Karvonen, M. Coreno, R. Camilloni, L. Avaldi, and M. de Simone, "A critical comparison of selected 1s and 2p core hole widths," *Journal of Electron Spectroscopy and Related Phenomena*, vol. 101, pp. 141–147, 1999.

- [53] J. Olivero and R. Longbothum, "Empirical fits to the Voigt line width: A brief review," *Journal of Quantitative Spectroscopy and Radiative Transfer*, vol. 17, no. 2, pp. 233–236, 1977.
- [54] M. Nagao, Y. Yamashita, S. Machida, K. Hamaguchi, F. Yasui, K. Mukai, and J. Yoshinobu, "Nature of interface bonding of ethylene and benzene with Si(100)c(4x2): angle-dependent Si2p high resolution photoelectron spectroscopy studies," *Surface Science*, vol. 513, no. 3, pp. 413–421, 2002.
- [55] F. J. Himpsel, B. S. Meyerson, F. R. McFeely, J. F. Morar, A. Taleb-Ibrahimi, and J. Yarmoff, *Proceedings of the International School of Physics Enrico Fermi*, Varenna, Ed., 1988.
- [56] E. Landemark, C. J. Karlsson, Y.-C. Chao, and R. I. Uhrberg, "Core-Level Spectroscopy of the Clean Si(001) Surface: Charge Transfer within Asymmetric Dimers of the (2x1) and c(4x2) Reconstructions," *Physical review letters*, vol. 69, no. 10, p. 1588, Jan. 1992.
- [57] A. Pasquarello, M. S. Hybertsen, and R. Car, "Si 2p core-level shifts at the Si(001) – SiO₂ interface: a first principles study," *Physical review letters*, vol. 74, no. 6, p. 1024, 1995.
- [58] H. Koh, J. Kim, W. Choi, and H. Yeom, "Reinvestigation of the Si 2p photoemission line shape from a clean Si(001)c(4x2) surface," *Physical Review B*, vol. 67, no. 7, p. 073306, Feb. 2003.
- [59] J. Yoshinobu, H. Tsuda, M. Onchi, and M. Nishijima, "Rehybridization of acetylene on the Si(111)-7x7 surface - a vibrational study," *Chemical Physics Letters*, vol. 130, no. 3, pp. 170–174, 1986.
- [60] J. M. Buriak, "Organometallic chemistry on silicon and germanium surfaces." *Chemical reviews*, vol. 102, no. 5, pp. 1271–308, May 2002.
- [61] C. Fan and G. Lopinski, "STM and HREELS investigation of gas phase silanization

- on hydroxylated Si(100)," *Surface Science*, vol. 604, no. 11-12, pp. 996–1001, Jun. 2010.
- [62] J.-J. Gallet, F. Bournel, F. Rochet, S. Kubsky, M. G. Silly, F. Sirotti, D. Pierucci, and U. Kohler, "Isolated silicon dangling bonds on a water-saturated n^+ -doped Si(001)-2x1 surface: an XPS and STM study," *Journal of Physical Chemistry C*, no. 001, pp. 7686–7693, 2011.
- [63] J. Gallet, F. Bournel, D. Pierucci, M. Bonato, A. Khaliq, F. Rochet, M. Silly, and F. Sirotti, "A synchrotron radiation X-ray photoemission spectroscopy study of n-propyltriethoxysilane adsorption on Si(001)-2x1 at room temperature," *Journal of physical chemistry C*, no. 001, pp. 21 450–21 456, 2010.
- [64] H. Rauscher, "The interaction of silanes with silicon single crystal surfaces : microscopic processes and structures," *Surface Science Reports*, vol. 42, pp. 207–328, 2001.
- [65] Y. Nishi and R. Doering, *Handbook of Semiconductor Manufacturing Technology, Second Edition*. CRC Press, 2007.
- [66] S. K. Ray, C. K. Maiti, S. K. Lahiri, and N. B. Chakrabarti, "TEOS-based PECVD of silicon dioxide for VLSI applications," *Advanced Materials for Optics and Electronics*, vol. 6, no. 2, pp. 73–82, Mar. 1996.
- [67] K. Maeda and S. Fisher, "CVD TEOS/O₃ development history and applications," *Solid state technology*, vol. 6, no. 83, 1993.
- [68] J. Bonzel, H. P. Pirug, and G. Verhasselt, "Low temperature growth of SiO₂ films on Si(100) using a hot molecular beam of tetraethoxysilane." *Chemical Physics Letters*, vol. 271, no. 113, 1997.
- [69] J. B. Danner, M. A. Rueter, and J. M. Vohs, "Pathways and intermediates in the reaction of tetraethoxysilane on silicon (100)-2x1," *Langmuir*, vol. 9, pp. 455–459, 1993.

- [70] F. Himpsel, F. McFeely, A. Taleb-Ibrahimi, J. Yarmoff, and G. Hollinger, "Microscopic structure of the SiO_2/Si interface," *Physical Review B*, vol. 38, no. 9, pp. 6084–6096, Sep. 1988.
- [71] F. Jolly, F. Rochet, G. Dufour, C. Grupp, and A. Taleb-Ibrahimi, "Oxidized silicon surfaces studied by high resolution Si 2p core-level photoelectron spectroscopy using synchrotron radiation," *Journal of Non-Crystalline Solids*, vol. 280, no. 1-3, pp. 150–155, Feb. 2001.
- [72] A. Pasquarello, M. Hybertsen, and R. Car, "Theory of Si 2p core-level shifts at the $\text{Si}(001) - \text{SiO}_2$ interface," *Physical Review B*, vol. 53, no. 16, pp. 10 942–10 950, Apr. 1996.
- [73] O. Yazyev and A. Pasquarello, "Origin of fine structure in Si 2p photoelectron spectra at silicon surfaces and interfaces," *Physical Review Letters*, vol. 96, no. 15, p. 157601, Apr. 2006.
- [74] W. L. Jolly, K. D. Bomben, and C. J. Eyermann, "Core-electron binding energies for gaseous atoms and molecules." *Atomic Data and Nuclear Data Tables*, vol. 31, pp. 433–493, 1984.
- [75] A. Khaliq, D. Pierucci, H. Tissot, J.-J. Gallet, F. Bournel, F. Rochet, M. Silly, and F. Sirotti, "Ene-like reaction of cyclopentene on $\text{Si}(001)\text{-}2\times 1$: An XPS and NEXAFS Study," *The Journal of Physical Chemistry C*, vol. 116, no. 23, pp. 12 680–12 686, Jun. 2012.
- [76] S. Carniato, J.-J. Gallet, F. Rochet, G. Dufour, F. Bournel, S. Rangan, A. Verdini, and L. Floreano, "Characterization of hydroxyl groups on water-reacted $\text{Si}(001)\text{-}2\times 1$ using synchrotron radiation O 1s core-level spectroscopies and core-excited state density-functional calculations," *Physical Review B*, vol. 76, no. 8, p. 085321, Aug. 2007.
- [77] H. Wilson, N. Marks, and D. McKenzie, "Defect-induced dimer pinning on the $\text{Si}(001)$ surface," *Surface Science*, vol. 587, no. 3, pp. 185–192, Aug. 2005.

- [78] J. P. Perdew and Y. Wang, "Accurate and simple analytic representation of the electron-gas correlation energy," *Physical Review B*, vol. 45, no. 23, pp. 244–249, Jun. 1992.
- [79] G. Kresse, "Efficient iterative schemes for ab initio total-energy calculations using a plane-wave basis set," *Physical Review B*, vol. 54, no. 16, pp. 11 169–11 186, Oct. 1996.
- [80] G. Kresse and J. Hafner, "Ab initio molecular dynamics for liquid metals," *Physical Review B*, vol. 47, no. 1, pp. 558–561, Jan. 1993.
- [81] G. Brocks, P. Kelly, and R. Car, "Binding and diffusion of a Si adatom on the Si(100) surface," *Physical review letters*, vol. 66, no. 13, pp. 1729–1732, 1991.
- [82] J. Tersoff and D. R. Hamann, "Theory of the scanning tunneling microscope," *Physical Review B*, vol. 31, no. 2, pp. 805–813, Jan. 1985.
- [83] R. A. Wolkow, "Evidence of adsorbed atom pairing during homoepitaxial growth of silicon," *Physical review letters*, vol. 74, no. 22, p. 4448, 1995.
- [84] Z. Zhang, F. Wu, and M. G. Lagally, "An atomistic view of Si (001) homoepitaxy," *Annual Review of Material Science*, vol. 27, pp. 525–553, 1997.
- [85] Y. Wang, M. Bronikowski, and R. Hamers, "An atomically resolved scanning tunneling microscopy study of the thermal decomposition of disilane on Si(001)." *Surface Science*, vol. 311, no. 64, 1994.
- [86] J. Vasek, Z. Zhang, C. Salling, and M. Lagally, "Effects of hydrogen impurities on the diffusion, nucleation, and growth of Si on Si(001)." *Physical Review B*, vol. 51, no. 17207, 1995.
- [87] M. Fehrenbacher, J. Spitzmüller, U. Memmert, H. Rauscher, and R. Behm, "Interaction of SiH_4 with Si(100)-2x1 and with Si(111)-7x7 at 690 K: A comparative scanning tunneling microscopy study," *Journal of Vacuum Science and Technology A: Vacuum, Surfaces, and Films*, vol. 14, no. 3, p. 1499, May 1996.

- [88] Y.-W. Mo, J. Kleiner, M. Webb, and M. Lagally, "Surface self-diffusion of Si on Si(001)," *Surface Science*, vol. 268, no. 1-3, pp. 275–295, Jan. 1992.
- [89] B. S. Swartzentruber, "Kinetics of Si monomer trapping at steps and islands on Si(001)," *Physical Review B*, vol. 55, no. 3, pp. 1322–1325, Jan. 1997.
- [90] B. Swartzentruber, "Direct measurement of surface diffusion using atom-tracking scanning tunneling microscopy." *Physical review letters*, vol. 76, no. 3, pp. 459–462, Jan. 1996.
- [91] P. J. Bedrossian, "Si binding and nucleation on Si(100)," *Physical Review B*, vol. 74, no. 18, 1995.
- [92] V. Milman, S. Pennycook, and D. Jesson, "Ab initio total energy study of adsorption and diffusion on the Si(100) surface," *Thin Solid Films*, vol. 272, no. 2, pp. 375–385, Jan. 1996.
- [93] T. Stillinger, F. H., Weber, "Computer simulation of local order in condensed phases of silicon," *Physical Review B*, vol. 31, no. 8, pp. 5262–5271, 1985.
- [94] J. Tersoff, "New empirical model for the structural properties of silicon," *Physical review letters*, vol. 56, no. 6, pp. 632–635, 1986.
- [95] N. Roberts and R. Needs, "Total energy calculations of dimer reconstructions on the silicon (001) surface," *Surface Science*, vol. 236, no. 1, pp. 112–121, 1990.
- [96] A. P. Smith, J. K. Wiggs, H. Jonsson, H. Yan, L. R. Corrales, P. Nachtigall, and K. D. Jordan, "Si adatom binding and diffusion on the Si(100) surface: Comparison of ab initio, semiempirical and empirical potential results," *The Journal of Chemical Physics*, vol. 102, no. 2, p. 1044, 1995.
- [97] D. Shu, F. Liu, and X. Gong, "Simple generic method for predicting the effect of strain on surface diffusion," *Physical Review B*, vol. 64, no. 24, p. 245410, Nov. 2001.
- [98] S. Somasi, B. Khomami, and R. Lovett, "A density functional view of transition state theory: Simulating the rates at which Si adatoms hop on a silicon surface," *The Journal of Chemical Physics*, vol. 119, no. 18, p. 9783, 2003.

- [99] C. Toh and C. K. Ong, "Diffusion of a Si atom on the Si(001)-2x1 surface: A Monte Carlo study," *Physical Review B*, vol. 45, no. 19, pp. 120–125, 1992.
- [100] V. S. Kharlamov, Y. V. Trushin, E. E. Zhurkin, M. N. Lubov, and J. Pezoldt, "Study of Si and C adatoms and SiC clusters on the silicon surface by the molecular dynamics method," *Technical Physics*, vol. 53, no. 11, pp. 1490–1503, Nov. 2008.
- [101] M. I. Baskes, "Calculation of the behaviour of Si ad-dimers on Si(001)," *Modelling and Simulation in Materials Science and Engineering*, vol. 5, no. 2, pp. 149–158, Mar. 1997.
- [102] J. Cai and J.-S. Wang, "Reconstruction of Si(001) and adsorption of Si adatoms and ad-dimers on the surface: Many-body potential calculations," *Physical Review B*, vol. 64, no. 3, p. 035402, Jun. 2001.
- [103] Z.-Y. Zhang, Y.-T. Lu, and H. Metiu, "Adsorption and diffusion sites of a Si atom on a reconstructed Si(100)-2x1 surface," *Surface Science Letters*, vol. 248, no. 1-2, pp. L250–L254, May 1991.
- [104] C. Wang, Y. Jia, X. Wang, X. Li, X. Hu, and S. Wang, "Molecular dynamics simulation of single Si adatom diffusion on the Si(001) surface and across single-layer Si(001) steps," *Modern Physics Letters B*, vol. 22, no. 02, pp. 117–125, Jan. 2008.
- [105] T. Iijima and O. Sugino, "Molecular dynamics study of adatom diffusion on Si(100) surface - importance of the exchange mechanism," *Surface Science*, vol. 391, no. 1-3, pp. L1199–L1204, Nov. 1997.
- [106] A. D. Becke, "Density-functional thermochemistry. III. The role of exact exchange," *The Journal of Chemical Physics*, vol. 98, no. 7, p. 5648, Apr. 1993.
- [107] C. Lee, W. Yang, and R. G. Parr, "Development of the Colle-Salvetti correlation-energy formula into a functional of the electron density," *Physical Review B*, vol. 37, no. 2, pp. 785–789, Jan. 1988.

- [108] H. Tissot, J.-j. Gallet, F. Bournel, and A. Naitabdi, "Silicon monomer formation and surface patterning of Si (001)-2x1 following TEOS dissociative adsorption at room temperature," *Journal of Physical Chemistry C*, no. 001, pp. 1–21.
- [109] J. Spitzmüller, J. Braun, H. Rauscher, and R. Behm, "Dissociative adsorption and site specificity in the initial stages of tetraethoxysilane (TEOS) interaction with Si(111)-(7x7)," *Surface Science*, vol. 400, no. 1-3, pp. 356–366, Mar. 1998.
- [110] F. Polack, M. Silly, C. Chauvet, B. Lagarde, N. Bergeard, M. Izquierdo, O. Chubar, D. Krizmancic, M. Ribbens, J.-P. Duval, C. Basset, S. Kubsky, F. Sirotti, R. Garrett, I. Gentle, K. Nugent, and S. Wilkins, "TEMPO: a new insertion device beamline at SOLEIL for time resolved photoelectron spectroscopy experiments on solids and interfaces," *AIP Conference Proceedings*, vol. 185, pp. 185–188, Jun. 2010.
- [111] R. Denecke, P. Vaterlein, M. Bassler, N. Wassdahl, S. Butorin, A. Nilsson, J.-E. Rubensson, J. Nordgren, N. Martensson, and R. NYholm, "Beamline I511 at MAX II , capabilities and performance," *Journal of Electron Spectroscopy and Related Phenomena*, no. 101-103, pp. 971–977, 1999.
- [112] K. Wong and S. Bent, *Functionalization of Semiconductor Surfaces*, John Wiley ed., F. F. Tao and S. L. Bernasek, Eds. Hoboken, NJ, USA: John Wiley and Sons, Inc., Mar. 2012.
- [113] C. Karlsson, E. Landemark, Y.-C. Chao, and R. Uhrberg, "Atomic origins of the surface components in the Si 2p core-level spectra of the Si(111)-7x7 surface," *Physical Review B*, vol. 50, no. 8, pp. 5767–5770, Aug. 1994.
- [114] G. Le Lay, M. Gothelid, T. M. Grehk, M. Bjorkquist, U. O. Karlsson, and V. Y. Aristov, "Surface core-level shifts of Si(111)-7x7: A fundamental reassessment," *Physical Review B*, vol. 50, no. 19, pp. 14 277–14 282, Nov. 1994.
- [115] K. Raghavachari and J. Eng, "New structural model for Si/SiO₂ interfaces derived from spherosiloxane clusters: implications for Si 2p photoemission spectroscopy," *Physical Review Letters*, vol. 84, no. 5, pp. 935–938, Jan. 2000.

- [116] T. Kato, S.-Y. Kang, X. Xu, and T. Yamabe, "Possible dissociative adsorption of CH_3OH and CH_3NH_2 on Si(100)-2x1 Surface," *The Journal of Physical Chemistry B*, vol. 105, no. 42, pp. 10 340–10 347, Oct. 2001.
- [117] P. L. Silvestrelli, "Adsorption of ethanol on Si(100) from first principles calculations," *Surface Science*, vol. 552, no. 1, pp. 17–26, 2004.
- [118] M. Casaletto, R. Zanoni, M. Carbone, M. Piancastelli, L. Aballe, K. Weiss, and K. Horn, "High-resolution photoemission study of ethanol on Si(100)2x1," *Surface Science*, vol. 447, no. 1-3, pp. 237–244, Feb. 2000.
- [119] M. Carbone, M. Piancastelli, J. Paggel, C. Weindel, and K. Horn, "A high-resolution photoemission study of ethanol adsorption on Si(111)-(7x7)," *Surface Science*, vol. 412-413, pp. 441–446, Sep. 1998.
- [120] U. Kohler, "Scanning tunneling microscopy study of low-temperature epitaxial growth of silicon on Si(111)-(7x7)," *Journal of Vacuum Science and Technology A: Vacuum, Surfaces, and Films*, vol. 7, no. 4, p. 2860, Jul. 1989.
- [121] L. Whitman, S. Joyce, J. Yarmoff, F. McFeely, and L. Terminello, "The chemisorption of chlorosilanes and chlorine on Si(111)-7x7," *Surface Science*, vol. 232, no. 3, pp. 297–306, 1990.
- [122] M. Mantega, I. Rungger, B. Naydenov, J. Boland, and S. Sanvito, "Spectroscopic characterization of a single dangling bond on a bare Si(100)-c(4x2) surface for n^- and p^- type doping," *Physical Review B*, vol. 86, no. 3, pp. 3–7, Jul. 2012.
- [123] P. Chen, M. Colaianni, and J. Yates, "Silicon backbond strain effects on NH_3 surface chemistry: Si(111)-(7x7) compared to Si(100)-(2x1)," *Surface Science*, vol. 274, no. 3, pp. L605–L610, 1992.
- [124] C. Poncey, F. F. Rochet, G. Dufour, H. Roulet, F. Sirotti, and G. Panaccione, "Adsorption of water on Si(001)-2x1 and Si(111)-7x7 surfaces at 90 and 300 K : a Si 2p core-level and valence band study with synchrotron radiation," *Surface Science*, vol. 338, pp. 143–156, 1995.

- [125] D. Pierucci, "The electronic structure and reactivity of tri-coordinated silicon atoms on water-covered Si(001) surface: time-resolved XPS and STM studies," Ph.D. dissertation, Université Pierre et Marie Curie, 2013.
- [126] M. Hossain, Y. Yamashita, K. Mukai, and J. Yoshinobu, "Model for C defect on Si(100): The dissociative adsorption of a single water molecule on two adjacent dimers," *Physical Review B*, vol. 67, no. 15, p. 153307, Apr. 2003.
- [127] R. J. Hamers, "Determination of the local electronic structure of atomic-sized defects on Si(001) by tunneling spectroscopy," *Journal of Vacuum Science and Technology A: Vacuum, Surfaces, and Films*, vol. 7, no. 4, p. 2854, Jul. 1989.
- [128] D. Pierucci, A. Naitabdi, F. Bournel, J.-J. Gallet, H. Tissot, S. Carniato, F. Rochet, U. Köhler, D. Laumann, S. Kubsky, M. G. Silly, and F. Sirotti, "Benzaldehyde on water-saturated Si(001): reaction with isolated silicon dangling bonds versus concerted hydrosilylation," *The Journal of Physical Chemistry C*, vol. 118, no. 19, pp. 10 005–10 016, May 2014.
- [129] A. Verdaguer, C. Weis, G. Oncins, G. Ketteler, H. Bluhm, and M. Salmeron, "Growth and structure of water on SiO_2 films on Si Investigated by Kelvin probe microscopy and in Situ X-ray spectroscopies." *Langmuir : the ACS journal of surfaces and colloids*, vol. 23, no. 19, pp. 9699–703, Sep. 2007.
- [130] E. Rauwel, M.-G. Willinger, F. Ducroquet, P. Rauwel, I. Matko, D. Kiselev, and N. Pinna, "Carboxylic acids as oxygen sources for the atomic layer deposition of high-K metal oxides," *Journal of Physical Chemistry C*, vol. 112, no. 33, pp. 12 754–12 759, Aug. 2008.
- [131] E. Rauwel, G. Clavel, M.-G. Willinger, P. Rauwel, and N. Pinna, "Non-aqueous routes to metal oxide thin films by atomic layer deposition." *Angewandte Chemie*, vol. 47, no. 19, pp. 3592–5, Jan. 2008.
- [132] F. J. Himpsel, F. R. McFeely, A. Taleb-Ibrahimi, A. Yarmoff, and G. Hollinger, "Microscopic structure of the SiO_2/Si interface," *Physical Review B*, vol. 38, no. 9, 1988.

- [133] J. D. Ferguson, E. R. Smith, A. W. Weimer, and S. M. George, "ALD of SiO_2 at room temperature using TEOS and H_2O with NH_3 as the catalyst," *Journal of The Electrochemical Society*, vol. 151, no. 8, p. G528, Aug. 2004.
- [134] Q. Du, R. Superfine, E. Freysz, and Y. Shen, "Vibrational spectroscopy of water at the vapor/water interface," *Physical Review Letters*, vol. 70, no. 15, pp. 2313–2316, Apr. 1993.
- [135] J. S. Bader, C. M. Cortis, and B. J. Berne, "Solvation and reorganization energies in polarizable molecular and continuum solvents," *The Journal of Chemical Physics*, vol. 106, no. 6, p. 2372, Feb. 1997.
- [136] E. A. Raymond and G. L. Richmond, "Probing the molecular structure and bonding of the surface of aqueous salt solutions," *The Journal of Physical Chemistry B*, vol. 108, no. 16, pp. 5051–5059, Apr. 2004.
- [137] T. L. Tarbuck, S. T. Ota, and G. L. Richmond, "Spectroscopic studies of solvated hydrogen and hydroxide ions at aqueous surfaces." *Journal of the American Chemical Society*, vol. 128, no. 45, pp. 14 519–27, Nov. 2006.
- [138] K. R. Wilson, M. Cavalleri, B. S. Rude, R. D. Schaller, A. Nilsson, L. G. M. Pettersson, N. Goldman, T. Catalano, J. D. Bozek, and R. J. Saykally, "Characterization of hydrogen bond acceptor molecules at the water surface using near-edge x-ray absorption fine-structure spectroscopy and density functional theory," *Journal of Physics: Condensed Matter*, vol. 14, no. 8, pp. L221–L226, Mar. 2002.
- [139] I.-F. W. Kuo and C. J. Mundy, "An ab initio molecular dynamics study of the aqueous liquid-vapor interface." *Science*, vol. 303, no. 5658, pp. 658–60, Jan. 2004.
- [140] B. Winter, R. Weber, W. Widdra, M. Dittmar, M. Faubel, and I. V. Hertel, "Full valence band photoemission from liquid water using EUV synchrotron radiation," *The Journal of Physical Chemistry A*, vol. 108, no. 14, pp. 2625–2632, Apr. 2004.
- [141] B. Winter, E. F. Aziz, U. Hergenhan, M. Faubel, and I. V. Hertel, "Hydrogen

- bonds in liquid water studied by photoelectron spectroscopy." *The Journal of chemical physics*, vol. 126, no. 12, p. 124504, Mar. 2007.
- [142] V. Padmanabhan, J. Daillant, L. Belloni, S. Mora, M. Alba, and O. Konovalov, "Specific ion adsorption and short-range interactions at the air aqueous solution interface," *Physical Review Letters*, vol. 99, no. 8, p. 086105, Aug. 2007.
- [143] K. Arima, P. Jiang, X. Deng, H. Bluhm, and M. Salmeron, "Water adsorption, solvation, and Deliquescence of potassium bromide thin films on SiO_2 studied by ambient-pressure X-ray photoelectron spectroscopy," *The Journal of physical chemistry C*, vol. 114, pp. 14 900–14 906, 2010.
- [144] M. C. Gurau, S.-M. S.-M. Lim, E. T. Castellana, F. Albertorio, S. Kataoka, P. S. Cremer, and A. Fernando, "On the mechanism of the Hofmeister effect," *The journal of the american chemical society*, vol. 126, no. 34, p. 10522, Sep. 2004.
- [145] P. Jungwirth and B. Winter, "Ions at aqueous interfaces: from water surface to hydrated proteins." *Annual review of physical chemistry*, vol. 59, pp. 343–66, Jan. 2008.
- [146] F. Hofmeister, "Zur Lehre von der Wirkung der Salze. Zweite Mittheilung." *Arch. Exp. Pathol. Pharmacol.*, vol. 24, pp. 247–260, 1888.
- [147] A. P. dos Santos, A. Diehl, and Y. Levin, "Surface tensions, surface potentials, and the Hofmeister series of electrolyte solutions." *Langmuir : the ACS journal of surfaces and colloids*, vol. 26, no. 13, pp. 10 778–83, Jul. 2010.
- [148] D. Liu, G. Ma, L. M. Levering, and H. C. Allen, "Vibrational spectroscopy of aqueous sodium halide solutions and air-liquid interfaces: observation of increased interfacial depth," *The Journal of Physical Chemistry B*, vol. 108, no. 7, pp. 2252–2260, Feb. 2004.
- [149] B. Winter and M. Faubel, "Photoemission from liquid aqueous solutions," *Chemical Reviews*, vol. 106, pp. 1176–1211, 2006.

- [150] S. Ghosal, J. C. Hemminger, H. Bluhm, B. S. B. S. Mun, E. L. D. Hebenstreit, G. Ketteler, D. F. Ogletree, F. G. Requejo, M. Salmeron, and L. D. Hebenstreit, "Electron spectroscopy of aqueous solution interfaces reveals surface enhancement of halides." *Science*, vol. 307, no. 5709, pp. 563–6, Jan. 2005.
- [151] M. H. Cheng, K. M. Callahan, A. M. Margarella, D. J. Tobias, J. C. Hemminger, H. Bluhm, and M. J. Krisch, "Ambient pressure X-ray photoelectron spectroscopy and molecular dynamics simulation studies of liquid/vapor interfaces of aqueous NaCl, RbCl, and RbBr solutions," *The Journal of Physical Chemistry C*, vol. 116, no. 7, pp. 4545–4555, Feb. 2012.
- [152] P. Bauduin, A. Renoncourt, D. Touraud, W. Kunz, and B. Ninham, "Hofmeister effect on enzymatic catalysis and colloidal structures," *Current Opinion in Colloid and Interface Science*, vol. 9, no. 1, pp. 43–47, 2004.
- [153] T. L. Barr, "Nature of the use of adventitious carbon as a binding energy standard," *Journal of Vacuum Science and Technology A: Vacuum, Surfaces, and Films*, vol. 13, no. 3, p. 1239, May 1995.
- [154] M. Michaud, A. Wen, and L. Sanche, "Cross sections for lowenergy (1-100 eV) electron elastic and inelastic scattering in amorphous ice." *Radiation research*, vol. 3, no. 159, 2003.
- [155] D. Emfietzoglou and H. Nikjoo, "The effect of model approximations on single-collision distributions of low-energy electrons in liquid water," *Radiation Research*, vol. 163, no. 1, pp. 98–111, Jan. 2005.
- [156] J. Yeh and I. Lindau, "WebCrossSections," *Atomic Data and Nuclear Data Tables*, vol. 32, pp. 1–155, 1985.
- [157] S. Ghosal, A. Shbeeb, and J. C. Hemminger, "Surface segregation of bromine in bromide doped NaCl: Implications for the seasonal variations in Arctic ozone," *Geophysical Research Letters*, vol. 27, no. 13, pp. 1879–1882, Jul. 2000.

- [158] A. Thomson, D. Attwood, E. Gullikson, M. Howells, K. Kim, J. Kirz, J. Kortright, I. Lindau, Y. Liu, P. Pianetta, A. Robinson, J. Scofield, J. Underwood, G. Williams, and H. Winick, *X-Ray Data Booklet*. Lawrence Berkeley National Laboratory, University of California, 2009.
- [159] F. Seitz, "Color centers in alkali halide crystals," *Reviews of Modern Physics*, vol. 18, no. 3, pp. 384–408, Jul. 1946.
- [160] H. Hersh, "Proposed excitonic mechanism of color-center formation in alkali halides," *Physical Review*, vol. 148, no. 2, pp. 928–932, Aug. 1966.
- [161] N. Itoh and K. Tanimura, "Formation of interstitial-vacancy pairs by electronic excitation in pure ionic crystals," *Journal of Physics and Chemistry of Solids*, vol. 51, no. 7, pp. 717–735, Jan. 1990.
- [162] A. Mamou, J. Rabani, and D. Behar, "Oxidation of aqueous bromide by hydroxyl radicals, studies by pulse radiolysis," *The Journal of Physical Chemistry*, vol. 81, no. 15, pp. 1447–1448, Jul. 1977.
- [163] E. Thomas, Y. Rudich, S. Trakhtenberg, and R. Ussyshkin, "Water adsorption by hydrophobic organic surfaces: Experimental evidence and implications to the atmospheric properties of organic aerosols," *Journal of Geophysical Research*, vol. 104, no. D13, p. 16053, Jul. 1999.
- [164] P. Jungwirth and D. J. Tobias, "Specific ion effects at the air/water interface." *Chemical reviews*, vol. 106, no. 4, pp. 1259–81, Apr. 2006.
- [165] S. Trasatti, "The absolute electrode potential: an explanatory note," *Pure and Applied Chemistry*, vol. 58, no. 7, 1986.
- [166] J. Cheng and M. Sprik, "Alignment of electronic energy levels at electrochemical interfaces." *Physical chemistry chemical physics : PCCP*, vol. 14, no. 32, pp. 11 245–67, Aug. 2012.
- [167] B. Winter, R. Weber, I. V. Hertel, M. Faubel, P. Jungwirth, E. C. Brown, and S. E. Bradforth, "Electron binding energies of aqueous alkali and halide ions: EUV

- photoelectron spectroscopy of liquid solutions and combined ab initio and molecular dynamics calculations." *Journal of the American Chemical Society*, vol. 127, no. 19, pp. 7203–14, May 2005.
- [168] R. Sankari, M. Ehara, H. Nakatsuji, Y. Senba, K. Hosokawa, H. Yoshida, A. De Fanis, Y. Tamenori, S. Aksela, and K. Ueda, "Vibrationally resolved O 1s photoelectron spectrum of water," *Chemical Physics Letters*, vol. 380, no. 5-6, pp. 647–653, Oct. 2003.
- [169] P. Delahay, "Photoelectron emission spectroscopy of aqueous solutions," *Accounts of Chemical Research*, vol. 15, no. 2, pp. 40–45, Feb. 1982.
- [170] A. J. Nozik and R. Memming, "Physical chemistry of semiconductor-liquid interfaces," *The Journal of Physical Chemistry*, vol. 100, no. 31, pp. 13 061–13 078, Jan. 1996.
- [171] A. Allen, *The radiation chemistry of water and aqueous solutions*, D. Van Nostrand Company, Ed., 1961.
- [172] J. G. Mesu, A. M. Beale, F. M. F. de Groot, and B. M. Weckhuysen, "Probing the influence of X-rays on aqueous copper solutions using time-resolved in situ combined video/X-ray absorption near-edge/ultraviolet-visible spectroscopy." *The journal of physical chemistry. B*, vol. 110, no. 35, pp. 17 671–7, Sep. 2006.
- [173] F. Maier, M. Riedel, B. Mantel, J. Ristein, and L. Ley, "Origin of surface conductivity in diamond," *Physical Review Letters*, vol. 85, no. 16, pp. 3472–3475, Oct. 2000.
- [174] W. Chen, D. Qi, X. Gao, and A. T. S. Wee, "Surface transfer doping of semiconductors," *Progress in Surface Science*, vol. 84, no. 9-10, pp. 279–321, Sep. 2009.
- [175] A. L. Linsebigler, G. Lu, and J. T. Yates, "Photocatalysis on TiO_2 surfaces: principles, mechanisms, and selected results," *Chemical Reviews*, vol. 95, no. 3, pp. 735–758, May 1995.

- [176] Z. Zhang and J. T. Yates, "Band bending in semiconductors: chemical and physical consequences at surfaces and interfaces." *Chemical reviews*, vol. 112, no. 10, pp. 5520–51, Oct. 2012.
- [177] V. Gionis, G. H. Kacandes, I. D. Kastritis, and G. Chryssikos, "On the structure of palygorskite by mid- and near-infrared spectroscopy," *American Mineralogist*, vol. 91, no. 7, pp. 1125–1133, Jul. 2006.
- [178] S. Morodome and K. Kawamura, "In situ X-ray diffraction study of the swelling of montmorillonite as affected by exchangeable cations and temperature," *Clays and Clays Minerals*, vol. 57, no. 2, pp. 150–160, 2009.
- [179] R. W. G. Wyckoff, *Crystal Structures*, John Wiley and Sons, Ed., 1968, vol. 4.
- [180] G. Sposito and R. Prost, "Structure of water adsorbed on smectites," *Chemical Reviews*, vol. 82, no. 6, p. 553, 1982.
- [181] I. Berend, J.-M. Cases, M. Francois, J.-P. Uriot, L. Michot, A. Masion, and F. Thomas, "Mechanism of adsorption and desorption of water vapor by homoionic montmorillonites; 2, The Li^+ , Na^+ , K^+ , Rb^+ and Cs^+ -exchanged forms," *Clays and Clay Minerals*, vol. 43, no. 3, pp. 324–336, Jun. 1995.
- [182] J. M. Cases, I. Berend, G. Besson, M. Francois, J. P. Uriot, F. Thomas, and J. E. Poirier, "Mechanism of adsorption and desorption of water vapor by homoionic montmorillonite. 1. The sodium-exchanged form," *Langmuir*, vol. 8, no. 11, pp. 2730–2739, Nov. 1992.
- [183] J. M. Cases, I. Berend, M. Francois, J. P. Uriot, L. J. Michot, and F. Thomas, "Mechanism of adsorption and desorption of water vapor by homoionic montmorillonite; 3, The Mg^{2+} , Ca^{2+} , and Ba^{3+} exchanged forms," *Clays and Clay Minerals*, vol. 45, no. 1, pp. 8–22, Feb. 1997.
- [184] J. Fripiat, J. Cases, M. Francois, and M. Letellier, "Thermodynamic and microdynamic behavior of water in clay suspensions and gels," *Journal of Colloid and Interface Science*, vol. 89, no. 2, pp. 378–400, Oct. 1982.

- [185] A. Delville, "Structure of liquids at a solid interface: an application to the swelling of clay by water," *Langmuir*, vol. 8, no. 7, pp. 1796–1805, Jul. 1992.
- [186] G. Sposito, R. Prost, and J.-P. Gaultier, "Infrared spectroscopic study of adsorbed water on reduced-charge Na/Li-montmorillonites," *Clays and Clay Minerals*, vol. 31, no. 1, pp. 9–16, Feb. 1983.
- [187] E. S. Boek, P. V. Coveney, and N. T. Skipper, "Molecular modeling of clay hydration: a study of hysteresis loops in the swelling curves of sodium montmorillonites," *Langmuir*, vol. 11, no. 12, pp. 4629–4631, Dec. 1995.
- [188] F.-R. C. Chang, N. T. Skipper, and G. Sposito, "Monte Carlo and molecular dynamics simulations of interfacial structure in lithium-montmorillonite hydrates," *Langmuir*, vol. 13, no. 7, pp. 2074–2082, Apr. 1997.
- [189] M. Chavez-Paez, L. DePablo, and J. J. DePablo, "Monte Carlo simulations of Ca-montmorillonite hydrates," *The Journal of Chemical Physics*, vol. 114, no. 24, p. 10948, Jun. 2001.
- [190] V. Marry, P. Turq, T. Cartailier, and D. Levesque, "Microscopic simulation of structure and dynamics of water and counterions in a monohydrated montmorillonite," *The Journal of Chemical Physics*, vol. 117, no. 7, p. 3454, 2002.
- [191] K. Faisandier, C. H. Pons, D. Tchoubar, and F. Thomas, "Structural organization of Na- and K-montmorillonite suspensions response to osmotic and thermal stresses," *Clays and Clay Minerals*, vol. 46, no. 6, pp. 636–648, Dec. 1998.
- [192] L. J. Michot, F. Villieras, M. Francois, I. Bihannic, M. Pelletier, and J. M. Cases, "Water organisation at the solid-aqueous solution interface," *C. R. Geosciences*, vol. 334, pp. 611–631, 2002.
- [193] F. Salles, J.-M. Douillard, O. Bildstein, C. Gaudin, B. Prelot, J. Zajac, and H. Van Damme, "Driving force for the hydration of the swelling clays: case of montmorillonites saturated with alkaline-earth cations." *Journal of colloid and interface science*, vol. 395, pp. 269–76, Apr. 2013.

- [194] F. Salles, S. Devautour-Vinot, O. Bildstein, M. Jullien, G. Maurin, J.-C. Giuntini, J.-M. Douillard, and H. V. Damme, "Ionic mobility and hydration energies in montmorillonite clay," *The Journal of Physical Chemistry C*, vol. 112, no. 36, pp. 14 001–14 009, Sep. 2008.
- [195] E. J. M. Hensen and B. Smit, "Why clays swell," *The Journal of Physical Chemistry B*, vol. 106, no. 49, pp. 12 664–12 667, Dec. 2002.
- [196] H. Kalo, W. Milius, and J. Breu, "Single crystal structure refinement of one- and two-layer hydrates of sodium fluorohectorite," *RSC Advances*, vol. 2, no. 22, p. 8452, 2012.
- [197] B. Dazas, B. Lanson, J. Breu, J.-L. Robert, M. Pelletier, and E. Ferrage, "Smectite fluorination and its impact on interlayer water content and structure: A way to fine tune the hydrophilicity of clay surfaces?" *Microporous and Mesoporous Materials*, vol. 181, pp. 233–247, Nov. 2013.
- [198] A. Verdaguer, J. Jose, J. Fraxedas, and H. Bluhm, "Correlation between charge state of insulating NaCl surfaces and ionic mobility induced by water adsorption : a combined ambient pressure X-ray Photoelectron Spectroscopy and Scanning Force Microscopy study," *Journal of physical chemistry C*, vol. 21, pp. 16 898–16 901, 2008.
- [199] A. Shchukarev and S. Sjoberg, "XPS with fast-frozen samples: A renewed approach to study the real mineral/solution interface," *Surface Science*, vol. 584, no. 1, pp. 106–112, Jun. 2005.
- [200] A. Shchukarev, J. Rosenqvist, and S. Sjoberg, "XPS study of the silica–water interface," *Journal of Electron Spectroscopy and Related Phenomena*, vol. 137-140, no. April, pp. 171–176, Jul. 2004.
- [201] C. D. Wagner, D. E. Passoja, H. F. Hillery, T. G. Kinisky, H. A. Six, W. T. Jansen, and J. A. Taylor, "Auger and photoelectron line energy relationships in aluminium-oxygen and silicon-oxygen compounds," *Journal of Vacuum Science Technology*, vol. 21, p. 933, 1982.

- [202] D. Wagner and S. D. Company, "Chemical shifts of auger lines, and the auger parameter," 1975.
- [203] R. Weber, B. Winter, P. M. Schmidt, W. Widdra, I. V. Hertel, and D. Berlin, "Photoemission from aqueous alkali-metal - iodide salt solutions using EUV synchrotron radiation," *Journal of physical chemistry B*, pp. 4729–4736, 2004.
- [204] D. A. Laird, "Model for crystalline swelling of 2:1 phyllosilicates," *Clays and Clay Minerals*, vol. 44, no. 4, pp. 553–559, 1996.
- [205] Y. Marcus, "Ionic radii in aqueous solutions," *Chemical Reviews*, vol. 88, no. 8, pp. 1475–1498, Dec. 1988.
- [206] M. Z. Born, "Dielectric solvation and ion size," *Physik*, vol. 1, pp. 45–48, 1920.
- [207] M. Lundholm, H. Siegbahn, S. Holmberg, and M. Arbman, "Core electron spectroscopy of water solutions," *Journal of Electron Spectroscopy and Related Phenomena*, vol. 40, no. 2, pp. 163–180, Jan. 1986.
- [208] R. Weber, B. Winter, P. M. Schmidt, W. Widdra, I. V. Hertel, and D. Berlin, "Photoemission from aqueous alkali-metal - iodide salt solutions using EUV synchrotron radiation," pp. 4729–4736, 2004.